Department of Civil Engineering
University of Wales, Swansea

AN hp–ADAPTIVE FINITE ELEMENT PROCEDURE FOR ELECTROMAGNETIC SCATTERING PROBLEMS

PAUL DAVID LEDGER

BEng. MSc.

Thesis submitted to the University of Wales in candidature for the degree of Doctor of Philosophy

C/Ph/249/01

November 2001

Declaration

This work has not previously been accepted in substance for any degree and is not being concurrently submitted in candidature for any degree.

Signed . . . . . (Candidate)

Date . . . . . .

Statement 1

This thesis is the result of my own work/investigation except where otherwise stated. Other sources have been acknowledged by footnotes giving explicit references. A bibliography is appended.

Signed . . . . . (Candidate)

Date . . . . . .

Statement 2

I hereby give consent for my thesis, if accepted, to be available for photocopying and for inter–library loan, and for the title and summary to be made available to outside organizations

Signed . . . . . (Candidate)

Date . . . . . .

To my parents.

Acknowledgements

I would like to express my deepest gratitude to Professor K. Morgan whose expert advice and guidance has been invaluable throughout the course of this work. Thanks are also given to Dr. O. Hassan and Professor N.P. Weatherill for their help and advice on a variety of issues relating to this work. I would like to extend my gratitude to Professor J. Peraire of the Department of Astronautics and Aeronautics, M.I.T. for his helpful advice on issues relating to the error estimating process. Furthermore, I would like to to thank Professor M. Ainsworth and Dr. J. Coyle of the Department of Mathematics, University of Strathclyde and Dr. D.P. Rowse of BAE SYSTEMS for many fruitful discussions during the course of this work. I am indebted to my parents and to my sister who have always provided me with their support and encouragement. Finally, I wish to thank my friends for the friendship during the duration of this work, which has made may stay in Swansea enjoyable.

Summary

This thesis presents an adaptive finite element procedure for electromagnetic scattering problems in two dimensions. The work addresses the issues of higher order basis functions and demonstrates their advantages over lower order approximations. A new a–posteriori error estimator is derived which is capable of producing bounds on non–linear outputs of the scattering problem. Subsequently, this is used to automatically adapt both the polynomial order and the mesh spacing. The effectiveness of the procedures are demonstrated through a series of examples.

Contents

List of Figures

List of Tables

Nomenclature

$\boldsymbol{\Psi}$	Adjoint solution
θ	Angle of incidence
ϑ	Area coordinates for a triangle
$\phi_j^i, \phi_{j,k}^{I\xi} \cdots$	Basis functions
J_i	Bessel function of first kind, order i
Y_i	Bessel function of second kind, order i
N_i	Bilinear shape function for a quadrilateral
$\mathcal{A}$	Bilinear form for the scattering problem
a, m	Bilinear forms for stiffness and mass terms
Γ	Boundary to the domain Ω
Δ	Bound gap
$(x,\, y,\, z)$	Cartesian coordinates
σ^*	Conductivity
C	Constant
$\boldsymbol{a}^\xi, \boldsymbol{a}^\eta$	Contravariant vectors
$\boldsymbol{a}_\xi, \boldsymbol{a}_\eta, \boldsymbol{a}_z$	Covariant vectors

$(r,\, \phi)$	Cylindrical coordinates
d_j^p	Direction flag
Ω	A domain in $\mathbb{R}^2$
λ^U, λ^Ψ	Edge flux functionals
$\boldsymbol{f}_H^U, \boldsymbol{f}_H^\Psi$	Edge fluxes
$\tilde{\lambda}$	Eigenvalues
γ^*	Electric charge density
$\boldsymbol{J}_c^*$	Electric current density vector
$\boldsymbol{E}^*$	Electric field intensity vector
$\boldsymbol{D}^*$	Electric flux density vector
$\boldsymbol{e}$	Error in field variable
ω^*	Frequency
$\boldsymbol{A}, \boldsymbol{M}, \boldsymbol{L}$	Global stiffness, mass and boundary condition matrices
$\boldsymbol{\Phi}_i$	General real basis function
u_i	General complex coefficient
$H_i^{(2)}$	Hankel function of the second kind, order i
$\|\cdot\|_{\mathcal{H}^c}$	$\mathcal{H}(\text{curl}; \Omega)$ norm
$\mathcal{B}^s$	Hermitian positive definite bilinear form derived from $\mathcal{A}$
$\boldsymbol{I}$	Identity tensor
i	Imaginary unit ($= \sqrt{-1}$)
$\boldsymbol{U}^i$	Incident field vector

i, j, k, α, β	Indices
w_α	Integration weights for integration along an edge
wt_α	Integration weights for integration over a triangle
$P_j^{\alpha,\beta}$	Jacobi polynomial of order j and type α, β
$\boldsymbol{J}$	Jacobian matrix
$\|\cdot\|_{\mathcal{M}}$	L^2 type norm for the examination of the mass matrix convergence
p	Lagrange multiplier / Order of element[1]
q	Lagrange weighting function
L_j	Legendre polynomial of order j
ℓ_j	Integrated Legendre polynomial of order j
$\ell^{\mathcal{O}}$	Linear adjoint output
l	Linear form for boundary integral
ξ, η	Local master element coordinates
$\boldsymbol{H}^*$	Magnetic field intensity vector
$\boldsymbol{B}^*$	Magnetic flux density vector
ϖ	Measure of error used for adaptive purposes
$\mathcal{N}$	Non–linear output adjoint
$\mathcal{S}(\boldsymbol{U}^s; \phi)$	General output, which is a function of $\boldsymbol{U}^s$ and ϕ
ζ	Parameterisation between -1 and $+1$ along an edge
μ^*	Permeability

[1] It is unfortunate that p has a duplicate meaning, however, it should be obvious in the context of the expressions which meaning should apply

ϵ^*	Permittivity
$\boldsymbol{\Lambda}$	PML material coefficient tensor
σ	PML parameter
$\boldsymbol{R}^U, \boldsymbol{R}^\Psi$	Residual vectors
$\tilde{\boldsymbol{J}}$	Rotation matrix for PML mapping
κ	Scaling parameter
$\chi(\phi)$	Scattering width
$\|\cdot\|_{\mathcal{S}}$	Semi–norm for the examination of the stiffness matrix convergence
$\boldsymbol{U}$	Solution vector
$\boldsymbol{U}^s$	Scattered field vector
ς	Tolerance for adaptive algorithm
h	Truth mesh spacing
$\boldsymbol{\tau}$	Unit tangent vector
$\boldsymbol{n}$	Unit outward normal
s^+, s^-	Upper and lower bounds
δ	User input parameter to determine which polarisation is used
ϱ	User input parameter to determine the degree of refinement
λ	Wavelength
k	Wavenumber / Index[2]
$\boldsymbol{W}$	Weighting function

[2]It is unfortunate that k has a duplicate meaning, however, it should be obvious in the context of the expressions which meaning should apply

H	Working mesh spacing

Chapter 1

Introduction

1.1 Background

In the 17th century, Newton developed the mathematical notion of a gravitational force to describe planetary motion. Later came the concept of an elastic force, followed by the formulation of electric and magnetic forces.

Faraday discovered that electromagnetic forces were generated by fields, originating from charged objects. Furthermore, Maxwell found that an electromagnetic disturbance originated by a charged body is not immediately observed by another body, but instead travels out as a wave. Classical electromagnetic theory was mainly the product of research in the 19th century, but it has now been realised that electromagnetics has much wider applications than initially thought. To illustrate this, some modern application areas are now considered.

Antennae are used in the transmission of electromagnetic waves. They are now commonly visible on the roofs of tall buildings and on the tops of hills, often clearly visible from miles around. Their purpose is to provide communication links for radio, television and telephone systems. Many view antennae as an intrusion in to the countryside's natural beauty, but they are necessary as they provide an essential purpose of transmitting information around the globe.

Mobile phones operate by transmitting and receiving signals from antennae using electromagnetic waves. When these waves come in to contact with obstacles in

their path, scattering of the waves can occur. In addition, when waves are transmitted through penetrable media, such as the human brain, the energy from the waves may be absorbed. It is therefore of interest to medical personnel to find out how electromagnetic waves are transmitted through the brain and what, if any, effect they have.

Airline companies have banned the use of mobile phones on planes during flight. This is because the signals they produce may interfere with the aeroplanes electronic systems. This electromagnetic compatibility problem is currently of interest in the design of systems which are not effected by other electronic devices.

Electromagnetic waves can also be used in the detection of hidden targets. Determining the location of hidden land mines is a benefit that comes from the use of this technology. Another application is the discovery of geophysical features for use within the archeological community.

Radar is extensively used in the aerospace industry to track the course of civilian and military vehicles. The radar profile emerges from the scattering of electromagnetic waves across the surface of the vehicle. It is desirable to be able to predict a profile, in advance, to enable recognition. For certain military applications, such as the stealth fighter, it is desirable to minimise the radar profile observed.

Only a few topics in electromagnetics have been mentioned, but already it is possible to observe that the topic is wide ranging and has many applications.

1.2 Engineering Solutions

Traditionally engineers have used experimental and theoretical methods to solve problems in electromagnetics. However, theoretical methods tend to be limited in application to problems which involve simple geometries, whilst experimental methods can be expensive and place limits on the design cycle of a product.

To address these issues, there has been a move towards the use of computational methods, which are aimed at using a computer to produce a fast and cheap solution to engineering problems. This is an increasing trend which is driven in part by

the ever increasing capacity of modern machines. As these increases in computer resources have unfolded, there has been a concurrent development of new computational techniques. The accuracy of these computational techniques, is often measured by comparing the computational solution to an exact analytical solutions. This validation shows that accurate solutions can be obtained using a variety of different computational methods.

One area of electromagnetics which presents a significant computational challenge is the calculation of the radar profile for the electromagnetic scattering problem. For the frequencies of interest, the wavelength of the waves is very short compared to the length of the scatterer. This means that, even using current computational techniques on the world's most efficient computers, the solution to this problem still presents a significant challenge.

1.3 Computer Methods for Scattering Problems

A number of computer methods are currently employed to solve electromagnetic scattering problems. One of the most popular, and oldest, methods is the finite difference method. This method has been held in high respect, due to the efficiency of a particular implementation, called the Yee scheme [1]. This scheme provides a very fast method which is capable of producing accurate solutions in the time domain. However, the method suffers from the drawback that it only provides a pointwise approximation of the solution. In this sense, it can not provide accurate solutions for complex geometries which occur in real life problems.

In engineering mechanics, one of the most widely used technique for the numerical solution of differential equations is the finite element method [2]. This method was originally developed for the aerospace industry for the analysis of the stresses strains that were placed on a vehicle during flight. Over the last 30 years, the method has been shown to be flexible and it is now applied to a variety of challenging problems in different areas of engineering mechanics, including electromagnetics. In particular, the ability to model complex geometries by unstructured meshes has en-

abled the solution of a number of challenging problems, including electromagnetic scattering by a complete aircraft [3]. Unfortunately, the wavelengths which can be solved using this method are still much larger than those which are of interest to industry.

To address these issues, there has been an intense drive for efficient strategies over the last decade. In particular, we have seen how the use of parallel programming of the finite element method in the time domain has led to greater efficiency of the computational algorithm and allowed the solution of much larger problems [3]. Recently, the use of discontinuous Galerkin methods coupled with a spectral discretisation in the time domain [4] has also enabled the solution of some very large problems. There has been extensive research, eg. [5, 6, 7], in to alternative absorbing boundary conditions which allow the reduction in the size of the computational domain. The use of overlapping meshes in the finite difference time domain [8] has also led to its application to a number of new challenging problems.

In the frequency domain, the use of higher order elements [7, 9, 10, 11, 12, 13, 14, 15, 16, 17, 18] has allowed the efficient modelling of multilayer structures. The use of new novel finite elements [19, 20] also holds great promise for the solution of large scale scattering problems. The use of fast multipole methods [21], although currently limited in application, also shows that large scale scattering simulations can be undertaken with current computer resources.

The question of accuracy and reliability of numerical solutions has led to the development of a large number of efficient and accurate error estimators in engineering mechanics [22]. These estimators enable the quantification of the error for problems that have no analytical solution and therefore are of great interest. Very often, these estimates are then employed to adaptively refine until a desired tolerance is reached. Recent work [23, 24, 25, 26], which is of great interest, involves the ability to place rigorous upper and lower bounds on a computed numerical solution. In this way, one is able to iterate a design procedure until the desired tolerance is achieved. The application of this technique to the area of electromagnetics remains wide open.

1.4 Objective of the Work

The objective of this work is to generate a new adaptive finite element procedure for two dimensional electromagnetic scattering problems in the frequency domain. In particular, the approach is to be implemented on hybrid meshes of higher order quadrilateral and triangular elements. We intend to use an error bound evaluation procedure to place quantitative bounds on an engineering output of the scattering problem. It is then hoped that this will be able to provide an automatic adaptive finite element solution procedure.

Using this scheme, it is hoped that scattering by electrically large structures can be undertaken to a prescribed degree of accuracy. The success of these computations will show how viable a three dimensional extension may be. To achieve this objective, we split the work in to a number of specific stages, which are described in the outline of the thesis.

1.5 Outline of the Thesis

This thesis is composed of nine chapters. The main body of the work is contained in Chapters 2 to 8 and the conclusions of the work are presented in Chapter 9. In addition to the nine chapters, an appendix describes further details of some of the issues raised in the thesis. A brief description of the material covered in these chapters is:

- Chapter 2 is entitled Mathematical Model of Electromagnetics. This chapter describes the underlying theory of the electromagnetic problems described in this thesis. It also provides the mathematical tools which are employed in the remaining chapters.

- Chapter 3 is entitled Geometry Representation and Basis Functions. The aim of this chapter is provide the information that is required to implement the higher order finite element method which is advocated in this thesis. We

address the issues of how the field variables are represented and how the geometry is approximated.

- Chapter 4 is entitled Performance of the Edge Element Basis. This chapter seeks to address the convergence and accuracy of the proposed scheme by analyzing a model problem with known exact solution. Issues relating to the dispersion in the simulation of wave propagation problems are also raised.

- Chapter 5 is entitled Edge Element Formulation for Scattering Problems. The purpose of this chapter is to present a complete derivation of a finite element procedure for scattering problems. A summary of the available methods for truncation of the infinite domain is given.

- Chapter 6 is entitled Results of the Edge Element Approach for Scattering Problems. This chapter shows the effectiveness of the proposed scattering formulation through the solution of a series of numerical examples.

- Chapter 7 is entitled A–posteriori Error Estimator for Scattering Problems. This presents an application of the error bound evaluation procedure [23, 24, 25] to electromagnetic scattering problems. The chapter proposes an extension to the original method which is capable of dealing with higher order elements.

- Chapter 8 is entitled Adaptive Procedures for Electromagnetic Scattering Problems. In this chapter, the local contributions to the error estimator described in Chapter 7 are employed to adaptively refine the discretisation. Local refinement of the mesh and local refinement of the polynomial order are considered.

- Chapter 9 presents the conclusion and suggests some areas for further work.

Chapter 2

Mathematical Model of Electromagnetics

2.1 Introduction

Electromagnetic phenomena are governed by Maxwell's Equations. These equations relate the electric and magnetic field intensity vectors ($\boldsymbol{E}^*$ and $\boldsymbol{H}^*$ respectively) and the material properties of the medium. The full set of equations may be written as

$$\text{div } \boldsymbol{D}^* = \gamma^* \tag{2.1}$$

$$\text{div } \boldsymbol{B}^* = 0 \tag{2.2}$$

$$\text{curl } \boldsymbol{H}^* = \boldsymbol{J}_c^* + \frac{\partial \boldsymbol{D}^*}{\partial t} \tag{2.3}$$

$$\text{curl } \boldsymbol{E}^* = -\frac{\partial \boldsymbol{B}^*}{\partial t} \tag{2.4}$$

In addition, the auxiliary equations

$$\text{div } \boldsymbol{J}_c^* + \frac{\partial \gamma^*}{\partial t} = 0 \qquad \text{continuity equation} \tag{2.5}$$

$$\boldsymbol{D}^* = \epsilon^* \boldsymbol{E}^* \quad \boldsymbol{B}^* = \mu^* \boldsymbol{H}^* \quad \boldsymbol{J}^* = \sigma^* \boldsymbol{E}^* \qquad \text{constitutive equations} \tag{2.6}$$

must be added to complete the set. Here $\boldsymbol{D}^*$ is the electric flux density vector, γ^* is the electric charge density. $\boldsymbol{B}^*$ is the magnetic flux density vector and $\boldsymbol{J}_c^*$ is

the electric current density vector. In addition, $\epsilon^*,\ \mu^*,\ \sigma^*$ denote the permittivity, permeability and conductivity respectively of the medium.

For many practical problems, we can apply simplifying assumptions to the governing equations. The assumptions we wish to make concern the behaviour of the materials that we wish to use. For this thesis, we will assume that

1. the medium obeys Ohm's Law $\boldsymbol{J}_c^* = \sigma^* \boldsymbol{E}^*$;
2. the electric charge density is zero $(\gamma^* = 0)$;
3. all materials will be assumed to be non-lossy;
4. the conductivity of the materials is negligible $(\sigma^* = 0)$;
5. the permittivity and permeability do not vary in time;
6. problems will be restricted to two dimensions.

By imposing these conditions on Maxwell's equations, and employing the constitutive relations, it can be deduced that

$$\text{curl } \boldsymbol{H}^* = \epsilon^* \frac{\partial \boldsymbol{E}^*}{\partial t} \tag{2.7}$$

$$\text{curl } \boldsymbol{E}^* = -\mu^* \frac{\partial \boldsymbol{H}^*}{\partial t} \tag{2.8}$$

$$\text{div } \epsilon^* \boldsymbol{E}^* = 0 \tag{2.9}$$

$$\text{div } \mu^* \boldsymbol{H}^* = 0 \tag{2.10}$$

It should be observed that Maxwell's equations have now reduced to a set of two curl equations and two divergence equations involving only the electric and magnetic field intensity vectors and two material properties. It is the numerical solution of this set of four equations that will receive attention in this thesis.

2.2 Vector Wave Equations

In this section, we combine the two curl equations to form a vector wave equation, governing the variation of either the electric or the magnetic field intensity. Follow-

ing the approach outlined in Seely [27], we derive the wave equation for the electric field. Taking the curl of equation (2.8) gives

$$\text{curl } \left(\mu^{*-1}\text{curl } \boldsymbol{E}^*\right) = -\text{curl } \frac{\partial \boldsymbol{H}^*}{\partial t} \tag{2.11}$$

Interchanging the derivatives on the right hand side of the above equation, we can write

$$-\text{curl } \frac{\partial \boldsymbol{H}^*}{\partial t} = -\frac{\partial}{\partial t}(\text{curl } \boldsymbol{H}^*) \tag{2.12}$$

and, using equation (2.7), it follows that

$$\text{curl } \left(\mu^{*-1}\text{curl } \boldsymbol{E}^*\right) = -\frac{\partial}{\partial t}\left\{\epsilon^* \frac{\partial \boldsymbol{E}^*}{\partial t}\right\} \tag{2.13}$$

Finally, we have that the electric field satisfies the wave equation

$$\text{curl } \left(\mu^{*-1}\text{curl } \boldsymbol{E}^*\right) + \epsilon^* \frac{\partial^2 \boldsymbol{E}^*}{\partial t^2} = \boldsymbol{0} \tag{2.14}$$

It is noted that a similar process yields the result

$$\text{curl } \left(\epsilon^{*-1}\text{curl } \boldsymbol{H}^*\right) + \mu^* \frac{\partial^2 \boldsymbol{H}^*}{\partial t^2} = \boldsymbol{0} \tag{2.15}$$

for the magnetic field.

2.3 Eliminating Time Dependence

When the electric and magnetic fields are such that their time variation is harmonic (composed of sine or cosine waves), the mathematical analysis can be simplified. By restricting ourselves to a wave of single frequency, ω^*, we have that

$$\boldsymbol{E}^* = \boldsymbol{E}(\cos \omega^* t + \mathrm{i} \sin \omega^* t) = \boldsymbol{E} e^{\mathrm{i}\omega^* t} \tag{2.16}$$

$$\boldsymbol{H}^* = \boldsymbol{H}(\cos \omega^* t + \mathrm{i} \sin \omega^* t) = \boldsymbol{H} e^{\mathrm{i}\omega^* t} \tag{2.17}$$

where k denotes the wave number and $\boldsymbol{E}$ and $\boldsymbol{H}$ should now be interpreted as complex quantities. The wave number of a single frequency wave is given by

$$k^2 = \omega^{*2} \mu^* \epsilon^* \tag{2.18}$$

and it is therefore a function of the properties of the medium. On substituting equation (2.16) in to (2.14), and (2.17) into (2.15), the vector wave equations become

$$\text{curl } \left(\mu^{*-1}\text{curl } \boldsymbol{E}\right) - \omega^{*2}\epsilon^{*}\boldsymbol{E} = \boldsymbol{0} \tag{2.19}$$

$$\text{curl } \left(\epsilon^{*-1}\text{curl } \boldsymbol{H}\right) - \omega^{*2}\mu^{*}\boldsymbol{H} = \boldsymbol{0} \tag{2.20}$$

These equations are the usual starting point for the development of frequency domain algorithms.

2.4 Polarisation

For all problems in two dimensions, one can simplify the analysis by employing decomposition in to transverse electric (TE) and transverse magnetic (TM) polarisations. In the TE polarisation, we assume the z component of electric field to be zero. Hence this reduces the number of electric components that need to be solved. To reconstruct the magnetic field for the TE polarisation, reconsider equation (2.8) now assuming that the time variation is harmonic

$$\text{curl } \boldsymbol{E} = -\text{i}\mu^{*}\omega^{*}\boldsymbol{H} \tag{2.21}$$

Thus, once $\boldsymbol{E}$ has been found, we can determine $\boldsymbol{H}$ for the TE polarisation. Similarly, the TM polarisation assumes the z component of the magnetic field to be zero. Construction of the electric field follows from

$$\text{curl } \boldsymbol{H} = \text{i}\epsilon^{*}\omega^{*}\boldsymbol{E} \tag{2.22}$$

which is the equation which results from employing equations (2.16) and (2.17) in equation (2.7).

2.5 Boundary Conditions

No mention has yet been made of the boundary conditions which are to be applied to the governing wave equations (2.19) and (2.20).

2.5.1 PEC Wall

Suppose that the boundary, Γ_{PEC}, of a domain Ω, is adjacent to a region that has infinite conductivity. A material of infinite electrical conductivity is called a perfect electrical conductor. Perfect electrical conductors are often used to approximate regions of very high conductivity. In a perfect conductor, no normal magnetic or tangential electric field can exist. To simulate this, the conditions

$$\boldsymbol{n} \wedge \boldsymbol{E} = \boldsymbol{0} \qquad \boldsymbol{n} \cdot (\mu^* \boldsymbol{H}) = 0 \tag{2.23}$$

should be enforced on Γ_{PEC} where $\boldsymbol{n}$ is the unit outward normal to the surface.

2.5.2 Magnetic Wall

A magnetic wall [28] is introduced to aid application of PEC boundary conditions in the TM polarisation. The magnetic wall forms the boundary Γ_{MAG} to (part of) the domain Ω By swapping the electric and magnetic fields, and permeability for permittivity in equation (2.23) we obtain the conditions

$$\boldsymbol{n} \wedge \boldsymbol{H} = \boldsymbol{0} \qquad \boldsymbol{n} \cdot (\epsilon^* \boldsymbol{E}) = 0 \tag{2.24}$$

that should be enforced on Γ_{MAG}.

2.5.3 Dielectric Interface

At an interface between two distinct materials, a and b, the boundary conditions that should be enforced are

$$\boldsymbol{n} \wedge \boldsymbol{E}^a = \boldsymbol{n} \wedge \boldsymbol{E}^b \qquad \boldsymbol{n} \wedge \boldsymbol{H}^a = \boldsymbol{n} \wedge \boldsymbol{H}^b \tag{2.25}$$

$$\boldsymbol{n} \cdot \epsilon_a^* \boldsymbol{E}^a = \boldsymbol{n} \cdot \epsilon_b^* \boldsymbol{E}^b \qquad \boldsymbol{n} \cdot \mu_a^* \boldsymbol{H}^a = \boldsymbol{n} \cdot \mu_b^* \boldsymbol{H}^b \tag{2.26}$$

These require the tangential components of the electric and magnetic fields to be continuous over the interface. In addition, the normal components of electric and magnetic flux density vectors are to be continuous.

2.6 Non–Dimensional Strong Form

There is a common misconception amongst the electromagnetic community that, when solving the time harmonic curl curl equations, one can neglect the divergence condition. This, however, is not the case in general. If one determines a solution $\boldsymbol{E}$ which satisfies equation (2.19) then it follows, from taking divergence of (2.19), that this solution is only divergence free provided that $\omega^* > 0$ [29]. A similar argument applies for the magnetic field in equation (2.20). For the case when ω^* is not specified, then one cannot guarantee that the solution $\boldsymbol{E}$ to equation (2.19), or the solution $\boldsymbol{H}$ to equation (2.20) is divergence free. Here, we must include the divergence conditions.

Therefore, the governing equations are considered in the strong form

$$\text{curl } \left({\alpha_1}^{-1}\text{curl } \boldsymbol{U}\right) - \omega^2 \alpha_2 \boldsymbol{U} = \boldsymbol{0} \qquad \text{div } \alpha_2 \boldsymbol{U} = 0 \tag{2.27}$$

Here the solution vector $\boldsymbol{U}$ is defined as

$$\boldsymbol{U} = \begin{cases} \boldsymbol{E} & \text{for } \delta = 1 \\ \boldsymbol{H} & \text{for } \delta = -1 \end{cases} \tag{2.28}$$

where δ is parameter which is equal to 1 for the TE polarisation and equal to -1 for the TM polarisation and the problem coefficients

$$\alpha_1 = \mu \qquad \alpha_2 = \epsilon \qquad \text{for } \delta = 1 \tag{2.29}$$

$$\alpha_1 = \epsilon \qquad \alpha_2 = \mu \qquad \text{for } \delta = -1 \tag{2.30}$$

are written in terms of relative permeability and permittivity. These relative quantities are defined as

$$\epsilon = \frac{\epsilon^*}{\epsilon_{fs}} \qquad \mu = \frac{\mu^*}{\mu_{fs}} \tag{2.31}$$

where ϵ_{fs} and μ_{fs} are the values for free space and the scaled frequency is defined as

$$\omega = \omega^* \sqrt{\epsilon_{fs} \mu_{fs}} \tag{2.32}$$

The recovered field vector

$$\boldsymbol{V} = -\frac{\delta \alpha_1^{-1}}{\mathrm{i}\omega} \text{curl } \boldsymbol{U} = \begin{cases} \boldsymbol{H} \sqrt{\frac{\mu_{fs}}{\epsilon_{fs}}} & \text{for } \delta = 1 \\ \boldsymbol{E} \sqrt{\frac{\epsilon_{fs}}{\mu_{fs}}} & \text{for } \delta = -1 \end{cases} \tag{2.33}$$

is defined in terms of the solution vector and the problem coefficients. The boundary conditions at a perfect conductor or at a magnetic wall, are written as

$$\boldsymbol{n} \wedge \boldsymbol{U} = \boldsymbol{0} \qquad \text{on } \Gamma_D \tag{2.34}$$

$$\boldsymbol{n} \wedge \alpha_1^{-1}\text{curl } \boldsymbol{U} = \boldsymbol{0} \qquad \text{and} \qquad \boldsymbol{n} \cdot \alpha_2 \boldsymbol{U} = 0 \qquad \text{on } \Gamma_N \tag{2.35}$$

where

$$\Gamma_D = \begin{cases} \Gamma_{PEC} & \text{for } \delta = 1 \\ \Gamma_{MAG} & \text{for } \delta = -1 \end{cases} \tag{2.36}$$

$$\Gamma_N = \begin{cases} \Gamma_{MAG} & \text{for } \delta = 1 \\ \Gamma_{PEC} & \text{for } \delta = -1 \end{cases} \tag{2.37}$$

Note that the condition $\boldsymbol{n} \cdot \text{curl } \boldsymbol{U} = 0$ on Γ_D is not included in the set, as it is automatically satisfied by TE or TM waves. The material interface conditions are

$$\boldsymbol{n} \wedge \boldsymbol{U}^a = \boldsymbol{n} \wedge \boldsymbol{U}^b \qquad \boldsymbol{n} \wedge \alpha_1^{-1a}\text{curl } \boldsymbol{U}^a = \boldsymbol{n} \wedge \alpha_1^{-1b}\text{curl } \boldsymbol{U}^b \tag{2.38}$$

$$\boldsymbol{n} \cdot \alpha_2^a \boldsymbol{U}^a = \boldsymbol{n} \cdot \alpha_2^b \boldsymbol{U}^b \tag{2.39}$$

where the condition $\boldsymbol{n} \cdot \text{curl } \boldsymbol{U}^a = \boldsymbol{n} \cdot \text{curl } \boldsymbol{U}^b$ is not included also as it is automatically satisfied by TE or TM waves.

2.7 Uniqueness of the Strong Form

In this section we examine whether the solution that is admitted by the strong form is the only possible solution. We have already seen that including the divergence condition is necessary to enforce zero divergence if ω is not specified. To show uniqueness of the solution of Maxwell's curl equations, and hence of the vector wave equation (2.27), Balanis [28] considers two possible solutions $\boldsymbol{U}_a$ and $\boldsymbol{U}_b$ of the strong form. He shows that the difference $\Delta\boldsymbol{U} = \boldsymbol{U}_a - \boldsymbol{U}_b$ also satisfies Maxwells curl equations and that this difference is zero when $\boldsymbol{U}_a = \boldsymbol{U}_b$. In fact, Balanis obtains uniqueness for the following cases in a lossless medium:

1. if $\boldsymbol{n} \wedge \boldsymbol{U}$ is specified on Γ_D; then $\boldsymbol{n} \wedge \Delta\boldsymbol{U} = 0$ on Γ_D. No specification of the normal conditions are necessary when considering only the vector wave equation;

2. if $\boldsymbol{n} \wedge \alpha_1^{-1}\text{curl}\,\boldsymbol{U}$ is specified on Γ_N; then $\boldsymbol{n} \wedge \alpha_1^{-1}\text{curl}\,\Delta\boldsymbol{U} = 0$ over Γ_N;

The inclusion of normal conditions in the strong form is, therefore, only necessary due to the inclusion of the divergence condition.

2.8 An Initial Weak Variational Formulation

With a numerical solution procedure in mind, a weak variational formulation is derived. For this, we introduce the notion of a domain, Ω, where the solution is of interest and insist that this domain is strictly bounded by a boundary Γ_F on which the solution $\boldsymbol{U}$ is known and is divergence free.

It has been shown [29] that the correct mathematical space for the solution $\boldsymbol{U}$ of this problem is

$$Z = \{\boldsymbol{u} \in \mathcal{H}(\text{curl}; \Omega); \text{div}\,\alpha_2\boldsymbol{u} = 0\} \tag{2.40}$$

where

$$\mathcal{H}(\text{curl}; \Omega) = \left\{\boldsymbol{u} \in (L^2(\Omega))^3; \text{curl}\,\boldsymbol{u} \in L^2(\Omega)\right\} \tag{2.41}$$

Equipped with these definitions, the variational formulation of the problem may be derived. If we introduce a weighting function $\boldsymbol{W} \in \mathcal{H}(\text{curl}; \Omega)$, multiply its complex conjugate $\overline{\boldsymbol{W}}$ by the vector wave equation (2.27) and integrate over a domain Ω we deduce the variational form

$$\int_\Omega \left\{\text{curl}\,\alpha_1^{-1}\text{curl}\,\boldsymbol{U} \cdot \overline{\boldsymbol{W}} - \omega^2\alpha_2\boldsymbol{U} \cdot \overline{\boldsymbol{W}}\right\} \mathrm{d}\Omega = 0 \tag{2.42}$$

Application of the vector identity $(\text{curl}\,\boldsymbol{A}) \cdot \boldsymbol{B} = \boldsymbol{A} \cdot (\text{curl}\,\boldsymbol{B}) - \text{div}\,(\boldsymbol{B} \wedge \boldsymbol{A})$ leads to

$$\int_\Omega \left\{\alpha_1^{-1}\text{curl}\,\boldsymbol{U} \cdot \text{curl}\,\overline{\boldsymbol{W}} - \omega^2\alpha_2\boldsymbol{U} \cdot \overline{\boldsymbol{W}}\right\} \mathrm{d}\Omega = \int_\Omega \left\{\text{div}\,\left(\overline{\boldsymbol{W}} \wedge \alpha_1^{-1}\text{curl}\,\boldsymbol{U}\right)\right\} \mathrm{d}\Omega \tag{2.43}$$

The divergence theorem for a continuously differentiatable vector field $\boldsymbol{C}$ which exists in a domain Ω bounded by the closed surface Γ can be written as

$$\int_{\Omega} \operatorname{div} \boldsymbol{C} \, \mathrm{d}\Omega = \int_{\Gamma} \boldsymbol{n} \cdot \boldsymbol{C} \, \mathrm{d}\Gamma \tag{2.44}$$

where $\boldsymbol{n}$ is the unit outward normal to the surface. When the divergence theorem is applied to the right hand side of equation (2.43), we have

$$\int_{\Omega} \left\{ \alpha_1^{-1} \text{curl}\, \boldsymbol{U} \cdot \text{curl}\, \overline{\boldsymbol{W}} - \omega^2 \alpha_2 \, \boldsymbol{U} \cdot \overline{\boldsymbol{W}} \right\} \mathrm{d}\Omega = \int_{\Gamma_F} \left\{ \boldsymbol{n} \cdot \left(\overline{\boldsymbol{W}} \wedge \alpha_1^{-1} \text{curl}\, \boldsymbol{U} \right) \right\} \mathrm{d}\Gamma \tag{2.45}$$

This means that a weak variational formulation of the problem can be written as: find $\boldsymbol{U} \in Z$ such that

$$\int_{\Omega} \left\{ \alpha_1^{-1} \text{curl}\, \boldsymbol{U} \cdot \text{curl}\, \overline{\boldsymbol{W}} - \omega^2 \alpha_2 \boldsymbol{U} \cdot \overline{\boldsymbol{W}} \right\} \mathrm{d}\Omega = - \int_{\Gamma_F} \left\{ \overline{\boldsymbol{W}} \cdot \left(\boldsymbol{n} \wedge \alpha_1^{-1} \text{curl}\, \boldsymbol{U} \right) \right\} \mathrm{d}\Gamma \qquad \forall \boldsymbol{W} \in \mathcal{H}(\text{curl}; \Omega) \tag{2.46}$$

following manipulation of the scalar triple product.

2.9 An Initial Mixed Formulation

The approach of Kikuchi [29] and of Demkowicz [9, 10, 11, 7, 12], is to re-impose the divergence condition as a additional constraint to the problem. Firstly, they introduce a space of Lagrange multipliers

$$V = \left\{ p \in \mathcal{H}^1(\Omega) : p = 0 \text{ on } \Gamma_F \right\} \tag{2.47}$$

where the Lagrange multiplier p is set to zero on boundaries at which the constraint $\boldsymbol{n} \wedge \boldsymbol{U} = \boldsymbol{0}$ is to be imposed, or those which impose divergence free fields. Then, by substituting $\operatorname{grad} q$ (where $q \in V$) for $\boldsymbol{W}$ in equation (2.46) it follows that

$$- \int_{\Omega} \omega^2 \alpha_2 \boldsymbol{U} \cdot \operatorname{grad} \overline{q} \, \mathrm{d}\Omega = 0 \qquad \forall q \in V \tag{2.48}$$

This is the weak variational form of the divergence constraint. Finally, substituting $\boldsymbol{U} + \operatorname{grad} p$ for $\boldsymbol{U}$ in equation (2.46), and considering the new divergence constraint,

leads to the mixed form: find $\boldsymbol{U} \in \mathcal{H}(\text{curl}; \Omega)$ and $p \in V$ such that

$$\int_\Omega \left\{ \alpha_1^{-1} \text{curl}\, \boldsymbol{U} \cdot \text{curl}\, \overline{\boldsymbol{W}} - \omega^2 \alpha_2 (\boldsymbol{U} + \text{grad}\, p) \cdot \overline{\boldsymbol{W}} \right\} \mathrm{d}\Omega =$$

$$- \int_{\Gamma_F} \left\{ \overline{\boldsymbol{W}} \cdot \left(\boldsymbol{n} \wedge \alpha_1^{-1} \text{curl}\, \boldsymbol{U} \right) \right\} \mathrm{d}\Gamma \qquad \forall \boldsymbol{W} \in \mathcal{H}(\text{curl}; \Omega) \tag{2.49}$$

$$- \int_\Omega \omega^2 \alpha_2 \boldsymbol{U} \cdot \text{grad}\, \overline{q}\, \mathrm{d}\Omega = 0 \qquad \forall q \in V \tag{2.50}$$

It is convenient to introduce a new notation for this mixed formulation which enables it to be written more compactly. Defining the bilinear forms

$$a(\boldsymbol{u}, \boldsymbol{v}) = \int_\Omega \alpha_1^{-1} \text{curl}\, \boldsymbol{u} \cdot \text{curl}\, \overline{\boldsymbol{v}}\, \mathrm{d}\Omega \tag{2.51}$$

$$b(\boldsymbol{u}, \boldsymbol{v}) = \int_\Omega \omega^2 \alpha_2 \boldsymbol{u} \cdot \overline{\boldsymbol{v}}\, \mathrm{d}\Omega \tag{2.52}$$

and the linear form

$$l(\boldsymbol{v}) = - \int_{\Gamma_F} \overline{\boldsymbol{v}} \cdot \boldsymbol{n} \wedge \alpha_1^{-1} \text{curl}\, \boldsymbol{U}\, \mathrm{d}\Gamma \tag{2.53}$$

then the above mixed form can be written as: find $\boldsymbol{U} \in \mathcal{H}(\text{curl}; \Omega)$ and $p \in V$ such that

$$a(\boldsymbol{U}, \boldsymbol{W}) - b(\boldsymbol{U}, \boldsymbol{W}) - b(\text{grad}\, p, \boldsymbol{W}) = l(\boldsymbol{W}) \tag{2.54}$$

$$-b(\boldsymbol{U}, \text{grad}\, q) = 0 \tag{2.55}$$

for all $\boldsymbol{W} \in \mathcal{H}(\text{curl}; \Omega)$ and for all $q \in V$.

2.10 A Special Class of Problems

We now restrict consideration to a special class of problems where ω is specified to be a real constant, ie $\omega \gg 0$. We consider the choice of $\boldsymbol{W} = \text{grad}\, q$ for the test function in equation (2.49). This is valid choice, since the statement is true for all functions in $\mathcal{H}(\text{curl}; \Omega)$, and it yields the result

$$\alpha_2 \omega^2 \int_\Omega (\boldsymbol{U} + \text{grad}\, p) \cdot \text{grad}\, \overline{q}\, \mathrm{d}\Omega = 0 \qquad \forall q \in V \tag{2.56}$$

Upon substitution of equation (2.50), we have

$$\alpha_2\omega^2 \int_\Omega \text{grad}\, p \cdot \text{grad}\, \overline{q}\, \mathrm{d}\Omega = 0 \qquad \forall q \in V \tag{2.57}$$

Since $\omega \gg 0$, this expression implies that p is a constant, and it follows that since $p = 0$ on Γ_F, this constant is equal to 0. For any solution $\boldsymbol{U} \in \mathcal{H}(\text{curl}; \Omega)$, the Lagrange multiplier p is zero and may therefore be omitted. Hence, for this special class of problems, we may search for solutions which satisfy the simpler weak variational statement: find $\boldsymbol{U} \in \mathcal{H}(\text{curl}; \Omega)$ such that

$$a(\boldsymbol{U}, \boldsymbol{W}) - b(\boldsymbol{U}, \boldsymbol{W}) = l(\boldsymbol{W}) \qquad \forall \boldsymbol{W} \in \mathcal{H}(\text{curl}; \Omega) \tag{2.58}$$

This is identical to the initial weak variational form we derived without the use of the divergence condition.

2.11 A Mixed Formulation for all Occasions

Using techniques similar to those just described, Demkowicz and Vardapetyan [9] derived the mixed formulation which is capable of describing all the features given in the strong form. They defined the spaces

$$Z_0 = \{\boldsymbol{u} \in \mathcal{H}(\text{curl}; \Omega);\ \boldsymbol{n} \wedge \boldsymbol{u} = \boldsymbol{0} \text{ on } \Gamma_D\} \tag{2.59}$$

and

$$V_0 = \left\{p \in \mathcal{H}^1(\Omega);\ p = 0 \text{ on } \Gamma_D\right\} \tag{2.60}$$

and derived the mixed formulation: find $\boldsymbol{U} \in Z_0$ and $p \in V_0$ such that

$$a(\boldsymbol{U}, \boldsymbol{W}) - b(\boldsymbol{U}, \boldsymbol{W}) - b(\text{grad}\, p, \boldsymbol{W}) = 0 \qquad \forall \boldsymbol{W} \in Z_0 \tag{2.61}$$

$$-b(\boldsymbol{U}, \text{grad}\, q) = 0 \qquad \forall q \in V_0 \tag{2.62}$$

Demkowicz and Vardapetyan [9] show, by integrating, that this mixed form is equivalent to the original strong statement of the problem.

2.12 Uniqueness of the Mixed Formulation

When variational methods are applied to the Stokes equations, which govern viscous fluid flow, they can result in a mixed formulation [30]. The stability of this mixed system was investigated by Babuska and Brezzi [31] who independently derived the condition needed for a stable variational framework. In a similar manner, Demkowicz [9] has derived the Babuska–Brezzi condition

$$||(\boldsymbol{U}, p)||_{\mathcal{H}^c \wedge V} \leq c||l||_{\mathcal{H}^{c'} \wedge V'} \tag{2.63}$$

which is required for the stability of mixed system shown in section 2.11. In this expression, the notation $||\cdot||_{\mathcal{H}^c \wedge V}$ is used to denote a norm. A norm is a *measure* of a prescribed quantity and the precise definition of the $||\cdot||_{\mathcal{H}^c \wedge V}$ norm is

$$||(\boldsymbol{U}, p)||^2_{\mathcal{H}^c \wedge V} = ||\boldsymbol{U}||^2_{\mathcal{H}^c} + ||p||^2_V \tag{2.64}$$

where

$$||\boldsymbol{U}||^2_{\mathcal{H}^c} = \int_\Omega \left(\boldsymbol{U} \cdot \overline{\boldsymbol{U}} + \text{curl}\, \boldsymbol{U} \cdot \text{curl}\, \overline{\boldsymbol{U}}\right)\, \mathrm{d}\Omega \tag{2.65}$$

$$||p||^2_V = \omega^4 \int_\Omega \text{grad}\, p \cdot \text{grad}\, \overline{p}\, \mathrm{d}\Omega \tag{2.66}$$

and the constant c known as the inf–sup constant is given by

$$c = \max\left\{1 + \omega^2, \frac{1 + \tilde{\lambda}_i}{|\tilde{\lambda}_i - \omega^2|}, i = 1, 2, \cdots\right\} \tag{2.67}$$

In this expression, $\tilde{\lambda}_i$ represent the eigenvalues of the problem: find $\boldsymbol{U} \in \mathcal{H}(\text{curl}; \Omega)$ and $\tilde{\lambda} \in \mathbb{C}$ such that

$$\int_\Omega \alpha_1^{-1} \text{curl}\, \boldsymbol{U} \cdot \text{curl}\, \overline{\boldsymbol{W}}\, \mathrm{d}\Omega = \tilde{\lambda}\alpha_2 \int \boldsymbol{U} \cdot \overline{\boldsymbol{W}}\, \mathrm{d}\Omega \qquad \forall \boldsymbol{W} \in \mathcal{H}(\text{curl}; \Omega) \tag{2.68}$$

The Babuska–Brezzi condition shows that the solutions of the mixed systems given by either (2.50) and (2.49), or (2.61) and (2.62) are therefore unique, under the condition that $\omega^2 \neq \tilde{\lambda}_i$ and stable as $\omega \to 0$. Therefore this scheme is suitable for solving all possible problems which may be posed within the framework of the strong form.

In addition, Demkowicz [10] derives the estimate

$$||\boldsymbol{U}||_{\mathcal{H}^c} \leq c||l||_{\mathcal{H}^{c'}} \tag{2.69}$$

for the stability of the scheme given in equation (2.58) where

$$c = \max\left\{\frac{1}{\omega^2},\ \frac{1+\tilde{\lambda}_i}{|\tilde{\lambda}_i - \omega^2|}, i = 1, 2, \cdots\right\} \tag{2.70}$$

is the new constant. For this scheme, the stability deteriorates as $\omega \to 0$, however this is avoided in practice by the assumption that ω is large.

2.13 Summary

To summarise, using a mixed formulation guarantees stability and the satisfaction of the divergence condition as $\omega \to 0$. For problems involving the calculation of eigenvalues $\tilde{\lambda} = \omega^2$, then one should always adopt a mixed formulation to guarantee that the divergence condition is properly enforced. However, for wave propagation problems, where ω is known and sufficiently large, one may neglect the divergence condition. In particular, it can also be shown (see Appendix A) that scattering problems with large wavenumbers, which are the subject of later chapters, do not require the incorporation of the divergence condition.

Chapter 3

Geometry Representation and Basis Functions

3.1 Introduction

Given a weak variational form of the electromagnetic problem, the selection of trial functions from the correct functional space is described. The $\mathcal{H}(\mathrm{curl};\Omega)$ conforming finite element approximations to electromagnetics were introduced by Nédélec [32, 33] and, independently, in to the engineering literature by Lee [34]. Here, these approximations are known more commonly as *edge elements*. Following their introduction, edge elements have undergone extensive investigation and of particular interest is the work by Monk [35, 36]. This considers the analysis of various formulations, including *hp*–approximations (with *p* constant). Following the work of Monk, Demkowicz and co–workers [11, 9] have developed a 2 dimensional hierarchic basis for edge elements. This enables fully *hp*–adaptive approximations, on curved domains, to be undertaken.

Here, a technique that allows for the use of hybrid triangular and quadrilateral edge elements of arbitrary order is employed. The alternative form for the edge element shape functions defined recently by Ainsworth and Coyle [37] is employed, as it is has been shown to possess better conditioning properties.

The edge element basis cannot be used to represent the geometry. Therefore,

in addition, we require a method for approximating/representing the geometry. A description of linear approximation using traditional nodal methods is followed by a discussion of the method used for the representation of curved elements.

3.2 The Galerkin Approach for a Model Problem

Let us assume that the problem we wish to solve has the weak variational form: find $\boldsymbol{U} \in \mathcal{H}(\text{curl}; \Omega)$ such that

$$a(\boldsymbol{U}, \boldsymbol{W}) - \omega^2 m(\boldsymbol{U}, \boldsymbol{W}) = l(\boldsymbol{W}) \qquad \forall \boldsymbol{W} \in \mathcal{H}(\text{curl}; \Omega) \tag{3.1}$$

where the bilinear forms are defined as

$$a(\boldsymbol{u}, \boldsymbol{v}) = \int_\Omega \text{curl}\, \boldsymbol{u} \cdot \text{curl}\, \overline{\boldsymbol{v}}\, \mathrm{d}\Omega \qquad\qquad m(\boldsymbol{u}, \boldsymbol{v}) = \int_\Omega \boldsymbol{u} \cdot \overline{\boldsymbol{v}}\, \mathrm{d}\Omega \tag{3.2}$$

and the linear form is

$$l(\boldsymbol{v}) = -\int_\Gamma \overline{\boldsymbol{v}} \cdot (\boldsymbol{n} \wedge \text{curl}\, \boldsymbol{U})\ \mathrm{d}\Gamma \tag{3.3}$$

We show how the edge element basis and a geometry representation can be used to provide an approximation to this problem. Following the standard Galerkin approach, $\boldsymbol{U}$ is approximated by a discrete representation $\boldsymbol{U}_N$. This function $\boldsymbol{U}_N$ is composed of a series of N functions and can be expanded as

$$\boldsymbol{U}_N = \sum_{i=1}^{N} u_i \boldsymbol{\Phi}_i \tag{3.4}$$

where $\boldsymbol{\Phi}_i$ are real vector functions and u_i are complex coefficients. We choose the discrete test function to be

$$\boldsymbol{W}_N = \left[\begin{array}{cccccc} \boldsymbol{\Phi}_1 & \boldsymbol{\Phi}_2 & \cdots & \boldsymbol{\Phi}_{N-1} & \boldsymbol{\Phi}_N \end{array} \right]^T \tag{3.5}$$

i.e. a vector of the N real vector functions $\boldsymbol{\Phi}_i$. These vector functions are the same functions used to approximate the $\boldsymbol{U}$ field and are chosen so that they provide an approximation to the $\mathcal{H}(\text{curl}; \Omega)$ space. This means that the discrete problem is: find $\boldsymbol{U}_N \in \mathcal{H}_N(\text{curl}; \Omega)$ such that

$$a(\boldsymbol{U}_N, \boldsymbol{W}_N) - \omega^2 m(\boldsymbol{U}_N, \boldsymbol{W}_N) = l(\boldsymbol{W}_N) \qquad \forall \boldsymbol{W}_N \in \mathcal{H}_N(\text{curl}; \Omega) \tag{3.6}$$

By substitution of equations (3.4) and (3.5), this expression can be written in matrix notation as the finite linear system

$$\left(\boldsymbol{A} - \omega^2 \boldsymbol{M}\right) \boldsymbol{u} = \boldsymbol{L} \tag{3.7}$$

where $\boldsymbol{u} = [u_1, u_2, u_3, \cdots, u_N]^T$ and typical entries in $\boldsymbol{A}$, $\boldsymbol{M}$ and $\boldsymbol{L}$ are

$$A_{i,j} = \int_\Omega \text{curl}\, \boldsymbol{\Phi}_i \cdot \text{curl}\, \boldsymbol{\Phi}_j \, \mathrm{d}\Omega \qquad\qquad M_{i,j} = \int_\Omega \boldsymbol{\Phi}_i \cdot \boldsymbol{\Phi}_j \, \mathrm{d}\Omega \tag{3.8}$$

$$L_i = -\int_\Gamma \boldsymbol{\Phi}_i \cdot (\boldsymbol{n} \wedge \text{curl}\, \boldsymbol{U}) \, \mathrm{d}\Gamma \tag{3.9}$$

The vector functions are also chosen to be non–zero over only a small number of three sided or four sided figures called elements. The domain is then partitioned so that these elements do not overlap. If the part of the domain represented by the eth element is Ω_e then, the contributions made by the integrals $A_{i,j}$, $M_{i,j}$ and L_i from element e is given by

$$A^e_{i,j} = \int_{\Omega_e} \text{curl}\, \boldsymbol{\Phi}_i \cdot \text{curl}\, \boldsymbol{\Phi}_j \, \mathrm{d}\Omega \qquad\qquad M^e_{i,j} = \int_{\Omega_e} \boldsymbol{\Phi}_i \cdot \boldsymbol{\Phi}_j \, \mathrm{d}\Omega \tag{3.10}$$

$$L^e_i = -\int_{\Gamma_e} \boldsymbol{\Phi}_i \cdot (\boldsymbol{n} \wedge \text{curl}\, \boldsymbol{U}) \, \mathrm{d}\Gamma \tag{3.11}$$

where the integral L^e_i only appears for those elements which have an edge which lies on the boundary Γ. The specific choice of vector functions $\boldsymbol{\Phi}_i$, also known as the basis, will now be considered in more detail.

3.3 An Edge Element Basis

In computational electromagnetics, extensive use is made of the Whitney element [38] which is the lowest order triangular edge element. Edge elements are constructed to give an approximation of the $\mathcal{H}(\text{curl}; \Omega)$ space in which only the tangential component of the solution is continuous across element edges. For the Whitney element the tangential component is a constant on each edge. The level of accuracy achieved by this element is therefore low, enforcing the need for very large meshes

for the solution of practical problems. Consequently, researchers have begun to explore the use of higher order edge elements, where the tangential component of the field is approximated to a higher degree. In this context, Webb and Forghani [39] presented a hierarchical scheme for triangular elements up to order 4, in which the lowest order element was the Whitney element. Similar developments for quadrilateral edge elements have generally tended to be undertaken separately, so that, although higher order quadrilateral elements exist [40], they are not always directly compatible with the triangular elements.

Demkowicz and Rachowicz [11], developed a scheme of compatible, arbitrary order, quadrilateral and triangular edge elements. Recently, Ainsworth and Coyle [37] have developed a new family of compatible arbitrary order quadrilateral and triangular elements. These elements have been shown to have better conditioning properties. Good conditioning is essential for successful high order implementations and these elements are, therefore, adopted here.

3.3.1 Quadrilateral Edge Element

The master quadrilateral element is shown in Figure 3.1. For an element of order p, the variation of the electric field over this element is approximated as

$$\boldsymbol{U}(\xi,\eta) = \sum_{i=1}^{4}\sum_{j=0}^{p} u_j^i \boldsymbol{\phi}_j^i + \sum_{j=0}^{p}\sum_{k=1}^{p} u_{j,k}^{I_\xi} \boldsymbol{\phi}_{j,k}^{I_\xi} + \sum_{j=0}^{p}\sum_{k=1}^{p} u_{j,k}^{I_\eta} \boldsymbol{\phi}_{j,k}^{I_\eta} \tag{3.12}$$

In this expression, $\boldsymbol{\phi}$ denotes the vector form of the shape functions, while the scalars u are the unknowns. The basis functions $\boldsymbol{\phi}_j^i$ are associated with the element edges and are defined as

$$\boldsymbol{\phi}_j^1 = \frac{1}{2}(1-\eta)L_j(\xi)\boldsymbol{\tau}_1 \qquad \boldsymbol{\phi}_j^2 = \frac{1}{2}(1+\eta)L_j(-\xi)\boldsymbol{\tau}_2 \tag{3.13}$$

$$\boldsymbol{\phi}_j^3 = \frac{1}{2}(1-\xi)L_j(-\eta)\boldsymbol{\tau}_3 \qquad \boldsymbol{\phi}_j^4 = \frac{1}{2}(1+\eta)L_j(\eta)\boldsymbol{\tau}_4 \tag{3.14}$$

where $j = 0, 1, \ldots, p$, $\boldsymbol{\tau}_i$ is the tangential vector along edge $i; i = 1, 2, 3, 4$, and L_j is the Legendre polynomial of order j. The interior basis functions

$$\boldsymbol{\phi}_{j,k}^{I_\xi} = L_j(\xi)\ell_k(\eta)\boldsymbol{e}_\xi \qquad \boldsymbol{\phi}_{j,k}^{I\eta} = L_j(\eta)\ell_k(\xi)\boldsymbol{e}_\eta \tag{3.15}$$

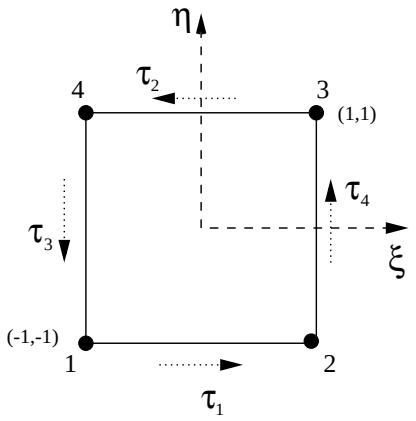

Figure 3.1: The quadrilateral master element

which have vanishing tangential component on the element edges, are included for $p \geq 1$. Here ℓ_k denotes the integrated Legendre polynomial of degree k and $\boldsymbol{e}_\xi$ and $\boldsymbol{e}_\eta$ are unit vectors in the ξ and η directions respectively.

3.3.2 Triangular Basis Functions

The master triangular edge element is taken to be the equilateral triangle shown in Figure 3.2. Over this element, the variation of the electric field is represented to a degree p, as

$$\boldsymbol{U}(\xi,\,\eta) = \sum_{i=1}^{3}\sum_{j=0}^{p} u_j^i \boldsymbol{\phi}_j^i + \sum_{i=1}^{3}\sum_{j=0}^{p-2} u_{i,j}^{PI}\boldsymbol{\phi}_{i,j}^{PI} + \underbrace{\sum_{j=0}^{p-3}\sum_{k=0}^{p-3} u_{j,k}^{GI_\xi}\boldsymbol{\phi}_{j,k}^{GI_\xi}}_{j+k\leq p-3} + \underbrace{\sum_{j=0}^{p-3}\sum_{k=0}^{p-3} u_{j,k}^{GI_\eta}\boldsymbol{\phi}_{j,k}^{GI_\eta}}_{j+k\leq p-3} \quad (3.16)$$

For $p = 0$, the basis functions

$$\boldsymbol{\phi}_0^1 = 2(\vartheta_1\,\mathrm{grad}\,\vartheta_2 - \vartheta_2\,\mathrm{grad}\,\vartheta_1) \qquad \boldsymbol{\phi}_0^2 = 2(\vartheta_2\,\mathrm{grad}\,\vartheta_3 - \vartheta_3\,\mathrm{grad}\,\vartheta_2) \quad (3.17)$$

$$\boldsymbol{\phi}_0^3 = 2(\vartheta_3\,\mathrm{grad}\,\vartheta_1 - \vartheta_1\,\mathrm{grad}\,\vartheta_3) \quad (3.18)$$

are associated with the edges of the triangle. These are identical to the basis functions for the Whitney elements. Here,

$$\vartheta_1 = \frac{1}{2\sqrt{3}}(\sqrt{3} + \sqrt{3}\xi - \eta) \qquad \vartheta_2 = \frac{1}{\sqrt{3}}\eta \quad (3.19)$$

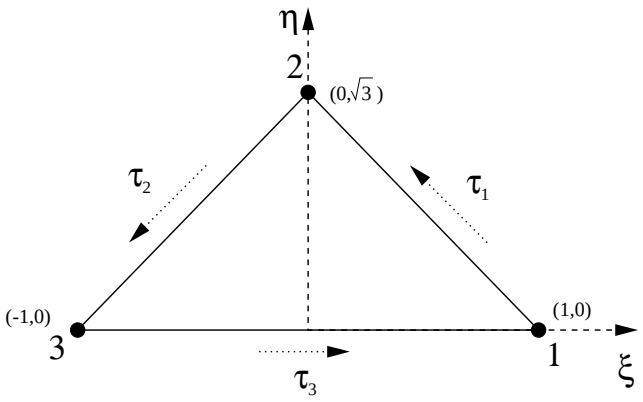

Figure 3.2: The triangular master element

$$\vartheta_3 = \frac{1}{2\sqrt{3}}(\sqrt{3} - \sqrt{3}\xi - \eta) \tag{3.20}$$

are the area coordinates. For $p = 1$, the basis functions associated with the triangle edges are

$$\boldsymbol{\phi}_1^1 = 2(\vartheta_1 \,\mathrm{grad}\,\vartheta_2 + \vartheta_2 \,\mathrm{grad}\,\vartheta_1) \qquad \boldsymbol{\phi}_1^2 = 2(\vartheta_2 \,\mathrm{grad}\,\vartheta_3 + \vartheta_3 \,\mathrm{grad}\,\vartheta_2) \tag{3.21}$$

$$\boldsymbol{\phi}_1^3 = 2(\vartheta_3 \,\mathrm{grad}\,\vartheta_1 + \vartheta_1 \,\mathrm{grad}\,\vartheta_3) \tag{3.22}$$

When $p \geq 2$, the recursive relations

$$\boldsymbol{\phi}_j^1 = \frac{1-2j}{j} L_{j-1}(\vartheta_2 - \vartheta_1)\boldsymbol{\phi}_1^1 - \frac{j-1}{j} L_{j-2}(\vartheta_2 - \vartheta_1)\boldsymbol{\phi}_0^1 \tag{3.23}$$

$$\boldsymbol{\phi}_j^2 = \frac{1-2j}{j} L_{j-1}(\vartheta_3 - \vartheta_2)\boldsymbol{\phi}_1^2 - \frac{j-1}{j} L_{j-2}(\vartheta_3 - \vartheta_2)\boldsymbol{\phi}_0^2 \tag{3.24}$$

$$\boldsymbol{\phi}_j^3 = \frac{1-2j}{j} L_{j-1}(\vartheta_1 - \vartheta_3)\boldsymbol{\phi}_1^3 - \frac{j-1}{j} L_{j-2}(\vartheta_1 - \vartheta_3)\boldsymbol{\phi}_0^3 \tag{3.25}$$

where $j = 2, 3, \ldots, p$, are employed to generate the necessary edge basis functions. For $p \geq 2$ the additional, pseudo–interior, basis functions

$$\boldsymbol{\phi}_{1,j}^{PI} = \vartheta_1\vartheta_2 \,\mathrm{grad}\,\vartheta_3 L_j(\vartheta_2 - \vartheta_1) \qquad \boldsymbol{\phi}_{2,j}^{PI} = \vartheta_2\vartheta_3 \,\mathrm{grad}\,\vartheta_1 L_j(\vartheta_3 - \vartheta_2) \tag{3.26}$$

$$\boldsymbol{\phi}_{3,j}^{PI} = \vartheta_3\vartheta_1 \,\mathrm{grad}\,\vartheta_2 L_j(\vartheta_1 - \vartheta_3) \tag{3.27}$$

where $j = 0, 1, \ldots, p-2$, must be added. These functions are such that their tangential component vanishes on the triangle edges. Finally, for $p \geq 3$, genuine

interior basis functions

$$\boldsymbol{\phi}_{j,k}^{GI_\xi} = \vartheta_1\vartheta_2\vartheta_3(1-\vartheta_1)^j P_j^{2,2}\left(\frac{\vartheta_1-\vartheta_3}{1-\vartheta_2}\right) P_k^{2j+5,2}(2\vartheta_2-1)\boldsymbol{e}_\xi \tag{3.28}$$

$$\boldsymbol{\phi}_{j,k}^{GI_\eta} = \vartheta_1\vartheta_2\vartheta_3(1-\vartheta_1)^j P_j^{2,2}\left(\frac{\vartheta_1-\vartheta_3}{1-\vartheta_2}\right) P_k^{2j+5,2}(2\vartheta_2-1)\boldsymbol{e}_\eta \tag{3.29}$$

are also included, where $0 \leq j, k, j+k \leq p-3$ and $P_q^{\alpha,\beta}(x)$ represents the Jacobi polynomial [41]. These functions vanish on the triangle edges.

3.3.3 Covariant Mapping

The basis for the quadrilaterial and triangular elements has been given in terms of master elements. Using curvilinear mappings, a covariant approach is employed to map the basis to a general triangle or quadrilateral. The components U_x and U_y of the electric field in Ω are then obtained as [42]

$$\boldsymbol{U}(x,y) = U_\xi \boldsymbol{a}^\xi + U_\eta \boldsymbol{a}^\eta \tag{3.30}$$

where U_ξ and U_η are the covariant components on the master element. Here,

$$\boldsymbol{a}^\xi = \frac{\boldsymbol{a}_\eta \wedge \boldsymbol{a}_z}{\boldsymbol{a}_\xi \cdot \boldsymbol{a}_\eta \wedge \boldsymbol{a}_z} \qquad \boldsymbol{a}^\eta = \frac{\boldsymbol{a}_z \wedge \boldsymbol{a}_\xi}{\boldsymbol{a}_\xi \cdot \boldsymbol{a}_\eta \wedge \boldsymbol{a}_z} \tag{3.31}$$

are the contravariant vectors, with

$$\boldsymbol{a}_\xi = \left[\frac{\partial x}{\partial \xi}, \frac{\partial y}{\partial \xi}, 0\right]^T \qquad \boldsymbol{a}_\eta = \left[\frac{\partial x}{\partial \eta}, \frac{\partial y}{\partial \eta}, 0\right]^T \qquad \boldsymbol{a}_z = [0,0,1]^T \tag{3.32}$$

The expression

$$\text{curl}\,\boldsymbol{U}(x,\ y) = \frac{1}{\boldsymbol{a}_\xi \cdot \boldsymbol{a}_\eta \wedge \boldsymbol{a}_z}\begin{bmatrix} 0 \\ 0 \\ \dfrac{\partial U_\eta}{\partial \xi} - \dfrac{\partial U_\xi}{\partial \eta} \end{bmatrix} \tag{3.33}$$

is used [42] to evaluate the variation of curl $\boldsymbol{U}$ over Ω.

3.3.4 Local to Global Numbering

The unknowns for the hierarchic edge elements fall in to two categories: edge based unknowns and interior unknowns. When assembling contributions from neighbour-

ing elements, the tangential component of the edge basis functions should be kept continuous. The interior unknowns are independent in each element.

Edge Based Numbering

Each edge in a general assembly of quadrilateral and trinagular elements is allocated a unique number and direction. If the same polynomial order is assumed to be employed in each element, the number of unknowns on each edge is $p+1$. A simple global numbering is then given by

$$\text{global unknown number} = [\text{global edge number}\,,\; i] \tag{3.34}$$

where $i = 1 \rightarrow p+1$. If the global numbering scheme relates $\boldsymbol{\Phi}_i$ to the mapped local edge basis function $\boldsymbol{\phi}_k^p$ and relates $\boldsymbol{\Phi}_j$ to the mapped edge basis function $\boldsymbol{\phi}_m^p$, the elemental contributions are given by

$$\begin{aligned}
A_{i,j}^e &= \int_{\Omega^e} \text{curl}\,\boldsymbol{\Phi}_i \cdot \text{curl}\,\boldsymbol{\Phi}_j \,\mathrm{d}\Omega \\
&= \int_{\Omega^e} \frac{d_k^p d_m^p}{(\boldsymbol{a}_\xi \cdot \boldsymbol{a}_\eta \wedge \boldsymbol{a}_z)^2} \left(\frac{\partial \phi_{k\eta}^p}{\partial \xi} - \frac{\partial \phi_{k\xi}^p}{\partial \eta}\right)\left(\frac{\partial \phi_{m\eta}^p}{\partial \xi} - \frac{\partial \phi_{m\xi}^p}{\partial \eta}\right) \mathrm{d}\Omega \qquad (3.35) \\
M_{i,j}^e &= \int_{\Omega^e} \boldsymbol{\Phi}_i \cdot \boldsymbol{\Phi}_j \,\mathrm{d}\Omega \\
&= \int_{\Omega^e} d_k^p d_m^p \left(\begin{bmatrix} \boldsymbol{a}^\xi & \boldsymbol{a}^\eta \end{bmatrix} \boldsymbol{\phi}_k^p\right) \cdot \left(\begin{bmatrix} \boldsymbol{a}^\xi & \boldsymbol{a}^\eta \end{bmatrix} \boldsymbol{\phi}_m^p\right) \mathrm{d}\Omega \qquad (3.36) \\
L_i^e &= -\int_{\Gamma^e} \boldsymbol{\Phi}_i \cdot (\boldsymbol{n} \wedge \text{curl}\,\boldsymbol{U}) \,\mathrm{d}\Gamma \\
&= -\int_{\Gamma^e} d_k^p \left(\begin{bmatrix} \boldsymbol{a}^\xi & \boldsymbol{a}^\eta \end{bmatrix} \boldsymbol{\phi}_k^p\right) \cdot (\boldsymbol{n} \wedge \text{curl}\,\boldsymbol{U}) \,\mathrm{d}\Gamma \qquad (3.37)
\end{aligned}$$

where d_k^p and d_m^p are direction flags to account for the case that the local direction differs from the defined global direction. When the local direction is the same as the global direction the direction coefficient is equal to 1. However when the local direction is opposite from the global direction, the coefficient d_k^p is computed from

$$d_k^p = (-1)^{p+1} \tag{3.38}$$

and d_m^p is computed in a similar manner.

Interior Numbering

As noted previously, no continuity requirements on the interior unknowns are imposed. Therefore, the numbering of these additional unknowns for either quadrilateral or triangular elements is straightforward. Typical integrals, for the pseudo interiors of the triangular elements, when the numbering relates the function $\mathbf{\Phi}_i$ to the mapped $\boldsymbol{\phi}^{PI}_{1,k}$ and relates $\mathbf{\Phi}_j$ to the mapped $\boldsymbol{\phi}^{PI}_{1,m}$, are

$$\begin{aligned} A^e_{i,j} &= \int_{\Omega^e} \text{curl}\,\mathbf{\Phi}_i \cdot \text{curl}\,\mathbf{\Phi}_j \,\mathrm{d}\Omega \\ &= \int_{\Omega^e} \frac{1}{(\boldsymbol{a}_\xi \cdot \boldsymbol{a}_\eta \wedge \boldsymbol{a}_z)^2} \left(\frac{\partial \phi^{PI}_{1,k\eta}}{\partial \xi} - \frac{\partial \phi^{PI}_{1,k\xi}}{\partial \eta} \right) \\ &\qquad \cdot \left(\frac{\partial \phi^{PI}_{1,m\eta}}{\partial \xi} - \frac{\partial \phi^{PI}_{1,m\xi}}{\partial \eta} \right) \mathrm{d}\Omega \end{aligned} \tag{3.39}$$

$$\begin{aligned} M^e_{i,j} &= \int_{\Omega^e} \mathbf{\Phi}_i \cdot \mathbf{\Phi}_j \,\mathrm{d}\Omega \\ &= \int_{\Omega^e} \left(\left[\begin{array}{cc} \boldsymbol{a}^\xi & \boldsymbol{a}^\eta \end{array} \right] \boldsymbol{\phi}^{PI}_{1,k} \right) \cdot \left(\left[\begin{array}{cc} \boldsymbol{a}^\xi & \boldsymbol{a}^\eta \end{array} \right] \boldsymbol{\phi}^{PI}_{1,m} \right) \mathrm{d}\Omega \end{aligned} \tag{3.40}$$

$$\begin{aligned} L^e_i &= -\int_{\Gamma^e} \mathbf{\Phi}_i \cdot (\boldsymbol{n} \wedge \text{curl}\,\boldsymbol{U}) \,\mathrm{d}\Gamma \\ &= -\int_{\Gamma^e} \left(\left[\begin{array}{cc} \boldsymbol{a}^\xi & \boldsymbol{a}^\eta \end{array} \right] \boldsymbol{\phi}^{PI}_{1,k} \right) \cdot (\boldsymbol{n} \wedge \text{curl}\,\boldsymbol{U}) \,\mathrm{d}\Gamma \end{aligned} \tag{3.41}$$

Similar expressions are then used for the interiors of the quadrilateral element and the genuine interiors of the triangle.

3.3.5 Towards A Linear System

The elemental matrix $\boldsymbol{A}^e$, once evaluated, can be decomposed in to four components as

$$\boldsymbol{A}^e = \left[\begin{array}{ccc} \boldsymbol{A}^e_{cc} & | & \boldsymbol{A}^e_{ci} \\ -- & -|- & -- \\ \boldsymbol{A}^e_{ic} & | & \boldsymbol{A}^e_{ii} \end{array} \right] \tag{3.42}$$

Here, $\boldsymbol{A}_{cc}$ relates to interactions between edge based basis functions, $\boldsymbol{A}^e_{ci}$ and $\boldsymbol{A}^e_{ic}$ relates interaction between edges and interiors and $\boldsymbol{A}^e_{ii}$ relates to interactions between interiors. The assembly of contributions of this matrix to the global matrix

$\boldsymbol{A}$ is shown in Figure 3.3. In a similar way $\boldsymbol{M}^e$ is decomposed as

$$\boldsymbol{M}^e = \left[\begin{array}{ccc} \boldsymbol{M}^e_{cc} & | & \boldsymbol{M}^e_{ci} \\ -- & -|- & -- \\ \boldsymbol{M}^e_{ic} & | & \boldsymbol{M}^e_{ii} \end{array}\right] \tag{3.43}$$

and contributions from this matrix are assembled in to the global matrix as shown in Figure 3.4. Finally, the right hand side contributions

$$\boldsymbol{L}^e = \left[\begin{array}{c} \boldsymbol{L}^e_c \\ - \\ \boldsymbol{L}^e_i \end{array}\right] \tag{3.44}$$

are located in the global right hand side vector as shown in Figure 3.5. To permit evaluation of these matrices, the actual representation of the geometry is now given in more detail.

3.4 Representation of Geometry

It is beneficial to introduce the terms *sub–parametric*, *iso–parametric* and *super–parametric*, previously defined by Zienkiewicz [2]. We recall that, *sub–parametric* is used to describe a mapping where the geometry is approximated to a lower degree than the field variable. *Iso–parametric* represent a mapping where both the geometry and the field variable are approximated to the same degree (the most popular in current finite element analysis). Finally, we remember that *super–parametric* is a mapping where the geometry is represented to a higher degree than the field variable.

3.4.1 Linear Approximation

In applications such as computational fluid dynamics and related methods such as computational electromagnetics, accurate solutions have been obtained using an *iso–parametric* linear representation. Here, the use of linear elements, is in part,

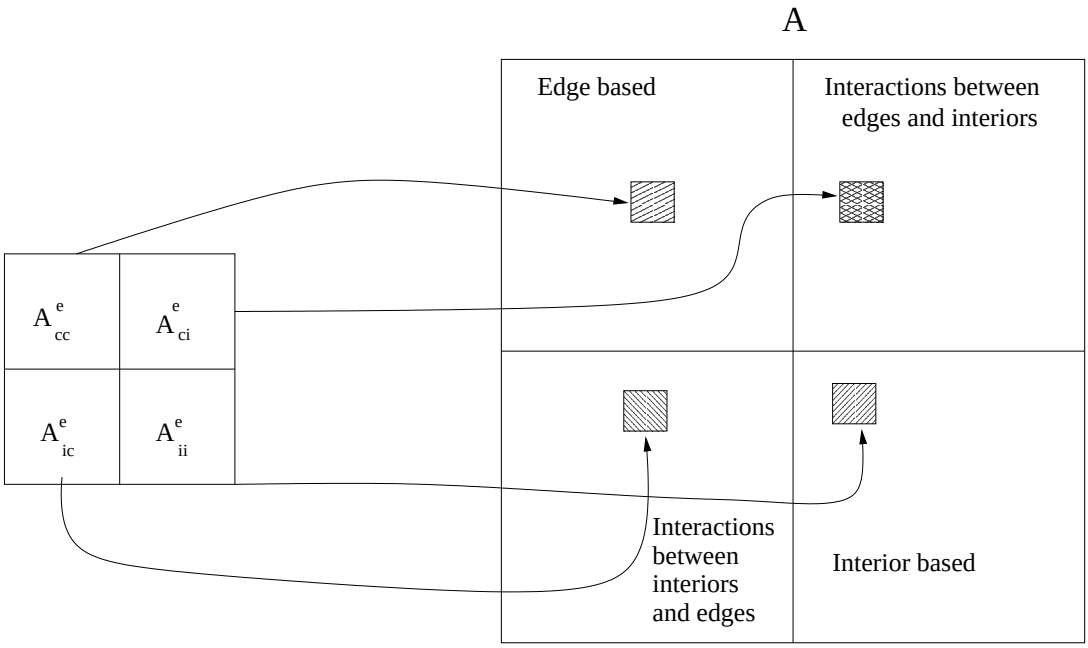

Figure 3.3: The assembly of contributions from an elemental matrix $\boldsymbol{A}^e$ in to the global matrix $\boldsymbol{A}$

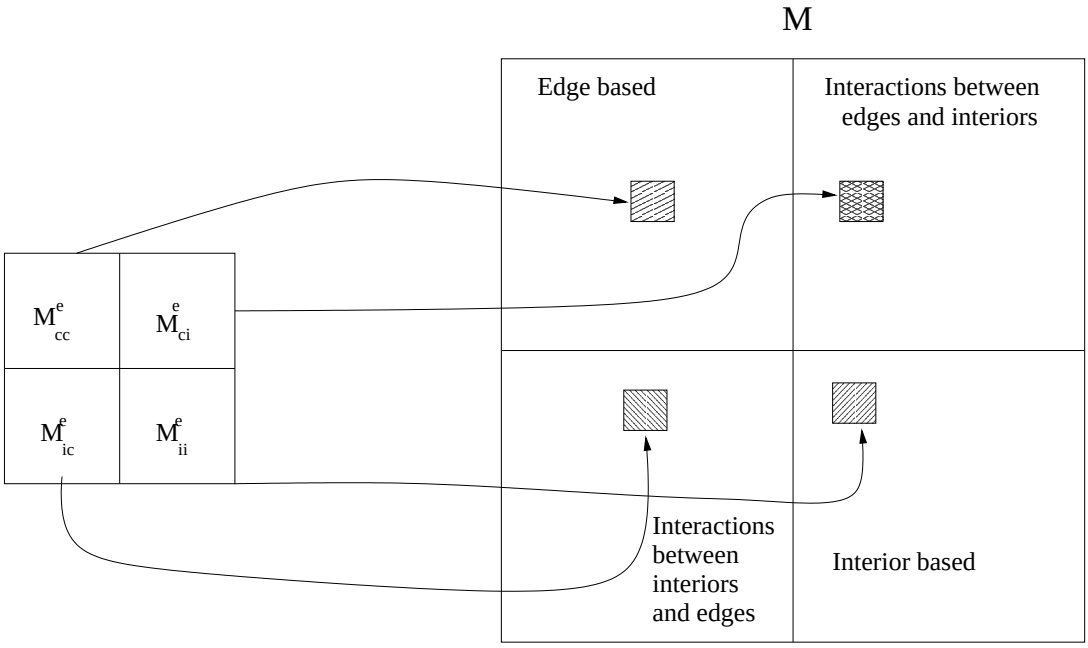

Figure 3.4: The assembly of contributions from an elemental matrix $\boldsymbol{M}^e$ in to the global matrix $\boldsymbol{M}$

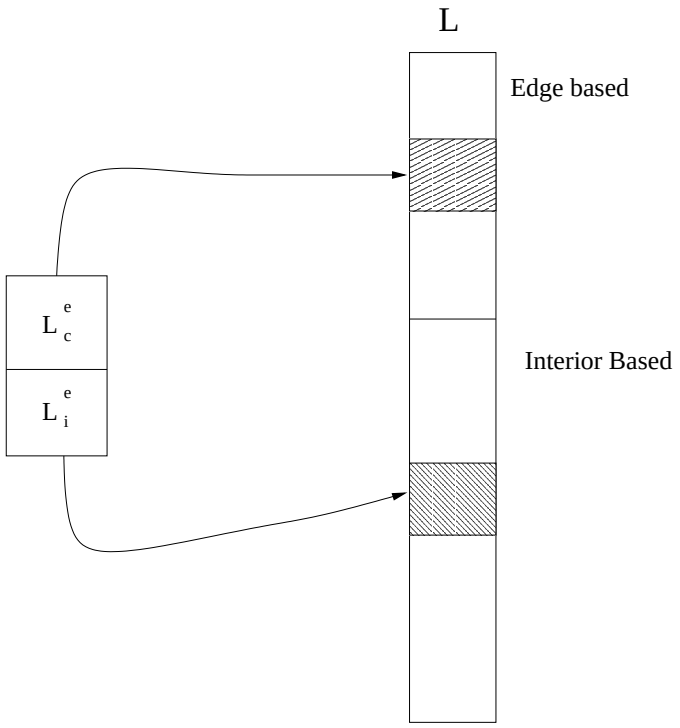

Figure 3.5: The assembly of contributions from an elemental matrix $\boldsymbol{L}^e$ in to the global matrix $\boldsymbol{L}$

due to the efficiency with which fine meshes of linear unstructured triangles can be generated [43, 44].

Linear representation of the geometry suffices for straight edged objects, and for curved objects, when a large enough number of elements is employed. When refinement of the mesh (h*–refinement*) is undertaken, the representation of the geometry along its boundaries tends to the true curve.

For a linear mapping, the expression

$$\begin{bmatrix} x \\ y \end{bmatrix} = \sum_{i=1}^{3} \vartheta_i \begin{bmatrix} x_i \\ y_i \end{bmatrix} \tag{3.45}$$

is employed to represent the geometry across a triangle. Here ϑ_i are the previously defined area coordinates (3.19), (3.20). The standard bilinear mapping

$$\begin{bmatrix} x \\ y \end{bmatrix} = \sum_{i=1}^{4} \begin{bmatrix} x_i \\ y_i \end{bmatrix} N_i(\xi,\, \eta) \tag{3.46}$$

gives a linear approximation of the geometry for the quadrilateral element, where

$$N_1 = \frac{1}{4}(1-\xi)(1-\eta) \qquad N_2 = \frac{1}{4}(1+\xi)(1-\eta) \tag{3.47}$$

$$N_3 = \frac{1}{4}(1+\xi)(1+\eta) \qquad N_4 = \frac{1}{4}(1-\xi)(1+\eta) \tag{3.48}$$

are the standard bilinear shape functions associated with the vertices of the element.

3.4.2 Curved Elements

When performing p*–refinement*, where the order of approximation of the field variable is increased and the mesh kept constant, the use of a linear *sub–parametric* discretisation can result in inaccurate solutions. This occurs for all cases where the true curve of the boundary is not made of straight segments. The extent to which the solution is inaccurate depends on the mesh spacing and problem difficulty.

The use of curved elements, in the vicinity of the boundaries of the domain, can alleviate this. The serendipity or Lagrange families of elements [2], offer possibilities for curved edges: here additional nodal points are introduced on the edges of the elements. One can then ensure that these points are located on the true boundaries of the domain. The curve, which is formed between the nodal positions, depends on the order of the serendipity or Lagrange elements.

In such a manner one can construct a superior *super–parametric* mapping, or a curved *iso–parametric* element, in which the converged solution is closer to the true solution. However, with increasing order of serendipity or Lagrange element, there is a necessity for additional points to be located on the boundary edges of the domain and there is no guarantee that the curved edge will have the same curve as the true geometry.

An alternative approach is the linear blending function method [31]. Here, there is no requirement for additional nodes on boundary edges of the element, and the curve of the boundary edges exactly follows the true curve of the boundary. The blending functions reduce to the linear approximations for elements with straight edges, and therefore make an ideal choice when using unstructured meshes with curved domains.

Blending Functions for Triangular Elements

The representation

$$\begin{bmatrix} x \\ y \end{bmatrix} = \sum_{i=1}^{3} \vartheta_i \begin{bmatrix} x_i \\ y_i \end{bmatrix} + \vartheta_1\vartheta_2 \begin{bmatrix} g_1^x(\vartheta_2 - \vartheta_1, x_1, x_2) \\ g_1^y(\vartheta_2 - \vartheta_1, y_1, y_2) \end{bmatrix} + \vartheta_2\vartheta_3 \begin{bmatrix} g_2^x(\vartheta_3 - \vartheta_2, x_2, x_3) \\ g_2^y(\vartheta_3 - \vartheta_2, y_2, y_2) \end{bmatrix} + \vartheta_3\vartheta_1 \begin{bmatrix} g_3^x(\vartheta_1 - \vartheta_3, x_3, x_1) \\ g_3^y(\vartheta_1 - \vartheta_3, y_3, y_1) \end{bmatrix} \quad (3.49)$$

is employed when a blending function representation is used. In this expression the functions

$$g_i^x(\zeta, x_j, x_k) = \frac{4}{1-\zeta^2}\left\{\tilde{g}_i^x(\zeta) - \left(\frac{1-\zeta}{2}\right)x_j - \left(\frac{1+\zeta}{2}\right)x_k\right\} \quad (3.50)$$

and

$$g_i^y(\zeta, y_j, y_k) = \frac{4}{1-\zeta^2}\left\{\tilde{g}_i^y(\zeta) - \left(\frac{1-\zeta}{2}\right)y_j - \left(\frac{1+\zeta}{2}\right)y_k\right\} \quad (3.51)$$

represent the difference between the linear approximation and the true profile of an edge. Here $\tilde{g}_i^x(\zeta)$ and $\tilde{g}_i^y(\zeta)$ define the exact shape of the edge, in terms of a non dimensional parameter ζ, which is -1 at vertex j and $+1$ at vertex k.

Blending Functions for Quadrilateral Elements

For a quadrilateral element, the expression

$$\begin{bmatrix} x \\ y \end{bmatrix} = \sum_{i=4}^{3} N_i \begin{bmatrix} x_i \\ y_i \end{bmatrix} + \left(\frac{1-\eta}{2}\right)\begin{bmatrix} f_1^x(\xi, x_1, x_2) \\ f_1^y(\xi, y_1, y_2) \end{bmatrix} + \left(\frac{1+\eta}{2}\right)\begin{bmatrix} f_2^x(\xi, x_4, x_3) \\ f_2^y(\xi, y_4, y_3) \end{bmatrix} + \left(\frac{1-\xi}{2}\right)\begin{bmatrix} f_3^x(\eta, x_1, x_4) \\ f_3^y(\eta, y_1, y_4) \end{bmatrix} + \left(\frac{1+\xi}{2}\right)\begin{bmatrix} f_4^x(\eta, x_2, x_3) \\ f_4^y(\eta, y_2, y_3) \end{bmatrix} \quad (3.52)$$

is used when employing a blending function approximation of coordinates. In this expression

$$f_i^x(\zeta, x_j, x_k) = \left\{\tilde{f}_i^x(\zeta) - \left(\frac{1-\zeta}{2}\right)x_j - \left(\frac{1+\zeta}{2}\right)x_k\right\} \quad (3.53)$$

and

$$f_i^y(\zeta, y_j, y_k) = \left\{ \tilde{f}_i^y(\zeta) - \left(\frac{1-\zeta}{2}\right) y_j - \left(\frac{1+\zeta}{2}\right) y_k \right\} \tag{3.54}$$

represent the difference between the linear approximation and the true profile of an edge. Here $\tilde{f}_i^x(\zeta)$ and $\tilde{f}_i^y(\zeta)$ define the exact shape of the edge.

3.5 Numerical Implementation

This section discusses issues related to the numerical implementation of the geometry representation and basis functions to enable a discrete solution to be obtained.

3.5.1 Mesh Generation and Preprocessing

In this work, the use of structured meshes is limited to simple geometries such as rectangular and circular domains. Elsewhere, unstructured mesh generation is employed and the advancing front technique of [43, 44] is used.

When applicable, the resolution of the boundaries is improved by the use of the blending function method. Following the generation of the mesh, the edges in the mesh are numbered and assigned a unique direction. An optimum bandwidth for the edges is obtained by employing a Cuthill–McKee algorithm [45] to renumber the global edge numbers in the mesh.

3.5.2 Generation of Legendre Polynomials

The numerical generation of the Legendre polynomials, for use in the triangular and quadrilateral basis functions, is achieved through the use of the expression [41]

$$L_j(\zeta) = \frac{1}{2^j} \sum_{i=0}^{j} \begin{pmatrix} j \\ i \end{pmatrix} \begin{pmatrix} j \\ j-i \end{pmatrix} (\zeta - 1)^{j-i} (\zeta + 1)^i \tag{3.55}$$

which allows the numerical generation of the jth order polynomial. This is a polynomial which is defined for the range $-1 \leq \zeta \leq 1$. Polynomials of order $j = 0, 1, 2, 3, 4, 5$ are shown in Figure 3.6.

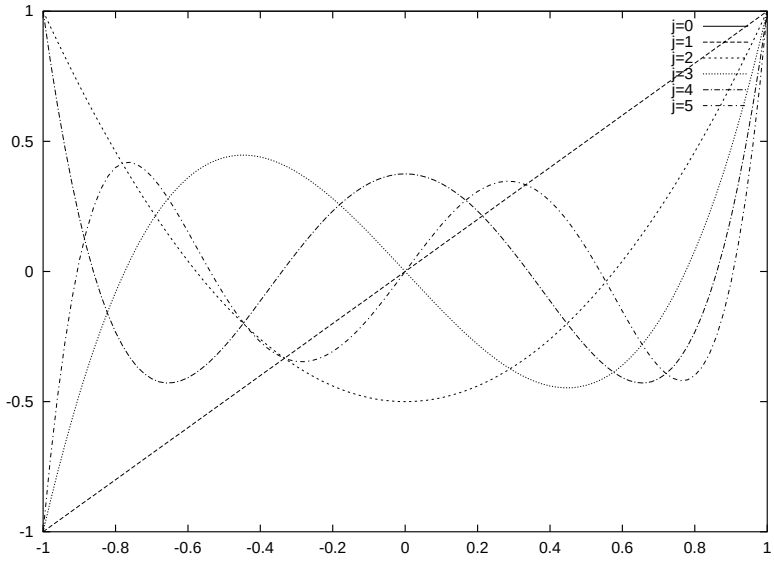

Figure 3.6: Legendre polynomial $L_j(\zeta)$ for $j = 0, 1, 2, 3, 4, 5$

When evaluating the curl of the basis, viz equation (3.33), repeated use of the chain rule leads to the requirement for knowledge of the derivative of the Legendre polynomial with respect to ζ. For this, the expression [41]

$$b_{1,j}\frac{\mathrm{d}L_j(\zeta)}{\mathrm{d}\zeta} = b_{2,j}L_j(\zeta) + b_{3,j}P_{j-1}(\zeta) \tag{3.56}$$

is employed with

$$\begin{aligned} b_{1,j} &= 2j(1-\zeta^2) \\ b_{2,j} &= -2j^2\zeta \\ b_{3,j} &= 2j^2 \end{aligned}$$

Balanis [28] defines

$$\ell_j(\zeta) = \int_{-1}^{\zeta} L_j(\zeta)\,\mathrm{d}\zeta = \frac{L_{j+1}(\zeta) - L_{j-1}(\zeta)}{(2j+1)} \tag{3.57}$$

as the integrated polynomial of order j. One may then evaluate the derivative with respect to ζ of the integrated Legendre polynomial as

$$\frac{\mathrm{d}\ell_j(\zeta)}{\mathrm{d}\zeta} = \frac{1}{2j+1}\left\{\frac{\mathrm{d}L_{j+1}(\zeta)}{\mathrm{d}\zeta} - \frac{\mathrm{d}L_{j-1}(\zeta)}{\mathrm{d}\zeta}\right\} \tag{3.58}$$

in terms of derivatives of the Legendre polynomial.

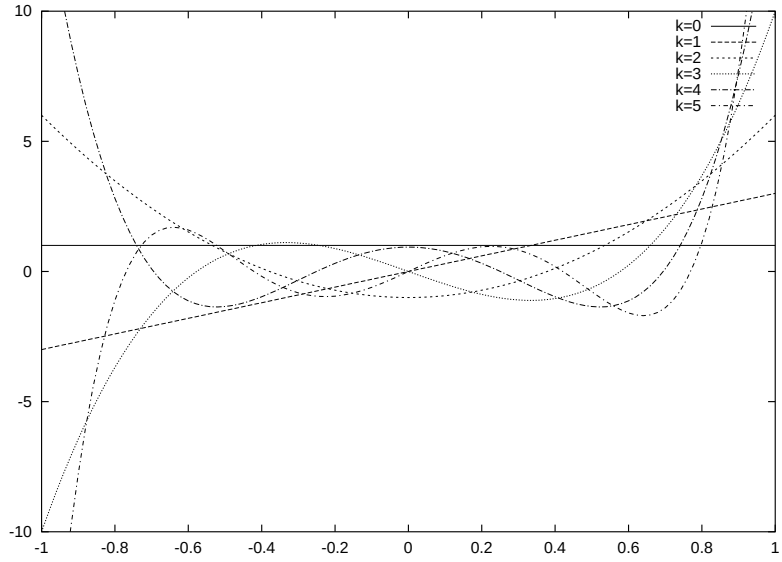

Figure 3.7: Jacobi polynomial $P_k^{2,2}(\zeta)$ for $k = 0, 1, 2, 3, 4, 5$

3.5.3 Generation of Jacobi Polynomials

In a similar manner, the relation [41]

$$P_k^{\alpha,\beta}(\zeta) = \frac{1}{2^k} \sum_{i=0}^{k} \left(\begin{array}{c} k+\alpha \\ i \end{array} \right) \left(\begin{array}{c} k+\beta \\ k-i \end{array} \right) (\zeta - 1)^{k-i} (\zeta + 1)^i \tag{3.59}$$

is employed to generate the Jacobi polynomial of degree k. An example of the Jacobi polynomial $P_k^{2,2}(\zeta)$ for $k = 0, 1, 2, 3, 4, 5$ is shown in Figure 3.7. In this Figure, we observe that the polynomials are asymmetric for odd orders and increase in magnitude with k. A second example, considering the polynomial $P_j^{2i+5,2}(\zeta)$ for $i = 1$ and $j = 0, 1, 2, 3, 4, 5$ is shown in Figure 3.8. Here, we observe a sharp increase in magnitude and gradient at $\zeta = 1$ for increasing polynomial order j.

The derivatives of the Jacobi polynomials, with respect to ζ, are computed as

$$b_{1,k} \frac{\mathrm{d}P_k^{\alpha,\beta}(\zeta)}{\mathrm{d}\zeta} = b_{2,k} P_k^{\alpha,\beta}(\zeta) + b_{3,k} P_{k-1}^{\alpha,\beta}(\zeta) \tag{3.60}$$

where

$$\begin{aligned} b_{1,k} &= (2k + \alpha + \beta)(1 - \zeta^2) \\ b_{2,k} &= k(\alpha - \beta - (2k + \alpha + \beta)\zeta) \\ b_{3,k} &= 2(k + \alpha)(k + \beta) \end{aligned}$$

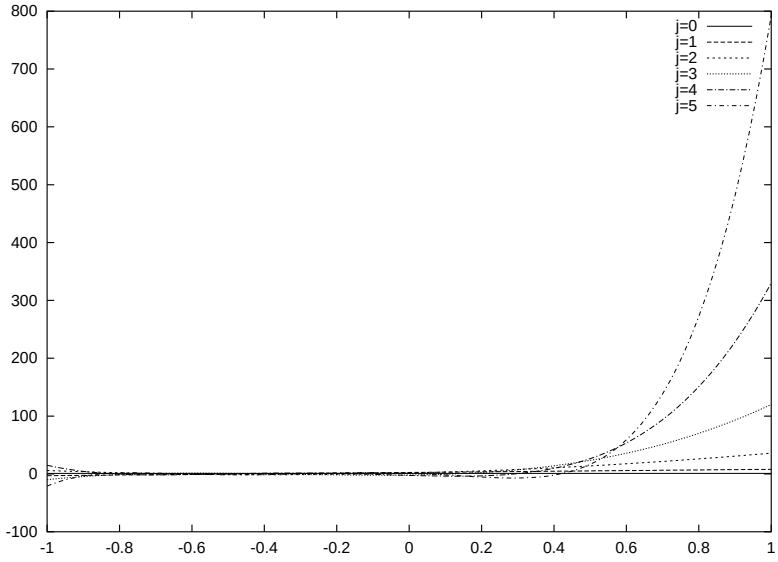

Figure 3.8: Jacobi polynomial $P_j^{2i+5,2}(\zeta)$ for $j = 0, 1, 2, 3, 4, 5$

are factors dependent on the order of polynomial.

3.5.4 Evaluation of Integrals

All integrals are evaluated numerically using Gauss Quadrature [2]. Area integrals are performed over the master element by using the transformation

$$\mathrm{d}\Omega^e = |\boldsymbol{J}|\mathrm{d}\xi\mathrm{d}\eta \qquad \text{where} \qquad \boldsymbol{J} = \begin{bmatrix} \frac{\partial x}{\partial \xi} & \frac{\partial y}{\partial \xi} \\ \frac{\partial x}{\partial \eta} & \frac{\partial y}{\partial \eta} \end{bmatrix} \tag{3.61}$$

In fact, it can be shown that $|\boldsymbol{J}|$ is equivalent to the term $\boldsymbol{a}_\xi \cdot (\boldsymbol{a}_\eta \wedge \boldsymbol{a}_z)$, used in the covariant mapping of the basis functions. The number of integrations points used to evaluate the expressions is chosen in relation to the order of the basis, so that sufficient integration points are used to integrate the integrand.

Numerical Integration for the Quadrilateral Element

For the quadrilateral element, ξ and η can be integrated independently by nip points in each direction, and therefore the integrals $A^e_{i,j}$ and $M^e_{i,j}$ for the edge basis func-

tions can be represented as the sums

$$A^e_{i,j} = \int_{-1}^{+1}\int_{-1}^{+1} \frac{d^p_k d^p_m}{(\boldsymbol{a}_\xi \cdot \boldsymbol{a}_\eta \wedge \boldsymbol{a}_z)} \left(\frac{\partial \phi^p_{k\eta}}{\partial \xi} - \frac{\partial \phi^p_{k\xi}}{\partial \eta}\right) \cdot \left(\frac{\partial \phi^p_{m\eta}}{\partial \xi} - \frac{\partial \phi^p_{m\xi}}{\partial \eta}\right) \mathrm{d}\xi \mathrm{d}\eta \quad (3.62)$$

$$\approx \sum_{\alpha=1}^{nip}\sum_{\beta=1}^{nip} \frac{d^p_k d^p_m}{(\boldsymbol{a}_\xi \cdot \boldsymbol{a}_\eta \wedge \boldsymbol{a}_z)} \left(\frac{\partial \phi^p_{k\eta}}{\partial \xi} - \frac{\partial \phi^p_{k\xi}}{\partial \eta}\right) \cdot \left(\frac{\partial \phi^p_{m\eta}}{\partial \xi} - \frac{\partial \phi^p_{m\xi}}{\partial \eta}\right) w_\alpha(\xi) w_\beta(\eta) \quad (3.63)$$

$$M^e_{i,j} = \int_{-1}^{+1}\int_{-1}^{+1} d^p_k d^p_m \left(\left[\begin{array}{ccc} \boldsymbol{a}^\xi & \boldsymbol{a}^\eta \end{array}\right] \boldsymbol{\phi}^p_k\right) \cdot \left(\left[\begin{array}{ccc} \boldsymbol{a}^\xi & \boldsymbol{a}^\eta \end{array}\right] \boldsymbol{\phi}^p_m\right) \cdot (\boldsymbol{a}_\xi \cdot \boldsymbol{a}_\eta \wedge \boldsymbol{a}_z)\, \mathrm{d}\xi \mathrm{d}\eta \quad (3.64)$$

$$\approx \sum_{\alpha=1}^{nip}\sum_{\beta=1}^{nip} d^p_k d^p_m \left(\left[\begin{array}{ccc} \boldsymbol{a}^\xi & \boldsymbol{a}^\eta \end{array}\right] \boldsymbol{\phi}^p_k\right) \cdot \left(\left[\begin{array}{ccc} \boldsymbol{a}^\xi & \boldsymbol{a}^\eta \end{array}\right] \boldsymbol{\phi}^p_m\right) \cdot (\boldsymbol{a}_\xi \cdot \boldsymbol{a}_\eta \wedge \boldsymbol{a}_z) w_\alpha(\xi) w_\beta(\eta) \quad (3.65)$$

where $w_\alpha(\xi)$ and $w_\beta(\eta)$ are the integration weights for the Gauss quadrature. To compute the elemental contribution L^e_i for a quadrilateral element, we first observe that

$$\mathrm{d}\Gamma^2 = \mathrm{d}x^2 + \mathrm{d}y^2 \qquad \mathrm{d}x = \frac{\partial x}{\partial \xi}\mathrm{d}\xi + \frac{\partial x}{\partial \eta}\mathrm{d}\eta \qquad \mathrm{d}y = \frac{\partial y}{\partial \xi}\mathrm{d}\xi + \frac{\partial y}{\partial \eta}\mathrm{d}\eta \quad (3.66)$$

It then follows that on edges 2 and 3 of the quadrilateral, where ξ is a constant, that

$$\mathrm{d}\Gamma^e = \sqrt{J^2_{21} + J^2_{22}}\mathrm{d}\eta \quad (3.67)$$

Here J_{21} and J_{22} are components of the Jacobian. In addition, on edges 1 and 2 where η is a constant we have

$$\mathrm{d}\Gamma^e = \sqrt{J^2_{11} + J^2_{12}}\mathrm{d}\xi \quad (3.68)$$

Hence the elemental contribution to L^e_i is either

$$L^e_i \approx -\sum_{\alpha=1}^{nip} d^p_k \left(\left[\begin{array}{ccc} \boldsymbol{a}^\xi & \boldsymbol{a}^\eta \end{array}\right] \boldsymbol{\phi}^p_k\right) \cdot (\boldsymbol{n} \wedge \mathrm{curl}\, \boldsymbol{U}) \sqrt{J^2_{21} + J^2_{22}} w_\alpha(\eta) \quad (3.69)$$

if ξ is a constant or

$$L_i^e \approx -\sum_{\alpha=1}^{nip} d_k^p \left(\left[\begin{array}{cc} \boldsymbol{a}^\xi & \boldsymbol{a}^\eta \end{array} \right] \boldsymbol{\phi}_k^p \right) \cdot (\boldsymbol{n} \wedge \operatorname{curl} \boldsymbol{U}) \sqrt{J_{11}^2 + J_{12}^2} w_\alpha(\xi) \tag{3.70}$$

if η is a constant.

Numerical Integration for the Triangular Element

For the triangular element, ξ and η directions must be integrated simultaneously. When a $nipt$ point scheme is employed for $A_{i,j}^e$ and $M_{i,j}^e$, the result is the sums

$$A_{i,j}^e = \int_{\Omega^e} \frac{d_k^p d_m^p}{(\boldsymbol{a}^\xi \cdot \boldsymbol{a}^\eta \wedge \boldsymbol{a}_z)} \left(\frac{\partial \phi_{k\eta}^p}{\partial \xi} - \frac{\partial \phi_{k\xi}^p}{\partial \eta} \right) \left(\frac{\partial \phi_{m\eta}^p}{\partial \xi} - \frac{\partial \phi_{m\xi}^p}{\partial \eta} \right) \mathrm{d}\xi \mathrm{d}\eta \tag{3.71}$$

$$\approx \sum_{\alpha=1}^{nipt} \frac{d_k^p d_m^p}{(\boldsymbol{a}_\xi \cdot \boldsymbol{a}_\eta \wedge \boldsymbol{a}_z)} \left(\frac{\partial \phi_{k\eta}^p}{\partial \xi} - \frac{\partial \phi_{k\xi}^p}{\partial \eta} \right) \left(\frac{\partial \phi_{m\eta}^p}{\partial \xi} - \frac{\partial \phi_{m\xi}^p}{\partial \eta} \right) wt_\alpha(\xi, \eta) \tag{3.72}$$

$$M_{i,j}^e = \int_{\Omega^e} d_k^p d_m^p \left(\left[\begin{array}{cc} \boldsymbol{a}^\xi & \boldsymbol{a}^\eta \end{array} \right] \boldsymbol{\phi}_k^p \right) \cdot \left(\left[\begin{array}{cc} \boldsymbol{a}^\xi & \boldsymbol{a}^\eta \end{array} \right] \boldsymbol{\phi}_m^p \right) \cdot (\boldsymbol{a}_\xi \cdot \boldsymbol{a}_\eta \wedge \boldsymbol{a}_z) \, \mathrm{d}\xi \mathrm{d}\eta \tag{3.73}$$

$$\approx \sum_{\alpha=1}^{nipt} d_k^p d_m^p \left(\left[\begin{array}{cc} \boldsymbol{a}^\xi & \boldsymbol{a}^\eta \end{array} \right] \boldsymbol{\phi}_k^p \right) \cdot \left(\left[\begin{array}{cc} \boldsymbol{a}^\xi & \boldsymbol{a}^\eta \end{array} \right] \boldsymbol{\phi}_m^p \right) \cdot (\boldsymbol{a}_\xi \cdot \boldsymbol{a}_\eta \wedge \boldsymbol{a}_z) wt_\alpha(\xi, \eta) \tag{3.74}$$

where $wt_\alpha(\xi, \eta)$ are the integration weights for the triangular Gauss quadrature. To compute the elemental contribution L_i^e for a triangular element, we introduce an additional variable ζ that is -1 at one end of the boundary edge and $+1$ at the other. Then a linear interpolation of ξ and η along the edge is given by

$$\xi = \frac{\xi_1}{2}(1 - \zeta) + \frac{\xi_2}{2}(1 + \zeta) \qquad \eta = \frac{\eta_1}{2}(1 - \zeta) + \frac{\eta_2}{2}(1 + \zeta) \tag{3.75}$$

where (ξ_1, η_1) denote the coordinates of the one end of the edge on the local triangle and (ξ_2, η_2) denotes the coordinates of the second end of the edge. Differentiating with respect to ζ, and substitution in to the expressions for $\mathrm{d}x$ and $\mathrm{d}y$ given in equation (3.66), yields

$$\mathrm{d}x = \frac{\partial x}{\partial \xi} \frac{(\xi_2 - \xi_1)}{2} \mathrm{d}\zeta + \frac{\partial x}{\partial \eta} \frac{(\eta_2 - \eta_1)}{2} \mathrm{d}\zeta \tag{3.76}$$

$$\mathrm{d}y = \frac{\partial y}{\partial \xi}\frac{(\xi_2 - \xi_1)}{2}\mathrm{d}\zeta + \frac{\partial y}{\partial \eta}\frac{(\eta_2 - \eta_1)}{2}\mathrm{d}\zeta \tag{3.77}$$

and finally

$$\mathrm{d}\Gamma = \frac{1}{2}\sqrt{(J_{11}^2 + J_{21}^2)(\xi_2 - \xi_1)^2 + (J_{12}^2 + J_{22}^2)(\eta_2 - \eta_1)^2}\mathrm{d}\zeta \tag{3.78}$$

The elemental contribution L_i^e for a triangular element is then given by

$$L_i^e \approx -\sum_{\alpha=1}^{nip}\frac{1}{2}d_k^p\left(\left[\begin{array}{cc} \boldsymbol{a}^\xi & \boldsymbol{a}^\eta \end{array}\right]\boldsymbol{\phi}_k^p\right)\cdot(\boldsymbol{n}\wedge\operatorname{curl}\boldsymbol{U}) \sqrt{(J_{11}^2 + J_{21}^2)(\xi_2 - \xi_1)^2 + (J_{12}^2 + J_{22}^2)(\eta_2 - \eta_1)^2}w_\alpha(\zeta) \tag{3.79}$$

3.5.5 Static Condensation

The interior degrees of freedom for the quadrilateral and triangular element have no inter–element connectivity. Therefore, by using static condensation [46], it is possible to reduce the number of unknowns in the global system by eliminating the interior unknowns. To examine how this works in the context of edge elements, we first revisit the linear system given in equation (3.7) and rewrite it in terms of interior and edge based unknowns

$$\left(\left[\begin{array}{ccc} \boldsymbol{A}_{cc} & | & \boldsymbol{A}_{ci} \\ -- & -|- & -- \\ \boldsymbol{A}_{ic} & | & \boldsymbol{A}_{ii} \end{array}\right] - \omega^2\left[\begin{array}{ccc} \boldsymbol{M}_{cc} & | & \boldsymbol{M}_{ci} \\ -- & -|- & -- \\ \boldsymbol{M}_{ic} & | & \boldsymbol{M}_{ii} \end{array}\right]\right)\left\{\begin{array}{c} \boldsymbol{u}_c \\ - \\ \boldsymbol{u}_i \end{array}\right\} = \left[\begin{array}{c} \boldsymbol{L}_c \\ - \\ \boldsymbol{L}_i \end{array}\right] \tag{3.80}$$

From the nature of basis functions, we conclude that the unknowns contained in $\boldsymbol{u}_i$ are independent between each element and therefore can be eliminated. We eliminate $\boldsymbol{u}_i$ as

$$\boldsymbol{u}_i = (\boldsymbol{A}_{ii} - \omega^2\boldsymbol{M}_{ii})^{-1}(\boldsymbol{L}_i - (\boldsymbol{A}_{ic} - \omega^2\boldsymbol{M}_{ic})\boldsymbol{u}_c) \tag{3.81}$$

and form the modified system

$$\boldsymbol{K}_{cc}\boldsymbol{u}_c = \boldsymbol{R}_c \tag{3.82}$$

where

$$\boldsymbol{K}_{cc} = (\boldsymbol{A}_{cc} - \omega^2 \boldsymbol{M}_{cc}) - (\boldsymbol{A}_{ci} - \omega^2 \boldsymbol{M}_{ci})(\boldsymbol{A}_{ii} - \omega^2 \boldsymbol{M}_{ii})^{-1} \cdot (\boldsymbol{A}_{ic} - \omega^2 \boldsymbol{M}_{ic}) \quad (3.83)$$

$$\boldsymbol{R}_c = \boldsymbol{L}_c - (\boldsymbol{A}_{ci} - \omega^2 \boldsymbol{M}_{ci})(\boldsymbol{A}_{ii} - \omega^2 \boldsymbol{M}_{ii})^{-1} \boldsymbol{L}_i \quad (3.84)$$

For an efficient implementation, the elemental contributions to $\boldsymbol{K}_{cc}$ and $\boldsymbol{R}_c$ may be evaluated as

$$\boldsymbol{K}^e_{cc} = (\boldsymbol{A}^e_{cc} - \omega^2 \boldsymbol{M}^e_{cc}) - (\boldsymbol{A}^e_{ci} - \omega^2 \boldsymbol{M}^e_{ci})(\boldsymbol{A}^e_{ii} - \omega^2 \boldsymbol{M}^e_{ii})^{-1}(\boldsymbol{A}^e_{ic} - \omega^2 \boldsymbol{M}^e_{ic}) \quad (3.85)$$

$$\boldsymbol{R}^e_c = \boldsymbol{L}^e_c - (\boldsymbol{A}^e_{ci} - \omega^2 \boldsymbol{M}^e_{ci})(\boldsymbol{A}^e_{ii} - \omega^2 \boldsymbol{M}^e_{ii})^{-1} \boldsymbol{L}^e_i \quad (3.86)$$

once $\boldsymbol{u}_c$ has been determined from the solution of the global system. The values of the interior unknowns inside each element, $\boldsymbol{u}^e_i$, can be determined from

$$\boldsymbol{u}^e_i = (\boldsymbol{A}^e_{ii} - \omega^2 \boldsymbol{M}^e_{ii})^{-1}(\boldsymbol{L}^e_i - (\boldsymbol{A}^e_{ic} - \omega^2 \boldsymbol{A}^e_{ic})\boldsymbol{u}^e_c) \quad (3.87)$$

where $\boldsymbol{u}^e_c$ is the part of $\boldsymbol{u}_c$ relating to element e.

3.5.6 Banded Linear System

By adopting a Cuthill–McKee renumbering scheme for the edges and careful numbering of the edge based unknowns the linear system $\boldsymbol{K}_{cc}\boldsymbol{u}_c = \boldsymbol{R}_c$ is of banded nature. The bandwidth of the matrix depends on ku and kl which are the upper and lower bandwidths which originate from the numbering of the edges. It also depends on the order of the elements employed in the mesh. In fact, the actual upper and lower bandwidths for a mesh of uniform order elements are

$$\text{upper band width} = ku(p+1) + p \qquad \text{lower band width} = kl(p+1) + p \quad (3.88)$$

An illustration of the banded nature of $\boldsymbol{K}_{cc}$ is shown in Figure 3.9, here, the elemental matrices $\boldsymbol{K}^e_{cc}$ and $\boldsymbol{R}^e_c$ are shown contributing to the banded system.

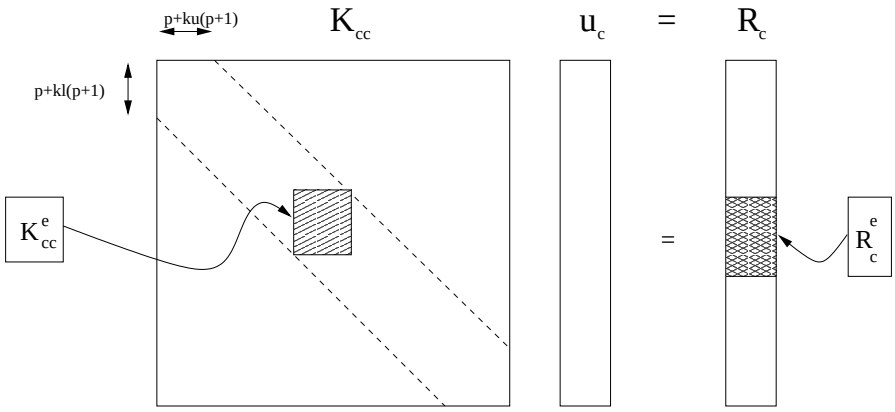

Figure 3.9: The assembly of contributions from elemental matrices $\boldsymbol{K}^e$ and $\boldsymbol{R}_c^e$ in to the global banded system $\boldsymbol{K}_{cc}\boldsymbol{u}_c = \boldsymbol{R}_c$

Chapter 4

Performance of the Edge Element Basis

4.1 Introduction

In this chapter, theoretical and numerical investigations are undertaken to determine the accuracy of the edge element discretisation which was described in Chapter 3. To verify the convergence of the scheme, we consider, the use of a–priori error estimates which enable a quantification of the theoretical convergence rates of finite element schemes. Monk [35] has derived an appropriate a–priori error estimate which is applicable for the higher order edge elements used in this thesis. In his estimate, the rate of convergence is dependent on the discretisation employed and the smoothness of the exact solution. For certain problems, his result also shows that exponential convergence can be obtained.

For purposes of numerical investigation, we consider a model problem which has no singularities. We then determine the numerical convergence of this problem for a variety of different discretisations and compare results to Monk's a–priori estimate. In addition, we also consider the convergence of a semi norm and a L^2 type norm, which gives further information about the convergence behaviour of the elements.

An important issue for all problems which involve the numerical propagation of

waves, is dispersion. Dispersion is measured by considering the difference between the exact wavenumber and the wavenumber of the computational solution. It is well known that the solution of the Helmholtz equation by a classical (linear) Galerkin finite element method deteriorates as the wavenumber increases, due to the effects of dispersion [47]. It is also been shown [47] that the solution of the Helmholtz equation can benefit from the use of the higher order, or the p–version, Galerkin finite element method. Ainsworth and Coyle [37] have recently investigated the effects of dispersion in Maxwell's equations when higher order quadrilateral edge elements are employed. For these elements, they were able to derive an exact relationship between the dispersion, mesh spacing and polynomial order for smoothly varying fields. Here, we consider a model problem and show how a series of refinement strategies can reduce and eradicate dispersion from solutions obtained on quadrilateral and triangular meshes.

4.2 Model Problem

For the purposes of analysis, a model problem is considered. This involves the propagation of a TE wave across a unit square domain Ω with boundary Γ. The problem has the exact solution

$$\boldsymbol{E}_0 = \begin{bmatrix} k_y \\ -k_x \end{bmatrix} e^{-\mathrm{i}(k_x x + k_y y)} \tag{4.1}$$

where $\omega^2 = k_x^2 + k_y^2$ is the wave number. The strong form of this problem is: find $\boldsymbol{E}(x,\, y)$ which satisfies the equation

$$\text{curl curl } \boldsymbol{E} - \omega^2 \boldsymbol{E} = \boldsymbol{0} \qquad\qquad \text{div}\boldsymbol{E} = 0 \tag{4.2}$$

subject to the condition

$$\boldsymbol{n} \wedge \text{curl } \boldsymbol{E} = \boldsymbol{n} \wedge \text{curl } \boldsymbol{E}_0 \qquad\qquad \text{on } \Gamma_F \tag{4.3}$$

where $\boldsymbol{n}$ is the unit outward normal to the boundary curve Γ_F. Following the approach outlined in Chapter 2, the weak variational form of this problem is: find

$\boldsymbol{E} \in \mathcal{H}(\text{curl}; \Omega)$ such that

$$a(\boldsymbol{E}, \boldsymbol{W}) - \omega^2 m(\boldsymbol{E}, \boldsymbol{W}) = l(\boldsymbol{W}) \qquad \forall \boldsymbol{W} \in \mathcal{H}(\text{curl}; \Omega) \tag{4.4}$$

where

$$a(\boldsymbol{u}, \boldsymbol{v}) = \int_\Omega \text{curl}\, \boldsymbol{u} \cdot \text{curl}\, \overline{\boldsymbol{v}}\, \mathrm{d}\Omega \qquad\qquad m(\boldsymbol{u}, \boldsymbol{v}) = \int_\Omega \boldsymbol{u} \cdot \overline{\boldsymbol{v}}\, \mathrm{d}\Omega \tag{4.5}$$

are bilinear forms and

$$l(\boldsymbol{v}) = -\int_{\Gamma_F} (\boldsymbol{n} \wedge \text{curl}\, \boldsymbol{E}_0) \cdot \overline{\boldsymbol{v}}\, \mathrm{d}\Gamma \tag{4.6}$$

is a linear form in $\boldsymbol{v}$. We set $X = \mathcal{H}(\text{curl}; \Omega)$ and let X_N denote the subspace of possible solutions on a finite element mesh of discretisation N with specified mesh spacing H and polynomial order p. The Galerkin approximation is found by employing the statement of equation (4.4) in the form: find $\boldsymbol{E}_N \in X_N$ such that

$$a(\boldsymbol{E}_N, \boldsymbol{W}) - \omega^2 m(\boldsymbol{E}_N, \boldsymbol{W}) = l(\boldsymbol{W}) \qquad \forall \boldsymbol{W} \in X_N \tag{4.7}$$

The integrals in this expression are evaluated using the approach outlined in Chapter 3.

4.3 A–priori Error Estimate

Monk [35] has derived an a–priori estimate which illustrates the convergence rates of three dimensional arbitrary order edge elements. To obtain the estimate, Monk used Nédélec's lower order three dimensional edge elements [32, 33] and extended them to higher order. Ainsworth and Coyle [37], who derived the basis that was presented in Chapter 3, constructed their elements in a similar manner. Monk's estimate is therefore also valid for these elements. His result, for uniformly spaced elements of uniform order, can be written in terms of the error in $\boldsymbol{E}_0$ as

$$||\boldsymbol{e}||_{\mathcal{H}^c} = ||\boldsymbol{E}_0 - \boldsymbol{E}_N||_{\mathcal{H}^c} \leq C H^{\min\,(s,t)} s^{-(t-\frac{1}{2})} ||\boldsymbol{E}_0||_{(\mathcal{H}^{t+1}(\Omega))^3} \tag{4.8}$$

In this expression t denotes the regularity [48], or smoothness, of the exact solution to the problem. If we consider $\boldsymbol{E}_0$ to be a smoothly varying field, then its regularity

is infinite. Conversely, a low t implies that the field has discontinuities. It is, therefore, apparent that the Sobolev space norm $||.||_{(\mathcal{H}^{t+1}(\Omega))^3}$ describes the smoothness of the field and the $\mathcal{H}(\text{curl};\Omega)$ norm

$$||\boldsymbol{e}||^2_{\mathcal{H}^c} = \int_\Omega |\boldsymbol{e}|^2 + |\text{curl}\,\boldsymbol{e}|^2 \,\mathrm{d}\Omega \tag{4.9}$$

represents a measure of the error in the solution. In Monk's notation, s represents the polynomial order employed in each edge element. The order assigned to each Ainsworth and Coyle element is denoted p. We distinguish between the two discretisations because an order s Monk element represents an element with convergence rate $\mathcal{O}(H^s)$ whilst an order s Ainsworth and Coyle element represents an element whose tangential component is of order s.

4.4 Numerical Convergence Rates

By studying the numerical convergence of a simple wave propagation problem, for which an analytical solution is known, the rates of convergence of $||\boldsymbol{E}_0 - \boldsymbol{E}_N||_{\mathcal{H}^c}$ for the triangular and quadrilateral edge elements is investigated. The exact solution for this problem is very smooth and hence t can be considered to be infinite. For smooth solutions, Monk's a–priori estimate indicates that an algebraic rate of convergence should be achieved for uniform mesh refinements with constant order elements. In addition, if a mesh of uniformly spaced elements remain unaltered, whilst uniformly increasing the polynomial order, an exponential rate of convergence should be obtained.

4.4.1 Algebraic Convergence

Figure 4.1 shows meshes consisting only of uniformly sized triangles with spacings $H = 1, 0.5, 0.25, 0.125$. Convergence curves of $||\boldsymbol{e}||_{\mathcal{H}^c}$ against H evaluated for $p = 0, 1, 2, 3$ are shown in Figure 4.2. For polynomial orders $p = 0$, $p = 1$ and $p = 2$ wave propagation problems $k_x = k_y = 1$ and $k_x = k_y = 2$ are considered. However, the computationally larger problems of $k_x = k_y = 3$ and $k_x = k_y = 4$

are undertaken for the higher polynomial order $p = 3$. This is to ensure that a better estimate of the rate of convergence for this polynomial order is obtained.

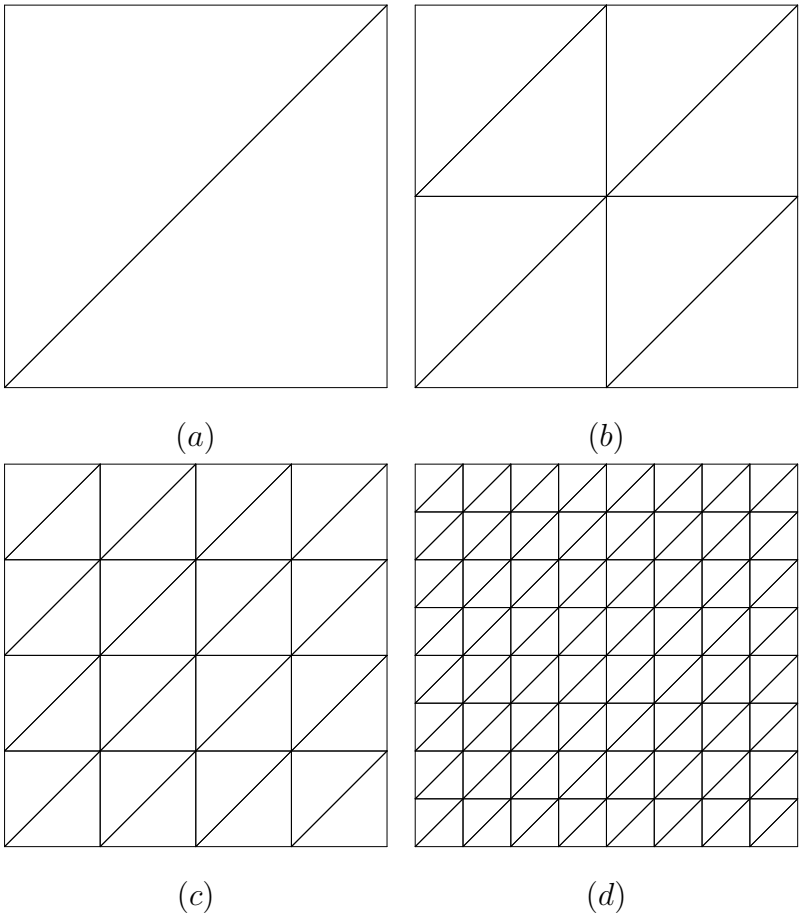

Figure 4.1: Wave propagation problem showing meshes of triangles with spacings: (a) $H = 1$, (b) $H = 0.5$, (c) $H = 0.25$ and (d) $H = 0.125$

By computing the gradients of these $\log$–$\log$ plots, the numerical convergence rates of $||\boldsymbol{e}||_{\mathcal{H}^c}$ for triangular elements with a fixed p and varying H may be estimated. The approximate convergence rates for the triangular elements are shown in Table 4.1. From Table 4.1, it is possible to observe that for $p \geq 1$ an increase in polynomial order leads to an increment in the rate of convergence (approximately $\mathcal{O}(H^p)$ for $p \geq 1$). This agrees with the algebraic convergence behaviour that Monk predicted in equation (4.8). The rate of convergence for $p = 0$ and $p = 1$ elements is the same because the additional basis functions for $p = 1$ give a linear variation in the tangential component of the field across the element, but, no increase in ac-

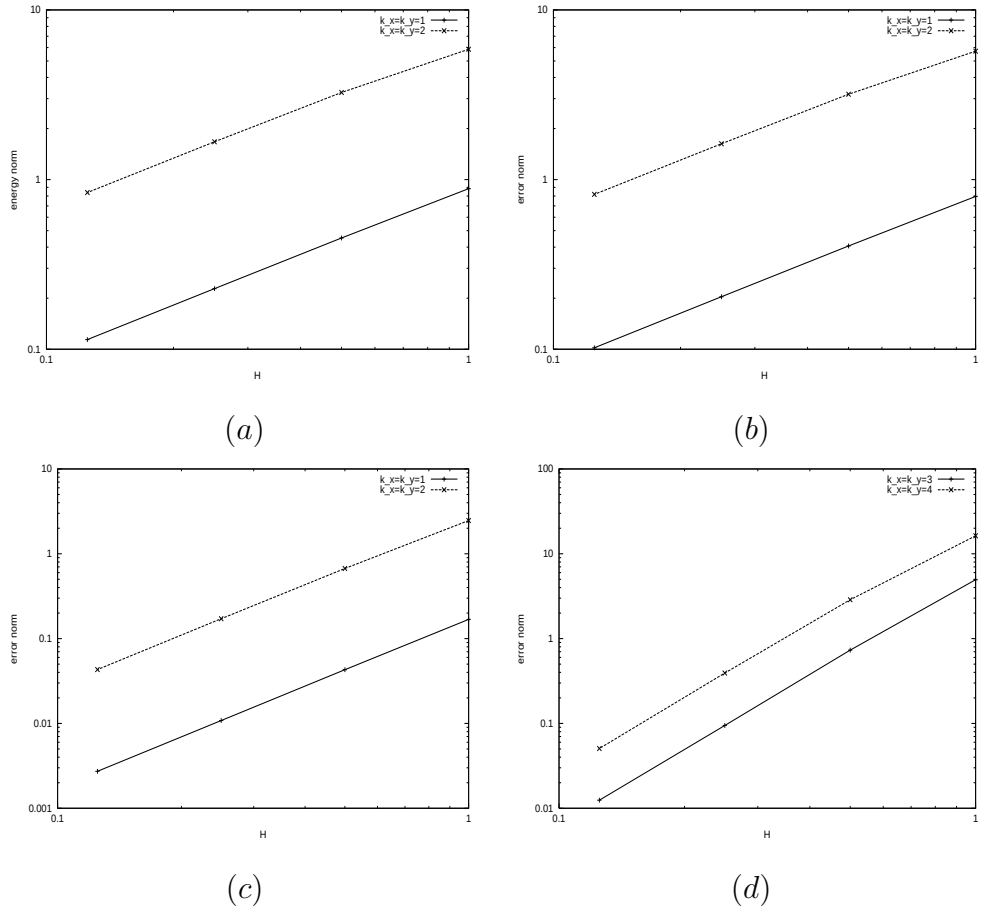

Figure 4.2: Experimental convergence of $||\boldsymbol{e}||_{\mathcal{H}^c}$ for $h-$refi nement on meshes of triangular elements with polynomial orders: (a) $p = 0$, (b) $p = 1$, (c) $p = 2$ and (d) $p = 3$.

curacy of the curl of the field. Indeed, for the cases of $p = 0$ and $p = 1$ the curl of the field is a constant across an element.

Figure 4.3 shows meshes consisting only of uniformly sized quadrilaterals with spacings $H = 1, 0.5, 0.25, 0.125$. Convergence curves of $||\boldsymbol{e}||_{\mathcal{H}^c}$ against H for $p = 0, 1, 2, 3$ are shown in Figure 4.4. For polynomial orders $p = 0$, $p = 1$ and $p = 2$ the wave propagation problems relating to $k_x = k_y = 1$ and $k_x = k_y = 2$ are considered. However, the computationally larger problems of $k_x = k_y = 3$ and $k_x = k_y = 3.5$ are undertaken for the higher polynomial order $p = 3$.

By computing the gradient of these $\log$–$\log$ plots, the numerical convergence rates of $||\boldsymbol{e}||_{\mathcal{H}^c}$ for the quadrilateral elements with fixed p and varying H may be

Table 4.1: Approximate convergence rates of $||\boldsymbol{e}||_{\mathcal{H}^c}$ for triangular elements obtained using a fi xed p and varying H for the wave propagation problem

p	0	1	2	3
$\|\|\boldsymbol{e}\|\|_{\mathcal{H}^c}$	0.99	0.99	1.97	2.95
$\mathcal{O}(H^p)$	–	1	2	3

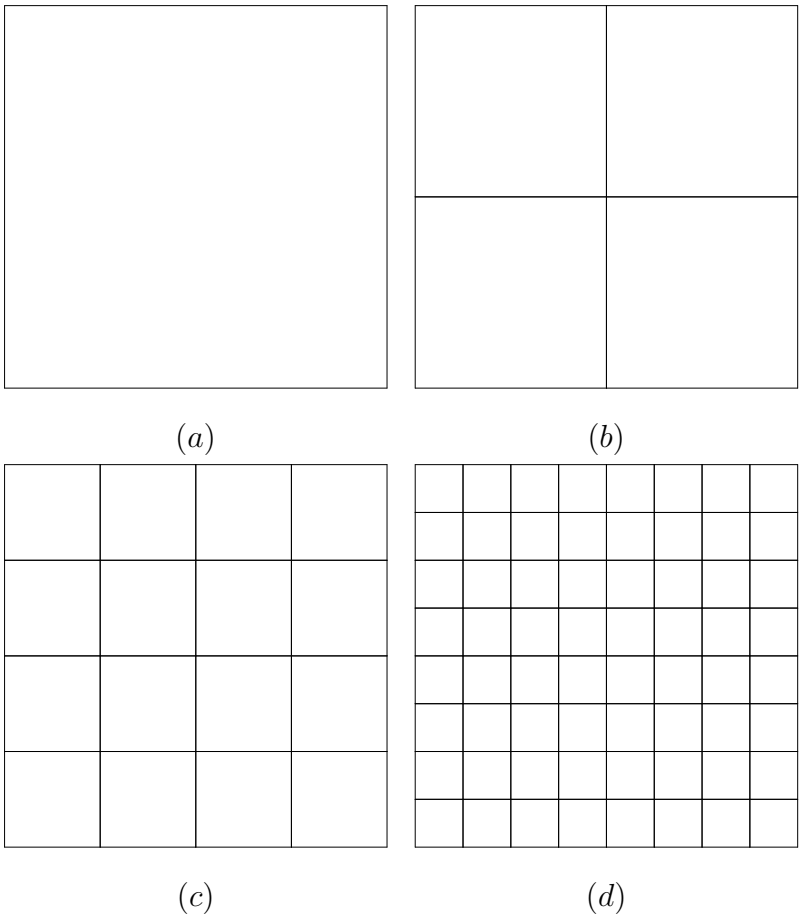

Figure 4.3: Wave propagation problem showing meshes of quadrilaterals with spacings: (a) $H = 1$, (b) $H = 0.5$, (c) $H = 0.25$ and (d) $H = 0.125$

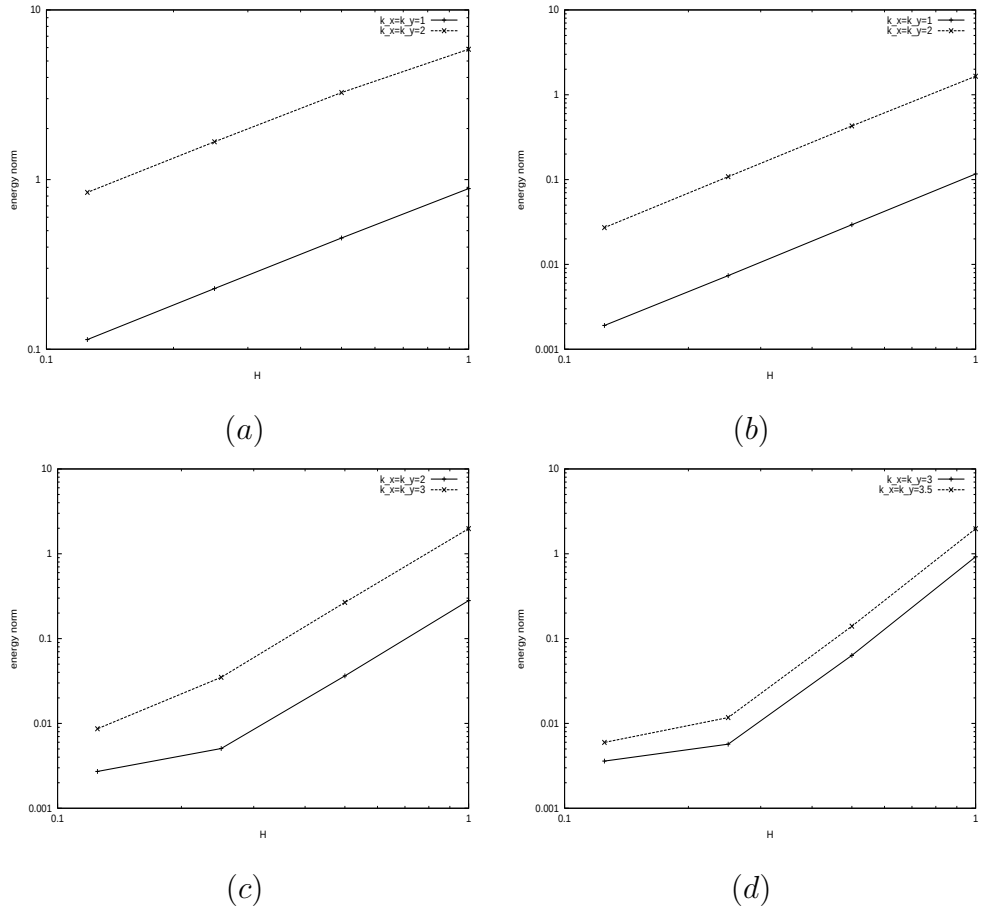

Figure 4.4: Experimental convergence of $||\boldsymbol{e}||_{\mathcal{H}^c}$ for $h-$refi nement on meshes of quadrilateral elements with polynomial orders: (a) $p = 0$, (b) $p = 1$, (c) $p = 2$ and (d) $p = 3$.

estimated. The approximate convergence rates for the quadrilateral elements are shown in Table 4.2. It is observed that for each increase in order, there is an increment in the rate of convergence in the $||\boldsymbol{e}||_{\mathcal{H}^c}$ norm (approximately $\mathcal{O}(H^{p+1})$). This indicates that the numerical convergence of the quadrilateral elements agrees with the algebraic convergence behaviour that was predicted by Monk in equation (4.8). In addition, the behaviour exhibited for the $p = 0$ triangular element does not manifest itself for the quadrilateral elements. This is because, for each increase in polynomial order, the curl of the field is approximated to a corresponding higher degree. The trailing off seen in the convergence curves shown in Figure 4.4 is due to the effects of numerical precision.

Table 4.2: Approximate convergence rates of $||\boldsymbol{e}||_{\mathcal{H}^c}$ for quadrilateral elements obtained using a fixed p and a varying H for the wave propagation problem

p	0	1	2	3
$\|\|\boldsymbol{e}\|\|_{\mathcal{H}^c}$	0.97	1.99	2.95	3.86
$\mathcal{O}(H^{p+1})$	1	2	3	4

4.4.2 Exponential Convergence

The numerical convergence of the $\mathcal{H}(\text{curl};\Omega)$ norm with p–refinement is investigated for meshes of triangles of spacing $H = 1, 0.5, 0.25, 0.125$. Figure 4.5 shows a $\log$–$\log$ plot of the convergence of $||\boldsymbol{e}||_{\mathcal{H}^c}$ with $p + 1$. The Figure illustrates the exponential convergence of the norm with p–refinement for a range of different wave numbers.

The numerical convergence of the $\mathcal{H}(\text{curl};\Omega)$ norm with p–refinement is now investigated for meshes of quadrilaterals with spacings $H = 1, 0.5, 0.25, 0.125$. Figure 4.6 shows a $\log$–$\log$ plot of the convergence of $||\boldsymbol{e}||_{\mathcal{H}^c}$ with $p + 1$. The Figure illustrates the exponential convergence of the norm with p–refinement for a range of different wave numbers.

4.4.3 Semi–Norm and L^2 Type Norm

In addition to considering the convergence of the $\mathcal{H}(\text{curl};\Omega)$ norm, the relative semi norm

$$||\boldsymbol{e}||_{\mathcal{S}} = \sqrt{\frac{a(\boldsymbol{e},\boldsymbol{e})}{a(\boldsymbol{E},\boldsymbol{E})}} \tag{4.10}$$

and the L^2 type norm

$$||\boldsymbol{e}||_{\mathcal{M}} = \sqrt{\frac{m(\boldsymbol{e},\boldsymbol{e})}{m(\boldsymbol{E},\boldsymbol{E})}} \tag{4.11}$$

are initially considered for meshes of triangular elements. In this case, meshes of uniformly spaced triangles corresponding to $H = 1, 0.5, 0.25, 0.125, 0.0625$ are

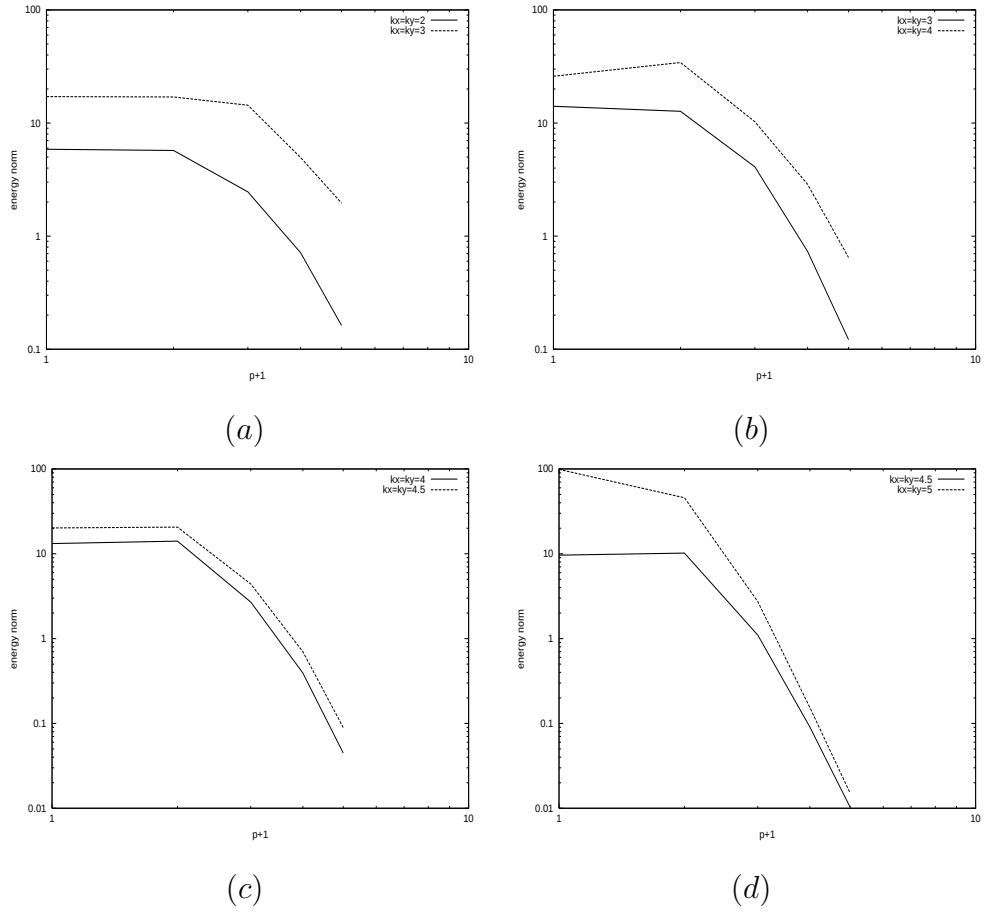

Figure 4.5: Experimental convergence of $||\boldsymbol{e}||_{\mathcal{H}^c}$ with p–refi nement for meshes of triangular elements with spacings: (a) $H = 1$, (b) $H = 0.5$, (c) $H = 0.25$ and (d) $H = 0.125$.

employed. A $\log$–$\log$ plot of $||\boldsymbol{e}||_{\mathcal{S}}$ and $||\boldsymbol{e}||_{\mathcal{M}}$ against H, for values of p fixed at $0, 1, 2, 3$, is shown in Figures 4.7 and 4.8. Solutions are computed for the cases $k_x = k_y = 1.5$ and $k_x = k_y = 2$ where the wave is propagated diagonally across the domain. In addition, cases where the wave propagates in the direction of the boundaries are also considered. From Figures 4.7 and 4.8, approximate convergence rates of $||\boldsymbol{e}||_{\mathcal{S}}$ and $||\boldsymbol{e}||_{\mathcal{M}}$ with H are computed. These are shown in Table 4.3.

In Table 4.3, we observe that for $p = 0$ the norms $||\boldsymbol{e}||_{\mathcal{S}}$ and $||\boldsymbol{e}||_{\mathcal{M}}$ converge at very similar rates, however for $p \geq 1$ we observe that $||\boldsymbol{e}||_{\mathcal{M}}$ converges substantially quicker than $||\boldsymbol{e}||_{\mathcal{S}}$. In fact, for $p > 0$, $||\boldsymbol{e}||_{\mathcal{S}}$ converges approximately at the rate $\mathcal{O}(H^p)$ and $||\boldsymbol{e}||_{\mathcal{M}}$ at the rate $\mathcal{O}(H^{p+1})$. If these rates are compared with the

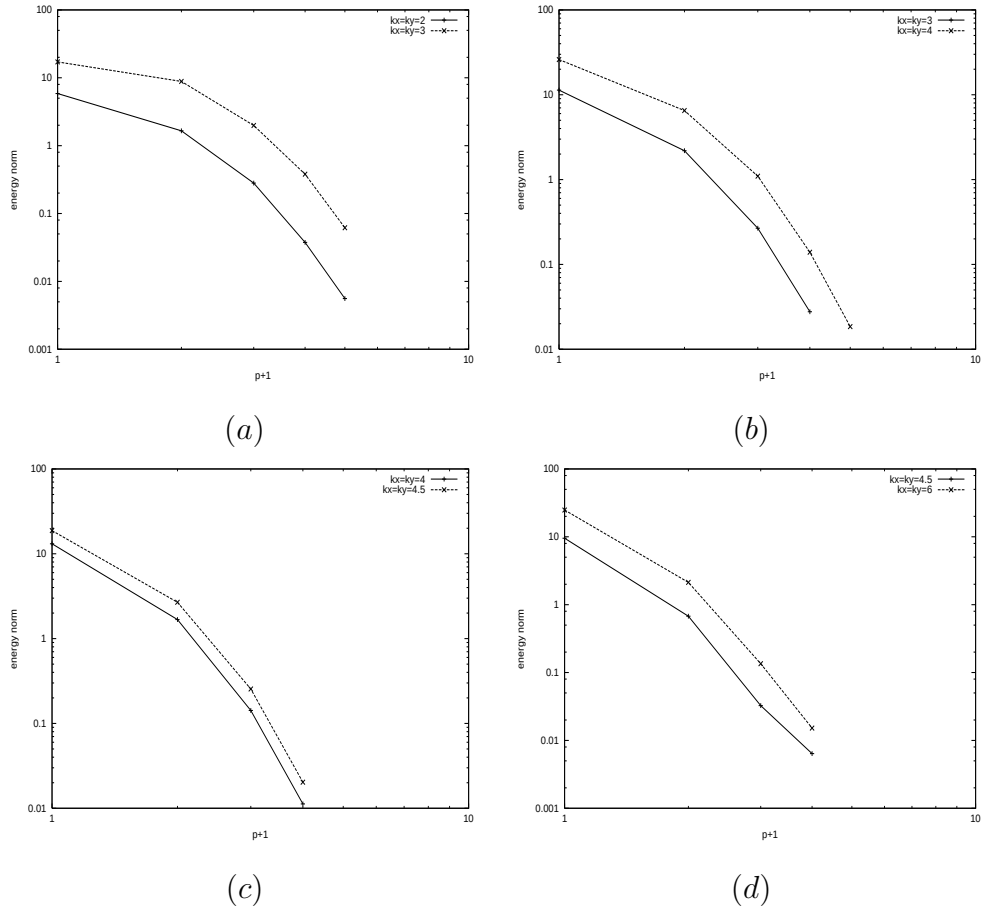

Figure 4.6: Experimental convergence of $||\boldsymbol{e}||_{\mathcal{H}^c}$ with p–refi nement for meshes of quadrilateral elements with spacings: (a) $H = 1$, (b) $H = 0.5$, (c) $H = 0.25$ and (d) $H = 0.125$.

convergence of $||\boldsymbol{e}||_{\mathcal{H}^c}$ it is observed that the $\mathcal{H}(\text{curl}; \Omega)$ norm is governed by $||\boldsymbol{e}||_{\mathcal{S}}$. This is what should be expected, as the norm $\mathcal{H}(\text{curl}; \Omega)$ can only converge as quick as it's slowest component.

The convergence of $||\boldsymbol{e}||_{\mathcal{S}}$ and $||\boldsymbol{e}||_{\mathcal{M}}$ are now examined for quadrilateral elements. For these elements, we consider waves which are propagated at angles between 45 and 90 degrees to the x axis. The convergence of $||\boldsymbol{e}||_{\mathcal{S}}$ with mesh spacing H is shown in Figure 4.9. Here, we observe that the convergence curves for waves which are propagated in directions close to the boundary overlap with those propagated directly along a boundary. This gives the visual appearance of only 2 lines. Figure 4.10 shows the convergence of $||\boldsymbol{e}||_{\mathcal{M}}$ with mesh spacing. In this Figure, it

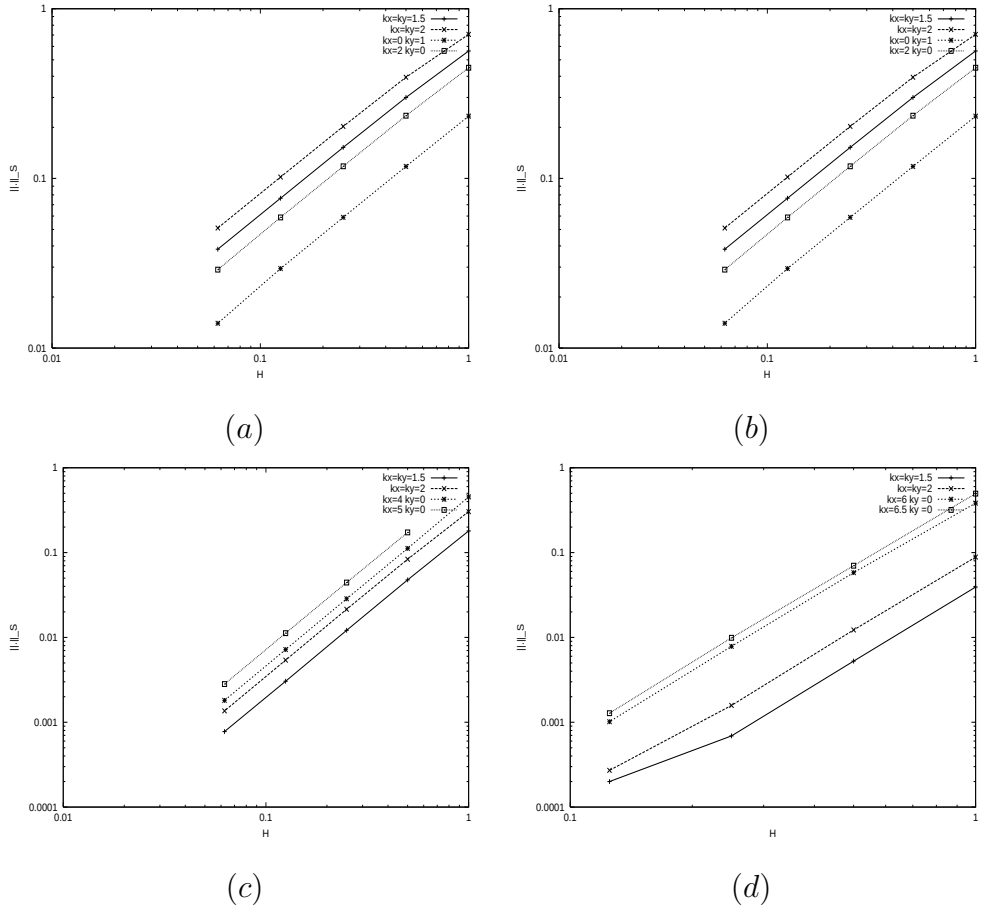

Figure 4.7: Convergence of $||\boldsymbol{e}||_{\mathcal{S}}$ for the wave propagation problem, when a variety of wavenumbers are employed on meshes of triangles with polynomial orders: (a) $p = 0$, (b) $p = 1$, (c) $p = 2$ and (d) $p = 3$

Table 4.3: Approximate convergence rates of $||\boldsymbol{e}||_{\mathcal{M}}$ and $||\boldsymbol{e}||_{\mathcal{S}}$ for triangular elements of fi xed polynomial order p and varying mesh spacing H

p	0	1	2	3
$\|\|\boldsymbol{e}\|\|_{\mathcal{M}}$	1.0	1.99	2.87	3.84
$\|\|\boldsymbol{e}\|\|_{\mathcal{S}}$	1.0	1.0	1.97	2.85

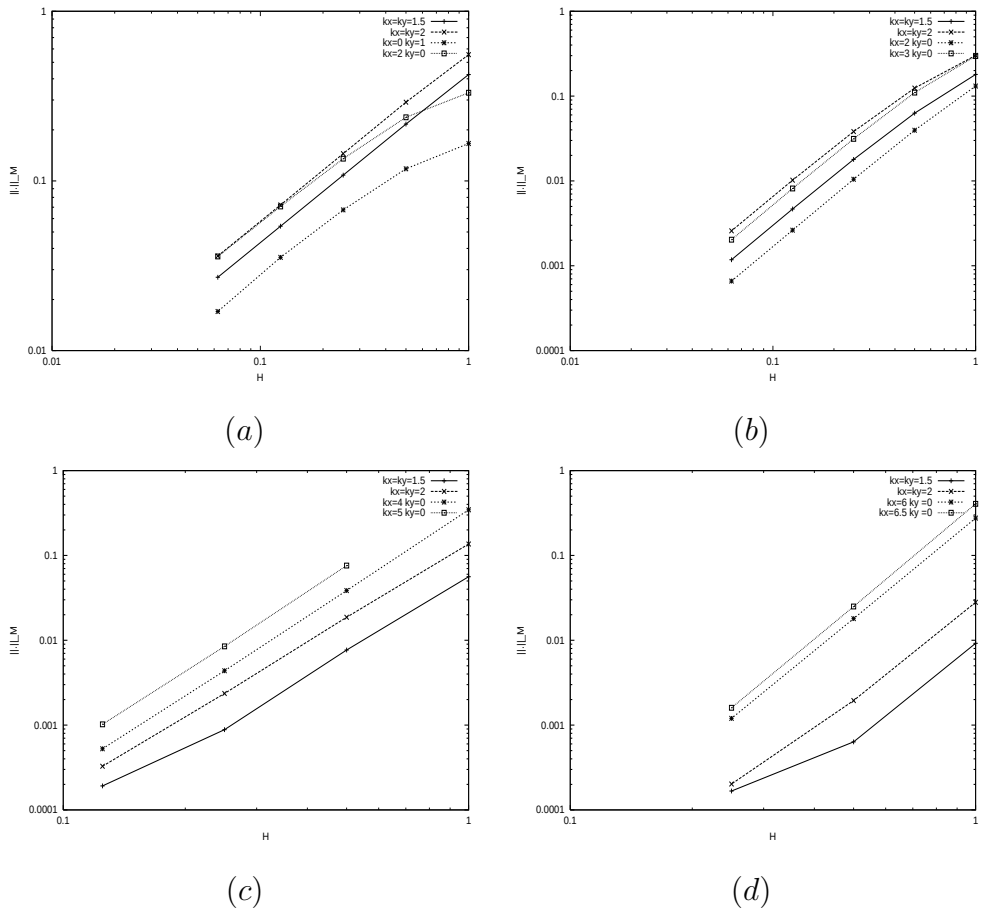

Figure 4.8: Convergence of $||\boldsymbol{e}||_{\mathcal{M}}$ for the wave propagation problem, when a variety of wavenumbers are employed on meshes of triangular elements with polynomial orders: (a) $p = 0$, (b) $p = 1$, (c) $p = 2$ and (d) $p = 3$

is observed that, when waves are propagated at different angles, they yield different convergence rates. Waves which are propagated diagonally across the computational domain have the slowest rate of convergence, and those which are propagated in a direction tangent to the boundaries have the fastest rate of convergence. The maximum and minimum rates of convergence are shown in Table 4.4, where $||\boldsymbol{e}||_{\mathcal{S}}$ converges approximately at the rate $\mathcal{O}(H^{p+1})$ and $||\boldsymbol{e}||_{\mathcal{M}}$ at rates between $\mathcal{O}(H^{p+1})$ and $\mathcal{O}(H^{p+2})$.

This behaviour seems at first unexpected, especially following the investigations for the triangles which showed rates of convergence to be independent of the angle of propagation. The reason for the behaviour can be explained by examining the spaces from which the edge element basis is constructed. Ainsworth and Coyle [37] give the space

$$\mathbb{E}_p = \{(E_\xi, E_\eta) : E_\xi \in \mathbb{Q}_{p,p+1}, E_\eta \in \mathbb{Q}_{p+1,p}\} \tag{4.12}$$

for the construction of quadrilateral elements and the space

$$\mathbb{E}_p = \{(E_\xi, E_\eta) : E_\xi, E_\eta \in \mathbb{P}_p\} \tag{4.13}$$

for the construction of the triangular elements. In these expressions $\mathbb{P}_p$ and $\mathbb{Q}_{p,p+1}$ represent the spaces for the construction of $\mathcal{H}^1$ scalar triangular and quadrilateral elements [31]. For the case of the quadrilateral elements, we observe that $\mathbb{E}_p$ is derived from adopting different order scalar $\mathcal{H}^1$ approximations in the local ξ and η directions for the E_ξ and E_η components. This will then lead to a variation of the convergence of $||\boldsymbol{e}||_{\mathcal{S}}$, so that the convergence rate is minimum when waves are propagated diagonally across a quadrilateral element and maximum when waves are propagated along quadrilateral edges. For the triangular elements, the E_ξ and E_η components are both constructed from $\mathbb{P}_p$. Therefore the same rate of convergence is achieved for all angles of propagation.

Table 4.4: Approximate convergence rates of $||\boldsymbol{e}||_{\mathcal{M}}$ and $||\boldsymbol{e}||_{\mathcal{S}}$ for quadrilateral elements of fi xed polynomial order p and varying mesh size H

p	0	1	2	3
$\|\|\boldsymbol{e}\|\|_{\mathcal{M}}$	$1.0 - 1.95$	$1.99 - 2.88$	$2.95 - 3.88$	$4 - 4.94$
$\|\|\boldsymbol{e}\|\|_{\mathcal{S}}$	0.95	1.95	2.95	4

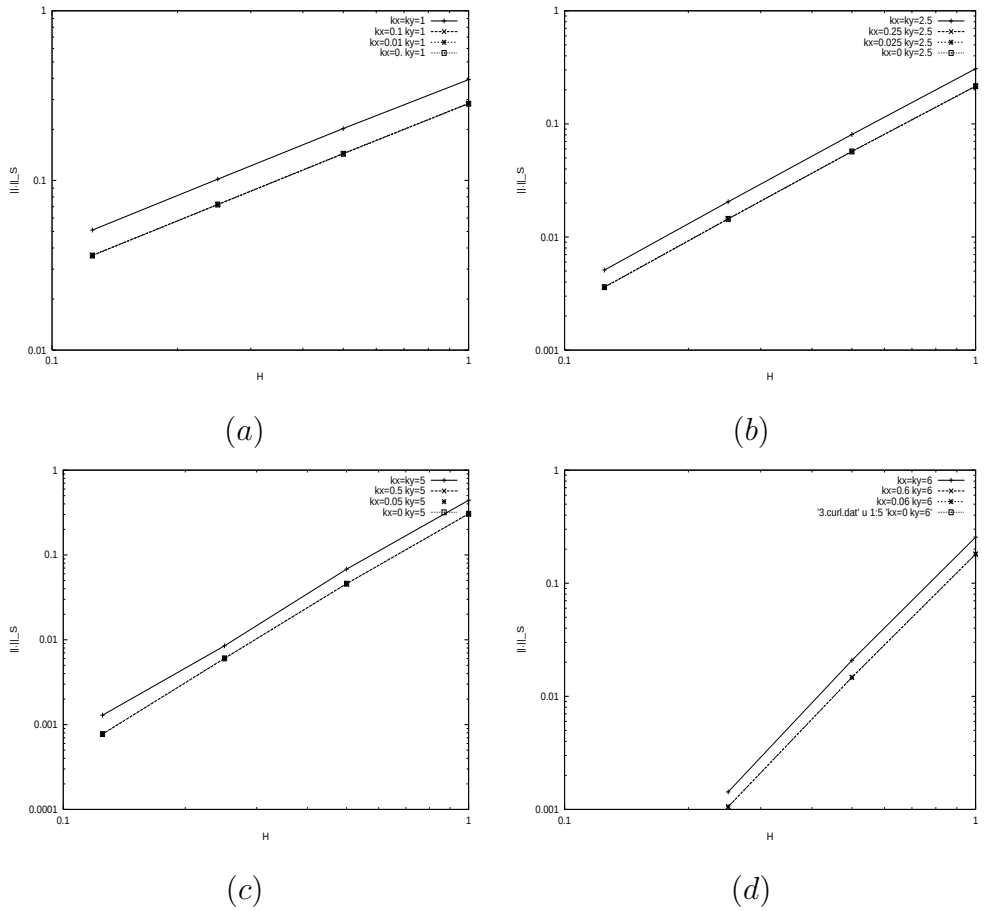

Figure 4.9: Convergence of $||\boldsymbol{e}||_{\mathcal{S}}$ for the wave propagation problem when a variety of wavenumbers are employed on meshes of quadrilaterals with polynomial orders: (a) $p = 0$, (b) $p = 1$, (c) $p = 2$ and (d) $p = 3$

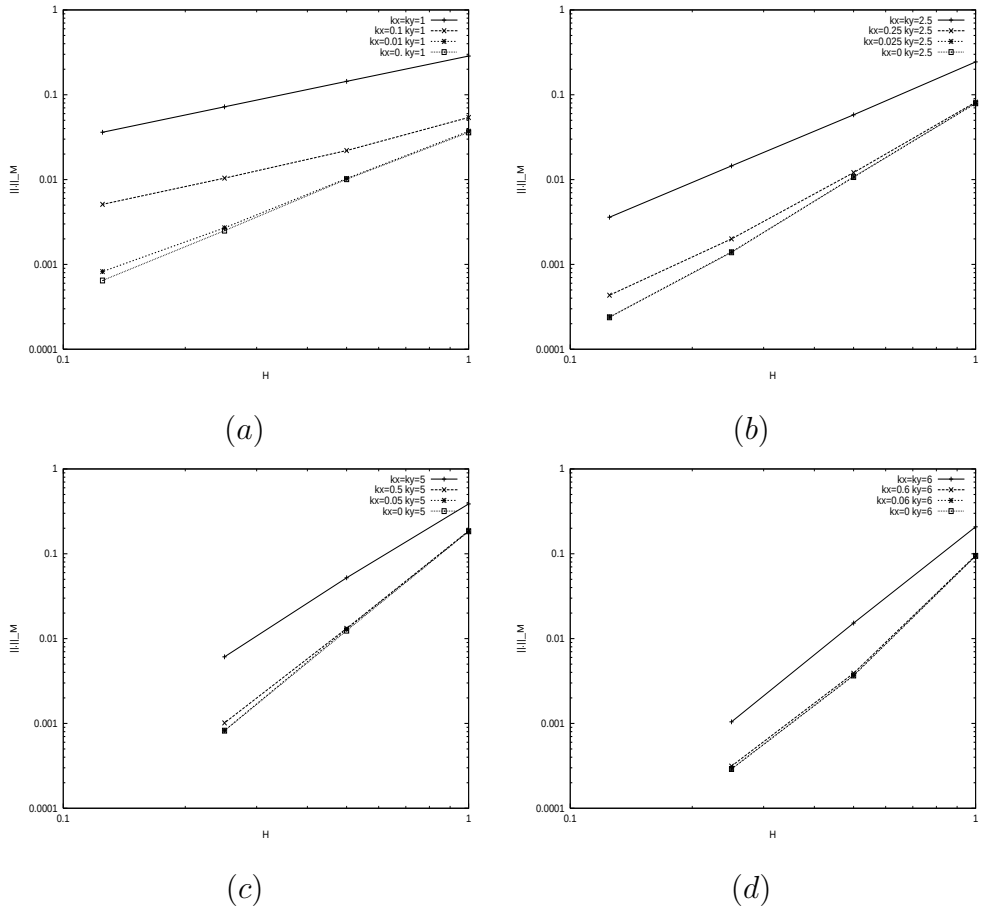

Figure 4.10: Convergence of $||\boldsymbol{e}||_{\mathcal{M}}$ for the wave propagation problem, when a variety of wavenumbers are employed on meshes of quadrilateral elements of polynomial order: (a) $p = 0$, (b) $p = 1$, (c) $p = 2$ and (d) $p = 3$

4.5 Dispersion Behaviour

For problems which involve the numerical propagation of waves, the effects of numerical dispersion are an important consideration. In this context, dispersion arises as the computed wavenumber is different from the true wave number of the solution. To observe this phenomena, Figure 4.11 shows the computed solution for $k_x = k_y = 4$ plotted with the exact solution along an axis $x = 0.501$, using $p = 0$ quadrilateral elements and mesh spacings $H = 1, 0.5, 0.25, 0.125, 0.0625, 0.03125$. In Figure 4.11, it can be observed that the computed solutions *lags behind* the true solution indicating a difference in wavenumber. As the mesh is refined, the difference between the true solution and computed solution diminishes. The final

computed solution, for the mesh with spacing $H = 0.03125$ shows a small error, indicating a small difference between computational and true wavenumber.

Figure 4.12 shows the computed solutions also using $k_x = k_y = 4$, but now with polynomial orders $p = 0, 1, 2, 3, 4, 5$ employed on a quadrilateral mesh of spacing $H = 1$. Initially, in common with the h–refined case, the solution *lags behind* the true solution. However, once dispersion is brought under control, the computed and true solutions become indistinguishable and therefore have the same wavenumber.

Table 4.5 shows the number of unknowns that are required to produce the solutions shown in Figure 4.11 where h–refinement is undertaken. Conversely, Table 4.6 shows the number of unknowns required to produce the solutions shown in Figure 4.12 where p–refinement is undertaken. From comparing the number of unknowns in these tables it is clear that the use of p–refinement to control dispersion is far superior to the use of h–refinement.

The dispersion of the triangular elements, with h–refinement is considered in Figure 4.13. Here, solutions are computed on meshes of spacings $H = 1, 0.5, 0.25, 0.125, 0.0625, 0.03125$ using elements of polynomial order $p = 0$. The numerical solutions are then compared with the exact solution of the model problem with $k_x = k_y = 2$. In Figure 4.13 the computed solutions lag behind the true solution, exhibiting the same behaviour as the quadrilateral elements. The dispersion of the triangular elements when p–refinement is undertaken is shown in Figure 4.14. In this Figure the computed solutions given by $p = 0, 1, 2, 3, 4, 5$ order elements on a mesh of spacing $H = 1$ are compared with the exact solution for $k_x = k_y = 2$. Once again, in common with the quadrilateral elements, it is observed that once dispersion is brought under control, the true and computed solutions become indistinguishable.

In a similar manner to the quadrilateral elements, we compare the number of unknowns for h– and p–refinement. The number of unknowns for the h–refinement scheme are shown in Table 4.7 and the number of unknowns for p–refinement are shown in Table 4.8. From these tables it is clear that using p–refinement to control dispersion is more beneficial than using h–refinement.

Dispersive effects will be considered in later chapters, when an estimate of the error in the numerical solution of problems, which have no analytical solutions, is considered.

Table 4.5: Number of unknowns employed for the propagation of a wave with wavenumber $k_x = k_y = 4$ on a mesh of quadrilaterals with varying mesh spacing and uniform $p = 0$ elements

H	1	0.5	0.25	0.125	0.0625	0.03125
Number of Unknowns	4	12	40	144	544	2112

Table 4.6: Number of unknowns employed for the propagation of a wave with wavenumber $k_x = k_y = 4$ on a mesh of quadrilaterals with spacing $H = 1$ and varying uniform order elements

p	0	1	2	3	4	5
Number of Unknowns	4	12	24	40	60	80

Table 4.7: Number of unknowns employed for the propagation of a wave with wavenumber $k_x = k_y = 2$ on a mesh of triangles with varying mesh spacing and uniform $p = 0$ elements

H	1	0.5	0.25	0.125	0.0625	0.03125
Number of Unknowns	5	16	56	208	800	3136

Table 4.8: Number of unknowns employed for the propagation of a wave with wavenumber $k_x = k_y = 2$ on a mesh of triangles with mesh spacing $H = 1$ and varying uniform order elements

p	0	1	2	3	4	5
Number of Unknowns	5	10	21	36	55	78

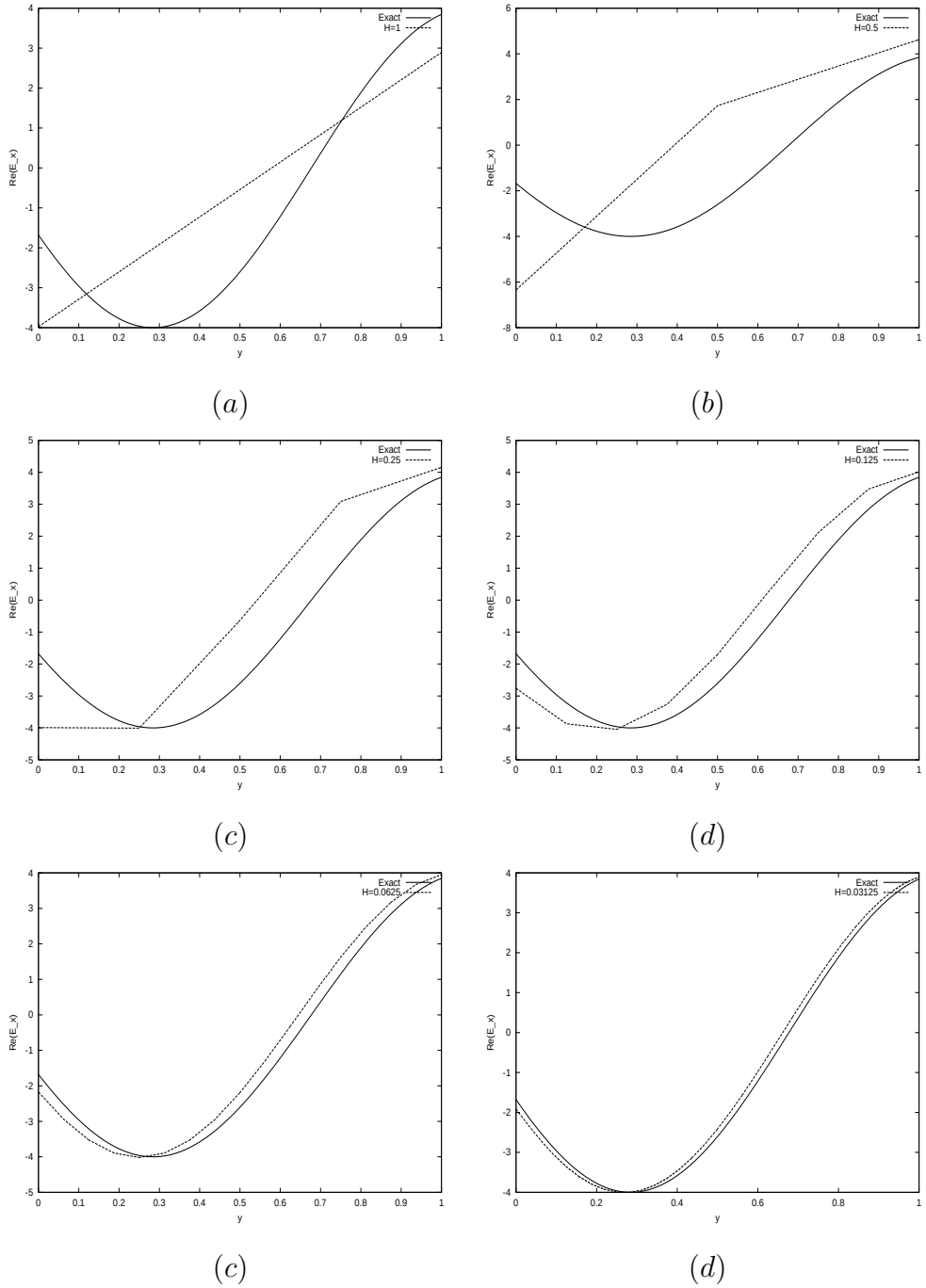

Figure 4.11: Dispersion in the wave propagation problem for meshes of quadrilaterals with mesh spacings: (a) $H = 1$, (b) $H = 0.5$, (c) $H = 0.25$, (d) $H = 0.125$, (e) $H = 0.0625$ and (f) $H = 0.03125$

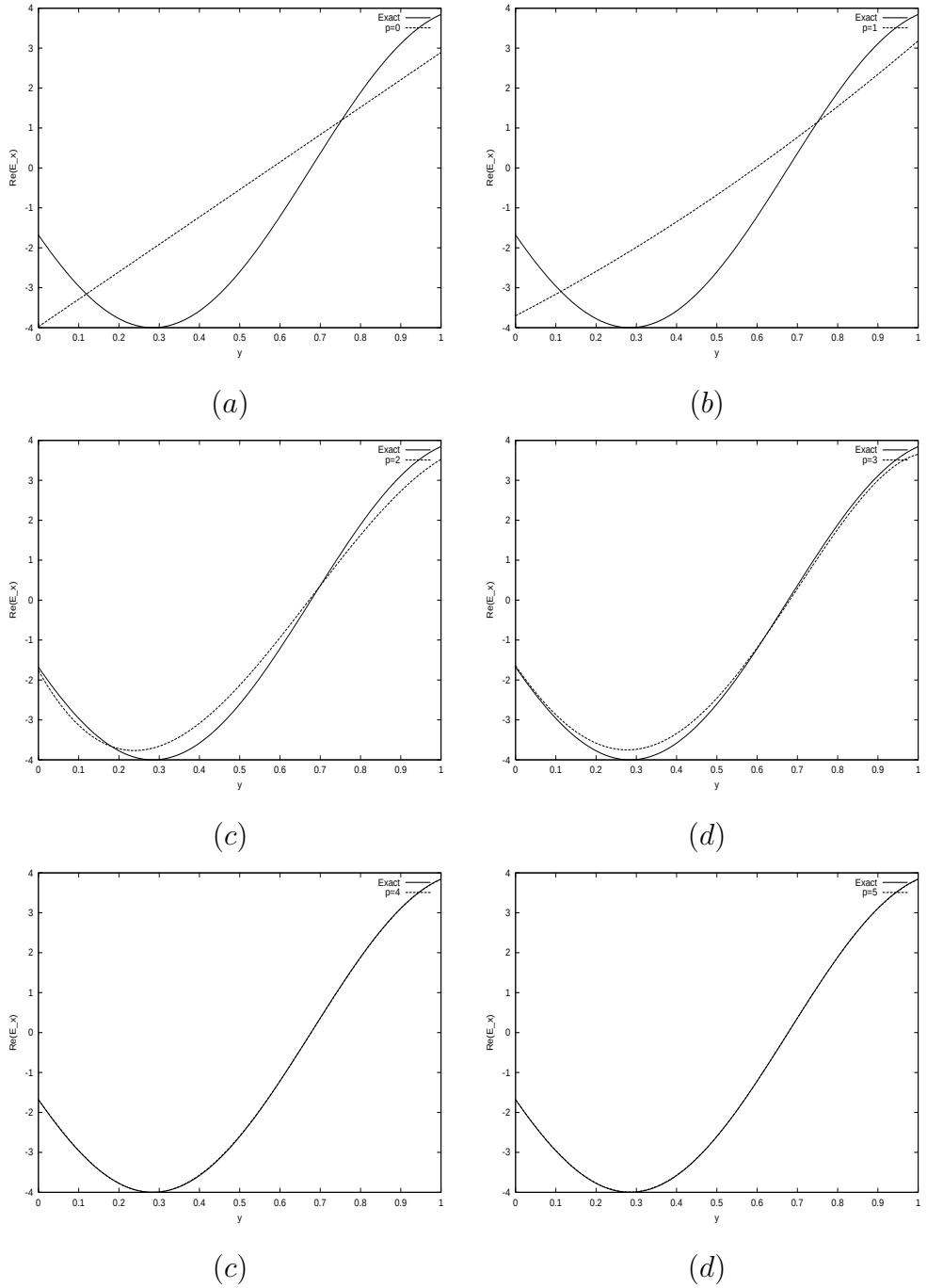

Figure 4.12: Dispersion in the wave propagation problem for meshes of quadrilaterals with polynomial orders: (a) $p = 0$, (b) $p = 1$, (c) $p = 2$, (d) $p = 3$, (e) $p = 4$ and (f) $p = 5$

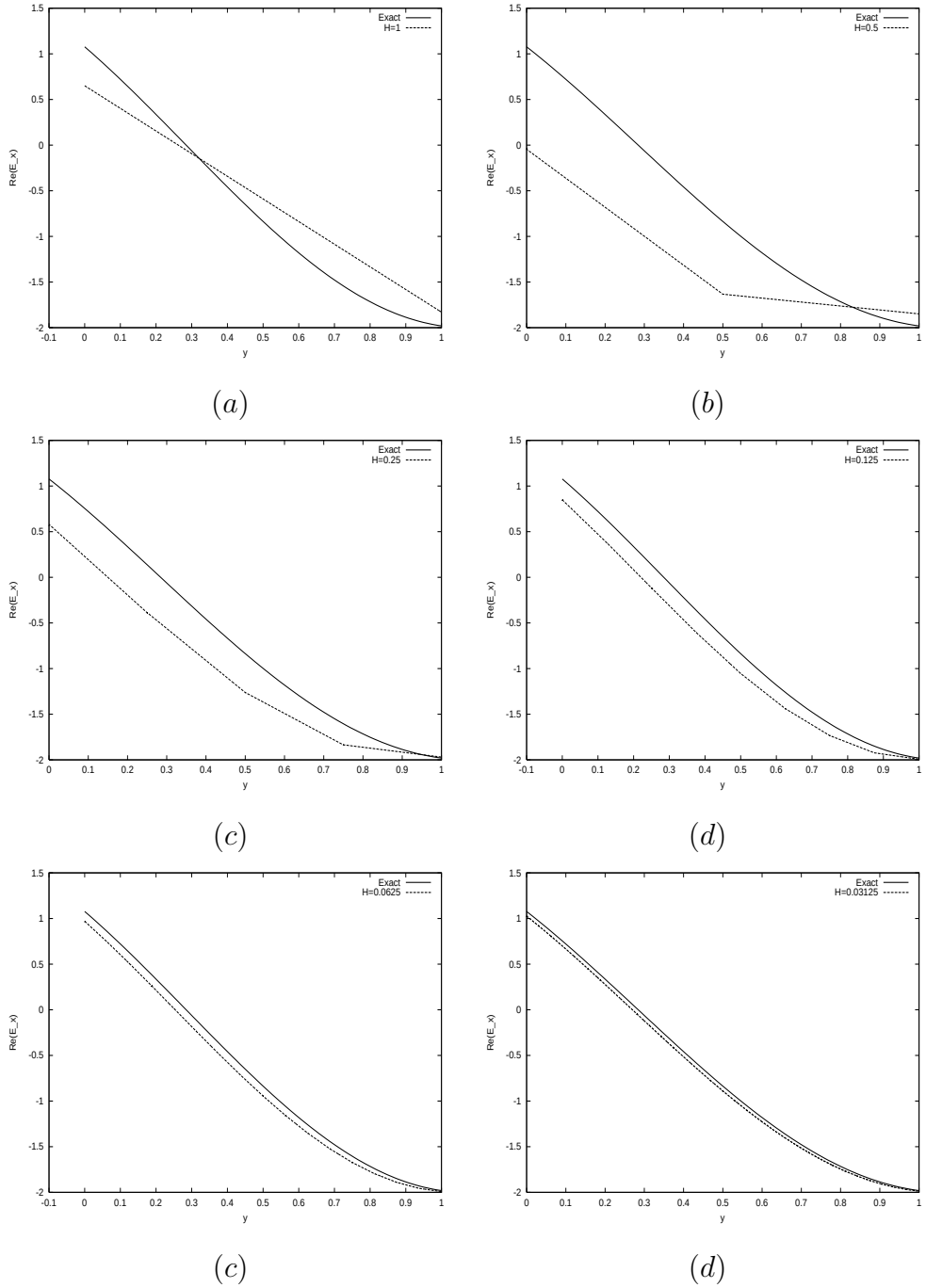

Figure 4.13: Dispersion in the wave propagation problem for meshes of triangles with mesh spacings: (a) $H = 1$, (b) $H = 0.5$, (c) $H = 0.25$, (d) $H = 0.125$, (e) $H = 0.0625$ and (f) $H = 0.03125$

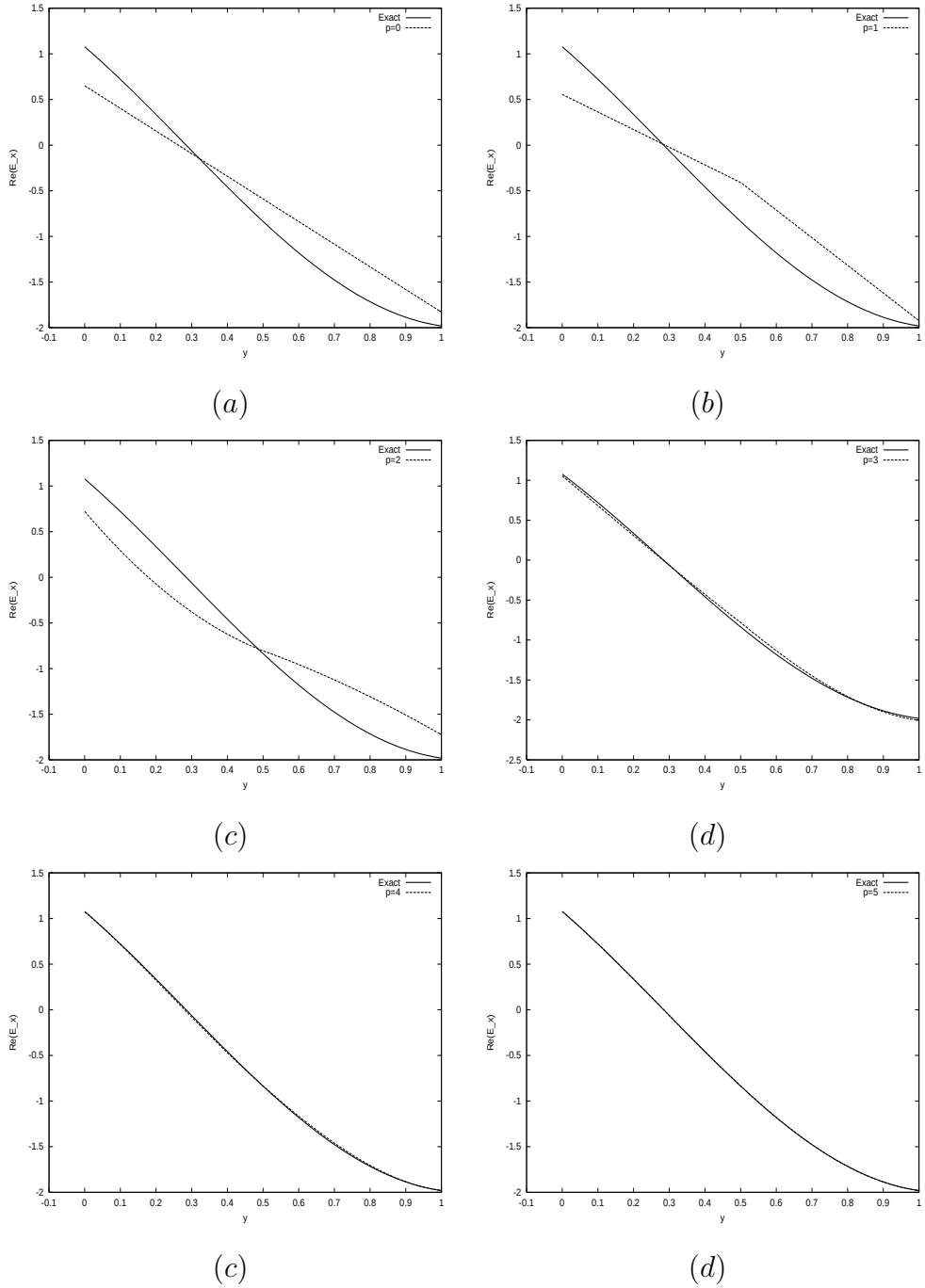

Figure 4.14: Dispersion in the wave propagation problem for meshes of triangles with polynomial orders: (a) $p = 0$, (b) $p = 1$, (c) $p = 2$, (d) $p = 3$, (e) $p = 4$ and (f) $p = 5$

Chapter 5

Edge Element Formulation for Scattering Problems

5.1 Introduction

This chapter introduces the variational framework which is to be employed for electromagnetic scattering problems. It builds on the theoretical discussions that were presented in Chapter 2 and the previously presented formulations [13, 38]. The chapter begins with the statement of the classical electromagnetic scattering problem. From this theoretical beginning, we derive the equations which will be used for the finite element solution of the scattering problem. To do this, it is necessary to introduce the truncation of an otherwise infinite domain. Various methods have been proposed for achieving this truncation and within this chapter, the merits of the different approaches will be discussed.

Following the derivation of the edge element formulation for scattering problems, consideration will be given to outputs of the electromagnetic scattering problem. In the aerospace industry, the radar cross section (RCS) is an output of particular interest. An explanation of how this quantity may be computed for scattering problems is given.

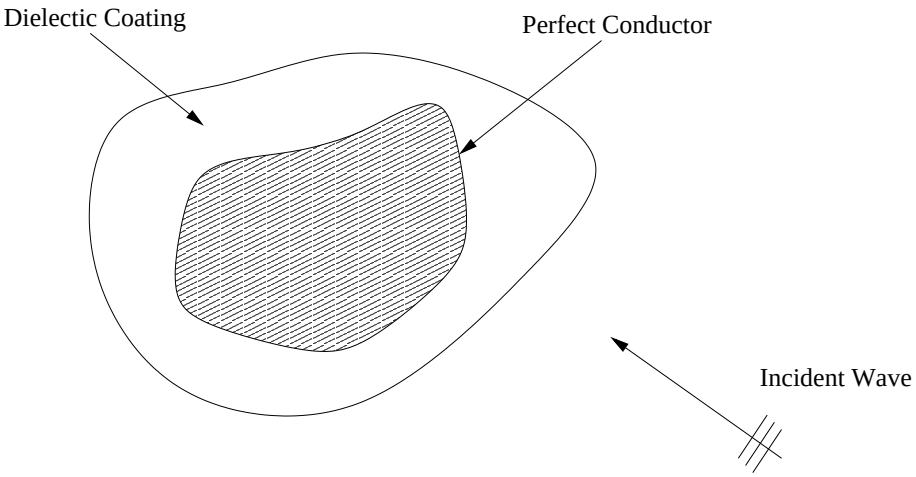

Figure 5.1: The electromagnetic scattering problem

5.2 Statement of the Classical Problem

We are interested in simulating problems in which waves, generated by an electromagnetic source, interact with a coated perfectly conducting obstacle. It is assumed that the coated scattering obstacle is surrounded by free space and that the source is located in the far field. This problem is illustrated diagrammatically in Figure 5.1. The unknowns are the electric and magnetic field intensity vectors, which are expressed, relative to a cartesian coordinate system $Oxyz$, in the form $\boldsymbol{E} = (E_x, E_y, E_z)^T$ and $\boldsymbol{H} = (H_x, H_y, H_z)^T$ respectively. For our purposes, it is convenient to decompose these fields into incident and scattered components, according to

$$\boldsymbol{E} = \boldsymbol{E}^s + \boldsymbol{E}^i \qquad\qquad \boldsymbol{H} = \boldsymbol{H}^s + \boldsymbol{H}^i \tag{5.1}$$

where the superscripts i and s denote the incident and scattered fields respectively. The governing equations for this problem are the Maxwell equations and, following the discussions in Chapter 2, the curl equations in two dimensions may be expressed in the dimensionless form

$$\text{curl}\, \boldsymbol{E} = -\mathrm{i}\omega \boldsymbol{\mu} \boldsymbol{H} \tag{5.2}$$

$$\text{curl}\, \boldsymbol{H} = \mathrm{i}\omega \boldsymbol{\epsilon} \boldsymbol{E} \tag{5.3}$$

and the divergence conditions written as

$$\text{div}\,(\boldsymbol{\epsilon}\boldsymbol{E}) = 0 \qquad\qquad \text{div}\,(\boldsymbol{\mu}\boldsymbol{H}) = 0 \tag{5.4}$$

Here $\mathrm{i} = \sqrt{-1}$ and $\omega = 2\pi/\lambda$, where λ is the wavelength of the incident wave. The quantities $\boldsymbol{\mu}$ and $\boldsymbol{\epsilon}$ represent the relative permeability and relative permittivity respectively of the propagation medium. For general media, the entries in these tensors may be complex valued functions of position, but, where the medium of propagation is free space, the tensors have the simple form

$$\boldsymbol{\mu} = \boldsymbol{I} \qquad\qquad \boldsymbol{\epsilon} = \boldsymbol{I} \tag{5.5}$$

where $\boldsymbol{I}$ is the unit tensor. In a dielectric the tensors are assumed to be of the form

$$\boldsymbol{\mu} = \mu_d \boldsymbol{I} \qquad\qquad \boldsymbol{\epsilon} = \epsilon_d \boldsymbol{I} \tag{5.6}$$

where μ_d and ϵ_d are specified real constants. Incident fields $\boldsymbol{E}^i$ and $\boldsymbol{H}^i$ are constructed to satisfy Maxwell's equations in free space, and so satisfy the vector equations

$$\text{curl}\,\left(\text{curl}\,\boldsymbol{E}^i\right) - \omega^2 \boldsymbol{E}^i = \boldsymbol{0} \tag{5.7}$$

and

$$\text{curl}\,\left(\text{curl}\,\boldsymbol{H}^i\right) - \omega^2 \boldsymbol{H}^i = \boldsymbol{0} \tag{5.8}$$

which are derived from (5.2) and (5.3). Similarly the total fields $\boldsymbol{E}$ and $\boldsymbol{H}$ satisfy the vector wave equations

$$\text{curl}\,\left(\boldsymbol{\mu}^{-1}\text{curl}\,\boldsymbol{E}\right) - \omega^2 \boldsymbol{\epsilon}\boldsymbol{E} = \boldsymbol{0} \tag{5.9}$$

and

$$\text{curl}\,\left(\boldsymbol{\epsilon}^{-1}\text{curl}\,\boldsymbol{H}\right) - \omega^2 \boldsymbol{\mu}\boldsymbol{H} = \boldsymbol{0} \tag{5.10}$$

both in the free space and in the dielectric. By subtraction of equation (5.7) from (5.9) and equation (5.8) from (5.10) we obtain

$$\text{curl}\,\left(\boldsymbol{\mu}^{-1}\text{curl}\,\boldsymbol{E}^s\right) - \omega^2 \boldsymbol{\epsilon}\boldsymbol{E}^s = \omega^2\left(\boldsymbol{\epsilon} - \boldsymbol{I}\right)\boldsymbol{E}^i - \text{curl}\,\left\{\left(\boldsymbol{\mu}^{-1} - \boldsymbol{I}\right)\text{curl}\,\boldsymbol{E}^i\right\} \tag{5.11}$$

$$\text{curl}\left(\boldsymbol{\epsilon}^{-1}\text{curl}\,\boldsymbol{H}^s\right) - \omega^2\boldsymbol{\mu}\boldsymbol{H}^s = \omega^2\left(\boldsymbol{\mu}-\boldsymbol{I}\right)\boldsymbol{H}^i - \text{curl}\left\{\left(\boldsymbol{\epsilon}^{-1}-\boldsymbol{I}\right)\text{curl}\,\boldsymbol{H}^i\right\} \tag{5.12}$$

These are the vector wave equations for the scattered field. In these expressions, we note the appearance of source terms, on the right hand side of the equations, which disappear in free space. If the incident field is specified, and divergence free, then following from the discussions in Chapter 2, equations (5.11) and (5.12), when coupled with tangential boundary conditions have a unique solution. The divergence conditions

$$\text{div}\,\boldsymbol{E}^s = 0 \qquad \text{and} \qquad \text{div}\,\boldsymbol{H}^s = 0 \tag{5.13}$$

may therefore be neglected. For completeness, in Appendix A we give a mixed formulation which imposes the divergence conditions. However, for this approach the Lagrange multiplier turns out to be zero.

5.2.1 Boundary Conditions

Perfectly Conducting Scatterer

The scattering obstacle is assumed to be a perfect conductor and the surface of the obstacle generally forms the internal boundary of the solution domain. On this boundary, the scattered magnetic field is subjected to the condition

$$\boldsymbol{n} \wedge \text{curl}\,\boldsymbol{H}^s = -\boldsymbol{n} \wedge \text{curl}\,\boldsymbol{H}^i \tag{5.14}$$

in TM simulations. Here $\boldsymbol{n}$ represents the unit outward normal vector to the surface and $\wedge$ denotes the vector product. In this case, the surface of the scatterer is denoted by Γ_1.

In TE simulations, the scattered electric field is subjected to the condition

$$\boldsymbol{n} \wedge \boldsymbol{E}^s = -\boldsymbol{n} \wedge \boldsymbol{E}^i \tag{5.15}$$

at the surface of the scatterer. In this case, the surface of the scatterer is denoted by Γ_2.

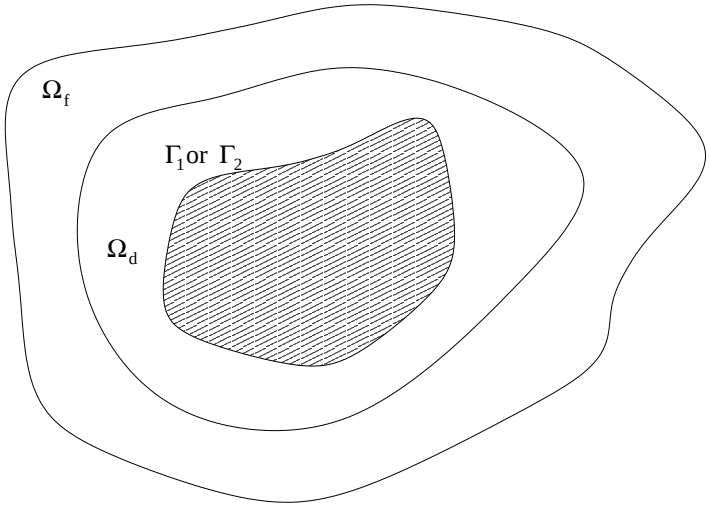

Figure 5.2: Creating the finite solution domain $\Omega_f + \Omega_d$

Dielectric Coating

At a dielectric interface the conditions

$$\boldsymbol{n} \wedge \boldsymbol{E}_f = \boldsymbol{n} \wedge \boldsymbol{E}_d \qquad \boldsymbol{n} \wedge \boldsymbol{H}_f = \boldsymbol{n} \wedge \boldsymbol{H}_d \tag{5.16}$$

on the total magnetic and electric fields are applied. In these expressions the subscript f refers to quantities on the free space side of the interface, and the subscript d refers to quantities on the dielectric side of the interface.

Far Field Treatment

Sufficiently far from the scattering obstacle, the scattered electric and magnetic field components consist of outgoing waves only. Much attention has been devoted to the problem of developing a suitable implementation of this condition, as it is always encountered in the numerical simulation of wave propagation problems defined on infinite domains. The standard approach involves the truncation, at a finite distance, of the infinite domain surrounding the scatterer to create a finite solution domain, $\Omega_f + \Omega_d$, as shown in Figure 5.2 here Ω_d represents the dielectric coating on the scatterer and Ω_f is the truncated free space region. At the newly created computational boundary, either absorbing boundary conditions [49, 50], the Dirichlet to Neumann (DtN) method [51], infinite elements [5, 11] or the wave envelope method [19] may

then be employed. Other alternatives involve the coupling of a domain method with a boundary procedure [52] or the use of an iterative method to update the solution on the far field boundary, using data calculated on the scatterer and an appropriate Green's function [53].

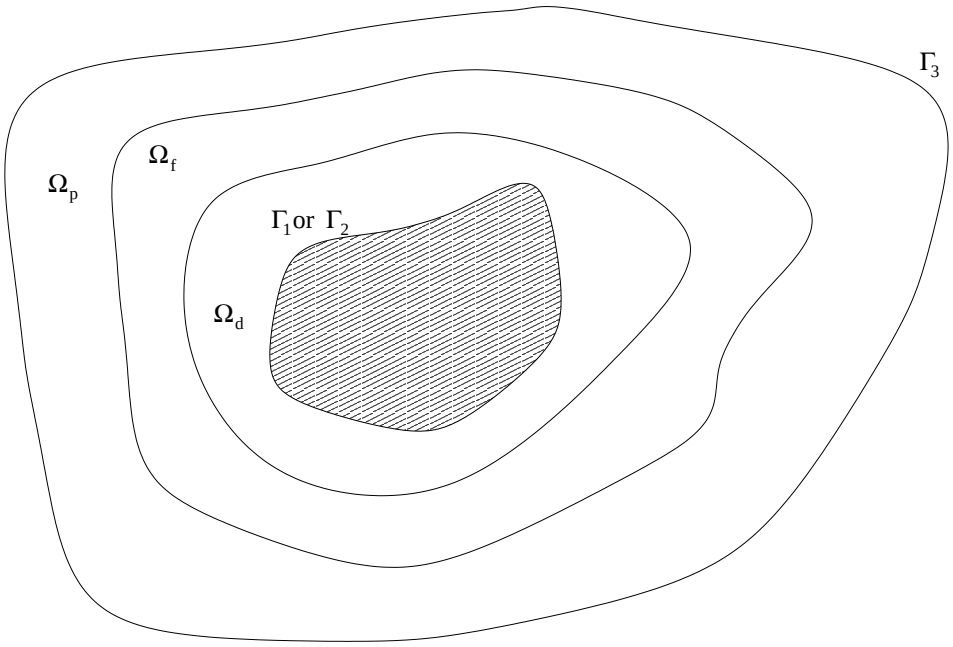

Figure 5.3: The addition of Ω_p, the PML region, to the domain Ω_f

Berenger [6] proposed the alternative perfectly matched layer (PML) technique. In his approach, an artificial material layer, Ω_p, is added to the free space domain, Ω_f, at the truncated far field boundary, as shown in Figure 5.3. The outer surface of the PML is denoted by Γ_3. Within the PML, Maxwell's curl equations are considered in the form

$$\text{curl}\, \boldsymbol{E}^s = -\mathrm{i}\omega \boldsymbol{\mu}_p \boldsymbol{H}^s \tag{5.17}$$

$$\text{curl}\, \boldsymbol{H}^s = \mathrm{i}\omega \boldsymbol{\epsilon}_p \boldsymbol{E}^s \tag{5.18}$$

These equations imply that, within the PML,

$$\text{curl}\, \left(\boldsymbol{\mu}_p^{-1} \text{curl}\, \boldsymbol{E}^s\right) - \omega^2 \boldsymbol{\epsilon}_p \boldsymbol{E}^s = \mathbf{0} \tag{5.19}$$

and

$$\text{curl}\, \left(\boldsymbol{\epsilon}_p^{-1} \text{curl}\, \boldsymbol{H}^s\right) - \omega^2 \boldsymbol{\mu}_p \boldsymbol{H}^s = \mathbf{0} \tag{5.20}$$

We try to choose the thickness of the PML, and to specify the variation in the material properties $\boldsymbol{\epsilon}_p$ and $\boldsymbol{\mu}_p$ through the PML, so as to ensure that the scattered wave is completely absorbed within the layer, without reflection. At the outer surface, Γ_3, the boundary condition

$$\boldsymbol{n} \wedge \boldsymbol{E}^s = \boldsymbol{0} \tag{5.21}$$

is applied in TE simulations, while the condition

$$\boldsymbol{n} \wedge \boldsymbol{H}^s = \boldsymbol{0} \tag{5.22}$$

is applied in the TM case.

5.3 Weak Variational Formulation

The governing differential equations (5.11), (5.12), (5.19) and (5.20) for this problem may be combined and written in the form

$$\text{curl}\,\left(\boldsymbol{\Lambda}_1^{-1}\text{curl}\,\boldsymbol{U}^s\right) - \omega^2\boldsymbol{\Lambda}_2\boldsymbol{U}^s = \omega^2\left(\boldsymbol{\Lambda}_2 - \boldsymbol{I}\right)\boldsymbol{U}^i - \text{curl}\,\left(\boldsymbol{\Lambda}_1^{-1} - \boldsymbol{I}\right)\text{curl}\,\boldsymbol{U}^i \tag{5.23}$$

where the unknown vector $\boldsymbol{U}^s$ is to be interpreted as the scattered electric field for the TE case and the scattered magnetic field in TM simulations. The corresponding incident field $\boldsymbol{U}^i$ exists only within physical media and is zero in Ω_p. In addition, within Ω_f and Ω_d we take

$$\boldsymbol{\Lambda}_1 = \boldsymbol{\mu} \qquad \boldsymbol{\Lambda}_2 = \boldsymbol{\epsilon} \tag{5.24}$$

for TE simulations and

$$\boldsymbol{\Lambda}_1 = \boldsymbol{\epsilon} \qquad \boldsymbol{\Lambda}_2 = \boldsymbol{\mu} \tag{5.25}$$

in the TM case. Within Ω_p we take

$$\boldsymbol{\Lambda}_1 = \boldsymbol{\mu}_p \qquad \boldsymbol{\Lambda}_2 = \boldsymbol{\epsilon}_p \tag{5.26}$$

for TE simulations and

$$\boldsymbol{\Lambda}_1 = \boldsymbol{\epsilon}_p \qquad \boldsymbol{\Lambda}_2 = \boldsymbol{\mu}_p \tag{5.27}$$

in the TM case. To develop a numerical solution procedure, a variational formulation of this problem is employed. Defining the spaces Z and Z^D as

$$Z^D = \{\boldsymbol{u} \,|\, \boldsymbol{u} \in \mathcal{H}(\text{curl}; \Omega);\ \boldsymbol{n} \wedge \boldsymbol{u} = -\boldsymbol{n} \wedge \boldsymbol{U}^i \text{ on } \Gamma_2;\ \boldsymbol{n} \wedge \boldsymbol{u} = \boldsymbol{0} \text{ on } \Gamma_3\} \quad (5.28)$$

$$Z = \{\boldsymbol{u} \,|\, \boldsymbol{u} \in \mathcal{H}(\text{curl}; \Omega);\ \boldsymbol{n} \wedge \boldsymbol{u} = \boldsymbol{0} \text{ on } \Gamma_2,\ \boldsymbol{n} \wedge \boldsymbol{u} = \boldsymbol{0} \text{ on } \Gamma_3\} \quad (5.29)$$

then a weak variational formulation of the problem is: find $\boldsymbol{U}^s \in Z^D$, such that

$$\begin{aligned} \int_{\Omega_f+\Omega_p+\Omega_d} \left(\boldsymbol{\Lambda}_1^{-1}\text{curl}\,\boldsymbol{U}^s \cdot \text{curl}\,\overline{\boldsymbol{W}} - \omega^2 \boldsymbol{\Lambda}_2 \boldsymbol{U}^s \cdot \overline{\boldsymbol{W}}\right) \mathrm{d}\Omega = \\ - \int_{\Gamma_1} \left(\boldsymbol{n} \wedge \boldsymbol{\Lambda}_1^{-1}\text{curl}\,\boldsymbol{U}^s\right) \cdot \overline{\boldsymbol{W}}\, \mathrm{d}\Gamma \\ - \left\{ \int_{\Omega_d} \left(\boldsymbol{\Lambda}_1^{-1} - \boldsymbol{I}\right) \text{curl}\,\boldsymbol{U}^i \cdot \text{curl}\,\overline{\boldsymbol{W}} - \omega^2 \left(\boldsymbol{\Lambda}_2 - \boldsymbol{I}\right) \boldsymbol{U}^i \cdot \overline{\boldsymbol{W}}\, \mathrm{d}\Omega \right\} \end{aligned} \quad (5.30)$$

for all $\boldsymbol{W}$ in Z.

5.4 Improved PML Condition

Monk and Callino [54] proposed an improved PML condition, where the Dirchlet condition on the truncated boundary Γ_3 is replaced by an absorbing boundary condition. Following their investigations, an alternative variational formulation is presented. The first order Bayliss-Turkel [49] absorbing boundary condition is chosen for the new far field condition. Following [50] this condition for Maxwell's equations can be written as

$$\text{curl}\,\boldsymbol{E}^s \approx -\mathrm{i}\omega \boldsymbol{n} \wedge \boldsymbol{E}^s \quad (5.31)$$

for the scattered electric field and

$$\text{curl}\,\boldsymbol{H}^s \approx -\mathrm{i}\omega \boldsymbol{n} \wedge \boldsymbol{H}^s \quad (5.32)$$

for the scattered magnetic field. Defining the spaces $\tilde{Z}^D$ and $\tilde{Z}$ as

$$\tilde{Z}^D = \{\boldsymbol{u} \,|\, \boldsymbol{u} \in \mathcal{H}(\text{curl}; \Omega);\ \boldsymbol{n} \wedge \boldsymbol{u} = -\boldsymbol{n} \wedge \boldsymbol{U}^i \text{ on } \Gamma_2\} \quad (5.33)$$

$$\tilde{Z} = \{\boldsymbol{u} \,|\, \boldsymbol{u} \in \mathcal{H}(\text{curl}; \Omega);\ \boldsymbol{n} \wedge \boldsymbol{u} = \boldsymbol{0} \text{ on } \Gamma_2\} \quad (5.34)$$

then the modified weak variational formulation of the problem is: find $\boldsymbol{U}^s \in \tilde{Z}^D$, such that

$$\begin{aligned}\int_{\Omega_f+\Omega_p+\Omega_d} \left(\boldsymbol{\Lambda}_1^{-1}\mathrm{curl}\,\boldsymbol{U}^s \cdot \mathrm{curl}\,\overline{\boldsymbol{W}} - \omega^2\boldsymbol{\Lambda}_2\boldsymbol{U}^s \cdot \overline{\boldsymbol{W}}\right)\mathrm{d}\Omega = \\ -\int_{\Gamma_1}\left(\boldsymbol{n}\wedge\boldsymbol{\Lambda}_1^{-1}\mathrm{curl}\,\boldsymbol{U}^s\right)\cdot\overline{\boldsymbol{W}}\,\mathrm{d}\Gamma - \mathrm{i}\omega\int_{\Gamma_3}\boldsymbol{n}\wedge\overline{\boldsymbol{W}}\cdot\boldsymbol{n}\wedge\boldsymbol{U}^s\,\mathrm{d}\Gamma \\ -\left\{\int_{\Omega_d}\left(\boldsymbol{\Lambda}_1^{-1}-\boldsymbol{I}\right)\mathrm{curl}\,\boldsymbol{U}^i\cdot\mathrm{curl}\,\overline{\boldsymbol{W}} - \omega^2\left(\boldsymbol{\Lambda}_2-\boldsymbol{I}\right)\boldsymbol{U}^i\cdot\overline{\boldsymbol{W}}\,\mathrm{d}\Omega\right\}\end{aligned} \tag{5.35}$$

for all $\boldsymbol{W}$ in $\tilde{Z}$.

5.5 Specification of the PML

The PML, Ω_p, is always taken to be in the form of a circular annulus of thickness 0.75λ and lies within the region that has been discretised with a structured mesh of elements. Within the PML, the entries in $\boldsymbol{\Lambda}_1$ and $\boldsymbol{\Lambda}_2$ are defined [55] to be complex–valued functions of position, according to

$$\boldsymbol{\Lambda}_1 = \boldsymbol{\Lambda}_2 = \boldsymbol{\Lambda} = \begin{bmatrix} \boldsymbol{\Lambda}^u & 0 \\ 0 & \alpha \end{bmatrix} \tag{5.36}$$

where

$$\boldsymbol{\Lambda}^u = \tilde{\boldsymbol{J}}^T \begin{bmatrix} \alpha & 0 \\ 0 & \alpha^{-1} \end{bmatrix} \tilde{\boldsymbol{J}} \qquad\qquad \alpha = 1 - (\mathrm{i}\sigma/\omega) \tag{5.37}$$

and $\tilde{\boldsymbol{J}}$ is a rotation matrix [55]. The PML parameter, σ, is defined to vary quadratically through the layer, according to

$$\sigma(x,y) = \sigma_{max}(r-r_1)^2/0.5625\lambda^2 \tag{5.38}$$

where r denotes the radial distance from the centre of the annulus to the point (x,y) and r_1 is the radius of the inner circle of the annulus. The optimum value

$$\sigma_{max} = 11/\lambda \tag{5.39}$$

has been determined as a result of a series of numerical experiments and is employed in all the computations reported in this thesis.

5.6 Specification of the Incident Wave

The form of the incident wave which is adopted in this thesis is

$$\boldsymbol{U}^i = \delta \begin{bmatrix} -\sin\theta \\ \cos\theta \end{bmatrix} e^{-\mathrm{i}\omega(x\cos\theta + y\sin\theta)} \tag{5.40}$$

where θ is the angle of incidence and δ is a parameter which is equal to $+1$ for TE simulations and equal to -1 for TM simulations. Unless explicitly stated, it is assumed that the angle of incidence is zero so that the incident wave propagates along the x axis.

5.7 Finite Element Solution

The application of the Galerkin approximation to the variational formulation of equation (5.30) results in the formulation of a complex linear equation system. This system can be expressed in the matrix form

$$\boldsymbol{K}\boldsymbol{u} = \boldsymbol{L} \tag{5.41}$$

where typical entries in the coefficient matrix, $\boldsymbol{K}$, and the right hand side vector, $\boldsymbol{L}$, are given by

$$K_{ij} = \int_{\Omega_f+\Omega_p+\Omega_d} \left(\boldsymbol{\Lambda}_1^{-1}\mathrm{curl}\,\boldsymbol{\Phi}_i \cdot \mathrm{curl}\,\boldsymbol{\Phi}_j - \omega^2 \boldsymbol{\Lambda}_2 \boldsymbol{\Phi}_i \cdot \boldsymbol{\Phi}_j\right)\,\mathrm{d}x\,\mathrm{d}y \tag{5.42}$$

and

$$\begin{aligned} L_j = &\int_{\Gamma_2} (\boldsymbol{n} \wedge \boldsymbol{\Lambda}_1^{-1}\,\mathrm{curl}\,\boldsymbol{U}^i) \cdot \boldsymbol{\Phi}_j \mathrm{d}\Gamma \\ &- \left\{ \int_{\Omega_d} \left(\boldsymbol{\Lambda}_1^{-1} - \boldsymbol{I}\right) \mathrm{curl}\,\boldsymbol{U}^i \cdot \mathrm{curl}\,\boldsymbol{\Phi}_j - \omega^2 \left(\boldsymbol{\Lambda}_2 - \boldsymbol{I}\right) \boldsymbol{U}^i \cdot \boldsymbol{\Phi}_j \,\mathrm{d}x\mathrm{d}y \right\} \end{aligned} \tag{5.43}$$

where $\boldsymbol{\Phi}_j$ denotes a typical real basis function. These integrals are evaluated by employing the covariant mapping described in Chapter 3. This involves mapping each element in turn to the master element and evaluating the elemental contributions to the linear system.

In Chapter 3 it was shown how static condensation can achieve an initial elimination of the interior degrees of freedom for higher order elements. Additional computational efficiency can then achieved by optimisation of the edge numbering to minimise the bandwidth of the linear equation system. This is accomplished by using a standard Cuthill–McKee algorithm [45]. The resulting equation system is solved using a direct LINPACK solver.

In a similar manner, the modified variational formulation given in equation (5.35), also results in a complex linear system. This is expressed in matrix form as

$$\tilde{\boldsymbol{K}}\boldsymbol{u} = \tilde{\boldsymbol{L}} \tag{5.44}$$

where typical entries in the coefficient matrix, $\tilde{\boldsymbol{K}}$, and the right hand side vector, $\tilde{\boldsymbol{L}}$ are given by

$$\tilde{K}_{ij} = \int_{\Omega_f+\Omega_p+\Omega_d} \left(\boldsymbol{\Lambda}_1^{-1}\text{curl}\,\boldsymbol{\Phi}_i \cdot \text{curl}\,\boldsymbol{\Phi}_j - \omega^2 \boldsymbol{\Lambda}_2 \boldsymbol{\Phi}_i \cdot \boldsymbol{\Phi}_j\right)\,\mathrm{d}x\,\mathrm{d}y + \mathrm{i}\omega \int_{\Gamma_3} \boldsymbol{n} \wedge \boldsymbol{\Phi}_i \cdot \boldsymbol{n} \wedge \boldsymbol{\Phi}_j \,\mathrm{d}\Gamma \tag{5.45}$$

and

$$\tilde{L}_j = \int_{\Gamma_2} (\boldsymbol{n} \wedge\, \boldsymbol{\Lambda}_1^{-1}\,\text{curl}\,\boldsymbol{U}^i) \cdot \boldsymbol{\Phi}_j d\Gamma - \left\{ \int_{\Omega_d} \left(\boldsymbol{\Lambda}_1^{-1} - \boldsymbol{I}\right) \text{curl}\,\boldsymbol{U}^i \cdot \text{curl}\,\boldsymbol{\Phi}_j - \omega^2 \left(\boldsymbol{\Lambda}_2 - \boldsymbol{I}\right) \boldsymbol{U}^i \cdot \boldsymbol{\Phi}_j \,\mathrm{d}x\,\mathrm{d}y \right\} \tag{5.46}$$

The same assembly procedures as used for the original weak variational formulation are again followed. After the solution of the complex linear system (viz equation (5.41) or (5.44)) then for either TE or TM analysis the scattered electric and magnetic fields may be recovered across the computational domain. Using these values contours of the solution may be made.

5.8 Radar Cross Section Evaluation

In addition to outputs generated directly from the computational solution, it is of interest to consider outputs which are derived from the computational solution. Such

a derived output is the scattering width, which is of interest to aerospace engineers. The scattering width, or radar cross section per unit length, for two dimensional TE problems is defined as

$$\chi(\phi) = \lim_{r\to\infty} 2\pi r \frac{|H_z^s|^2}{|H_z^i|^2} \tag{5.47}$$

and

$$\chi(\phi) = \lim_{r\to\infty} 2\pi r \frac{|E_z^s|^2}{|E_z^i|^2} \tag{5.48}$$

for TM problems. Obviously, these expressions cannot be evaluated directly from the computational solution as they require far field data. However, it can be shown [38] that, using a near field to far field transformation, the scattering width can be evaluated as

$$\chi(\phi) = \frac{\omega}{4}\left|\int_{\Gamma_c} (\boldsymbol{n}\wedge\boldsymbol{U}^s\cdot\boldsymbol{V} + \boldsymbol{n}\wedge\operatorname{curl}\boldsymbol{U}^s\cdot\boldsymbol{Y})\,\mathrm{d}\Gamma'\right|^2 \tag{5.49}$$

where (x', y') denotes the coordinates of a general point on a collection surface Γ_c and

$$\boldsymbol{V} = \begin{bmatrix} 0 \\ 0 \\ -\delta \end{bmatrix} e^{\mathrm{i}\omega(x'\cos\phi + y'\sin\phi)} \tag{5.50}$$

$$\boldsymbol{Y} = \frac{\delta}{\mathrm{i}\omega}\begin{bmatrix} \sin\phi \\ -\cos\phi \\ 0 \end{bmatrix} e^{\mathrm{i}\omega(x'\cos\phi + y'\sin\phi)} \tag{5.51}$$

In these equations, r and ϕ denote the cylindrical polar coordinates of a general observation point in the far field. In addition, we specify that the collection surface is chosen so that it lies in free space and completely encloses the scatterer. The corresponding discrete expression for the scattering width is given as

$$\chi_H(\phi) = \frac{\omega}{4}\left|\int_{\Gamma_c} (\boldsymbol{n}\wedge\boldsymbol{U}_H^s\cdot\boldsymbol{V} + \boldsymbol{n}\wedge\operatorname{curl}\boldsymbol{U}_H^s\cdot\boldsymbol{Y})\,\mathrm{d}\Gamma'\right|^2 \tag{5.52}$$

which can be evaluated using data from the computational solution to the problem. When the results of the numerical simulations are presented, it is the quantity

$$RCS = 10\log_{10}\chi_H \tag{5.53}$$

that will be plotted. In this way, the scattering width is expressed in decibels and provides a meaningful description of the far field scattering from the object.

5.9 Analytical Solutions

Analytical solutions to the scattering problem will be used to verify the numerical simulations. Analytical solutions are available for the TE and TM scattering observed from circular cylinders of infinite extent in the z direction. Classical texts such as Harrington [56] or Balanis [28] give derivations of the expansions for the analytical solution across the computational domain. For completeness Balanis's expansions for the scattering width observed from a PEC cylinder and coated PEC cylinder are given.

5.9.1 PEC Cylinder

PEC cylinders of infinite extent in the z direction are considered.

TE Case

The exact expression for the scattering width for a 2 dimensional TE cylinder of radius a is given as

$$\chi(\phi) = \frac{4}{\omega}\left|\sum_{i=0}^{\infty}\varepsilon_i \frac{J_i'(\omega a)}{H_i^{(2)'}(\omega a)}\cos i\phi\right|^2 \tag{5.54}$$

where ε_i is defined as

$$\varepsilon_i = \begin{cases} 1 & i = 0 \\ 2 & i \neq 0 \end{cases} \tag{5.55}$$

In addition, $J_i(x)$ is the Bessel function of the first kind, of order i with argument x and $H_i^{(2)}(x)$ is the Hankel function of the second kind of order i. The prime indicates differentiation with respect to the argument of the function. These functions can be generated by using recursive relations [57]. To plot this function, the infinite series is truncated when the functions in the series become sufficiently small.

TM Case

The corresponding expression for the scattering width for a TM cylinder is given by

$$\chi(\phi) = \frac{4}{\omega}\left|\sum_{i=0}^{\infty}\varepsilon_i \frac{J_i(\omega a)}{H_i^{(2)}(\omega a)}\cos i\phi\right|^2 \tag{5.56}$$

which again is truncated approximately.

5.9.2 Coated PEC Cylinder

Lossless singly coated PEC cylinders which are of infinite extent in the z direction are considered.

TE Case

The exact expression for the scattering width for a 2 dimensional TE coated cylinder, for which the inner radius of the PEC is a and outer radius of the dielectric coating b, is

$$\chi(\phi) = \frac{\omega}{4}\left|\sum_{i=0}^{\infty}\frac{J_i'(\omega b)\,a_i - \sqrt{\frac{\mu_d}{\epsilon_d}}J_i(\omega b)\,b_i}{\sqrt{\frac{\mu_d}{\epsilon_d}}H_i^{(2)}(\omega b)\,b_n - H_i^{(2)'}(\omega b)\,a_i}\varepsilon_i\cos i\phi\right|^2 \tag{5.57}$$

where

$$a_i = \frac{Y_i(k_d b)}{Y_i'(k_d a)} - \frac{J_i(k_d b)}{J_i'(k_d a)} \tag{5.58}$$

$$b_i = \frac{Y_i'(k_d b)}{Y_i'(k_d a)} - \frac{J_i'(k_d b)}{J_i'(k_d a)} \tag{5.59}$$

In these expressions $Y_i(x)$ is the Bessel function of the second kind, of order i with argument x, and k_d represents the wavenumber is the dielectric medium given by

$$k_d = \omega\sqrt{\epsilon_d \mu_d} \tag{5.60}$$

where ϵ_d and μ_d are the properties of the dielectric medium.

TM Case

Similarly, the expression for the 2 dimensional scattering width of the the TM coated cylinder is given by

$$\chi(\phi) = \frac{\omega}{4}\left|\sum_{i=0}^{\infty} \frac{J_i^{'}(\omega b)\, c_i - \sqrt{\frac{\epsilon_d}{\mu_d}} J_i(\omega b)\, d_i}{\sqrt{\frac{\epsilon_d}{\mu_d}} H_i^{(2)}(\omega b)\, d_i - H_i^{(2)'}(\omega b)\, c_i} \varepsilon_i \cos i\phi\right|^2 \tag{5.61}$$

where

$$c_i = \frac{Y_i(k_d b)}{Y_i(k_d a)} - \frac{J_i(k_d b)}{J_i(k_d a)} \tag{5.62}$$

$$d_i = \frac{Y_i^{'}(k_d b)}{Y_i(k_d a)} - \frac{J_i^{'}(k_d b)}{J_i(k_d a)} \tag{5.63}$$

are functions which complete the expansion.

Chapter 6

Results of the Edge Element Approach for Scattering Problems

6.1 Introduction

This chapter presents and discusses the results of using the edge element approach advocated in Chapter 5 for scattering problems. Initially, problems with no dielectric coating are considered and, for these problems, the numerical convergence of the approach is investigated. To show convergence, the scattering width output of electromagnetic scattering problems is monitored. Verification of the numerical solution procedure then follows from a series of comparisons of the computed scattering width output with exact analytical solutions. In addition, contours of the scattered field are also presented for converged solutions.

Mesh independent solutions are investigated when the linear blending function method is employed for geometry representation. Refinement strategies are discussed, in relation to the number of unknowns and the computational accuracy. Subsequent numerical computations employ these refinement strategies to obtain the desired solutions.

Following validation of the numerical solution, a series of numerical examples for which no analytical solution is available is considered. Where applicable, the results of these computations are compared to those produced by a time domain

finite element procedure.

Investigations are extended to consider scatterers with dielectric coatings. To verify the accuracy of these simulations, a comparison with exact analytical solutions is made. In addition, the benefits of using a coupled PML/ABC technique over the basic PML approach are considered for both coated scatterers and scatterers without a coating.

6.2 Definition of Electrical Length

In this chapter, the size of the computational problems is expressed in terms of electrical length. This is a measure of the number of wavelengths which occupy a specified length scale of the scatterer (for circular scatterers, this is the diameter). Therefore, the larger the electrical length the greater the computational challenge the problem represents.

6.3 Numerical Convergence of the Solution

The numerical convergence of the scattering width is monitored by first considering the scattering by 2λ TE and TM circular cylinders. Here, p–refinement on structured meshes of elements is undertaken. In these examples, linear geometry representation is employed and it is therefore necessary to generate meshes which accurately represent the boundaries, otherwise the converged numerical solution will differ from the true solution to the problem. A structured mesh of quadrilaterals, a structured mesh of triangles and hybrid meshes of structured quadrilaterals and triangles with different interface positions are considered.

6.3.1 Structured Mesh of Quadrilaterals

Convergence of the scattering width output is considered on a structured mesh of quadrilaterals. A mesh consisting of 320 quadrilaterals in the form of circular annulus was found to be adequate for describing the geometry of the boundaries. The

circular annulus mesh is of inner radius 1λ and outer radius 2λ, an illustration of the distribution of the elements in the mesh is shown in Figure 6.1. The PML layer for this mesh occupies the region $1.25\lambda \leq r \leq 2\lambda$ of quadrilateral elements. Figure 6.2 shows the convergence in the TE scattering width, when solutions are computed using uniform polynomial orders of $p = 0, 1, 2, 3, 4, 5$ in turn. It can be observed that, with increasing polynomial order, the initial asymmetric distribution converges to a symmetric distribution. In addition, once a converged solution is reached, further increases in polynomial order do not change the scattering width distribution. Figure 6.3 shows the convergence of the corresponding TM scattering width for uniform polynomial orders of $p = 0, 1, 2, 3, 4, 5$ in turn. As in the TE case, the solution converges with increasing polynomial order.

6.3.2 Structured Mesh of Triangles

Convergence of the solution for the scattering width is now considered when a structured mesh of triangles is used. The structured mesh employed results from splitting each quadrilateral in the mesh shown previously into two triangular elements. An illustration of the mesh produced is shown in Figure 6.4. The PML layer for this mesh occupies the region $1.25\lambda \leq r \leq 2\lambda$ of triangular elements.

The convergence of the scattering width for the TE problem is illustrated in Figure 6.5. In this figure, it is observed that, with increasing polynomial order, an initial asymmetric scattering width distribution converges to a symmetric distribution. Convergence of the scattering width for the corresponding TM problem is shown in Figure 6.6. As in previous cases, increase in polynomial order produces a symmetric distribution.

6.3.3 Hybrid Structured Meshes

We construct a series of hybrid meshes by splitting different proportions of the quadrilaterals in the mesh shown in Figure 6.1 into triangles. Elements adjacent to the scatterer are chosen to be triangular, and elements towards the far field are

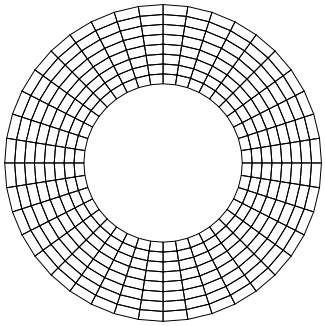

Figure 6.1: Scattering by a circular cylinder of electrical length 2λ: a structured mesh consisting of 320 quadrilaterals

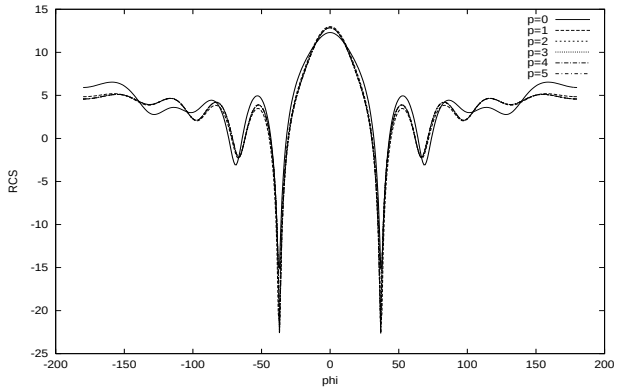

Figure 6.2: Scattering of a TE wave by a circular cylinder of electrical length 2λ: convergence of the RCS distribution on a structured mesh of quadrilaterals with increase in p

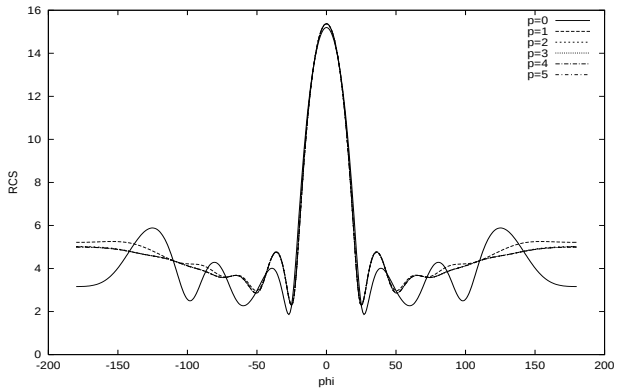

Figure 6.3: Scattering of a TM wave by a circular cylinder of electrical length 2λ: convergence of the RCS distribution on a structured mesh of quadrilaterals with increase in p

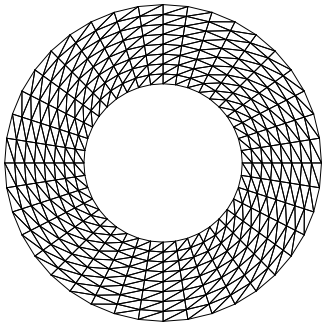

Figure 6.4: Scattering by a circular cylinder of electrical length 2λ: a structured mesh consisting of 640 triangles

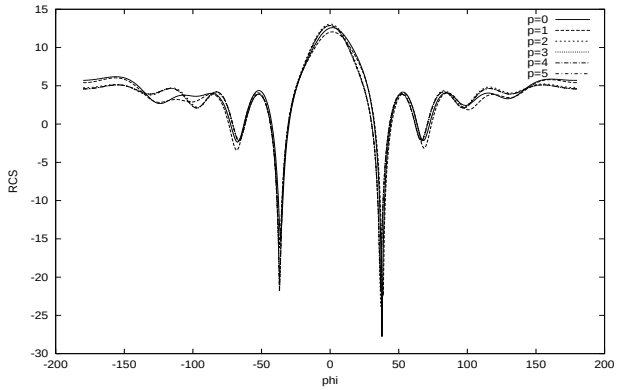

Figure 6.5: Scattering of a TE wave by a circular cylinder of electrical length 2λ: convergence of the RCS distribution on a structured mesh of triangles with increase in p

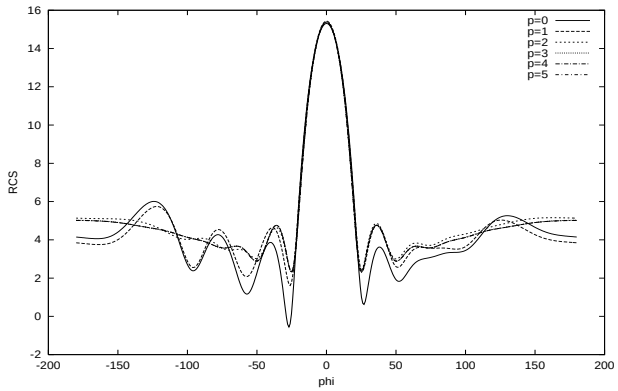

Figure 6.6: Scattering of a TM wave by a circular cylinder of electrical length 2λ: convergence of the RCS distribution on a structured mesh of triangles with increase in p

chosen to be quadrilateral. This combination is investigated because for complex geometries it is easier to generate an unstructured mesh of triangles around the object and then attach a structured layer of quadrilateral elements to apply the PML condition. Initially, triangles are chosen to occupy the region $1\lambda \leq r \leq 1.25\lambda$ of free space and quadrilaterals to occupy the region $1.25\lambda \leq r \leq 2\lambda$ of the PML layer. An illustration of the resulting hybrid mesh is shown in Figure 6.7. The computed scattering width distributions for a TE problem when uniform polynomial orders of $p = 0, 1, 2, 3, 4, 5$ are employed across the mesh are shown in Figure 6.8. The computed scattering width distributions for a TM problem when uniform polynomial orders of $p = 0, 1, 2, 3, 4, 5$ are employed across the mesh are shown in Figure 6.9.

A second hybrid mesh, in which the inner region $1\lambda \leq r \leq 1.5\lambda$ is occupied by triangles and the outer region $1.5\lambda \leq r \leq 2\lambda$ of the circular annulus is occupied by quadrilaterals is now considered. An illustration of the mesh can be found in Figure 6.10. For this example the PML layer, of thickness 0.75λ, extends in to the region of triangular elements. The resulting scattering width distributions for the case of scattering of a TE wave when uniform polynomial orders of $p = 0, 1, 2, 3, 4, 5$ are employed are shown in Figure 6.11. In this figure, it can be observed that the solution converges to a symmetric distribution in the same manner as the previous examples. The corresponding TM scattering width distributions in Figure 6.12 also display the same behaviour.

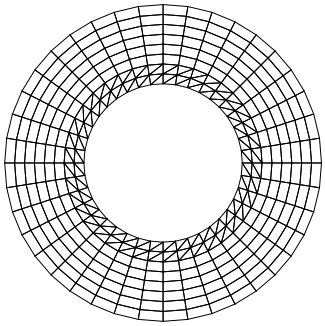

Figure 6.7: Scattering by a circular cylinder of electrical length 2λ: a structured hybrid mesh consisting of 160 triangles and 240 quadrilaterals

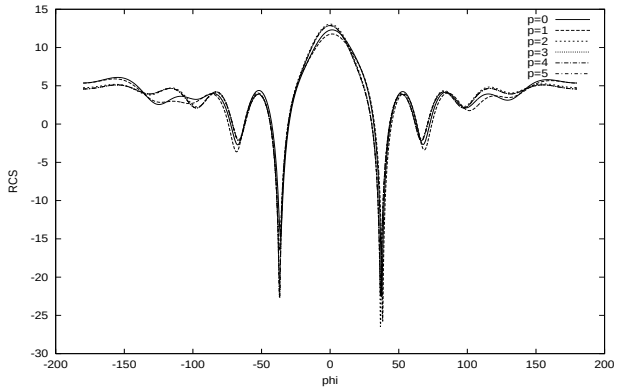

Figure 6.8: Scattering of a TE wave by a circular cylinder of electrical length 2λ: convergence of the RCS distribution on a hybrid structured mesh with increase in p

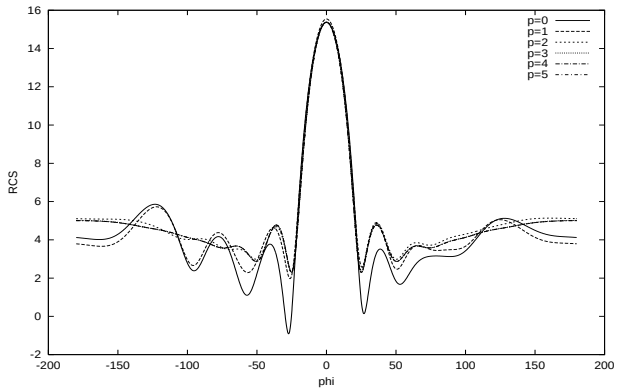

Figure 6.9: Scattering of a TM wave by a circular cylinder of electrical length 2λ: convergence of the RCS distribution on a hybrid structured mesh with increase in p

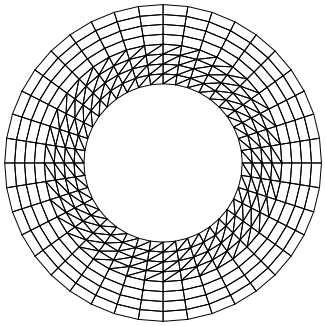

Figure 6.10: Scattering by a circular cylinder of electrical length 2λ: a structured hybrid mesh consisting of 320 triangles and 160 quadrilaterals

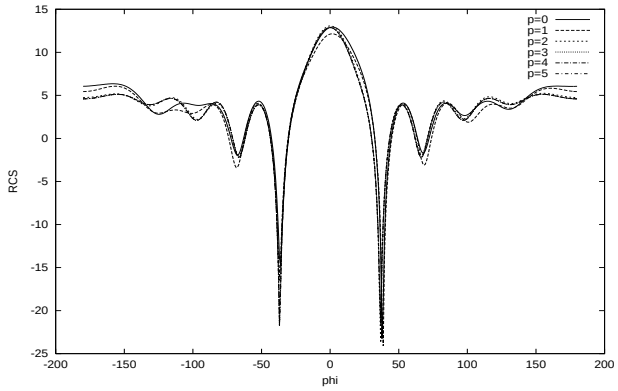

Figure 6.11: Scattering of a TE wave by a circular cylinder of electrical length 2λ: convergence of the RCS distribution on a hybrid structured mesh with increase in p

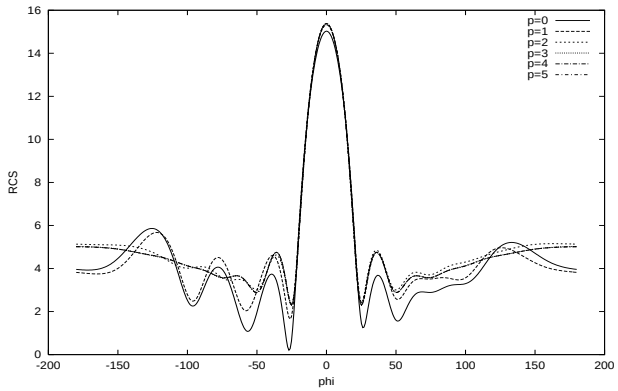

Figure 6.12: Scattering of a TM wave by a circular cylinder of electrical length 2λ: convergence of the RCS distribution on a hybrid structured mesh with increase in p

6.4 Verification of the Numerical Procedure

Verification of the numerical procedure is achieved by comparing scattering width distributions obtained for the converged solutions for the 2λ scattering problem in the previous section with the exact analytical solution. This comparison, for the TE problem is shown in Figure 6.13. It can be observed that, on this scale, the scattering width distributions produced with a structured mesh of quadrilaterals, a structured mesh of triangles and hybrid meshes are all indistinguishable from the exact. Therefore, meshes comprising of quadrilateral or triangles and hybrid combinations are equally successful at predicting the correct scattering width distribution for this TE problem. In addition, we note that the location of the interface between triangular and quadrilateral elements for hybrid meshes does not effect the solution. The corresponding comparison for the TM problem is shown in Figure 6.14. Once again the agreement obtained on this scale between the converged numerical solution on each of the structured meshes and the exact distribution is excellent. At this stage, the numerical performance of the 2λ scattering problems have been verified. To provide an insight in to the form of the solution across the computational domain, contours of the scattered magnetic field (for the TE problem) and the electric field (for the TM problem) are plotted. Figures 6.15 and 6.16 show contours of $Re(H_z^s)$ and $Im(H_z^s)$ for the converged TE solution. Figures 6.17 and 6.18 show contours of $Re(E_z^s)$ and $Im(E_z^s)$ for the converged TM solution.

Numerical solutions are undertaken for a circular cylinder of larger electrical length of 15λ. For this problem, a single hybrid mesh of 400 triangles and 600 quadrilaterals is considered as illustrated in Figure 6.19. A denser mesh is considered, since as λ decreases the resolution of the geometry of the scatterer becomes more important. For this reason, the number of elements in the radial direction of the mesh is increased. The outer circle of the mesh given in Figure 6.19 is a circle of radius $15\lambda = 2$ and the PML layer for this problem occupies the region $14.25\lambda \leq r \leq 15\lambda$ of quadrilaterals in the mesh. The computed scattering width distributions for the scattering by TE and TM waves when $p = 6$ elements are em-

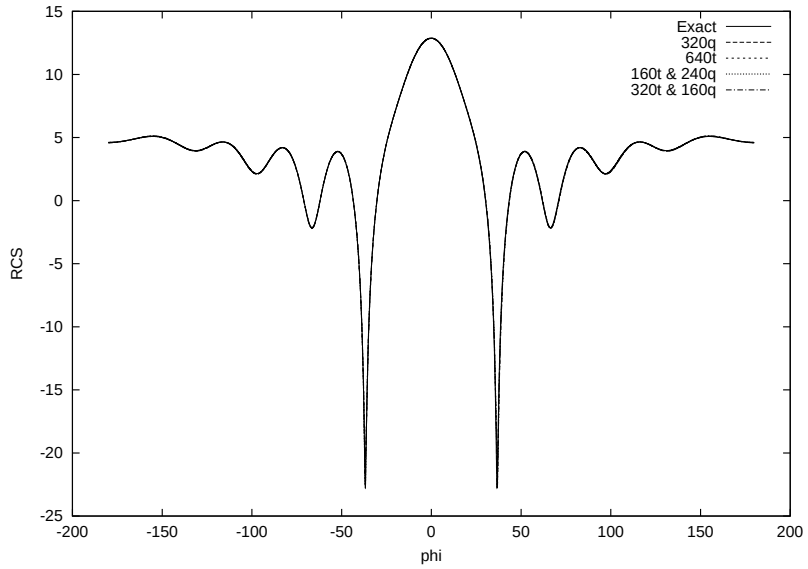

Figure 6.13: Scattering of a TE wave by a circular cylinder of electrical length 2λ: comparison between the exact distribution and the results obtained from a PML boundary condition

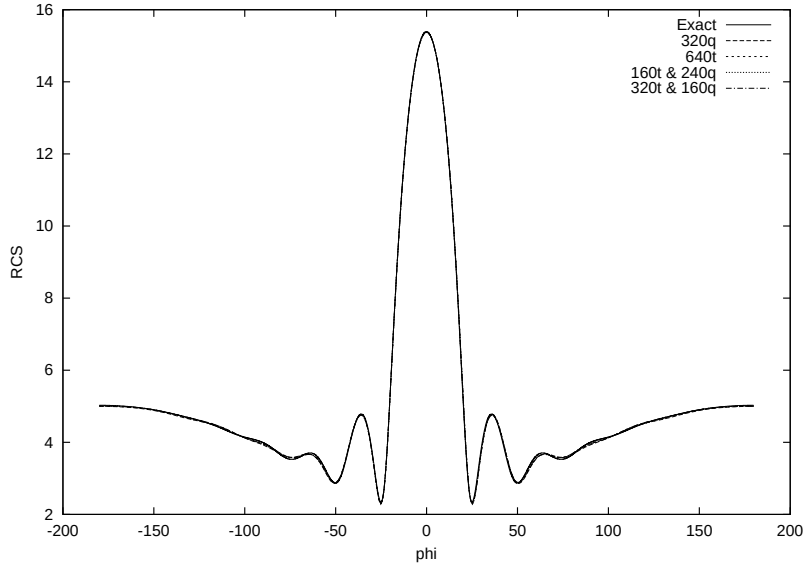

Figure 6.14: Scattering of a TM wave by a circular cylinder of electrical length 2λ: comparison between the exact distribution and the results obtained from a PML boundary condition

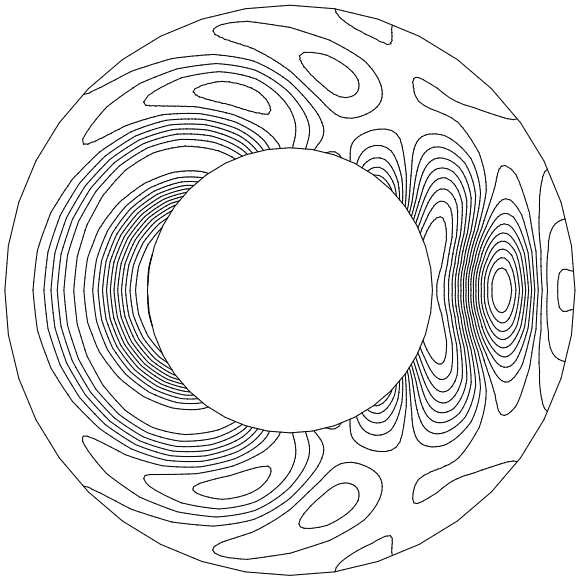

Figure 6.15: Scattering of a TE wave by a circular cylinder of electrical length 2λ: contours of $Re(H_z^s)$ using the converged solution

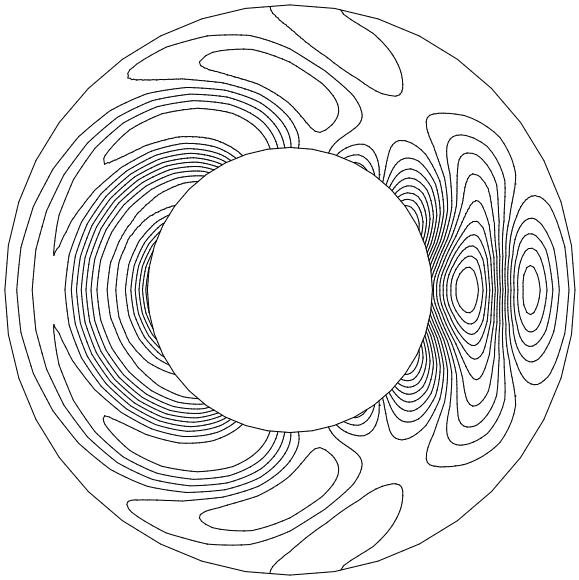

Figure 6.16: Scattering of a TE wave by a circular cylinder of electrical length 2λ: contours of $Im(H_z^s)$ using the converged solution

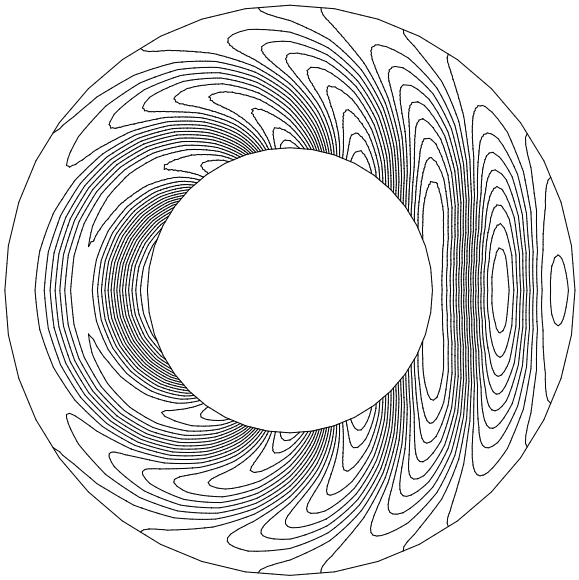

Figure 6.17: Scattering of a TM wave by a circular cylinder of electrical length 2λ: contours of $Re(E_z^s)$ using the converged solution

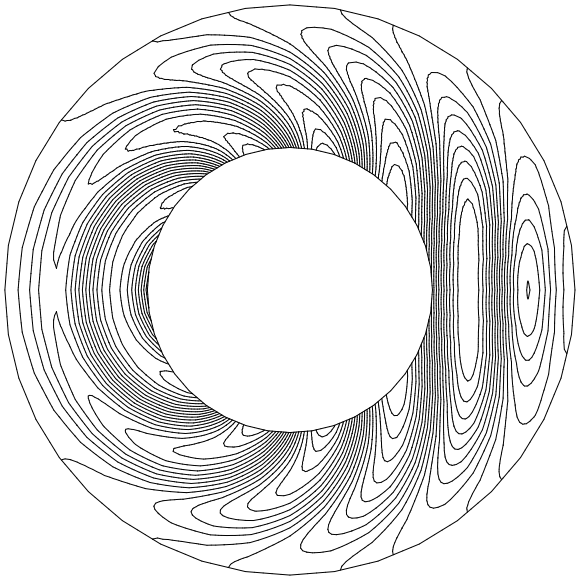

Figure 6.18: Scattering of a TM wave by a circular cylinder of electrical length 2λ: contours of $Im(E_z^s)$ using the converged solution

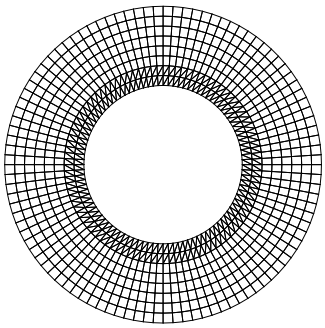

Figure 6.19: Scattering by a circular cylinder of electrical length 15λ: a structured hybrid mesh consisting of 400 triangles and 600 quadrilaterals

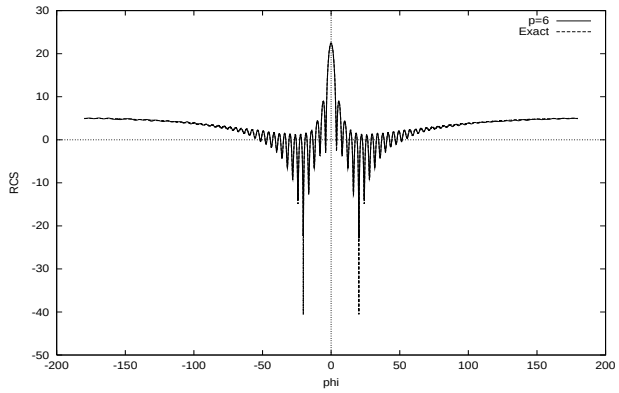

Figure 6.20: Scattering of a TE wave by a circular cylinder of electrical length 15λ: comparison between the exact distribution and the results obtained from a PML boundary condition

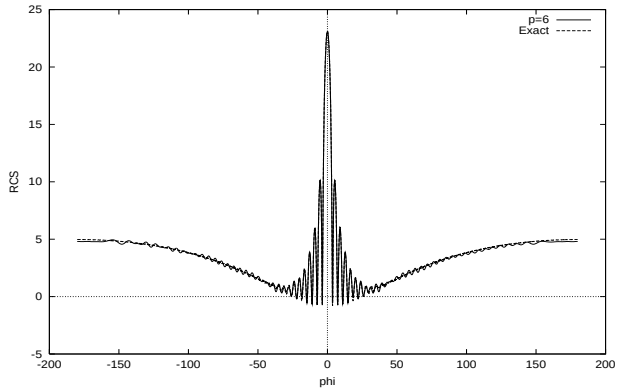

Figure 6.21: Scattering of a TM wave by a circular cylinder of electrical length 15λ: comparison between the exact distribution and the results obtained from a PML boundary condition

ployed uniformly across the mesh are shown in Figures 6.20 and 6.21 respectively. Both computations produce results that, on this scale, are in excellent agreement with the exact solution. Contours of $Re(H_z^s)$ and $Im(H_z^s)$ for the TE problem are shown in Figures 6.22 and 6.23 respectively.

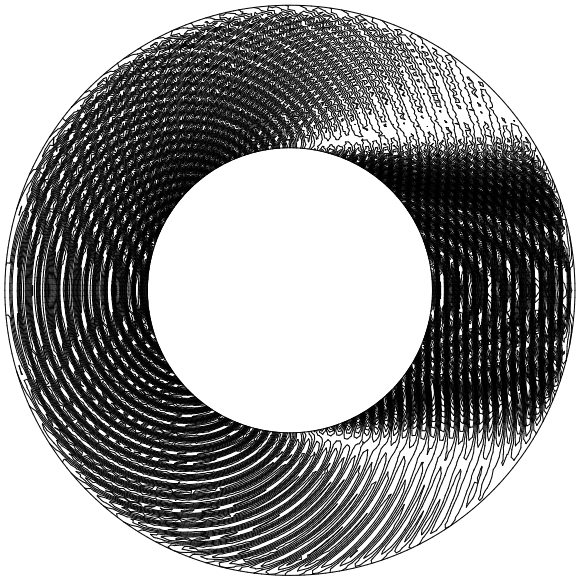

Figure 6.22: Scattering of a TE wave by a circular cylinder of electrical length 15λ: contours of $Re(H_z^s)$ using the converged solution

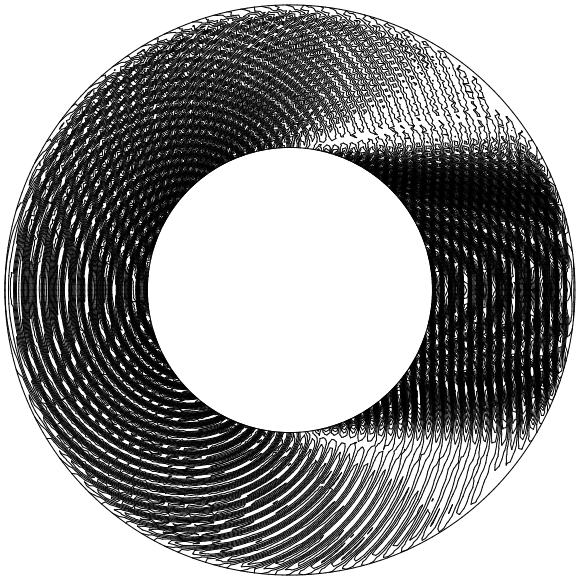

Figure 6.23: Scattering of a TE wave by a circular cylinder of electrical length 15λ: contours of $Im(H_z^s)$ using the converged solution

6.5 Mesh Independent Solutions

Using a linear representation for the geometry can produce accurate results, as demonstrated in the previous examples. But the converged solutions that are obtained in this way are only as good as the description of the geometry that results. In other words, if the mesh does not adequately describe the geometry of the scatterer, the converged solution will not be the true solution to the problem. However, by adopting the linear blending function method for geometry resolution, as described in Chapter 3, then accurate mesh independent solutions can be achieved. To show that this is the case, the solutions given by the linear geometry approximation and the representation given by the linear blending function method are compared on a sequence of meshes. The initial generated mesh contains 96 quadrilaterals. Subsequent meshes in the sequence are obtained by first splitting each element in the original mesh into 4 and then into 16. Comparisons are made by considering the converged solution on each mesh for the 15λ TE circular cylinder example.

The initial mesh is shown in Figure 6.24 (a) and the corresponding solutions are shown in Figure 6.24 (b). It is observed that the converged solution given by the linear geometry approximation is incorrect. However, the converged solution given by the linear blending function method is indistinguishable from the exact. Splitting each element in to 4, as illustrated in Figure 6.25 (a) leads to an improvement in the converged solution given by linear geometry approximation, as shown in Figure 6.25 (b). The converged solution given by the linear blending function remains indistinguishable from the exact. However, it is not until the elements in the original mesh are split 16 times, as shown in Figure 6.26 (a), that the converged solution given by the linear geometry approximation, shown in Figure 6.26 (b), is indistinguishable from the exact distribution. Therefore, it is apparent that the linear blending function method should be adopted, if mesh independent solutions are to be obtained economically.

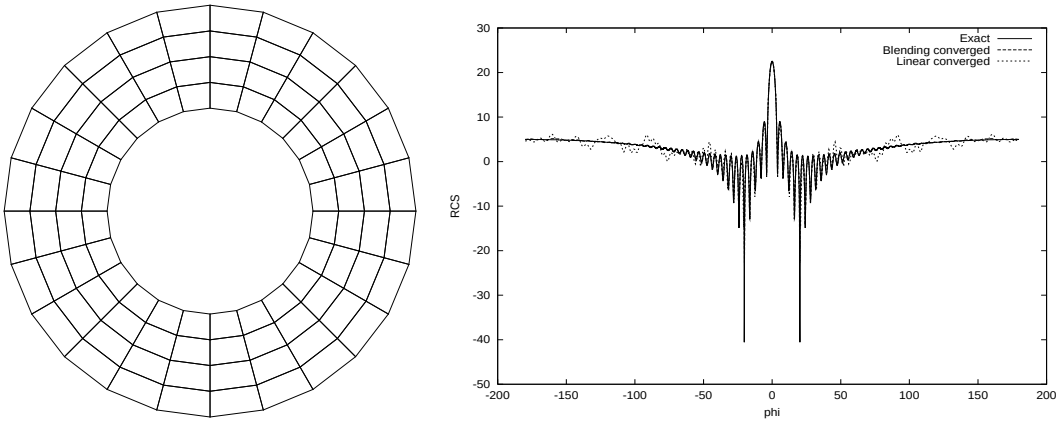

(a) (b)

Figure 6.24: Scattering of a TE wave by a circular cylinder of electrical length 15λ: (a) a structured mesh of 96 quadrilaterals and (b) comparison between the distribution given by using linear geometry and blending function representation

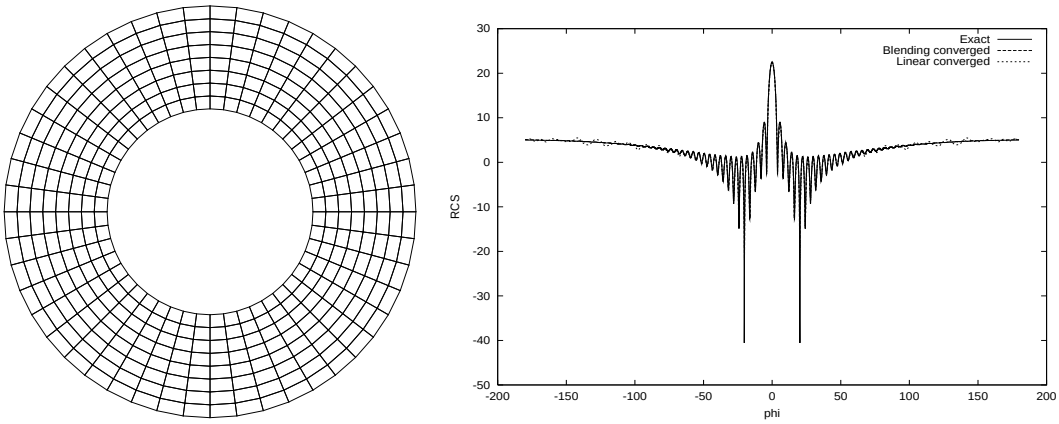

(a) (b)

Figure 6.25: Scattering of a TE wave by a circular cylinder of electrical length 15λ: (a) a structured mesh of 384 quadrilaterals and (b) comparison between the distribution given by using linear geometry and blending function representation

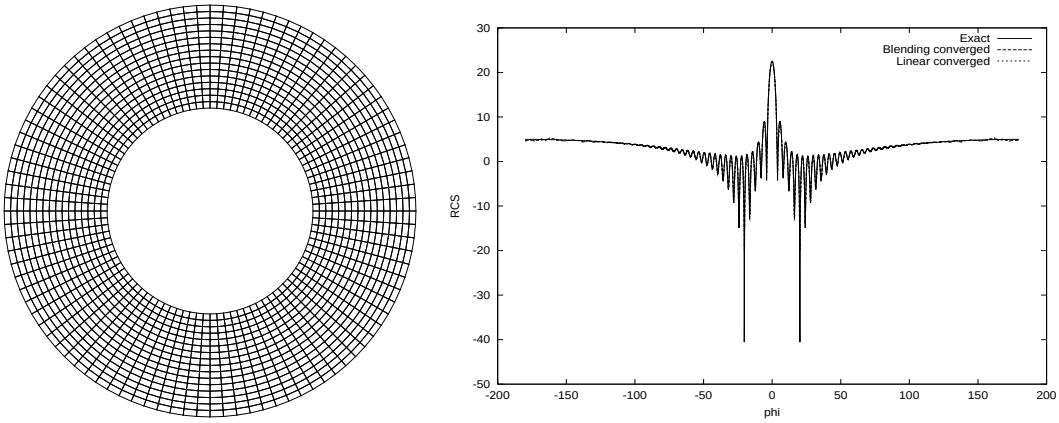

(a) (b)

Figure 6.26: Scattering of a TE wave by a circular cylinder of electrical length 15λ: (a) a structured mesh of 1536 quadrilaterals and (b) comparison between the distribution given by using linear geometry and blending function representation

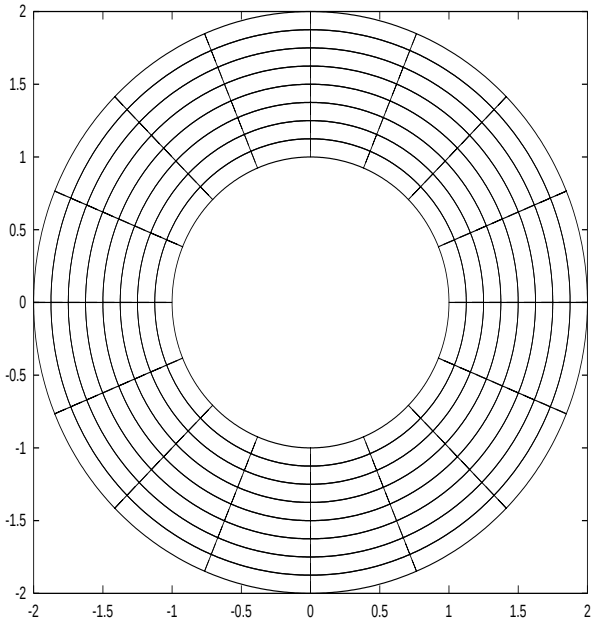

(a)

Figure 6.27: Scattering of a TE wave by a circular cylinder of electrical length 2λ: the initial mesh of 128 quadrilateral elements

6.6 Refinement Strategies

The question of whether it is better to refine the mesh or to increase the polynomial order is now examined. To investigate these different strategies fully, the linear blending function method of geometry representation is adopted. To determine a suitable refinement strategy, we examine the computational accuracy of a series of solutions to a model problem and compare this to the number of unknowns required to obtain the numerical solution. The model problem considered here involves the scattering of a TE wave by a cylinder of electrical length 2λ.

A comparison of the accuracy given by the computed solutions which employ a strategy of h–refinement is compared with that produced by employing a strategy of p–refinement. The initial mesh, before refinement is undertaken, consists of 128 quadrilateral elements and is shown in Figure 6.27. For the h–refinement strategy, the second and third meshes in the sequence are constructed by splitting the initial mesh into 4 and then 16. Here, $p = 0$ quadrilaterals are used uniformly across all the meshes. For the p–refinement strategy, the spacing in the initial mesh is retained and solutions are computed using uniform polynomial orders of $p = 0, 1, 2, 3$.

The computed distributions, when p–refinement is undertaken on the initial mesh is shown in Figure 6.28. It can be observed that increasing the order from $p = 0$ to $p = 3$ leads to convergence of the distribution to the exact solution. In comparison, the effect of refining the mesh is shown in Figure 6.29. The effect of splitting the mesh into 4 and then 16 has yet to converge the solution. A much finer spacing is required to reach a converged solution using h–refinement [58].

A total number of 4160 unknowns are required to compute the $p = 3$ solution on the initial mesh. This is exactly the same number as results from computing the $p = 0$ solution for the second h–refinement. It is, therefore, more beneficial to increase the polynomial order as opposed to refining the mesh.

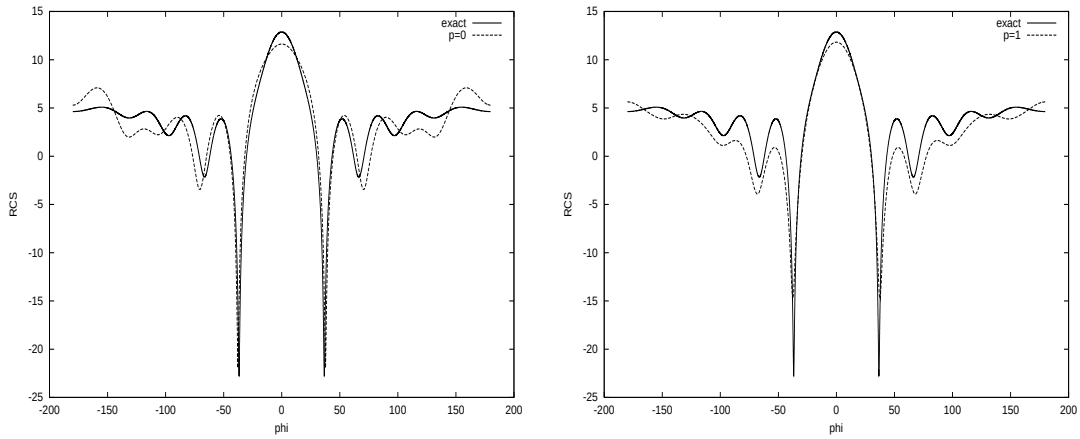

(a)

(b)

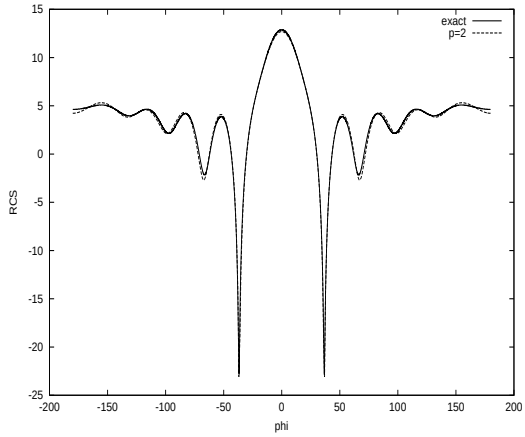

(c)

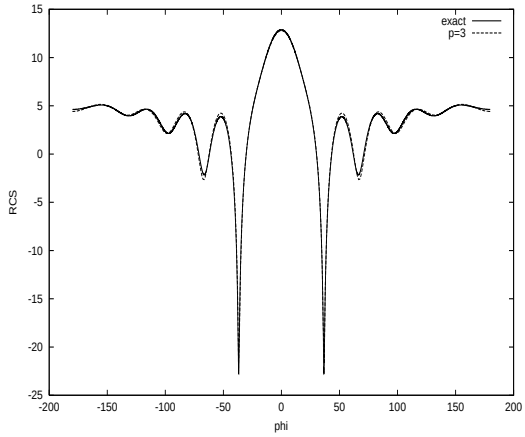

(d)

Figure 6.28: Scattering of a TE wave by a circular cylinder of electrical length 2λ showing the computed scattering width distributions for: (a) $p = 0$, (b) $p = 1$, (c) $p = 2$ and (d) $p = 3$ on the the initial mesh.

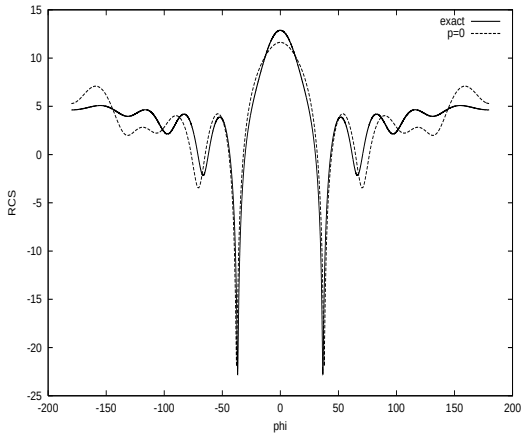

(a)

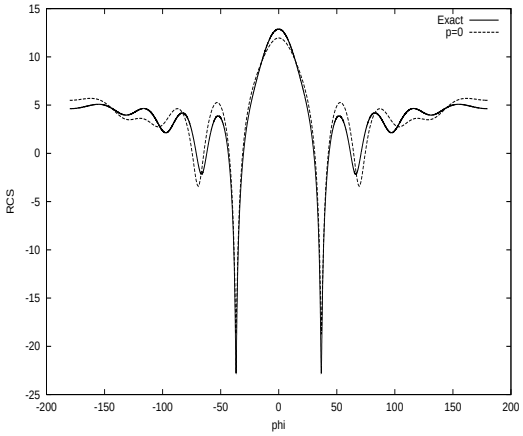

(b)

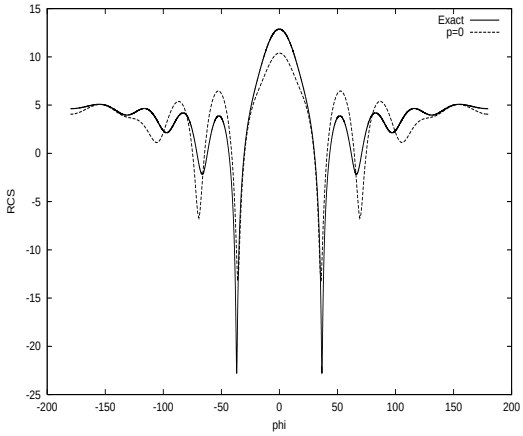

(c)

Figure 6.29: Scattering of a TE wave by a circular cylinder of electrical length 2λ showing the computed scattering width distributions for: (a) $p = 0$ on the initial mesh, (b) $p = 0$ on the first h–refinement and (c) $p = 0$ on the second h–refinement

6.7 Scattering By Obstacles of More General Shape

To illustrate the predictive capability of the procedure, we now consider the simulation of problems involving scatterers of more complex shape, for which no analytical solution is available. The simulations included involve scattering by a semi–open cavity and by a NACA0012 aerofoil. For these non–cylindrical scatterers, an advancing front procedure [43] is employed to initially generate a truly unstructured mesh of triangles. A structured mesh of quadrilaterals is then attached to the outer surface of the triangulated region and is terminated at the desired distance from the scatterer. The PML lies within this structured mesh region. The location of the interface between the quadrilateral and triangular elements can be arbitrarily located and the number of layers of elements in the structured mesh may be arbitrarily defined. However, in practice, we attempt to ensure that the hybrid meshes which result are of approximately uniform spacing.

6.7.1 Semi–Open Cavity

Geometrically, the perfectly conducting semi–open cavity consists of two parallel walls which are connected at their right–hand end. This produces a cavity in the shape of a letter U rotated through 90 degrees. The thickness of the walls is denoted by d and the outer dimensions are given by $b + d$ in the x direction and $c + 2d$ in the y direction. The implication here is that the inner cavity has dimensions b and c. We consider the particular cavity which is defined by the specific values $d = 0.4\lambda = 0.2$, $b = 8\lambda = 4$ and $c = 2\lambda = 1$. A TE simulation is performed in which the incident wave propagates in a direction which lies at an angle of $\theta = 30$ degrees to the x axis. An unstructured mesh of triangles is generated within the region bounded by a circle of radius $6\lambda = 3$ and a structured mesh, consisting of 1 layer of quadrilaterals of thickness $1.5\lambda = 0.75$ in this case, is then attached. A view of this mesh is given in Figure 6.30. The PML layer for this example occupies the region $6.75\lambda \leq r \leq 7.5\lambda$ inside the structured layer of quadrilaterals.

The order of the edge elements is increased uniformly across the mesh until

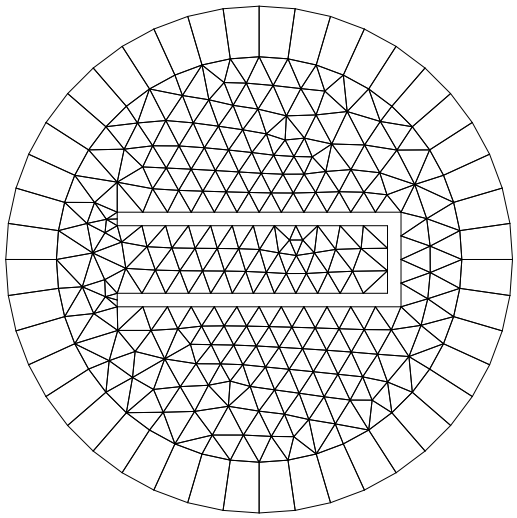

Figure 6.30: Scattering by semi–open cavity: a hybrid mesh consisting of 407 triangles and 44 quadrilaterals

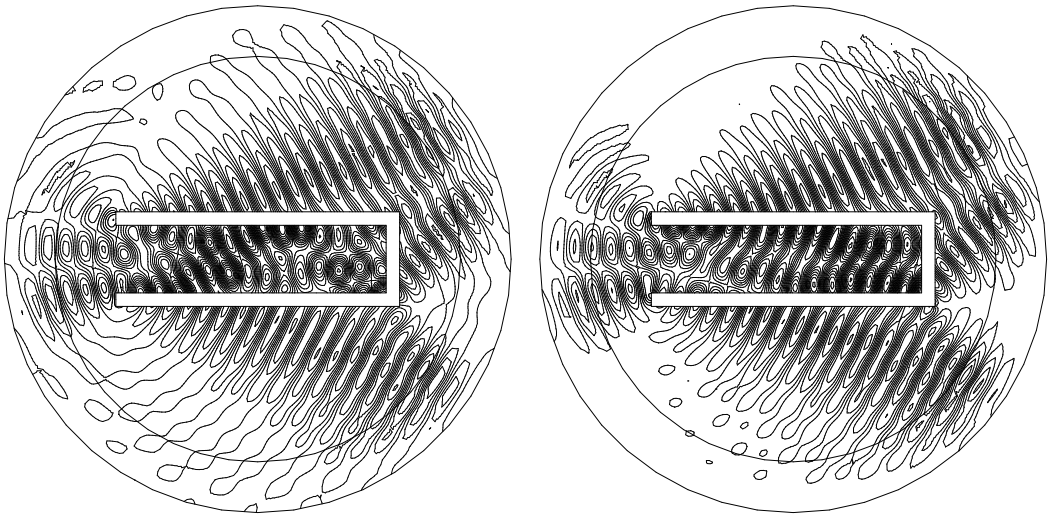

(a) (b)

Figure 6.31: Scattering of a TE wave by a semi–open cavity: contours of (a) $Re(H_z^s)$ and (b) $Im(H_z^s)$

convergence of the RCS distribution is obtained. Following this approach, the RCS distributions obtained using $p = 7$ and $p = 8$ were found to be indistinguishable and convergence of the numerical solution was achieved. The corresponding contours of the real and imaginary components of the scattered magnetic field are shown in Figures 6.31 (a) and (b). The converged distribution of the RCS is compared in Figure 6.32 with the distribution produced by a finite element time domain solution approach [59]. The two RCS distributions are very similar, although at some locations the time domain solution does not reproduce the sharp troughs that are apparent in the frequency domain solution.

In addition, a computation is undertaken in which a TE incident wave is propagated along the x axis ($\theta = 0$). The order of approximation for this example is increased uniformly across the mesh until the converged RCS distribution is obtained. As in the previous example, the converged solution was obtained for $p = 8$. The corresponding contours of the real and imaginary components of the scattered magnetic field are shown in Figures 6.33 (a) and (b). The distribution of the RCS for $p = 7$ and $p = 8$ are shown in Figure 6.34, and the convergence of the solution can be observed.

6.7.2 NACA0012 Aerofoil

The final example involves the simulation of the scattering of a TE wave by a perfectly conducting NACA0012 aerofoil. The chord length, c, of the aerofoil is assumed to be given by $c = 2\lambda = 1$. An unstructured mesh consisting of 499 triangles is used to discretise the region bounded internally by the aerofoil and externally by the circle of radius $r = 1.25 = 2.5\lambda$. The remaining area is bounded externally by the circle of radius $r = 2 = 4\lambda$ and is discretised with a structured mesh of 52 quadrilaterals. This mesh is shown in Figure 6.35. It can be seen that the mesh is refined near the leading and trailing edges of the aerofoil in order to provide the required geometrical definition. The PML layer for this example occupies the region $3.25\lambda \leq r \leq 4\lambda$ inside the final layer of quadrilaterals in the structured mesh.

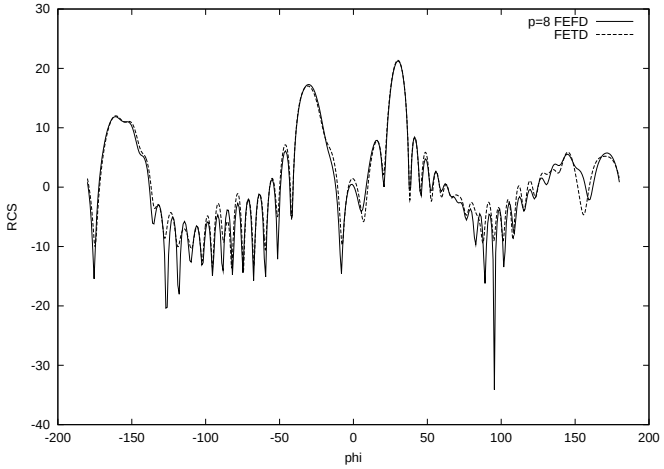

Figure 6.32: Scattering of a TE wave by a semi–open cavity: comparison of the computed RCS distribution with that produced by a time domain finite element method

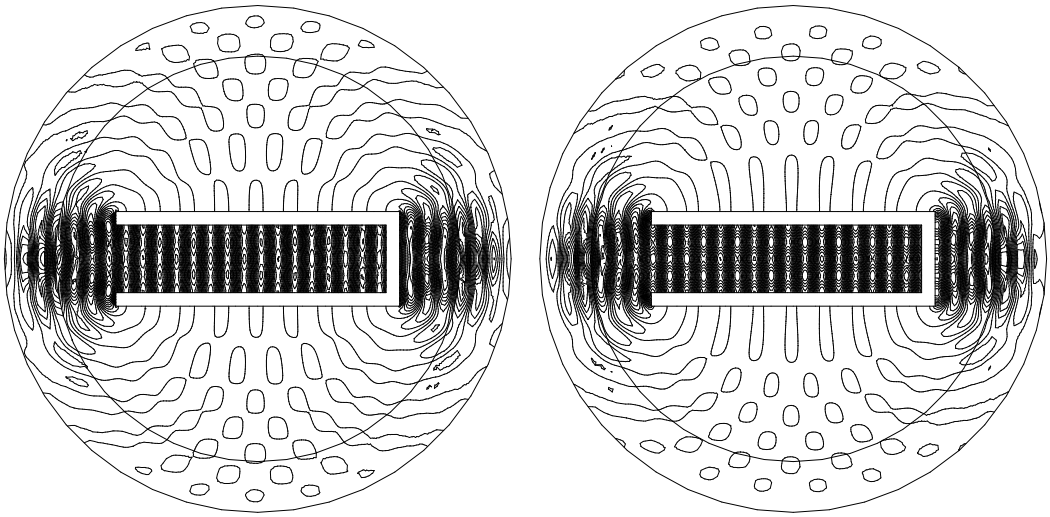

(a) (b)

Figure 6.33: Scattering of a TE wave by a semi–open cavity: contours of (a) $Re(H_z^s)$ and (b) $Im(H_z^s)$

Two separate simulations are performed. The first involves illumination from the front of the aerofoil, while the illumination in the second simulation is from the rear. In each case, as before, the order of approximation employed is increased uniformly across the mesh until convergence of the RCS distribution is obtained. The manner in which the mesh convergence is achieved is apparent from Figure 6.36 (a) and (b), which show the calculated RCS distributions. The initial solution, computed with order $p = 0$ on each element, is asymmetric, reflecting the asymmetric nature of the mesh. However, with increase in the order p of the approximation employed, it is clear that the effect of the mesh becomes less important and the solution rapidly converges to a symmetric distribution.

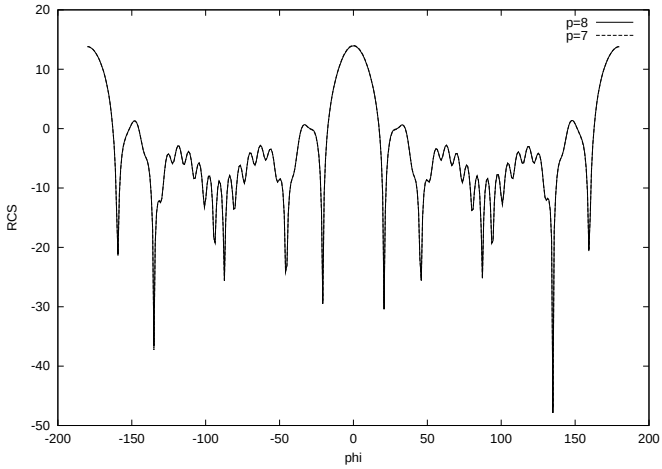

Figure 6.34: Scattering of a TE wave by a semi−open cavity: convergence of the numerical solution for an incident wave propagated along the x axis

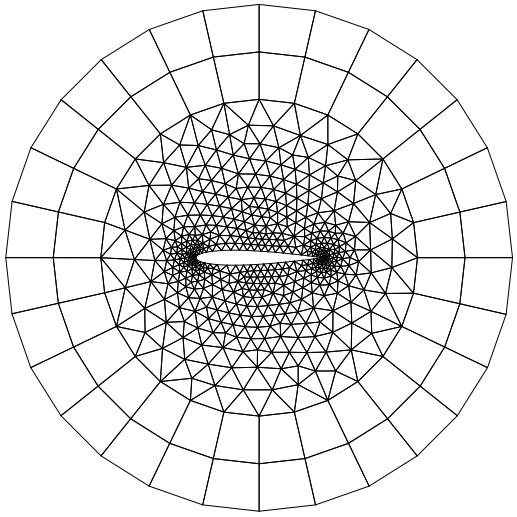

Figure 6.35: Scattering by a NACA0012 aerofoil of electrical length 2λ: a hybrid mesh consisting of 499 triangles and 52 quadrilaterals

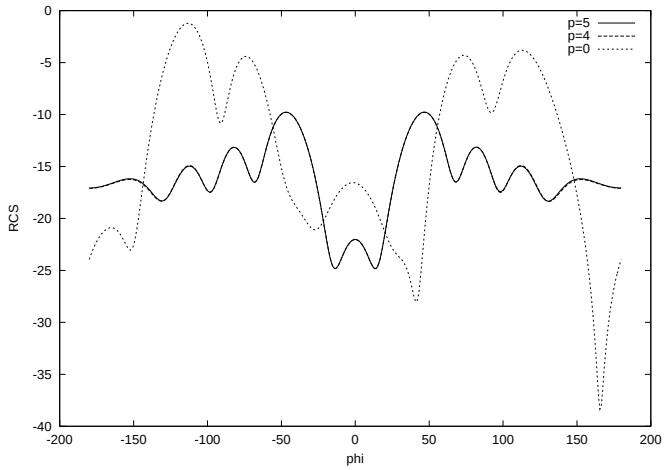

(a)

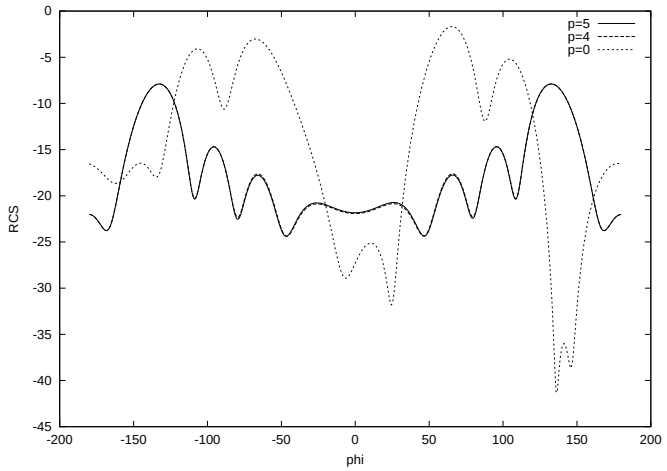

(b)

Figure 6.36: Scattering of a TE wave by a perfectly conducting NACA0012 aerofoil: computed RCS distributions when the aerofoil is illuminated (a) from the front and (b) from the rear

6.8 Coated Scatterers

Examples involving a PEC obstacle with a dielectric coating are now considered. To validate the approach advocated in Chapter 5, numerical computations are undertaken for coated circular cylinders. The approach is applicable to multi–layered structures, but for the purposes of validation we restrict ourselves to a single coating. Here, the PEC cylinder is chosen to be of electrical length 15λ and the thickness of the coating to be 1.875λ. The dielectric is defined in terms of the constants

$$\epsilon_d = 2.56 \qquad \mu_d = 1 \tag{6.1}$$

To describe the computational domain a structured hybrid mesh of 800 triangles and 600 quadrilaterals is generated, as shown in Figure 6.37. The mesh is the form of a circular annulus with inner radius 7.5λ and outer radius 16.875λ. Here, the triangles occupy the region $7.5\lambda \leq r \leq 11.25\lambda$ and the quadrilaterals occupy the region $11.25\lambda \leq r \leq 16.875\lambda$. The dielectric coating is discretised by triangular elements, the free space is discretised by combination of quadrilaterals and triangular elements. The PML layer occupies the region $16.125\lambda \leq r \leq 16.875\lambda$ of the quadrilateral elements. The scattering width distribution, for a TE problem when $p = 7$ elements are employed uniformly over the mesh, is presented in Figure 6.38. Here, it can be observed that, on this scale, the scattering width distribution produced by the finite element solution is indistinguishable from the exact. The corresponding scattering width distribution for the scattering of a TM wave is given in Figure 6.39. Once again the agreement observed between the finite element solution and the exact solution is excellent.

The approach described in Chapter 5 for the scattering which occurs from coated scatterers has therefore been successfully validated for problems involving coated circular cylinders.

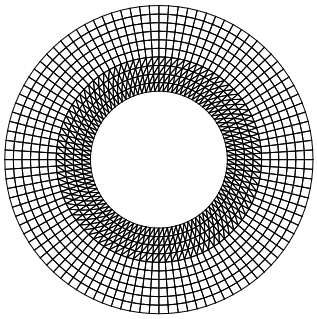

Figure 6.37: Scattering by a coated circular cylinder of electrical length 15λ: a structured hybrid mesh consisting of 800 triangles and 600 quadrilaterals

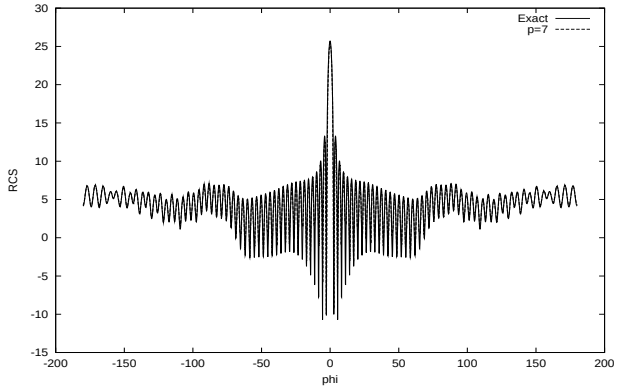

Figure 6.38: Scattering of a TE wave by a coated circular cylinder of electrical length 15λ: comparison between the exact distribution and the results obtained from a PML boundary condition

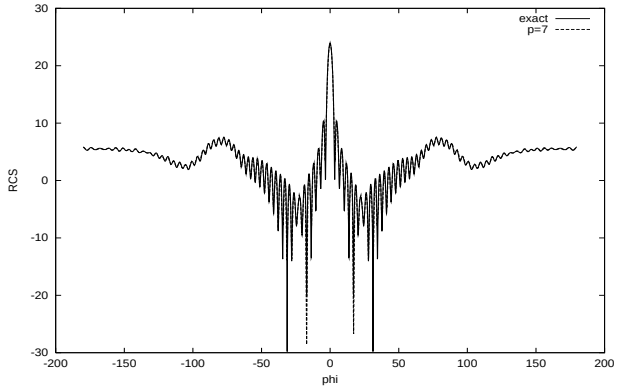

Figure 6.39: Scattering of a TM wave by a coated circular cylinder of electrical length 15λ: comparison between the exact distribution and the results obtained from a PML boundary condition

6.9 Coupled ABC/PML Approach

In this section, the coupled ABC/PML approach is explored for close placement of the far field boundary to the scatterer. This is especially important for problems of large electrical length, because the computational size grows rapidly with the amount of free space considered. Using the PML approach close to the scatterer for large electrical lengths can produce some small oscillations in the scattering width distribution which are not dampened out by increasing the polynomial order. This is illustrated by considering the scattering of a TM wave by a cylinder of electrical length 15λ. The mesh which is employed for this problem consists of 120 quadrilateral elements and describes a circular annulus of inner radius 7.5λ and outer radius 8.5λ. It consists of the region $7.5\lambda \leq r \leq 7.75\lambda$ of free space and the region $7.75\lambda \leq r \leq 8.5\lambda$ of PML, as shown in Figure 6.40. The computed scattering width distribution using a PML approach and $p = 7$ elements is shown in Figure 6.41. Here, it is observed that the computed scattering width distribution has additional small oscillations which do not appear in the exact distribution. Further increases in polynomial order do not diminish these oscillations. The scattering width resulting from a coupled PML/ABC approach is shown in Figure 6.42, and it is clear that no additional oscillations appear. Therefore, this suggests that the method which should be adopted for close placement of the far field boundary for large electrical lengths is a coupled PML/ABC approach.

The coupled PML/ABC approach is now employed for the scattering which occurs from a cylinder of electrical length 30λ. Figure 6.43 shows the mesh employed. This consists of 180 quadrilaterals and 120 triangles in the shape of a circular annulus with inner radius 15λ and outer radius 16λ. The mesh is composed of the free space region, $15\lambda \leq r \leq 15.25\lambda$, and the PML region, $15.25\lambda \leq r \leq 16\lambda$. The computed scattering width distribution for the scattering of a TE wave when $p = 8$ elements are used uniformly across the mesh is shown in Figure 6.44. It is observed that, on this scale, the agreement with the exact distribution is excellent. The agreement for the corresponding TM solution, shown in Figure 6.45, is also

excellent.

Finally, a coated cylinder of electrical length 30λ is considered. The coating for this problem is assumed to be of thickness 1λ and to have material properties $\epsilon_d = 1$ and $\mu_d = 2.56$. For this problem a structured hybrid mesh which describes a circular annulus of inner radius 15λ and outer radius 17λ is generated. It consists of the region $15\lambda \leq r \leq 16\lambda$ of dielectric, the region $16\lambda \leq r \leq 16.25\lambda$ of free space and the region $16.25\lambda \leq r \leq 17\lambda$ of PML, as illustrated in Figure 6.46. The computed scattering width distribution shown in Figure 6.47 for the scattering of a TE wave using $p = 9$ elements uniform across the mesh is in excellent agreement with the exact distribution on this scale. The corresponding TM solution shown in Figure 6.48 is also in excellent agreement with exact distribution.

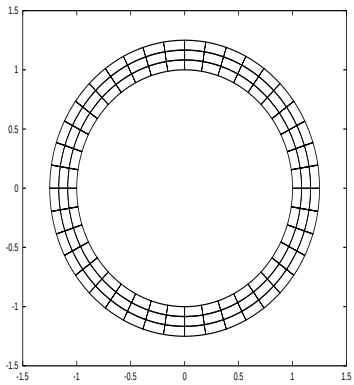

Figure 6.40: Scattering by a circular cylinder of electrical length 15λ: a structured mesh consisting of 120 quadrilaterals

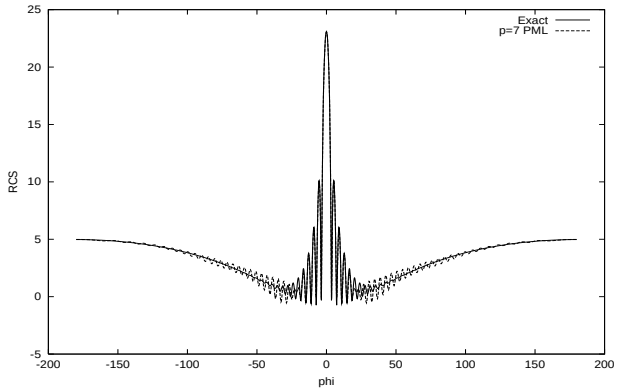

Figure 6.41: Scattering of a TM wave by a circular cylinder of electrical length 15λ: computed RCS distribution using a PML on a structured mesh of quadrilaterals

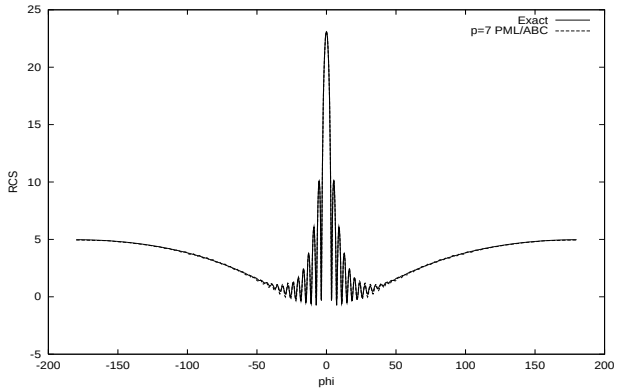

Figure 6.42: Scattering of a TM wave by a circular cylinder of electrical length 15λ: computed RCS distribution using a coupled PML/ABC on a structured mesh of quadrilaterals

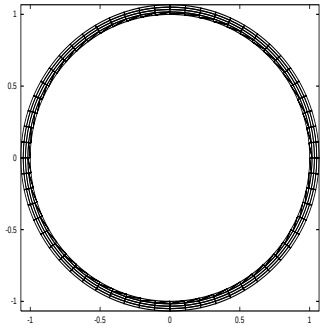

Figure 6.43: Scattering by a circular cylinder of electrical length 30λ: a structured hybrid mesh consisting of 120 triangles and 180 quadrilaterals

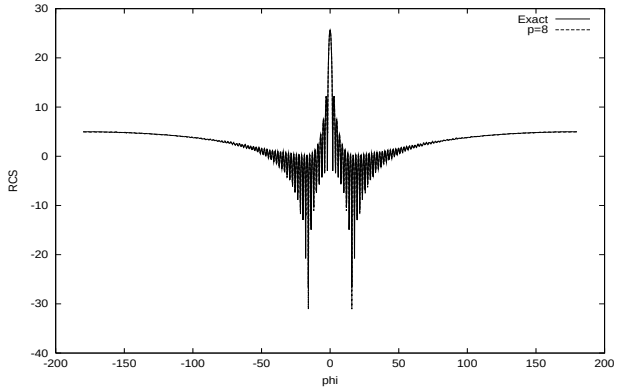

Figure 6.44: Scattering of a TE wave by a circular cylinder of electrical length 30λ: comparison between computed RCS distribution using a coupled PML/ABC and exact distribution

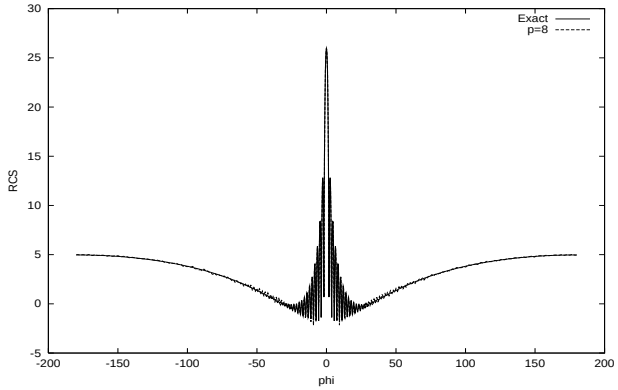

Figure 6.45: Scattering of a TM wave by a circular cylinder of electrical length 30λ: comparison between computed RCS distribution using a coupled PML/ABC and exact distribution

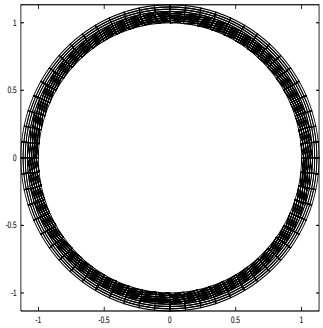

Figure 6.46: Scattering by a coated circular cylinder of electrical length 30λ: a structured hybrid mesh consisting of 600 triangles and 180 quadrilaterals

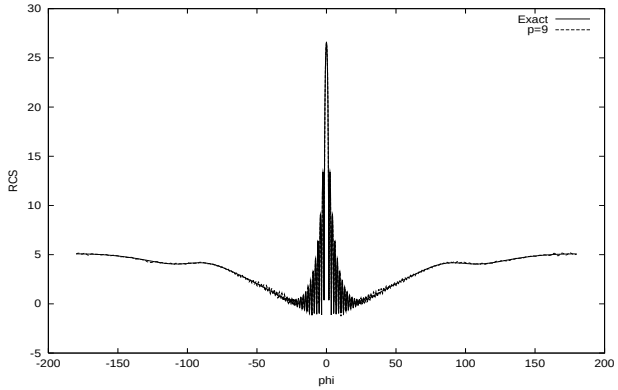

Figure 6.47: Scattering of a TE wave by a coated circular cylinder of electrical length 30λ: comparison between computed RCS distribution using a coupled PML/ABC and exact distribution

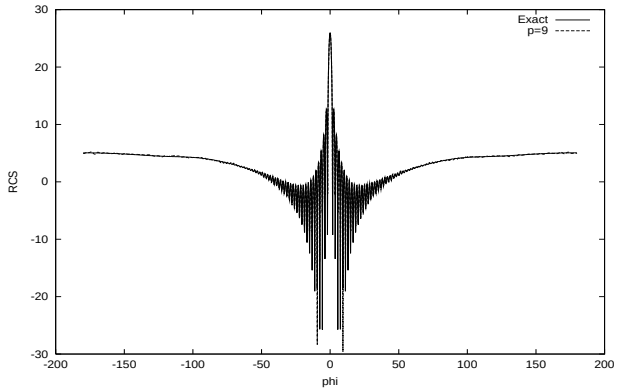

Figure 6.48: Scattering of a TM wave by a coated circular cylinder of electrical length 30λ: comparison between computed RCS distribution using a coupled PML/ABC and exact distribution

Chapter 7

A–posteriori Error Estimator for Scattering Problems

7.1 Introduction

This chapter presents the derivation of an a–posteriori error estimation procedure applied to the electromagnetic scattering problems. In common with all a–posteriori error estimators, the estimation of an error in the solution follows *after* the numerical solution to the problem. A–priori estimates discussed in Chapter 4 give an insight in to the rates of convergence of numerical solution but do not provide a quantitative estimate of the error in the numerical solution.

In addition to deriving an a–posteriori error estimation procedure, the aim is to provide a set of quantitative upper and lower bounds on a chosen output of interest. Bounds of this type have important implications for practical applications where, typically, engineers are interested in knowing a specified output value to a given tolerance.

A–posteriori error estimation has undergone extensive research over the last decade. A recent extensive review of the current approaches employed has been presented in the monograph by Ainsworth and Oden [22]. The use of output bounds in a–posteriori error estimation is also not new. In particular, this work draws on the work of Maday, Patera and Peraire [23] who provided a general framework for

the calculation of a–posteriori bounds for output quantities. Subsequently they have extended this approach to wide class of problems including: linear outputs of the Helmholtz and Burgers equation [24], non–linear outputs of the Helmholtz equation [25] and linear and non–linear outputs of convection dominated problems [60].

To develop an a–posteriori procedure, we revisit the electromagnetic scattering problem and rewrite it in more convenient notation. Then, for the purposes of the analysis we introduce a series of constructions which are to be used in the error estimator. The steps required to obtain the error estimate of upper and lower bounds on a general non–linear output are presented. A proof is then included to show that the bounds obtained are indeed upper and lower bounds on the output quantity.

As an application of the estimating process, the scattering width is selected as the output and the construction of error bounds is considered. Following the development of the required theory, a number of numerical examples are presented to show the effectiveness of the bounding procedure.

7.2 The Scattering Problem Re–visited

The weak variational framework for scattering problems which employs a PML far field condition, as derived in Chapter 5, is: find $\boldsymbol{U}^s \in Z^D$, such that

$$\begin{aligned}\int_{\Omega_f+\Omega_p+\Omega_d} \left(\boldsymbol{\Lambda}_1^{-1}\mathrm{curl}\,\boldsymbol{U}^s \cdot \mathrm{curl}\,\overline{\boldsymbol{W}} - \omega^2\boldsymbol{\Lambda}_2\boldsymbol{U}^s \cdot \overline{\boldsymbol{W}}\right)\mathrm{d}\Omega = \\ \int_{\Gamma_1}\left(\boldsymbol{n}\wedge\boldsymbol{\Lambda}_1^{-1}\mathrm{curl}\,\boldsymbol{U}^i\right)\cdot\overline{\boldsymbol{W}}\,\mathrm{d}\Gamma \\ -\left\{\int_{\Omega_d}\left(\boldsymbol{\Lambda}_1^{-1}-\boldsymbol{I}\right)\mathrm{curl}\,\boldsymbol{U}^i\cdot\mathrm{curl}\,\overline{\boldsymbol{W}} - \omega^2\left(\boldsymbol{\Lambda}_2-\boldsymbol{I}\right)\boldsymbol{U}^i\cdot\overline{\boldsymbol{W}}\,\mathrm{d}\Omega\right\} \quad (7.1)\end{aligned}$$

for all $\boldsymbol{W}$ in Z. Here, the spaces are defined as

$$Z^D = \{\boldsymbol{u}\,|\,\boldsymbol{u}\in\mathcal{H}(\mathrm{curl};\Omega);\ \boldsymbol{n}\wedge\boldsymbol{u} = -\boldsymbol{n}\wedge\boldsymbol{U}^i \text{ on } \Gamma_2;\ \boldsymbol{n}\wedge\boldsymbol{u} = \boldsymbol{0} \text{ on } \Gamma_3\} \quad (7.2)$$

$$Z = \{\boldsymbol{v}\,|\,\boldsymbol{u}\in\mathcal{H}(\mathrm{curl};\Omega);\ \boldsymbol{n}\wedge\boldsymbol{u} = \boldsymbol{0} \text{ on } \Gamma_2,\ \boldsymbol{n}\wedge\boldsymbol{u} = \boldsymbol{0} \text{ on } \Gamma_3\} \quad (7.3)$$

It has been observed, in the numerical results of Chapter 6, that the application of a coupled ABC/PML approach for large electrical lengths can achieve better

accuracy when the far field boundary is placed close to the scatterer. But for sake of simplicity, the error estimator is derived based on the original PML approach. The extension to the coupled ABC/PML requires certain additional modifications.

7.2.1 Compact Form

The weak variational statement given by equation (7.1) is rewritten in the more compact form: find $\boldsymbol{U}^s \in Z^D$, such that

$$\mathcal{A}(\boldsymbol{U}^s, \boldsymbol{W}) =< \boldsymbol{U}^i, \boldsymbol{W} > \qquad \forall \boldsymbol{W} \in Z \tag{7.4}$$

where

$$\mathcal{A}(\boldsymbol{U}^s, \boldsymbol{W}) = a(\boldsymbol{U}^s, \boldsymbol{W}) - \omega^2 m(\boldsymbol{U}^s, \boldsymbol{W}) \tag{7.5}$$

The bilinear forms employed in this expression are defined as

$$a(\boldsymbol{u}, \boldsymbol{v}) = \int_{\Omega_f+\Omega_p+\Omega_d} \text{curl}\, \overline{\boldsymbol{v}} \cdot \boldsymbol{\Lambda}_1^{-1} \text{curl}\, \boldsymbol{u}\, \mathrm{d}\Omega \tag{7.6}$$

$$m(\boldsymbol{u}, \boldsymbol{v}) = \int_{\Omega_f+\Omega_p+\Omega_d} \overline{\boldsymbol{v}} \cdot \boldsymbol{\Lambda}_2 \boldsymbol{u}\, \mathrm{d}\Omega \tag{7.7}$$

The duality pairing used in equation (7.4) is defined as

$$\begin{aligned} < \boldsymbol{u}, \boldsymbol{v} >= & \int_{\Gamma_1} \boldsymbol{n} \wedge {\boldsymbol{\Lambda}_1}^{-1} \text{curl}\, \boldsymbol{u} \cdot \overline{\boldsymbol{v}}\, \mathrm{d}\Gamma \\ & - \left\{ \int_{\Omega_d} \left(\boldsymbol{\Lambda}_1^{-1} - \boldsymbol{I} \right) \text{curl}\, \boldsymbol{u} \cdot \text{curl}\, \overline{\boldsymbol{v}} - \omega^2 \left(\boldsymbol{\Lambda}_2 - \boldsymbol{I} \right) \boldsymbol{u} \cdot \overline{\boldsymbol{v}}\, \mathrm{d}\Omega \right\} \end{aligned} \tag{7.8}$$

It has been noted in Chapter 5 that the discrete equations are produced by a Galerkin approximation to the weak variational statement of equation (7.4). Introducing the subspace Z_H of Z, to represent the computational trial solution domain, and the subspace Z_H^D of Z^D, to represent the computational test function domain, the discrete form is: find $\boldsymbol{U}_H^s \in Z_H^D$ such that

$$\mathcal{A}(\boldsymbol{U}_H^s, \boldsymbol{W}) =< \boldsymbol{U}^i, \boldsymbol{W} > \qquad \forall \boldsymbol{W} \in Z_H \tag{7.9}$$

Meshes of quadrilateral and triangular edge elements are employed to discretise the solution domain. In Chapter 6, the use of this approach has been seen to produce accurate results for a number of scattering problems.

7.2.2 Hermitian Bilinear forms

For future use, it is also convenient to introduce, at this stage, the hermitian bilinear forms

$$a^s(\boldsymbol{U}^s, \boldsymbol{W}) = \frac{1}{2}\left[a(\boldsymbol{U}^s, \boldsymbol{W}) + \overline{a(\boldsymbol{W}, \boldsymbol{U}^s)}\right] \tag{7.10}$$

$$m^s(\boldsymbol{U}^s, \boldsymbol{W}) = \frac{1}{2}\left[m(\boldsymbol{U}^s, \boldsymbol{W}) + \overline{m(\boldsymbol{W}, \boldsymbol{U}^s)}\right] \tag{7.11}$$

which satisfy $a^s(\boldsymbol{W}, \boldsymbol{W}) = \overline{a^s(\boldsymbol{W}, \boldsymbol{W})}$ and $m^s(\boldsymbol{W}, \boldsymbol{W}) = \overline{m^s(\boldsymbol{W}, \boldsymbol{W})}$ for every $\boldsymbol{W}$. From these definitions it is clear that

$$\mathcal{B}^s(\boldsymbol{U}^s, \boldsymbol{W}) = a^s(\boldsymbol{U}^s, \boldsymbol{W}) + \omega^2 m^s(\boldsymbol{U}^s, \boldsymbol{W}) \tag{7.12}$$

is such that $\mathcal{B}^s(\boldsymbol{W}, \boldsymbol{W})$ is real and non–negative for every $\boldsymbol{W}$.

7.2.3 Output Specification

Once the solution to the variational form has been established, our interest lies in the form of real outputs, $s = \text{Re}\{S(\boldsymbol{U}^s, \phi)\}$. These outputs may be non–linear or linear functionals of the solution $\boldsymbol{U}^s$ and in addition they may be functions of another variable ϕ. Ideally, we would like to compute this output on a very fine discretisation. However, for certain problems, this can be expensive. We therefore consider the possibilities offered by an a–posteriori error estimator.

The objective of the a–posteriori error estimator is to place upper and lower bounds on the discrete output $s_H = \text{Re}\{S(\boldsymbol{U}^s_H, \phi)\}$ which is computed on the working discretisation Z_H. It should be noted that any non–linear output functional may be linearised and expressed in the form

$$S(\boldsymbol{U}^s_H + \boldsymbol{v}; \phi) = S(\boldsymbol{U}_H; \phi) + \ell^{\mathcal{O}}(\boldsymbol{v}; \phi) + \mathcal{N}(\boldsymbol{v}, \boldsymbol{v}; \phi) \tag{7.13}$$

where $\ell^{\mathcal{O}}$ and $\mathcal{N}$ denote linear and non–linear contributions respectively. We require that $\mathcal{N}$ be L^2 continuous. In particular, $|\mathcal{N}(\boldsymbol{w}, \boldsymbol{w})| \leq C||\boldsymbol{w}||^2_{\mathcal{M}}$, where C is a constant independent of H and $||\boldsymbol{w}||^2_{\mathcal{M}}$ is the L^2 type norm defined in Chapter 4.

7.3 Calculating Error Bounds

For the Maxwell equations, the process of computing upper and lower bounds may be subdivided into a number of distinct steps. The process that is adopted here is an extension to that originally developed in the context of the Helmholtz equation [25].

Step 1

On the working mesh, obtain $\boldsymbol{U}_H^s \in Z_H^D$, from

$$\mathcal{A}(\boldsymbol{U}_H^s, \boldsymbol{W}) = \langle \boldsymbol{U}^i, \boldsymbol{W} \rangle \qquad \forall \boldsymbol{W} \in Z_H \tag{7.14}$$

The residual

$$\mathcal{R}^U(\boldsymbol{W}) = \langle \boldsymbol{U}^i, \boldsymbol{W} \rangle - \mathcal{A}(\boldsymbol{U}_H^s, \boldsymbol{W}) \tag{7.15}$$

is also defined and we note that $\mathcal{R}^U(\boldsymbol{W}) = 0 \; \forall \boldsymbol{W} \in Z_H$.

Step 2

On the working mesh, compute an output adjoint $\boldsymbol{\Psi}_H \in Z_H$ from

$$\mathcal{A}(\boldsymbol{W}, \boldsymbol{\Psi}_H) = -\ell^{\mathcal{O}}(\boldsymbol{W}; \phi) \qquad \forall \boldsymbol{W} \in Z_H \tag{7.16}$$

The residual

$$\mathcal{R}^{\Psi}(\boldsymbol{W}) = -\overline{\ell^{\mathcal{O}}(\boldsymbol{W}; \phi)} - \overline{\mathcal{A}(\boldsymbol{W}, \boldsymbol{\Psi}_H)} \tag{7.17}$$

is also defined and again we note that $\mathcal{R}^{\Psi}(\boldsymbol{W}) = 0 \; \forall \boldsymbol{W} \in Z_H$.

Step 3

A truth mesh is constructed by a refinement of each coarse mesh element T_H. The refinement may be accomplished by either subdividing the element, or increasing the polynomial order on the element, or by a combination of both. Then, for each coarse mesh element T_H, a coarse broken space is defined as

$$\hat{Z}^H = \left\{ \boldsymbol{u} |\; \boldsymbol{u} \in L^2, \boldsymbol{u}|_{T_H} \in Z_H(T_H), \forall T_H \right\} \tag{7.18}$$

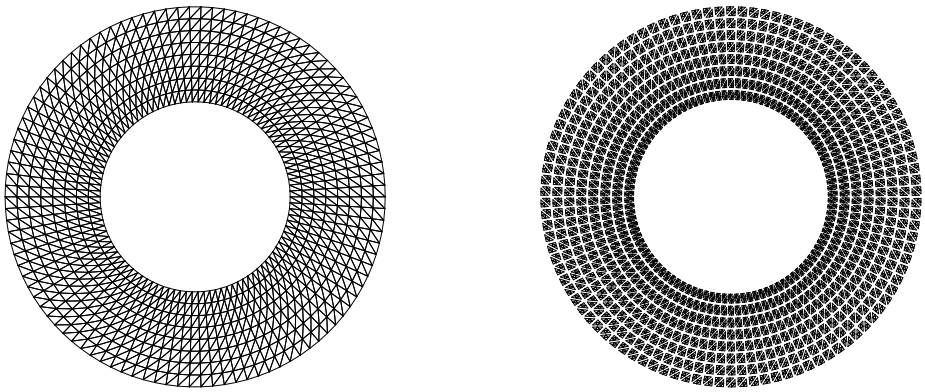

(a) (b)

Figure 7.1: Mesh employed for the electromagnetic scattering problem showing (a) the working mesh for $H = 0.12$ and (b) the corresponding truth mesh

and a corresponding fine broken space as

$$\hat{Z}^h = \left\{ \boldsymbol{u} |\ \boldsymbol{u} \in L^2, \boldsymbol{u}|_{T_H} \in Z_h(T_H), \forall T_H \right\} \tag{7.19}$$

This process is illustrated for a mesh of triangles in Figure 7.1. When the broken spaces are introduced, edge fluxes are necessary to ensure that the solution computed on the broken elements remains in balance. To achieve this, following Demkowicz [11], we define edge flux functionals λ^U and λ^Ψ as

$$\lambda^U(\boldsymbol{W}) = \int_{\partial T_H} (\boldsymbol{n} \wedge \boldsymbol{W}) \cdot \boldsymbol{f}_H^U \mathrm{d}s \tag{7.20}$$

$$\lambda^\Psi(\boldsymbol{W}) = \int_{\partial T_H} (\boldsymbol{n} \wedge \boldsymbol{W}) \cdot \boldsymbol{f}_H^\Psi \mathrm{d}s \tag{7.21}$$

and determine $\boldsymbol{f}_H^E, \boldsymbol{f}_H^\Psi \in \{\boldsymbol{n} \wedge \boldsymbol{W}|_{\partial T_H}, \boldsymbol{W} \in \hat{Z}^H\}$ from the requirement that

$$\lambda^U(\boldsymbol{W}) = \mathcal{R}^U(\boldsymbol{W}) \qquad \forall \boldsymbol{W} \in \hat{Z}^H \tag{7.22}$$

$$\lambda^\Psi(\boldsymbol{W}) = \mathcal{R}^\Psi(\boldsymbol{W}) \qquad \forall \boldsymbol{W} \in \hat{Z}^H \tag{7.23}$$

Step 4

The reconstructed errors are computed in the decoupled truth space as

$$2\mathcal{B}^s(\hat{\boldsymbol{e}}^U, \boldsymbol{W}) = \mathcal{R}^U(\boldsymbol{W}) - \lambda^U(\boldsymbol{W}) \qquad \forall \boldsymbol{W} \in \hat{Z}^h \tag{7.24}$$

$$2\mathcal{B}^s(\hat{\boldsymbol{e}}^{\Psi}, \boldsymbol{W}) = \mathcal{R}^{\Psi}(\boldsymbol{W}) - \lambda^{\Psi}(\boldsymbol{W}) \qquad \forall \boldsymbol{W} \in \hat{Z}^h \tag{7.25}$$

and, then,

$$\hat{\boldsymbol{e}}^{\pm} = \hat{\boldsymbol{e}}^{U} \mp \frac{1}{\kappa}\hat{\boldsymbol{e}}^{\Psi} \tag{7.26}$$

where κ is a suitably defined scaling parameter.

Step 5

Finally, the lower and upper bounds are computed as

$$s^{-} = \text{Re}\{S(\boldsymbol{U}^s_H; \phi)\} - \kappa\mathcal{B}^s(\hat{\boldsymbol{e}}^{-}, \hat{\boldsymbol{e}}^{-}) \tag{7.27}$$

$$s^{+} = \text{Re}\{S(\boldsymbol{U}^s_H; \phi)\} + \kappa\mathcal{B}^s(\hat{\boldsymbol{e}}^{+}, \hat{\boldsymbol{e}}^{+}) \tag{7.28}$$

with these lower and upper bounds being optimised [61] by choosing the scaling parameter, κ, according to

$$\kappa = \sqrt{\frac{\mathcal{B}^s(\hat{\boldsymbol{e}}^{\Psi}, \hat{\boldsymbol{e}}^{\Psi})}{\mathcal{B}^s(\hat{\boldsymbol{e}}^{U}, \hat{\boldsymbol{e}}^{U})}} \tag{7.29}$$

7.3.1 Proof of Bounding Properties

In this section, we demonstrate that the quantities given in equations (7.27) and (7.28) are indeed valid lower and upper bounds on the prescribed output. To achieve this, the field variable error

$$\boldsymbol{e} = \boldsymbol{U}^s_h - \boldsymbol{U}^s_H \tag{7.30}$$

which is the difference between the fine and coarse mesh approximations, is introduced. Combining equations (7.24) and (7.25), and choosing $\boldsymbol{W} = \boldsymbol{e}$, it follows that

$$2\kappa\mathcal{B}^s(\hat{\boldsymbol{e}}^{-}, \boldsymbol{e}) - \kappa\mathcal{A}(\boldsymbol{e}, \boldsymbol{e}) - \overline{\ell^{\mathcal{O}}(\boldsymbol{e}; \phi)} = 0 \tag{7.31}$$

and, in particular,

$$Re[2\kappa\overline{\mathcal{B}^s(\hat{\boldsymbol{e}}^{-}, \boldsymbol{e})}] - \kappa Re[\overline{\mathcal{A}(\boldsymbol{e}, \boldsymbol{e})}] + Re[\ell^{\mathcal{O}}(\boldsymbol{e}; \phi)] = 0 \tag{7.32}$$

But, on expanding the left hand side, and adding the resulting equation to equation (7.27), it can be seen that

$$s^- = \text{Re}\{S(\boldsymbol{U}_h;\phi)\} - \kappa\mathcal{B}^s(\boldsymbol{e}-\hat{\boldsymbol{e}}^-,\boldsymbol{e}-\hat{\boldsymbol{e}}^-) - \Big[\text{Re}\left\{\mathcal{N}(\boldsymbol{e},\boldsymbol{e};\phi)\right\} - \kappa\mathcal{B}^s(\boldsymbol{e},\boldsymbol{e}) + \kappa\text{Re}\{\overline{\mathcal{A}(\boldsymbol{e},\boldsymbol{e})}\}\Big] \quad (7.33)$$

This simplifies to

$$s^- = \text{Re}\{S(\boldsymbol{U}_h;\phi)\} - \kappa\mathcal{B}^s(\boldsymbol{e}-\hat{\boldsymbol{e}}^-,\boldsymbol{e}-\hat{\boldsymbol{e}}^-) - \left[\text{Re}\left\{\mathcal{N}(\boldsymbol{e},\boldsymbol{e};\phi)\right\} - 2\omega^2\kappa\text{Re}\left\{m(\boldsymbol{e},\boldsymbol{e})\right\}\right] \quad (7.34)$$

using the properties of the bilinear forms $\mathcal{B}^s$ and $\mathcal{A}$. Numerical experiments in Chapter 4 have shown that for triangular elements with $p > 0$, $\text{Re}\left\{\mathcal{N}(\boldsymbol{e},\boldsymbol{e};\phi)\right\} - 2\omega^2\kappa\text{Re}\left\{m(\boldsymbol{e},\boldsymbol{e})\right\}$ vanishes as $\mathcal{O}(H^{2(p+1)})$, i.e. much faster than $\kappa\mathcal{B}^s(\boldsymbol{e}-\hat{\boldsymbol{e}}^-,\boldsymbol{e}-\hat{\boldsymbol{e}}^-)$, which vanishes as $\mathcal{O}(H^{2p})$. It then follows that, since $\mathcal{B}^s$ is positive definite, s^- will approach $\text{Re}\{S(\boldsymbol{U}_h,\phi)\}$ from below. Similar arguments show s^+ to be an upper bound on $\text{Re}\{S(\boldsymbol{U}_h,\phi)\}$ for triangular elements.

For quadrilateral elements, numerical experiments in Chapter 4 have shown that $\text{Re}\left\{\mathcal{N}(\boldsymbol{e},\boldsymbol{e};\phi)\right\} - 2\omega^2\kappa\text{Re}\left\{m(\boldsymbol{e},\boldsymbol{e})\right\}$ locally vanishes at rates between $\mathcal{O}(H^{2(p+1)})$ and $\mathcal{O}(H^{2(p+2)})$ depending on the angle of propagation of the wave in each element. But, more importantly, since the term $\kappa\mathcal{B}^s(\boldsymbol{e}-\hat{\boldsymbol{e}}^-,\boldsymbol{e}-\hat{\boldsymbol{e}}^-)$ globally vanishes as $\mathcal{O}(H^{2(p+1)})$ and, as the angle of propagation for a scattering problem is different in each element, it then follows that $\text{Re}\left\{\mathcal{N}(\boldsymbol{e},\boldsymbol{e};\phi)\right\} - 2\omega^2\kappa\text{Re}\left\{m(\boldsymbol{e},\boldsymbol{e})\right\}$ will globally vanish faster. Finally, since $\mathcal{B}^s$ is positive definite, this then implies that s^- will approach $\text{Re}\{S(\boldsymbol{U}_h,\phi)\}$ from below. Similar arguments show s^+ to be an upper bound on $\text{Re}\{S(\boldsymbol{U}_h,\phi)\}$ for quadrilateral elements.

7.3.2 Computation of the Edge Fluxes

When the broken spaces are introduced, it has been noted that edge fluxes are necessary to ensure that the solutions on the broken elements remains in balance. To achieve this, the edge functional given in expression (7.20) and (7.21) are employed. In these expressions, the fluxes $\boldsymbol{f}_H^U$ and $\boldsymbol{f}_H^\Psi$ associated with an element T_H are

unknown. The properties of the tangential components of the weighting function enable an edge–wise decoupling of $\boldsymbol{f}_H^U$ and $\boldsymbol{f}_H^\Psi$ in the form

$$\boldsymbol{f}_H^U = \sum_{i=1}^{ne} \boldsymbol{f}_H^{Ui} \qquad \boldsymbol{f}_H^{Ui} = \sum_{j=0}^{p} f_{Hj}^{Ui} \boldsymbol{n} \wedge \boldsymbol{\phi}_j^i \tag{7.35}$$

$$\boldsymbol{f}_H^\Psi = \sum_{i=1}^{ne} \boldsymbol{f}_H^{\Psi i} \qquad \boldsymbol{f}_H^{\Psi i} = \sum_{j=0}^{p} f_{Hj}^{\Psi i} \boldsymbol{n} \wedge \boldsymbol{\phi}_j^i \tag{7.36}$$

where ne is 3 for a triangular element and 4 for a quadrilateral element. In addition, $\boldsymbol{f}_H^{Ui}$ and $\boldsymbol{f}_H^{\Psi i}$ are the fluxes associated with an edge i. Computation of the edge flux coefficients f_{Hj}^{Ui} and $f_{Hj}^{\Psi i}$ then follow by solving a small linear system on each edge of T_H. For example, in the case $p = 1$, the two linear systems which must be solved on each edge i of T_H are

$$\int_{\partial T_H|_i} \begin{bmatrix} \boldsymbol{n} \times \hat{\boldsymbol{\phi}}_0^{\,i} \cdot \boldsymbol{n} \times \hat{\boldsymbol{\phi}}_0^{\,i} & \boldsymbol{n} \times \hat{\boldsymbol{\phi}}_0^{\,i} \cdot \boldsymbol{n} \times \hat{\boldsymbol{\phi}}_1^{\,i} \\ \boldsymbol{n} \times \hat{\boldsymbol{\phi}}_1^{\,i} \cdot \boldsymbol{n} \times \hat{\boldsymbol{\phi}}_0^{\,i} & \boldsymbol{n} \times \hat{\boldsymbol{\phi}}_1^{\,i} \cdot \boldsymbol{n} \times \hat{\boldsymbol{\phi}}_1^{\,i} \end{bmatrix} \mathrm{d}s \begin{bmatrix} f_{H0}^{Ui} \\ f_{H1}^{Ui} \end{bmatrix} = \begin{bmatrix} \lambda_0^{Ui} \\ \lambda_1^{Ui} \end{bmatrix} \tag{7.37}$$

$$\int_{\partial T_H|_i} \begin{bmatrix} \boldsymbol{n} \times \hat{\boldsymbol{\phi}}_0^{\,i} \cdot \boldsymbol{n} \times \hat{\boldsymbol{\phi}}_0^{\,i} & \boldsymbol{n} \times \hat{\boldsymbol{\phi}}_0^{\,i} \cdot \boldsymbol{n} \times \hat{\boldsymbol{\phi}}_1^{\,i} \\ \boldsymbol{n} \times \hat{\boldsymbol{\phi}}_1^{\,i} \cdot \boldsymbol{n} \times \hat{\boldsymbol{\phi}}_0^{\,i} & \boldsymbol{n} \times \hat{\boldsymbol{\phi}}_1^{\,i} \cdot \boldsymbol{n} \times \hat{\boldsymbol{\phi}}_1^{\,i} \end{bmatrix} \mathrm{d}s \begin{bmatrix} f_{H0}^{\Psi i} \\ f_{H1}^{\Psi i} \end{bmatrix} = \begin{bmatrix} \lambda_0^{\Psi i} \\ \lambda_1^{\Psi i} \end{bmatrix} \tag{7.38}$$

with higher order elements giving rise to larger systems in an obvious manner. The edge flux functional extended for the fine mesh is then given by equations (7.20) and (7.21), where now, $\boldsymbol{W} \in \hat{Z}^h$.

7.4 Dispersive Considerations

Before computing upper and lower bounds, we must consider the effects of dispersion. If the working mesh discretisation does not resolve the wave accurately, then the fluxes we compute may, in extreme circumstances, lead to bounds which do not bound the true solution. If the error estimator is subsequently used to adapt the working mesh discretisation, the adaptive procedure may focus on an incorrect portion of the domain.

To overcome this, the initial working mesh discretisation is chosen so as to reduce the level of dispersion in the resulting solution. This is accomplished by

first generating a mesh and then determining the polynomial order which will give an acceptable level of dispersion. The polynomial order is computed by considering the dispersion relation

$$\omega^2 - |\boldsymbol{\Xi}|^2 = \frac{H^{2(p+1)}}{2(p+1)+1}\left[\frac{(p+1)!}{(2(p+1))!}\right]\left(\Xi_1^{2(p+1)+2} + \Xi_2^{2(p+1)+2}\right) + \mathcal{O}(H^{2(p+1)+2}) \quad (7.39)$$

which has been derived by Ainsworth and Coyle [37] for meshes consisting of an infinite number of uniformly spaced square quadrilateral elements. In this expression $\boldsymbol{\Xi} = [\Xi_1, \Xi_2]^T$ is the wavenumber of the computational procedure. The polynomial order, p, which will give rise to an acceptable level of dispersion for a mesh of quadrilaterals, is obtained approximately from

$$\frac{H^{2(p+1)}(p+1)!(2\omega^{2(p+1)+2})}{(2(p+1))!(2(p+1)+1)!} < 0.05\omega \quad (7.40)$$

Unfortunately, the triangles do not easily admit an exact dispersion relationship for smooth fields. However, one can estimate dispersion approximately by assuming that for the same mesh spacing, a pth order quadrilateral element is replaced by a $p+1$ order triangle. This is justified on the basis that a pth order quadrilateral converges at a rate $\mathcal{O}(H^{p+1})$ compared to $\mathcal{O}(H^p)$ for a pth order triangle when $p \geq 1$ (see Chapter 4).

7.5 Application to the Scattering Width Output

As we have seen in previous chapters, a non–linear output, which is of particular interest, is the scattering width or radar cross section per unit length. The evaluation of this parameter, requires the use of a near to far field transformation. This has been seen in Chapter 5 to be given by

$$\chi_H(\phi) = \frac{\omega}{4}\left|\int_{\Gamma_c} (\boldsymbol{n} \wedge \boldsymbol{U}_H^s \cdot \boldsymbol{V} + \boldsymbol{n} \wedge \mathrm{curl}\, \boldsymbol{U}_H^s \cdot \boldsymbol{Y})\, \mathrm{d}\Gamma'\right|^2 \quad (7.41)$$

The integral is performed on a collection surface Γ_c, when the solution of $\boldsymbol{U}_H^s$ over the computational domain is complete. For completeness, the definitions of the

vectors $\boldsymbol{V}$ and $\boldsymbol{Y}$ are repeated as

$$\boldsymbol{V} = \begin{bmatrix} 0 \\ 0 \\ -\delta \end{bmatrix} e^{-\mathrm{i}\omega(x'\cos\phi + y'\sin\phi)} \tag{7.42}$$

$$\boldsymbol{Y} = \frac{\delta}{\mathrm{i}\omega} \begin{bmatrix} \sin\phi \\ -\cos\phi \\ 0 \end{bmatrix} e^{-\mathrm{i}\omega(x'\cos\phi + y'\sin\phi)} \tag{7.43}$$

where δ is parameter which is equal to $+1$ for TE simulations and equal to -1 for TM simulations.

When using an edge element discretistaion to evaluate the scattering width, the term $\operatorname{curl} \boldsymbol{U}_H^s$ is always approximated to a lower degree than $\boldsymbol{U}_H$. To compensate for this, Monk and coworkers [62, 63, 64] have derived an alternative approach, in which the accuracy of the curl term is improved.

In their approach, the term $(\boldsymbol{n} \wedge \operatorname{curl} \boldsymbol{U}_H^s) \cdot \boldsymbol{Y}$ in equation (7.41) is replaced by an area integral, over a layer of elements adjacent to Γ_c. To do this, they recognized that $(\boldsymbol{n} \wedge \operatorname{curl} \boldsymbol{U}_H^s) \cdot \boldsymbol{Y}$ forms the right hand side to the variational statement: find $\boldsymbol{U}^s \in \mathcal{H}(\operatorname{curl}; \Omega)$ where

$$\int_{\Omega_f} \left(\operatorname{curl} \boldsymbol{U}^s \cdot \operatorname{curl} \overline{\boldsymbol{W}} - \omega^2 \boldsymbol{U}^s \cdot \overline{\boldsymbol{W}} \right) \mathrm{d}\Omega = - \int_{\partial\Omega_f} (\boldsymbol{n} \wedge \operatorname{curl} \boldsymbol{U}^s) \cdot \overline{\boldsymbol{W}} \, \mathrm{d}\Gamma \tag{7.44}$$

with

$$\boldsymbol{W} = \begin{cases} \overline{\boldsymbol{Y}} & \text{on } \Gamma_c \cup \partial\Omega_f \\ \boldsymbol{0} & \text{in } \Omega_f \end{cases} \tag{7.45}$$

This means that the discrete integral in equation (7.41) is replaced by [64]

$$\chi_H(\phi) = \frac{\omega}{4} \left| \int_{\Gamma_c} (\boldsymbol{n} \wedge \boldsymbol{U}_H^s \cdot \boldsymbol{V}) \, \mathrm{d}\Gamma \right. + \left. \sum_{\substack{k \in \Omega_f \\ \partial k \cup \Gamma_c \neq \emptyset}} \int_k \left(\omega^2 \boldsymbol{U}_H^s \cdot \boldsymbol{y}_H - \operatorname{curl} \boldsymbol{U}_H^s \cdot \operatorname{curl} \boldsymbol{y}_H \right) \mathrm{d}\Omega \right|^2 \tag{7.46}$$

where $\boldsymbol{y}_H$ is chosen to be the edge element interpolation of $\boldsymbol{Y}$ on Γ_c and equal to zero at all interpolation points in Ω_f.

7.5.1 Bounding the scattering width

If bounds on the output given by the discrete non–linear functional in equation (7.41) are pursued, the resulting adjoint problem is singular. However, if the alternative method for evaluating this functional proposed by Monk and coworkers is adopted viz equation (7.46), a singular adjoint problem does not result. Therefore, the approach employed to evaluate bounds on the scattering width, is to consider outputs of the form

$$S(\boldsymbol{U}_H^s;\phi) = \mathcal{L}^{\mathcal{O}}(\boldsymbol{U}_H^s;\phi)\overline{\mathcal{L}^{\mathcal{O}}(\boldsymbol{U}_H^s;\phi)} \tag{7.47}$$

where

$$\begin{aligned}\mathcal{L}^{\mathcal{O}}(\boldsymbol{U}_H^s;\phi) = &\int_{\Gamma_c} (\boldsymbol{n}\wedge\boldsymbol{U}_H^s\cdot\boldsymbol{V}\,)\,\mathrm{d}\Gamma \\ &+ \sum_{\substack{k\in\Omega_f \\ \partial k\cup\Gamma_c\neq\emptyset}} \int_k \left(\omega^2\boldsymbol{U}_H^s\cdot\boldsymbol{y}_H - \mathrm{curl}\,\boldsymbol{U}_H^s\cdot\mathrm{curl}\,\boldsymbol{y}_H\right)\,\mathrm{d}\Omega\end{aligned} \tag{7.48}$$

It follows that the scattering width is given by $\chi(\phi) = (\omega/4)S(\boldsymbol{U}_H^s;\phi)$, which is a constant factor, multiplied by the output $S(\boldsymbol{U}_H^s;\phi)$. Expanding the output S by the Taylor Series gives

$$\ell^{\mathcal{O}}(\boldsymbol{v};\phi) = \mathcal{L}^{\mathcal{O}}(\boldsymbol{U}_H^s;\phi)\overline{\mathcal{L}^{\mathcal{O}}(\boldsymbol{v};\phi)} + \mathcal{L}^{\mathcal{O}}(\boldsymbol{v};\phi)\overline{\mathcal{L}^{\mathcal{O}}(\boldsymbol{U}_H^s;\phi)} \tag{7.49}$$

$$\mathcal{N}(\boldsymbol{v},\boldsymbol{v};\phi) = \mathcal{L}^{\mathcal{O}}(\boldsymbol{v};\phi)\overline{\mathcal{L}^{\mathcal{O}}(\boldsymbol{v};\phi)} \tag{7.50}$$

where $\mathcal{L}$ and $\mathcal{N}$ are the linear and nonlinear components defined in equation (7.13). Before, evaluating bounds on $S(\boldsymbol{U}_H;\phi)$ we need to show that $|\mathcal{N}(\boldsymbol{w},\boldsymbol{w});\phi| \leq C||\boldsymbol{w}||^2_{\mathcal{M}}$. To do this, a series of numerical experiments is undertaken, in which the convergence of $|\mathcal{N}(\boldsymbol{w},\boldsymbol{w};\phi)|$ is explored for the model problem given in Chapter 4, where $\boldsymbol{w} = \boldsymbol{E}_0 - \boldsymbol{E}_N$. The result of this investigation is then compared to the convergence of $||\boldsymbol{w}||^2_{\mathcal{M}}$ which was also investigated in Chapter 4. For triangular

Table 7.1: Approximate convergence rates of $\mathcal{N}(\boldsymbol{w}, \boldsymbol{w}; \phi)$ compared to $||\boldsymbol{w}||^2_{\mathcal{M}}$ for the triangular element

p	1	2	3
$\mathcal{N}(\boldsymbol{w}, \boldsymbol{w}; \phi)$	4.25	9.16	12.54
$\|\|\boldsymbol{w}\|\|^2_{\mathcal{M}}$	4	6	8

Table 7.2: Approximate convergence rates of $\mathcal{N}(\boldsymbol{w}, \boldsymbol{w}; \phi)$ compared to $||\boldsymbol{w}||^2_{\mathcal{M}}$ for the quadrilateral element

p	1	2	3
$\mathcal{N}(\boldsymbol{w}, \boldsymbol{w}; \phi)$	6.67	8.54	10.80
$\|\|\boldsymbol{w}\|\|^2_{\mathcal{M}}$	4-6	6-8	8-10

elements of polynomial order $p = 1, 2, 3$ this comparison is shown in 7.1. From Table 7.1 it is clear that, $|\mathcal{N}(\boldsymbol{w}, \boldsymbol{w}; \phi)|$ converges faster to zero than $||\boldsymbol{w}||^2_{\mathcal{M}}$ and therefore satisfies the required property. In a similar manner, Table 7.2 shows that $|\mathcal{N}(\boldsymbol{w}, \boldsymbol{w}; \phi)|$ converges faster to zero than $||\boldsymbol{w}||^2_{\mathcal{M}}$ for the quadrilateral element.

Evaluation of bounds on the scattering width then follows the general procedure of section 7.3.

7.6 Results given by the Estimator

This section presents a number of numerical examples, where strict bounds have been obtained on the scattering width output. Initially, bounds are considered when meshes consisting only of triangular elements are used. We consider the case of the scattering of a TE wave by a 2λ cylinder and compute bounds using two different refinement strategies. For the first refinement strategy, we keep the polynomial

order constant and refine the mesh, and for the second refinement strategy, we keep the mesh fixed and increase the polynomial order. An initial mesh with spacing $H = 0.31$ is selected for these refinement strategies. On this mesh, the dispersion relationship shows that elements of order $p = 4$ are required to give an acceptable level of dispersion. To evaluate bounds a truth mesh is required. When performing only h–refinement the truth mesh is selected as $h = H/5$ and in the case when the polynomial order is increased, the truth mesh is then chosen to be given by $p = 8$ elements.

Bounds are computed on working discretisations in which the mesh spacing lies between the initial mesh spacing and the spacing of truth mesh. In particular, working meshes of spacings $H, H/2, H/3, H/4$ are considered and bounds on the scattering width output are computed at the locations $\phi = 0, 90, 180$. The result of this investigation is shown in Figure 7.2 (a), where the relative bounds s^+/s_h and s^-/s_h are plotted against the working mesh spacing. In this Figure it is observed that the bounds converge with decreasing mesh spacing and that the smallest bounds at any given spacing are for $\phi = 0$.

Figure 7.2 (b) shows the computed bounds, when working meshes with increasing polynomial orders are considered. For this example, working discretsiations corresponding to polynomial orders of $p = 4, 5, 6, 7$ on a fixed mesh spacing $H = 0.31$ are considered. In Figure 7.2 (b), the rate at which the bounds for $\phi = 0, 90, 180$ converge to the fine mesh solution is quicker than that achieved for working meshes with refined H.

Bounds are now computed for the scattering of a TM wave. The results of this investigation are shown in Figures 7.3 (a) and (b). Figure 7.3 (a) shows the computed bounds, when refinement of the mesh is undertaken and Figure 7.3 (b) shows the corresponding bounds when the polynomial order is increased. The behaviour exhibited in these figures is similar to that shown for the TE case.

Next, a discretisation employing only quadrilateral elements is considered. Using the dispersion relationship, it is found that a minimum polynomial order of $p = 3$ is required to obtain an acceptable level of dispersion on a mesh of spacing

$H = 0.31$. For this example, the truth mesh is selected as $h = H/5$, when refinement of the mesh is undertaken and in the case when the polynomial order is increased the truth mesh is then chosen to be given by $p = 8$ elements. Figure 7.4 (a) shows the relative upper and lower computed bounds against working mesh spacing H for the TE problem. This Figure exhibits similar behaviour to that already observed for meshes of triangles. Figure 7.4 (b) shows the computed bounds for the case when p–refinement is undertaken, again showing similar behaviour to the triangles.

The computed bounds on a series of working meshes of quadrilaterals for the scattering of a TM wave by a 2λ cylinder are shown in Figures 7.5 (a) and (b). Figure 7.5 (a) show the convergence of the bounds to the fine mesh solution when h–refinement is undertaken and Figure 7.5 (b) shows the convergence when p–refinement is undertaken.

7.6.1 Convergence of the Bounds

Figure 7.6 (a) illustrates the convergence of the bounds on the scattering width for the case of the scattering of a TE wave by a 2λ cylinder when triangular elements are employed. To examine the convergence, $(s^+ - s^-)/s_h$ is plotted against working mesh spacing H and here it is observed that as the working mesh spacing is reduced, the relative bound gap converges. Initially, the rate of convergence is algebraic and then the rate of convergence slows down. This behaviour occurs due to the finite numerical precision of the method. Figure 7.6 (b) shows $(s^+ - s^-)/s_h$ plotted against polynomial order, for working discretisations in which the order of polynomial is refined. An algebraic rate of convergence is again exhibited.

Following the same procedure for the case of the scattering of a TM wave by a 2λ cylinder, yields Figure 7.7 (a) which shows the convergence of $(s^+ - s^-)/s_h$ with working mesh spacing H and Figure 7.7 (b) which shows the convergence of $(s^+ - s^-)/s_h$ with increasing working polynomial order. The behaviour exhibited by these two figures is similar to that shown in Figures 7.6 (a) and (b).

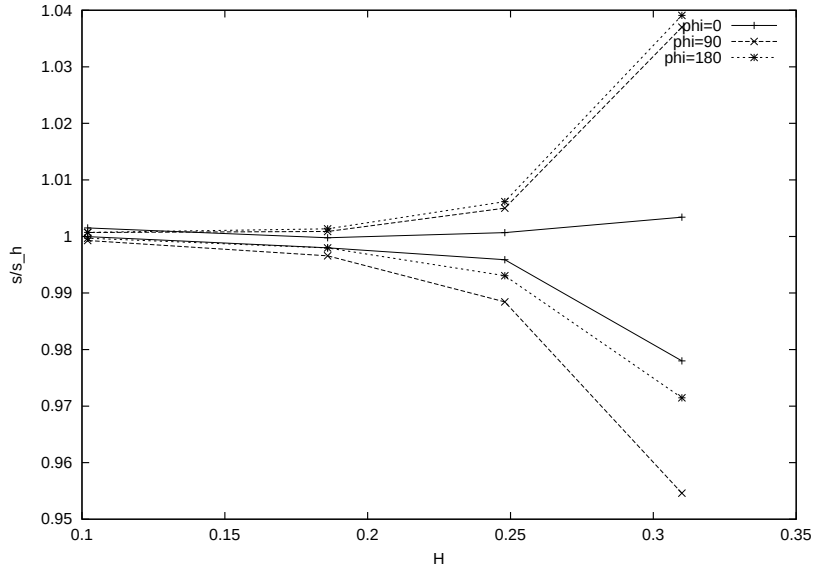

(a)

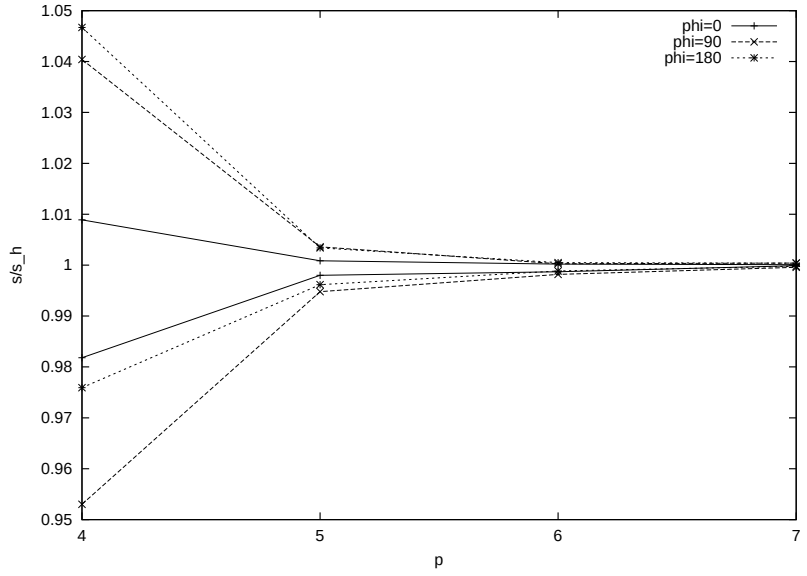

(b)

Figure 7.2: Scattering by a 2λ cylinder by a TE wave using a mesh of triangular elements showing bounds computed using a series of working meshes with: (a) refi ned H and (b) using increasing p

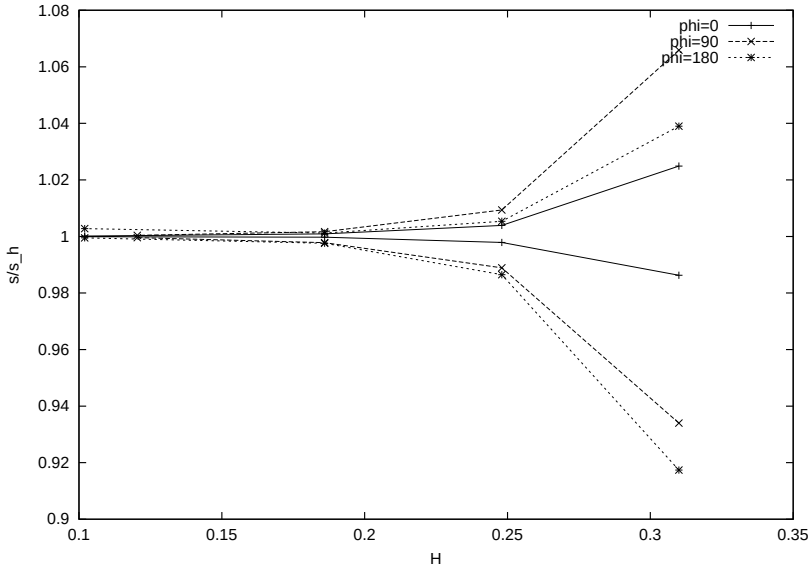

(a)

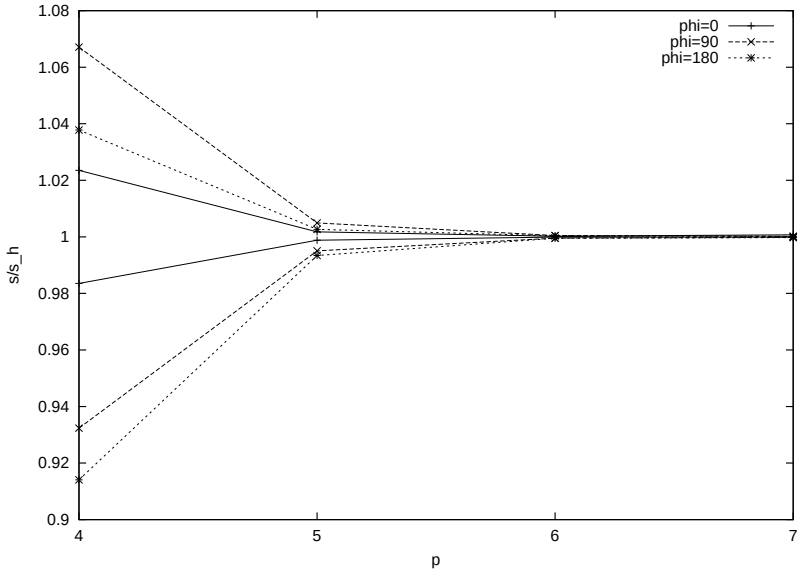

(b)

Figure 7.3: Scattering by a 2λ cylinder by a TM wave using a mesh of triangular elements, showing, bounds computed using a series of working meshes with: (a) refi ned H and (b) using increasing p

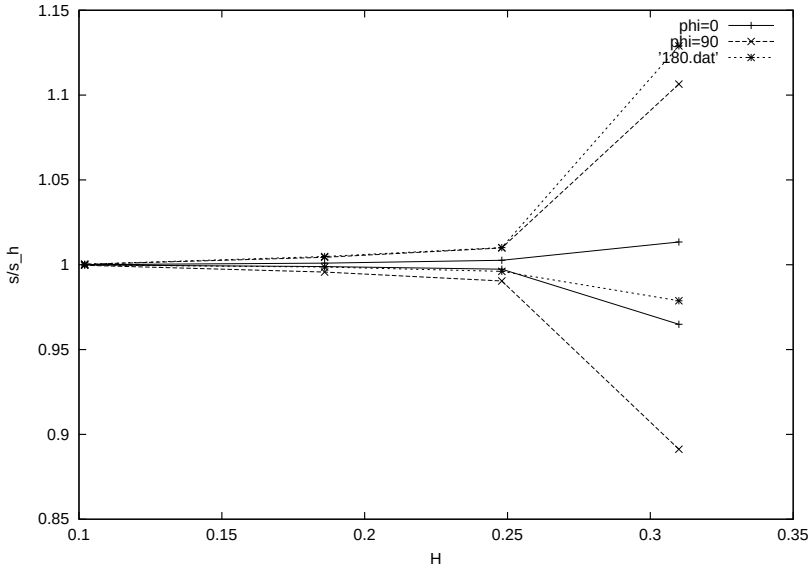

(a)

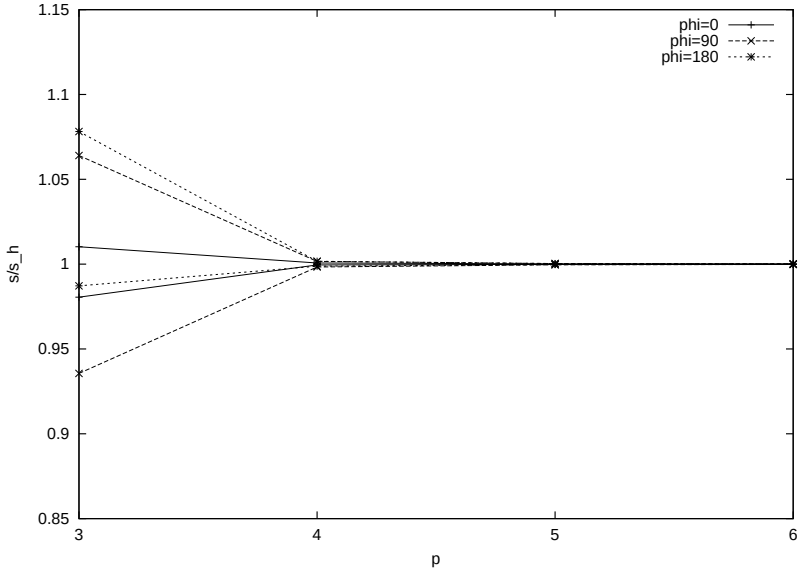

(b)

Figure 7.4: Scattering of a 2λ cylinder by a TE wave using a mesh of quadrilaterals, showing, bounds computed using a series of working meshes with: (a) refined H and (b) using increasing p

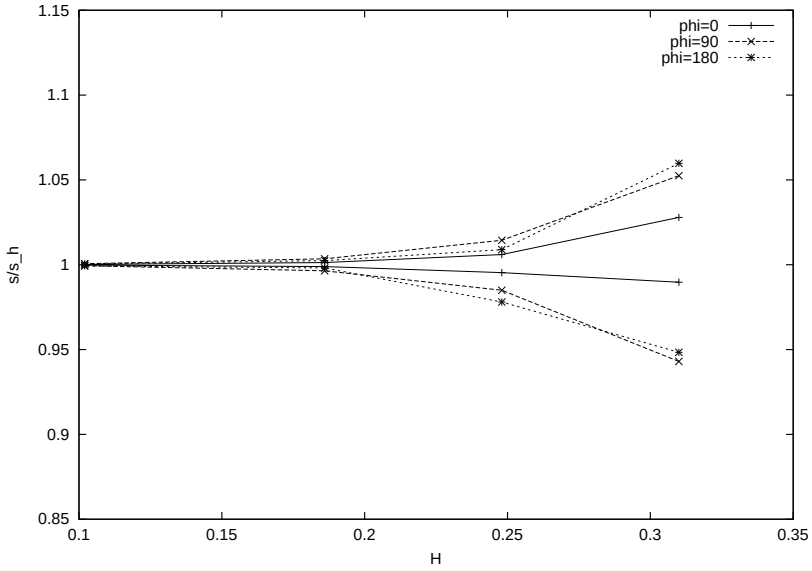

(a)

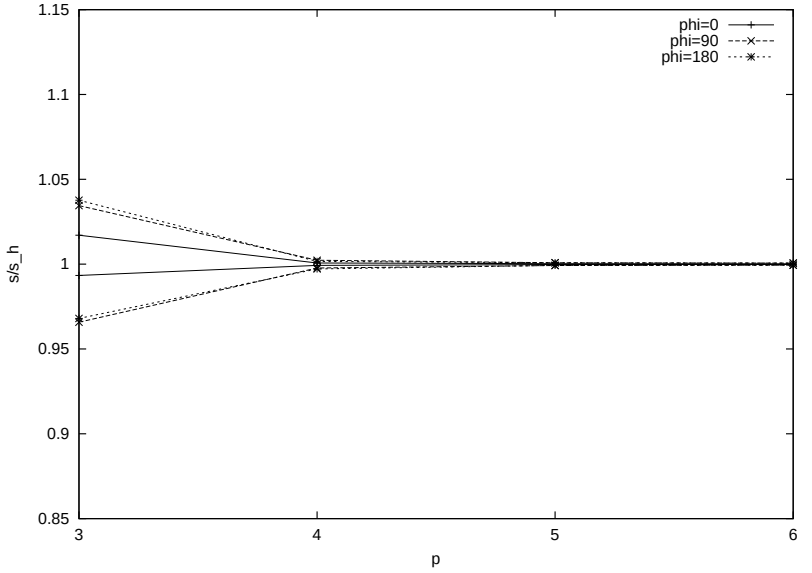

(b)

Figure 7.5: Scattering of a 2λ cylinder by a TM wave using a mesh of quadrilaterals, showing, bounds computed using a series of working meshes with: (a) refined H and (b) using increasing p

The convergence of the bounds on the scattering width for the scattering of a TE wave by a 2λ cylinder, when quadrilateral elements are employed, is now considered. Figure 7.8 (a) shows the convergence of the bounds for working discretisation in which the mesh spacing is refined. The corresponding case, where the working discretisation consist of refinements of the polynomial order is shown in Figure 7.8 (b). Both exhibit an algebraic rate of convergence, before the rate of convergence slows due to finite numerical precision.

The convergence of the bounds on the scattering width for the corresponding scattering of a TM wave is considered. Figure 7.9 (a) shows the convergence of the bounds for working discretisations in which the mesh spacing is refined. The corresponding case, where the working discretisations consist of refinement of the polynomial order is shown in Figure 7.9 (b). Once again both Figures exhibit an algebraic rate of convergence.

7.6.2 Accuracy of the Computed Bounds

The accuracy of the computed bounds is analyzed for a problem with a known exact solution. For this, we consider the scattering of a TM wave by a 2λ cylinder with bounds computed on a mesh of triangular elements. To show the accuracy of the computed bounds, we display the bounds at the locations $\phi = 0$, $\phi = 90$ and $\phi = 180$ as vertical lines on the scattering width distributions. Alongside this, a contour plot of the scattered field across the computational domain are included to show the smoothness of the solution. Figure 7.10 (a) shows contours of $Re(E_Z^s)$ for $p = 4$ elements uniform across the mesh of spacing $H = 0.31$ and Figure 7.10 (b) shows the resulting bounds on the scattering width. In addition, Figure 7.10 (b) also shows the scattering width evaluated using both Monk's technique and the original technique. Both produce distributions which are in close agreement with the exact distribution. However, the computed bounds show a small envelope in which the solutions could lie. The reason for this is that there is a small difference between the smoothness of the contours of the solution on the $H = 0.31$ mesh and the

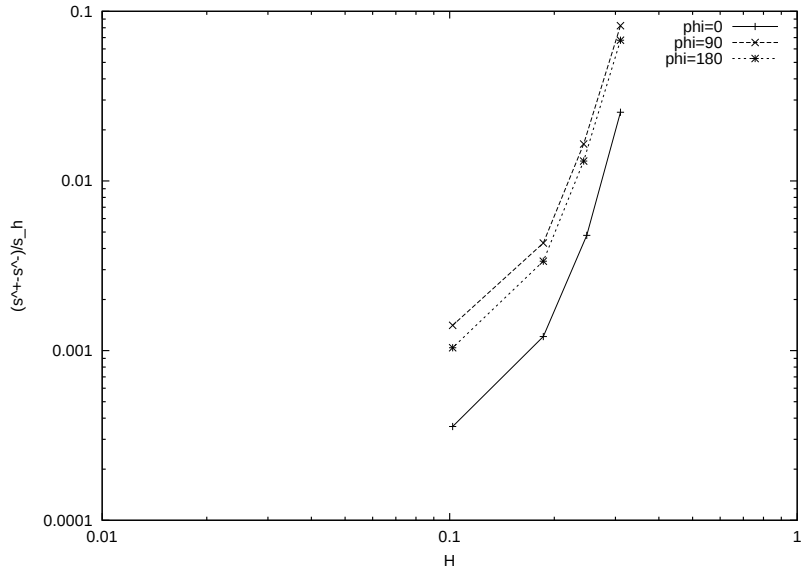

(a)

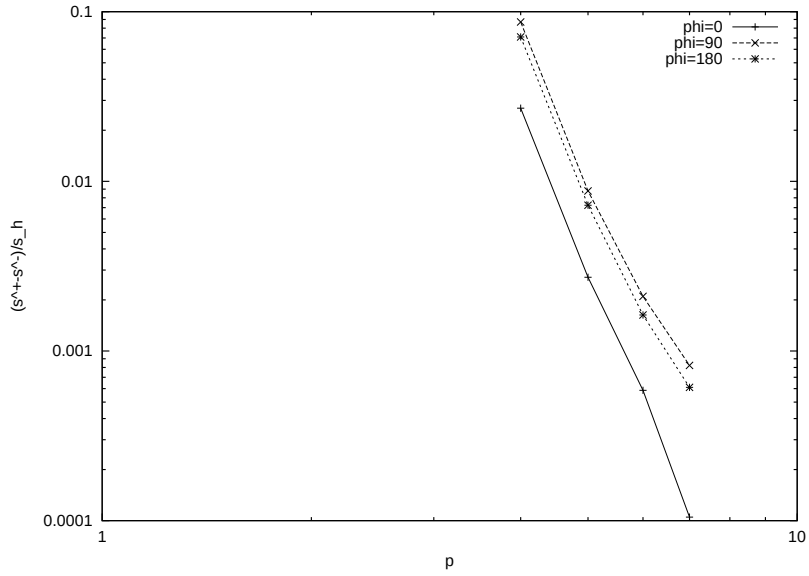

(b)

Figure 7.6: Scattering of a 2λ cylinder by a TE wave, showing $(s^+ - s^-)/s_h$ with: (a) refi ned working mesh spacing H and (b) refi ned polynomial order p on working meshes

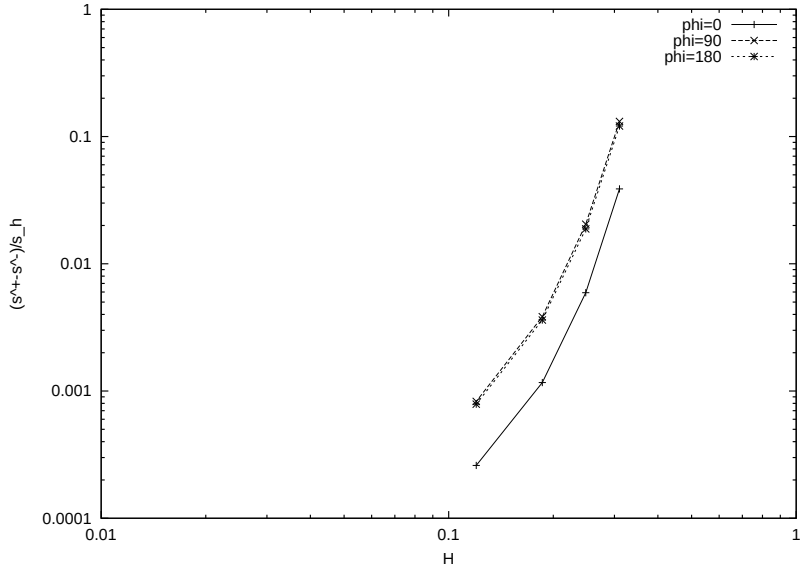

(a)

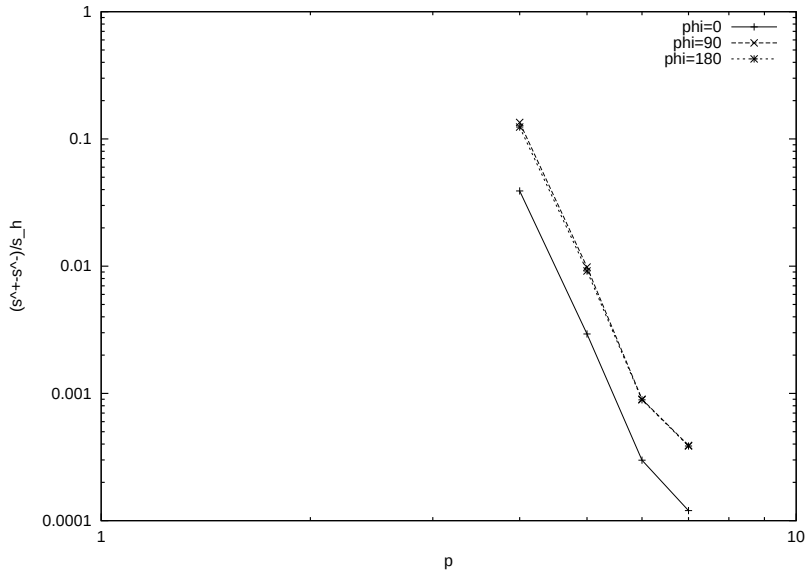

(b)

Figure 7.7: Scattering of a 2λ cylinder by a TM wave, showing $(s^+ - s^-)/s_h$ with: (a) refi ned working mesh spacing H and (b) refi ned polynomial order p on working meshes

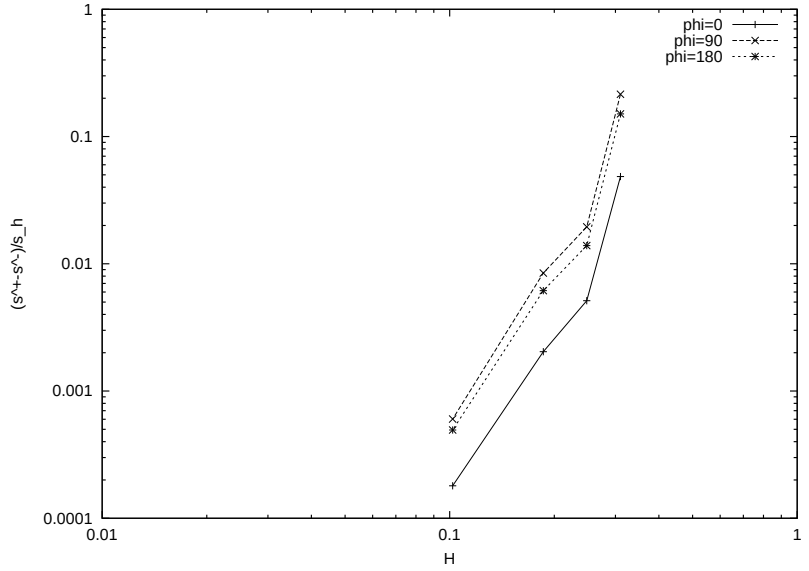

(a)

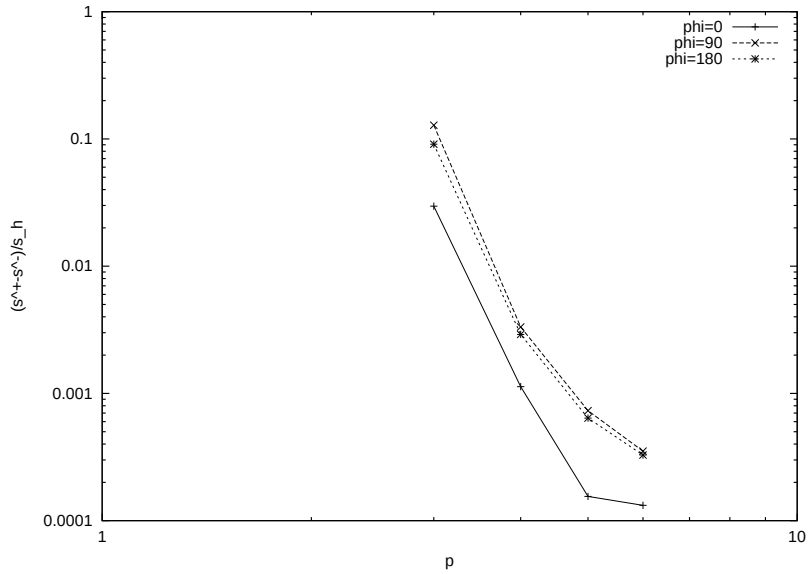

(b)

Figure 7.8: Scattering of a 2λ cylinder by a TE wave, showing $(s^+ - s^-)/s_h$ with: (a) refi ned working mesh spacing H and (b) refi ned polynomial order p on working meshes

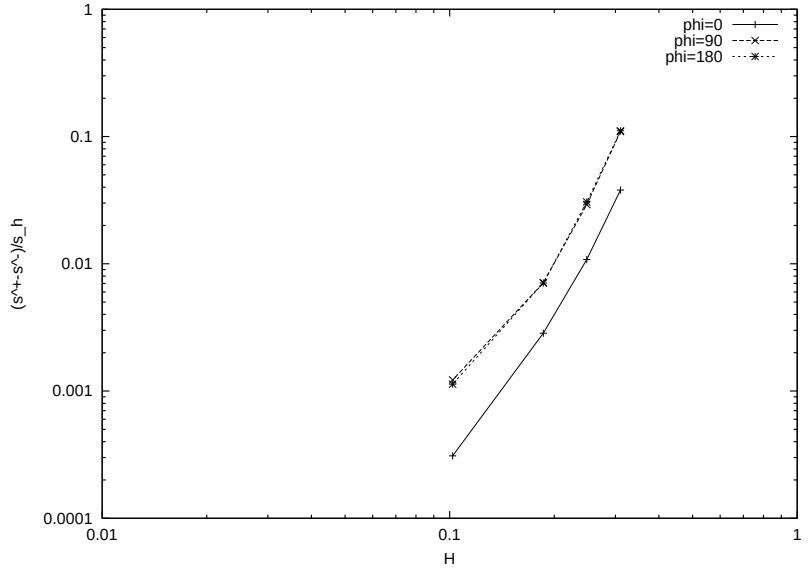

(a)

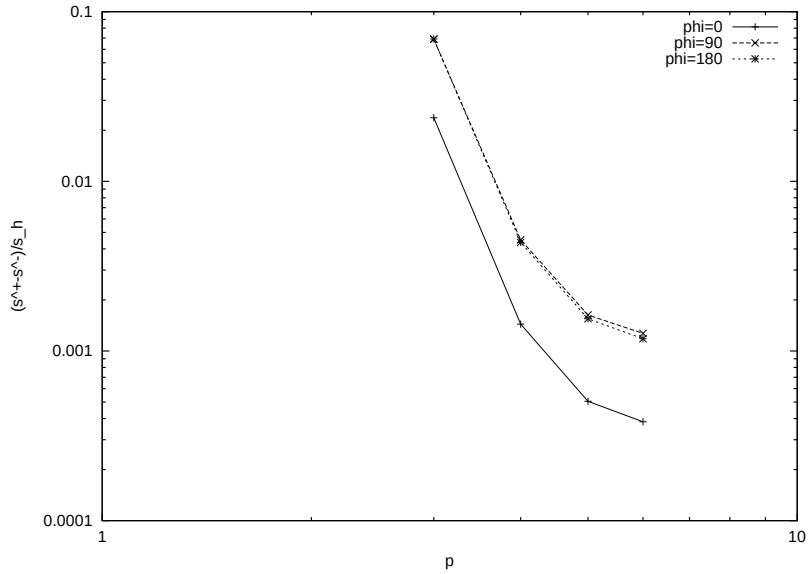

(b)

Figure 7.9: Scattering of a 2λ cylinder by a TM wave, showing $(s^+ - s^-)/s_h$ with: (a) refi ned working mesh spacing H and (b) refi ned polynomial order p on working meshes

smoothness of the contours of the solution on the truth mesh.

Figure 7.10 (c) and (d) the contour and computed distributions when the working discretisation is refined to have $p = 5$ elements. Here, it is observed that the envelope provided by the bounds have almost vanished to the computational solution. In addition, the contour of $Re(E_z^s)$ has become smoother than for the $p = 4$ elements.

The next refinement, which uses $p = 6$ elements, is shown in Figure 7.10 (e) and (f), here the bounds have vanished to the computational solution and the contour plot has become smooth.

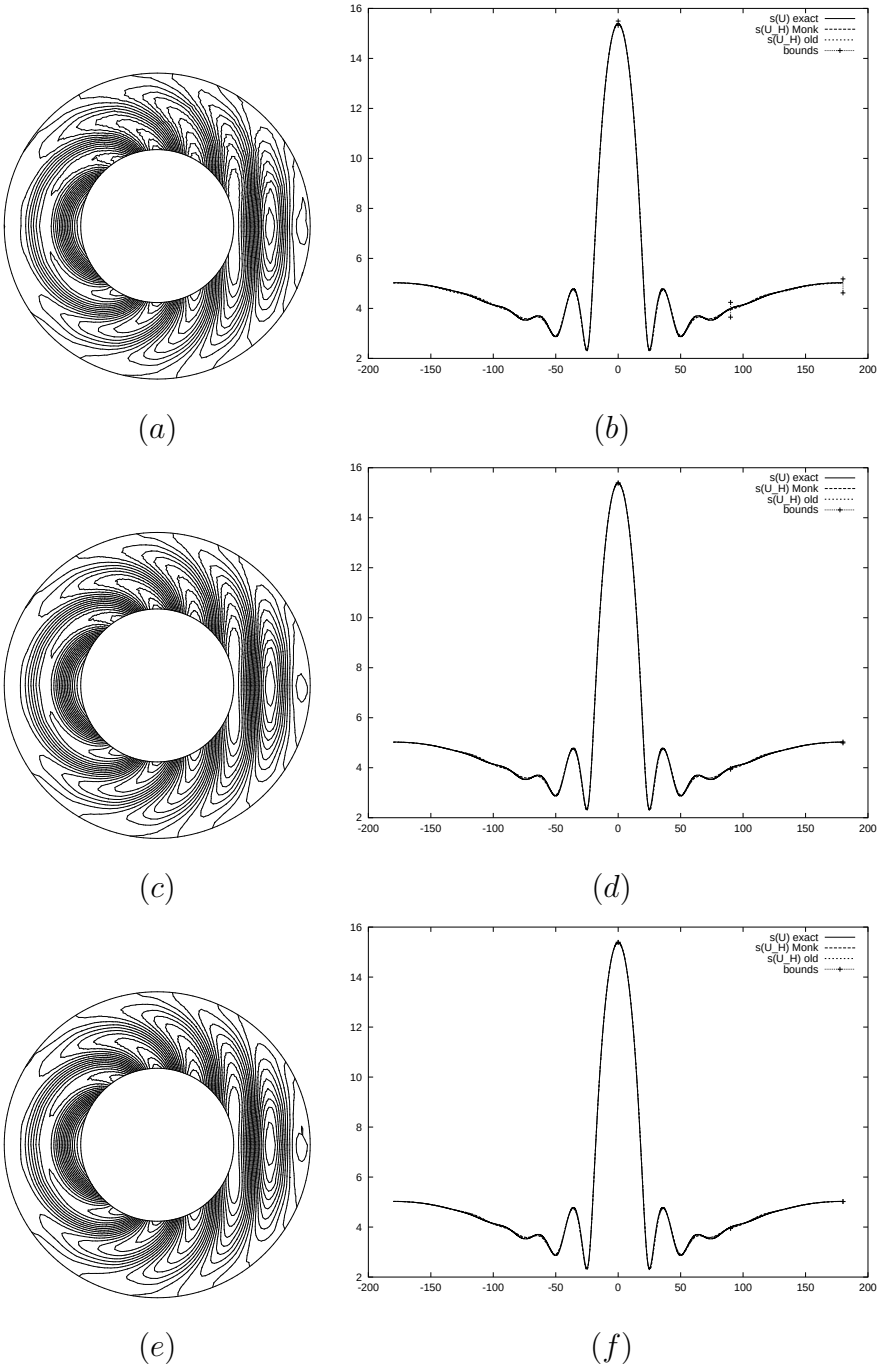

Figure 7.10: Scattering of a 2λ cylinder by a TM wave, showing bounds, scattering width distributions and contours for: (a) and (b), $p = 4$, (c) and (d), $p = 5$, and (e) and (f), $p = 6$

Chapter 8

Adaptive Procedures for Electromagnetic Scattering Problems

8.1 Introduction

This chapter describes adaptive procedures that can be used in conjunction with an error estimator to automatically improve the accuracy of a given solution. Here, the error estimator which was proposed in Chapter 7 is used to drive the adaptivity process. The chapter begins by presenting the basic adaptive algorithm, in which the magnitude of the local contributions to the bound gap are used to identify where to refine. In this chapter, two types of adaptive refinement are considered, viz. h–adaptive refinement, where the size of the elements in the mesh is locally reduced in an attempt to improve the accuracy of the solution, and p–adaptive refinement, where the order of the elements in the mesh is locally increased to improve the accuracy of the solution.

Adaptive refinement is often preferred to global refinement, due to the computational savings it offers. Therefore, for each adaptive refinement strategy a series of examples is used to indicate the savings in the number of unknowns that can obtained by employing an adaptive procedure.

8.2 Basic Adaptive Algorithm

The basic adaptive algorithm which is employed, to distinguish which elements should be flagged for refinement, is adapted from that presented by Ainsworth and Senior [48]. They introduce a parameter ϖ which is some measure of the error in a finite element solution, and let

$$\varpi = \sum_{k \in \Omega} \varpi_k \tag{8.1}$$

denote the sum of its elemental contributions. In addition, they prescribe a tolerance ς which dictates the level of accuracy required. Ainsworth and Senior then define their adaptive algorithm as

1. input $\varrho \in (0, 1)$ and $\varsigma > 0$. Set $X_0 = X_H$ and $i = 0$;
2. compute the Galerkin approximation $\boldsymbol{U}_H \in X_i$;
3. evaluate error estimators on each element: ϖ_k;
4. If $\varpi \leq \varsigma$ then
   (a) stop;

   else
   (a) refine all elements k' such that $\varpi_{k'} \geq \varrho \max_k \varpi_k$;
   (b) construct a new subspace X_{i+1}. Increment i. Goto step 2.

To implement this adaptive algorithm in the context of finite element bounds, we examine contributions to the bound gap Δ. To compute Δ, we subtract s^- from s^+ to obtain

$$s^+ - s^- = \kappa \mathcal{B}^s(\hat{\boldsymbol{e}}^+, \hat{\boldsymbol{e}}^+) + \kappa \mathcal{B}^s(\hat{\boldsymbol{e}}^-, \boldsymbol{e}^-) \tag{8.2}$$

Since

$$\hat{\boldsymbol{e}}^{\pm} = \hat{\boldsymbol{e}}^U \mp \frac{1}{\kappa} \hat{\boldsymbol{e}}^{\Psi} \tag{8.3}$$

this gives

$$s^+ - s^- = 2\kappa\mathcal{B}^s(\hat{\boldsymbol{e}}^U, \hat{\boldsymbol{e}}^U) + 2\frac{1}{\kappa}\mathcal{B}^s(\hat{\boldsymbol{e}}^\Psi, \boldsymbol{e}^\Psi) \tag{8.4}$$

which may be written as

$$s^+ - s^- = 2\Delta \tag{8.5}$$

In the adaptive procedure, ϖ is replaced by Δ and the elemental contributions to the bound gap are given by

$$\Delta_k = \kappa\mathcal{B}_k^s(\hat{\boldsymbol{e}}^U, \hat{\boldsymbol{e}}^U) + \frac{1}{\kappa}\mathcal{B}_k^s(\hat{\boldsymbol{e}}^\Psi, \boldsymbol{e}^\Psi) \tag{8.6}$$

so that

$$\Delta = \sum_{k\in\Omega} \Delta_k \tag{8.7}$$

The type of refinement may either be p–refinement, where the order of the elements is locally increased, or h–refinement, where the spacing of the elements is locally decreased. We end the adaptive refinement once the tolerance is achieved. Typically, we choose the tolerance as a small percentage of the working mesh solution, eg, $\varsigma = 0.05\mathcal{S}(\mathbf{U}_h; \phi)$.

8.3 p–Adaptivity

This section considers the case of p–adaptivity, where the magnitude of elemental contributions to the bound gap are used to drive an adaptive process in which the order of the elements is locally increased. Locally increasing the order of the elements might imply that the order on the interface of two neighbouring elements differs. Consider the case where two elements share an edge, with the left hand element of order p_l and the right hand element of order p_r. We will allow the order of the polynomial to vary on each local edge inside an element, as illustrated in Figure 8.1. However, initially we set the order of polynomial on each local edge to be the same as the interiors, so that $p_l^1 = p_l^2 = p_l^3 = p_l$ and $p_r^1 = p_r^2 = p_r^3 = p_r$. Then, to ensure continuity of the field across this elemental boundary, the technique of constrained approximation [11] is employed. Constrained approximation

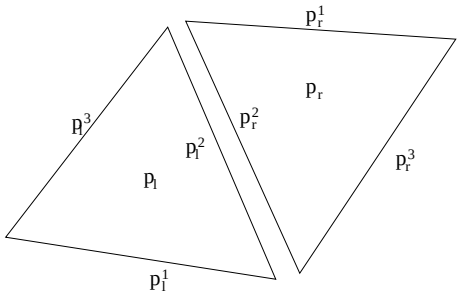

Figure 8.1: Two neighboring elements with local polynomial orders of p_l and p_r

in this context requires that the order of polynomial on the neighbouring edge to be $p_{edge} = \min\{p_l^2, p_r^2\}$. This means that the additional functions corresponding to the higher polynomial are not required to be assembled in the linear system, as they are taken to be zero. By applying this technique, to all elements which share an edge, the correct continuity of the field between neighbouring elements is obtained.

8.3.1 Numerical Examples

A series of numerical examples are undertaken to demonstrate the effectiveness of the algorithm. Here, we only consider examples which include a singularity. Scattering by circular cylinders is not considered as the adaptive process would simply indicate that refinements are required in each element in the mesh. A suitable candidate here is the scattering by a cylindrical cavity with a gap and infinitely thin PEC walls.

Illustrations of Adaptive p Distributions

The scattering of a TE wave by a cavity of electrical length 2λ with an aperture of 45 degrees is considered. An initial distribution of p, in which the dispersion is reduced to an acceptable level, is obtained by using the dispersion relationship given in Chapter 7 of this thesis. The truth mesh for this problem is selected as a distribution of uniform order $p = 8$ elements. The angle of interest is specified as $\phi = 0$. Using this initial data, the adaptive procedure is followed until the tolerance of $\varsigma = 0.1\mathcal{S}(\boldsymbol{U}_H^s; \phi)$ is reached. Figure 8.2 shows the distributions of p

which are produced by the adaptive algorithm. The initial distribution of p, shown in Figure 8.2 (a), contains elements of different order, due to the variation of mesh spacing across the computational domain. In Figure 8.2 (b)–(f), we observe that the adaptive algorithm automatically increases the order of the elements in the vicinity of the aperture of the cylindrical cavity. Once the singularities are resolved to the same degree as the truth mesh, the adaptive algorithm selects other elements for refinement.

The efficiency of the computational algorithm is considered in Figure 8.3. This figure compares the relative bound gap $(s^+ - s^-)/s_h$ with the number of unknowns for adaptive and uniform increments of p. We observe that, for the same accuracy, the adaptive procedure produces distributions which use less unknowns than the uniform distributions. Contours of $Re(H_z^s)$ and $Im(H_z^s)$ for the converged solution are shown in Figure 8.4. Alongside these contours, the RCS distributions obtained from the uniform and adaptive p solutions are shown. One can observe that the uniform and adaptive distributions are in excellent agreement.

Next, we consider the scattering of a TM wave by a cylindrical cavity of electrical length 2λ and aperture 20 degrees. The adaptive distributions of p are shown in Figure 8.5 and Figure 8.6. These figures illustrate how the adaptive algorithm first produces p–refinement in the neighbourhood of the singular points and then, once the discretisation is resolved to the same order as the truth mesh, refinement occurs elsewhere in the mesh. The convergence of the adaptive and uniform increments of p is shown in Figure 8.7. As in the TE case, a clear saving in the number of unknowns can be obtained by adopting the adaptive algorithm. For the converged solution, the computed contours of $Re(E_z^s)$ and $Im(E_z^s)$ are illustrated in Figure 8.8. In addition, Figure 8.8 also compares the final RCS distributions for the adaptive and uniform p calculations.

Electrically Large Objects

The aerospace community is interested in computation of scattering of waves by electrically large objects. For this reason, we examine the possibilities that adaptive

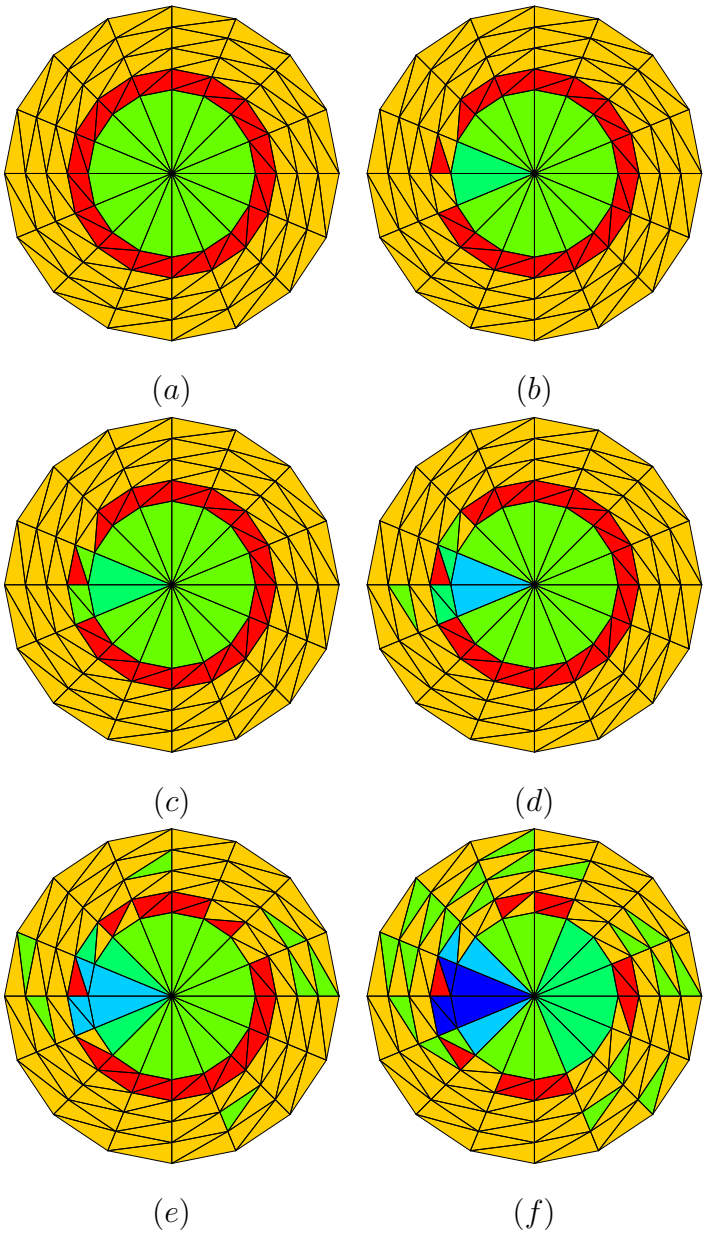

Figure 8.2: Scattering of a TE wave by a cylindrical cavity of electrical length 2λ showing the adaptive polynomial distributions:(a) initial distribution from dispersion relation, (b) first, (c) second, (d) third, (e) fourth and (f) fifth refinements when red is $p = 3$, yellow is $p = 4$, green is $p = 5$, dark green is $p = 6$, blue is $p = 7$ and dark blue is $p = 8$

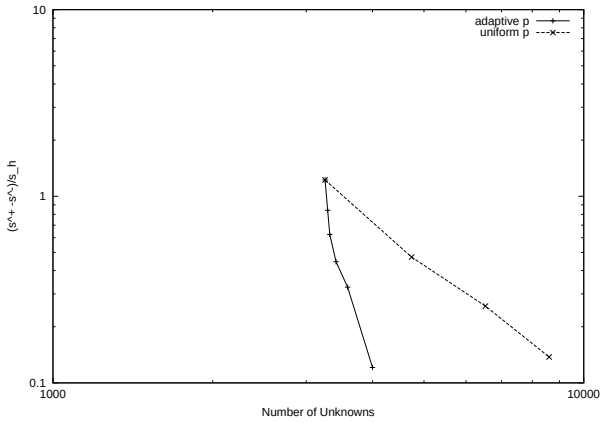

Figure 8.3: Scattering of a TE wave by a cylindrical cavity of electrical length 2λ: the convergence of the relative bound gap $(s^+ - s^-)/s_h$ with number of unknowns for $\phi = 0$ when uniform and adaptive p–refi nement strategies are employed

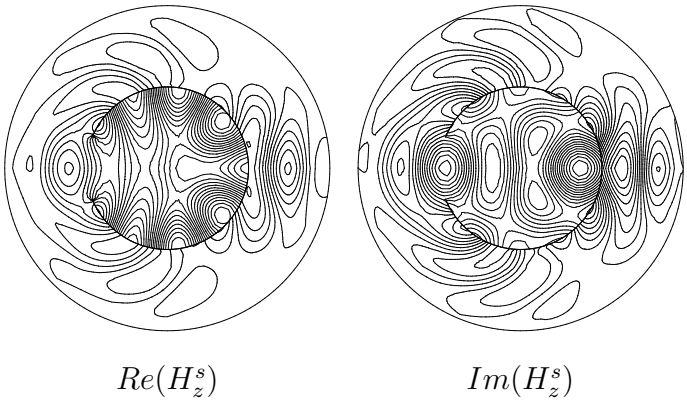

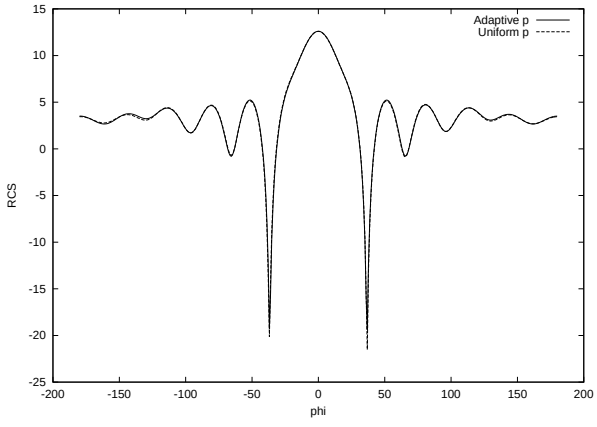

Figure 8.4: Scattering of a TE wave by a cylindrical cavity of electrical length 2λ: contours of $Re(H_z^s)$ and $Im(H_z^s)$ and the computed distribution of RCS for the converged solution

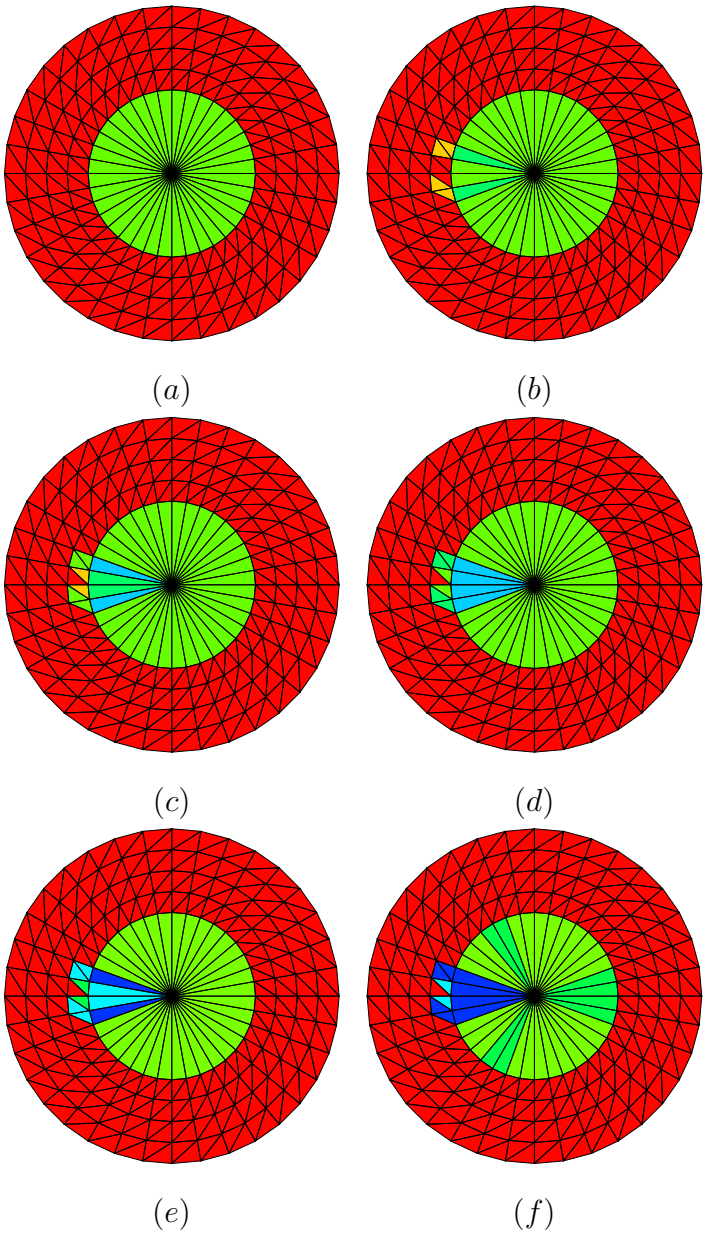

Figure 8.5: Scattering of a TM wave by a cylindrical cavity of electrical length 2λ showing the adaptive polynomial distributions:(a) initial distribution from dispersion relation, (b) first, (c) second, (d) third, (e) fourth and (f) fifth refinements when red is $p = 3$, yellow is $p = 4$, green is $p = 5$, dark green is $p = 6$, blue is $p = 7$ and dark blue is $p = 8$

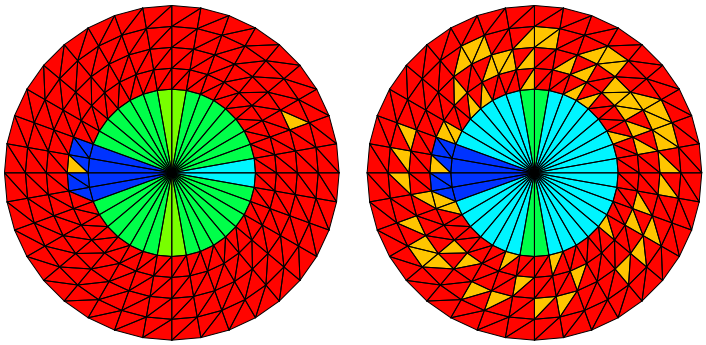

(a) (b)

Figure 8.6: Scattering of a TM wave by a cylindrical cavity of electrical length 2λ showing the adaptive polynomial distributions:(a) sixth and (b) seventh refinements when red is $p = 3$, yellow is $p = 4$, green is $p = 5$, dark green is $p = 6$, blue is $p = 7$ and dark blue is $p = 8$

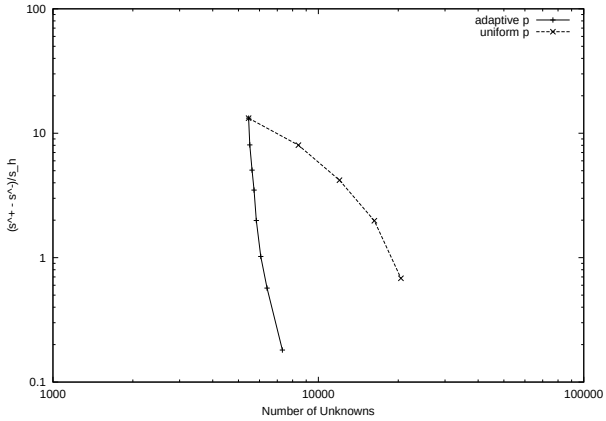

Figure 8.7: Scattering of a TM wave by a cylindrical cavity of electrical length 2λ: the convergence of the relative bound gap $(s^+ - s^-)/s_h$ with number of unknowns for $\phi = 180$ when uniform and adaptive p–refinement strategies are employed

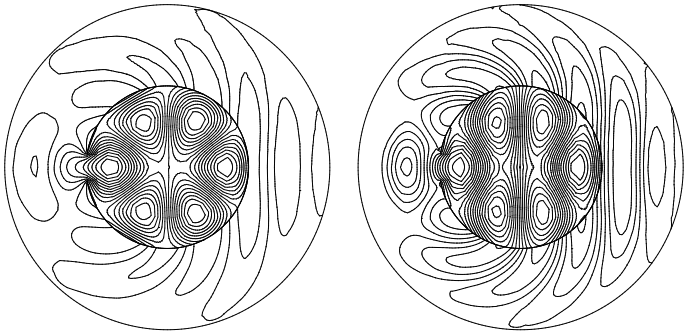

$Re(E_z^s)$ $Im(E_z^s)$

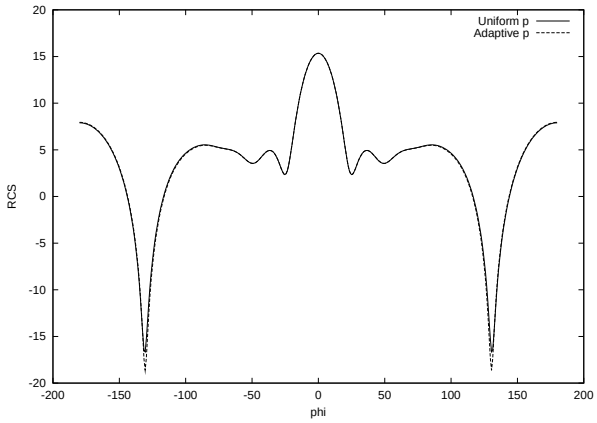

Figure 8.8: Scattering of a TM wave by a cylindrical cavity of electrical length 2λ: contours of $Re(E_z^s)$ and $Im(E_z^s)$ and the computed distribution of RCS for the converged solution

procedures offer for such examples. We consider the scattering of a TM wave by cylindrical cavities of electrical lengths 4λ, 8λ and 16λ, when the size of the aperture is 20 degrees. For each electrical length, we show the convergence of the relative bound gap with the number of unknowns. We compare the bound gap that is produced by an adaptive p procedure which begins on a coarse discretisation, an adaptive procedure which uses the dispersion relation and the case of uniform polynomial refinement. In all cases, the adaptive procedure is terminated when the tolerance of $\varsigma = 0.01\mathcal{S}(\boldsymbol{U};\phi)$ is reached for the specified angle of $\phi = 0$. Finally, we provide RCS distributions and contour plots for the converged solution.

Starting with the 4λ case, Figure 8.9 shows the convergence of the relative bound gap for the different adaptive strategies. The truth discretisation for this problem employs $p = 8$ elements. When an adaptive p procedure is initiated on a coarse discretisation, it initially follows the same convergence path as a uniform p–refinement curve. Then, at a certain point, the curves diverge and henceforth the adaptive p procedure produces solutions of the same accuracy for less unknowns. We emphasize that the bounds we obtain in these calculation always bound the true solution. On very coarse discretisations the bounds are quantitatively very large. However, as the discretisations becomes finer, the bound gap decreases. When the dispersion relation is employed, the initial discretisation is good and therefore requires less adaptions to reach the desired tolerance. Indeed, the 19640 unknowns which are required for final adaptive p–refinement is very similar to 20611 unknowns which are required for the final adaption when the dispersion relation is employed. Contours of the computed solution and the converged RCS are shown in Figure 8.10.

We now consider the scattering of a TM wave by an 8λ cavity. For this case, Figure 8.11 shows the convergence of the relative bound gap for the selection of adaptive strategies where the truth discretisation for this problem has been selected as $p = 10$ elements. In Figure 8.11, we observe that, when an adaptive p strategy is initiated on a very coarse discretisation, it first behaves rather erratically with the relative bound gap decreasing and then increasing again. However, following a few

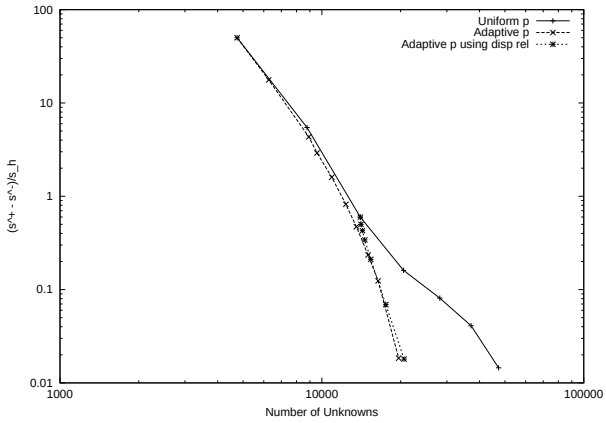

Figure 8.9: Scattering of a TM wave by a cylindrical cavity of electrical length 4λ: the convergence of the relative bound gap $(s^+ - s^-)/s_h$ with number of unknowns for $\phi = 0$ when uniform and adaptive p–refi nement strategies are employed

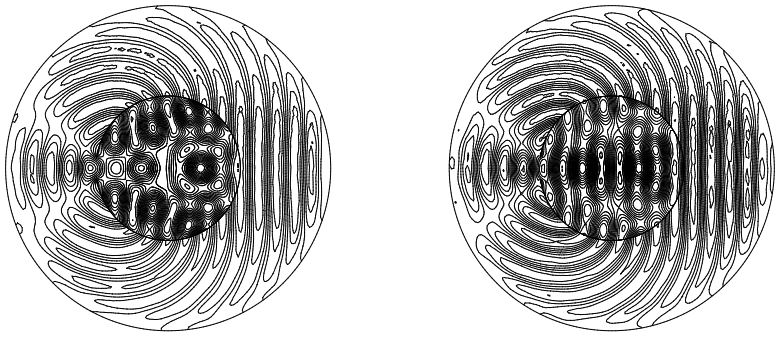

$Re(E_z^s)$ $Im(E_z^s)$

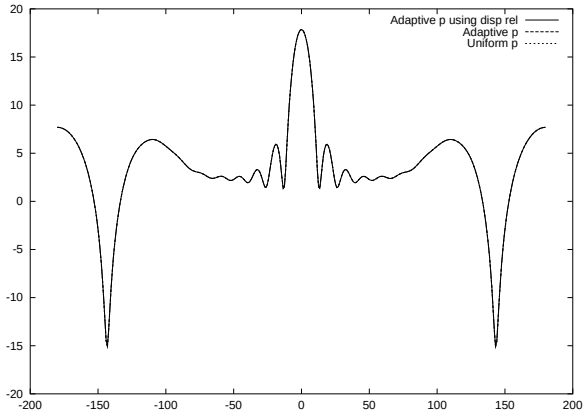

Figure 8.10: Scattering of a TM wave by a cylindrical cavity of electrical length 4λ: contours of $Re(E_z^s)$ and $Im(E_z^s)$ and the computed distribution of RCS for the converged solution

more refinement steps, the procedure settles down and produces a solution which requires less unknowns than uniform refinement. When the dispersion relationship is employed to generate an initial p distribution, the convergence is rapid and without oscillation. As in the 4λ case, the number of unknowns used in the two adaptive procedures is very similar. Contours of the computed solution and the converged RCS are shown in Figure 8.12.

Finally, we consider the scattering of a TM wave by a 16λ cavity. For this case, Figure 8.13 shows the convergence of the relative bound gap. The truth discretisation for this problem is $p = 14$ elements. When an adaptive p strategy is initiated on a coarse discretisation, the convergence behaviour is very erratic and is characterised by wild increases and decreases in the size of the bound gap. After 15 adaptive steps, no convergence is obtained and therefore this adaptive strategy is stopped. When uniform increments in p are adopted the solution convergence is uniform throughout. Following an adaptive p strategy which uses the dispersion relationship to obtain an initial distribution of $p = 10$ elements, we observe that the solutions produced require less unknowns than the uniform p strategy. Therefore, for large electrical lengths it is essential that the dispersion relationship is used to create a meaningful starting point for the adaptive procedure. To complete the 16λ example we show the contours of $Re(E_z^s)$ and $Im(E_z^s)$ and plot the distribution of the RCS in Figure 8.14.

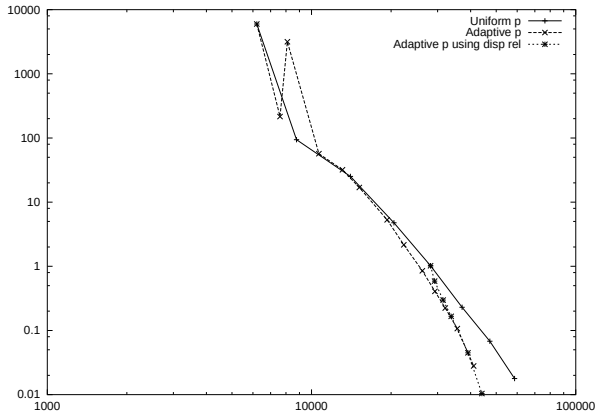

Figure 8.11: Scattering of a TM wave by a cylindrical cavity of electrical length 8λ: the convergence of the relative bound gap $(s^+ - s^-)/s_h$ with number of unknowns for $\phi = 0$ when uniform and adaptive p–refi nement strategies are employed

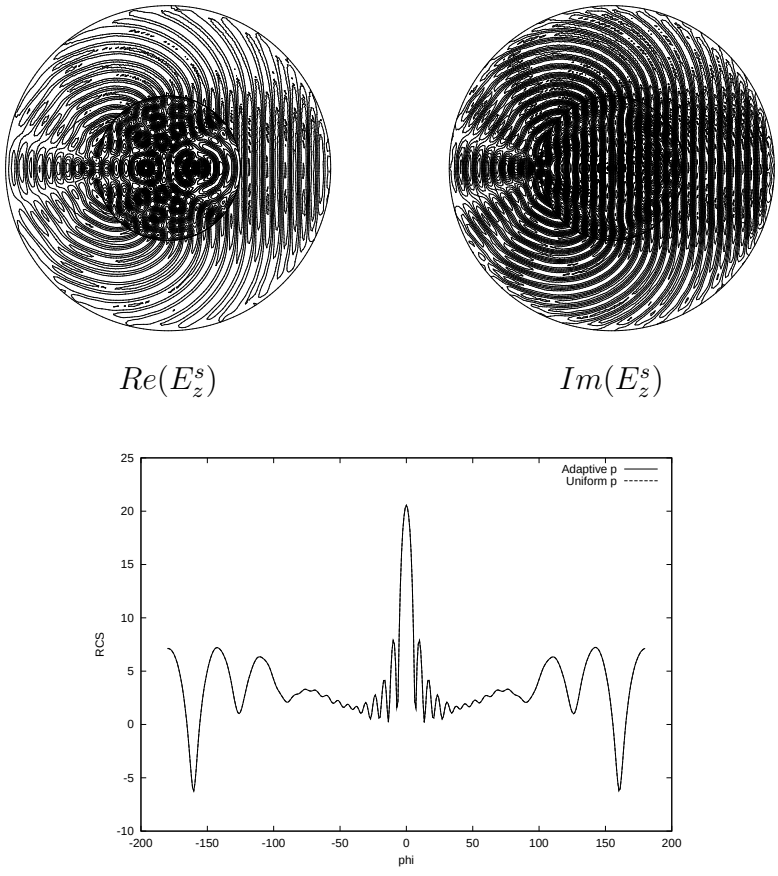

Figure 8.12: Scattering of a TM wave by a cylindrical cavity of electrical length 8λ: contours of $Re(E_z^s)$ and $Im(E_z^s)$ and the computed distribution of RCS for the converged solution

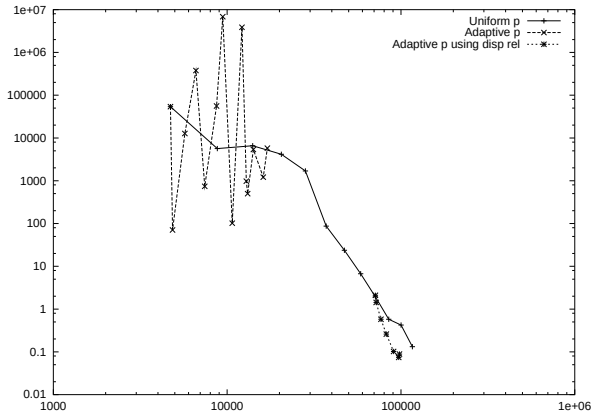

Figure 8.13: Scattering of a TM wave by a cylindrical cavity of electrical length 16λ: the convergence of the relative bound gap $(s^+ - s^-)/s_h$ with number of unknowns for $\phi = 0$ when uniform and adaptive p–refi nement strategies are employed

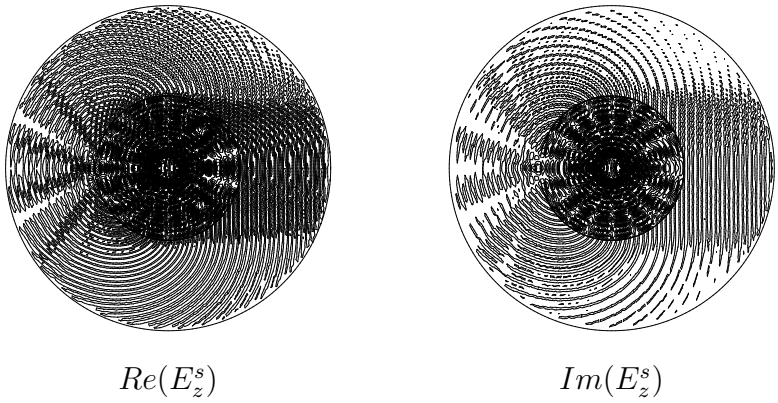

$Re(E_z^s)$ $Im(E_z^s)$

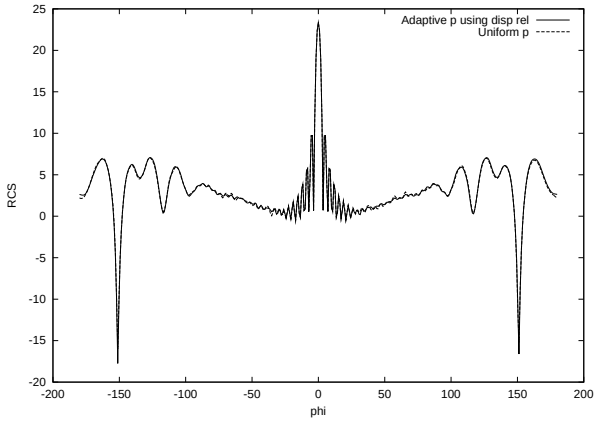

Figure 8.14: Scattering of a TM wave by a cylindrical cavity of electrical length 16λ: contours of $Re(E_z^s)$ and $Im(E_z^s)$ and the computed distribution of RCS for the converged solution

8.4 h-Adaptivity

This section considers using an adaptive process to locally refine the spacing in the mesh. A number of approaches for locally refining a mesh exist in the finite element literature. The first, and perhaps the most obvious, is to regenerate the whole mesh with smaller spacings in the vicinity of elements flagged for refinement. For small meshes this can easily be accomplished, however, for larger meshes the approach becomes expensive. Another approach considers allowing hanging nodes, which are constructions where a node does not have a full set of connectivities and is simply left hanging on an adjacent edge. This approach involves a simple subdivision of flagged triangular and quadrilateral elements in to 4 sub elements, but has the disadvantage that it requires a solver which is capable of catering for the hanging nodes. The final approach is the one considered in this section, and uses the local subdivision of flagged elements and their direct neighbours so that no hanging nodes are produced. By careful subdivision of elements in the vicinity of a flagged element, the resulting elements are of a good quality and for this reason this approach is adopted here.

We restrict ourselves to refining meshes of triangular elements. The initial mesh may be structured or unstructured in nature, but the resulting mesh is always unstructured. We also restrict h-refinement to a region outside the PML, as refining the structured PML layer would destroy the structured mapping which is employed there to determine the level of absorption. The actual triangular mesh splitting algorithm which is employed has been developed from the ideas presented in [53]. Below, we present the general algorithm.

1. all those elements which are flagged for refinement are split in to 4 sub–elements (Figure 8.15);

2. determine the number of elements with 3 hanging nodes;

3. split elements with 3 hanging nodes in to 4 sub–elements (Figure 8.16);

4. determine the number of elements with 2 hanging nodes;

5. if there are elements with 2 hanging nodes then

   (a) if the longest edge does not have a hanging node then

      i. split each of these elements in to 4 sub–elements (Figure 8.17 (a));

      ii. goto step 2;

   else

      i. split each of these elements in to 3 sub–elements (Figure 8.17 (b));

      ii. goto step 2;

6. determine the number of elements with 1 hanging node;

7. if there are elements with 1 hanging node then

   (a) if the hanging node is on the longest edge then

      i. split each of these elements in to 2 sub–elements (Figure 8.18 (a));

      ii. goto step 2;

   else

      i. split these elements in to 3 sub–elements (Figure 8.18 (b));

      ii. goto step 2;

8. if no hanging nodes exist stop.

The essential point of the algorithm is always to split the longest edge of an element.

8.4.1 Numerical Examples

It would been of interest to compare the performance of h–adaptivity directly with the adaptive p examples shown previously. However, the several draw backs to doing this. Firstly, it is impossible to ensure that the truth mesh that is chosen for the adaptive p–refinement case is the same as the truth mesh for the adaptive

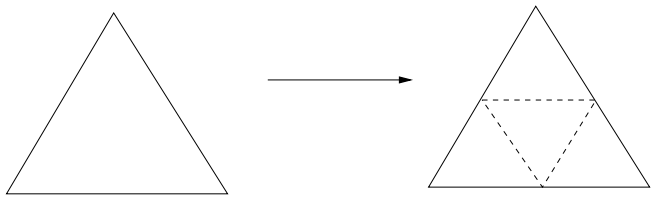

Figure 8.15: Splitting of a triangular element in to 4 sub elements.

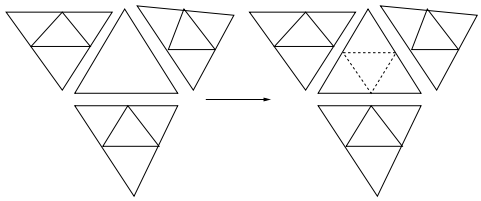

Figure 8.16: Splitting of a triangular element with 3 hanging nodes in to 4 sub elements.

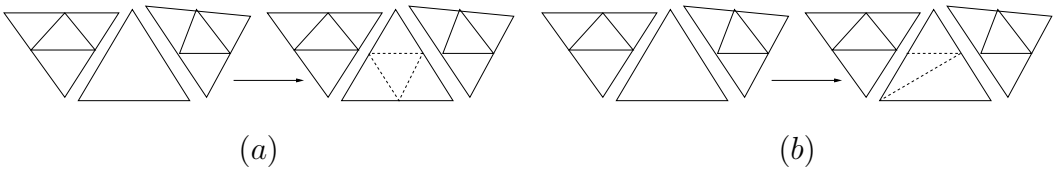

(a) (b)

Figure 8.17: Splitting of a triangular element with 2 hanging nodes in to:(a) 4 sub elements and (b) 3 sub elements.

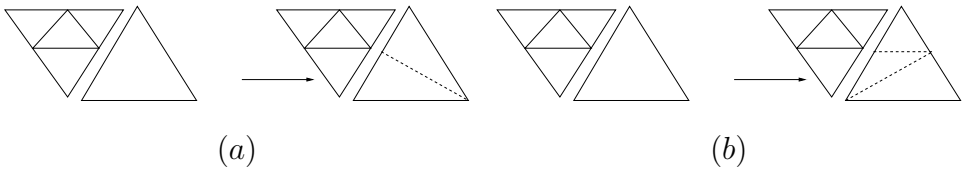

(a) (b)

Figure 8.18: Splitting of a triangular element with 1 hanging node in to:(a) 2 sub elements and (b) 3 sub elements.

h–refinement case. This is because the truth mesh for the adaptive p–refinement involves using a higher polynomial order and fixed mesh and adaptive h–refinement involves using a fixed order and refining the mesh spacing. Secondly, the structured meshes employed for the adaptive p examples are not of sufficient quality to enable continued element splitting. When using a mesh splitting algorithm it is better to begin with an unstructured mesh where all elements are of a reasonable quality.

We therefore choose examples in which an unstructured mesh generator is used to generate the initial mesh of triangles. Following the approach given in Chapter 6, we attach a structured layer of quadrilaterals to apply the PML condition and produce a hybrid mesh.

The first example we choose is the scattering of a TE wave by a U shaped cavity which has been rotated through 90 degrees. The general dimensions of this cavity have been presented in Chapter 6, here we consider the case where $t = 0.2\lambda = 0.2$, $b = 4\lambda = 0.4$ and $c = 2\lambda = 1$. Specifically our interest lies with the evaluation of $\mathcal{S}(\boldsymbol{U};\phi)$ to a tolerance of $\varsigma = 0.03\mathcal{S}(\boldsymbol{U};\phi)$ when the angle of interest is specified as $\phi = 0$. Figure 8.19 (a)–(e) shows the series of adaptive meshes that were produced in the calculation. The initial mesh of 44 quadrilateral and 407 triangles is shown in Figure 8.19 (a) and the dispersion relation indicates that uniform order $p = 3$ elements are required to reduce the effects of dispersions to an acceptable level. The adaptive meshes shown in Figure 8.19 (b)–(e) illustrate how the error estimator has flagged elements close to the singular points for refinement. Elements are refined around this region until the truth spacing of $h = 0.1$ is reached. Figure 8.20 shows the computed relative bound gap against number of unknowns for the adaptive and uniform h–refinements. In this figure, it is observed that employing the adaptive h–refinement procedure requires less unknowns than the uniform h–refinement procedure. Contours of the converged solution alongside the computed RCS distribution can be found in Figure 8.21. In particular, the RCS distributions given by adaptive and uniform h–refinement are found to be in excellent agreement.

As a further example, we consider the scattering of waves from a PEC square which is of infinite extent in the z direction and of electrical length 2λ. The scat-

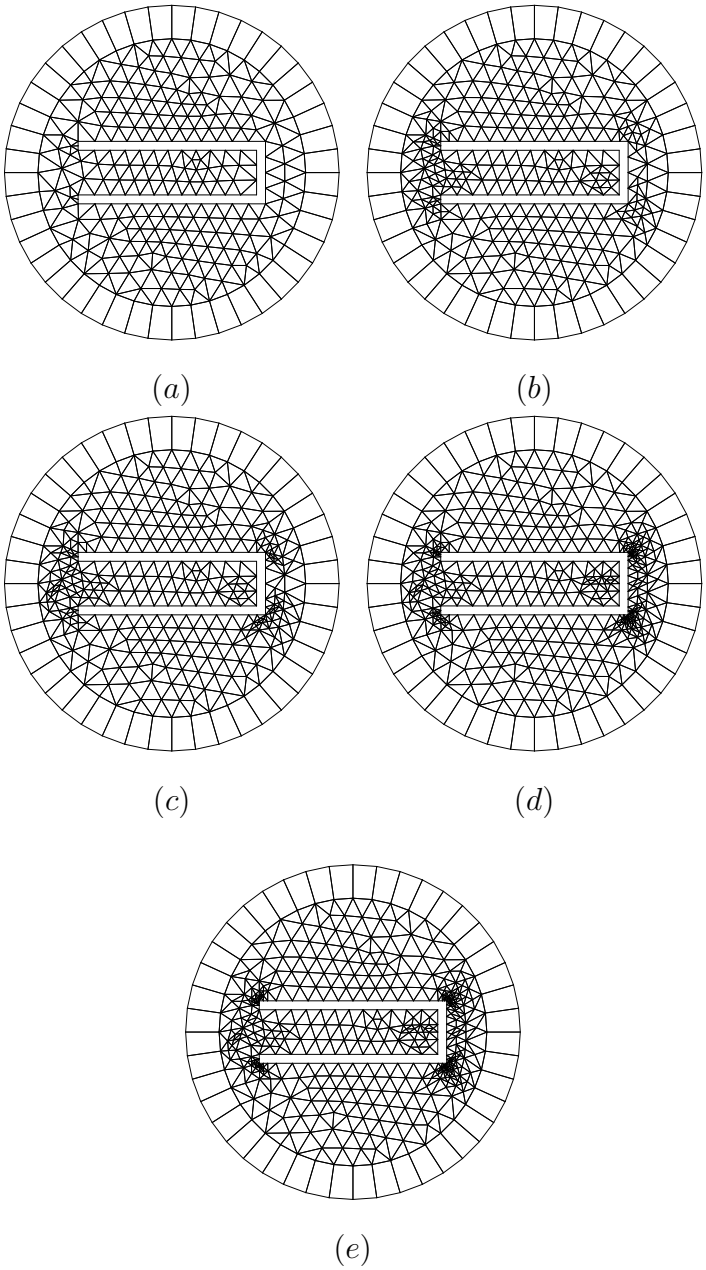

Figure 8.19: Scattering of a TE wave by a cavity of electrical length 4λ showing the adaptive meshes:(a) initial mesh, (b) first, (c) second, (d) third, (e) fourth mesh refinements

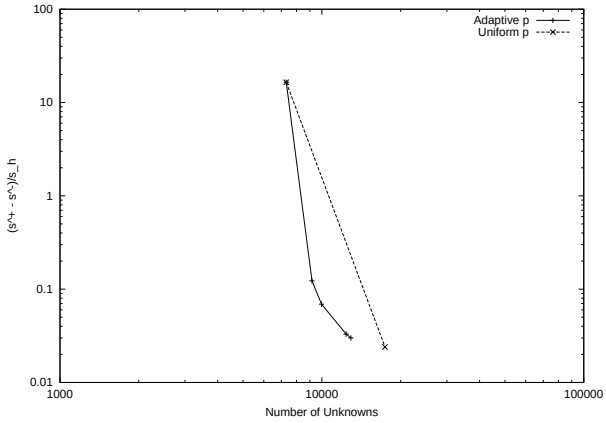

Figure 8.20: Scattering of a TE wave cavity of electrical length 4λ: convergence of the relative bound gap $(s^+ - s^-)/s_h$ with number of unknowns for $\phi = 0$ when uniform and adaptive h–refi nement strategies are employed.

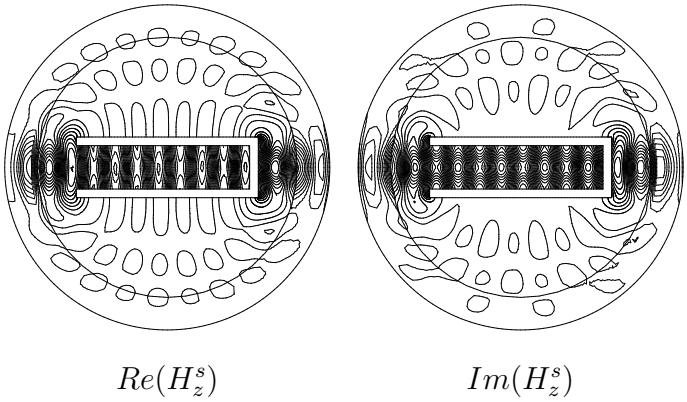

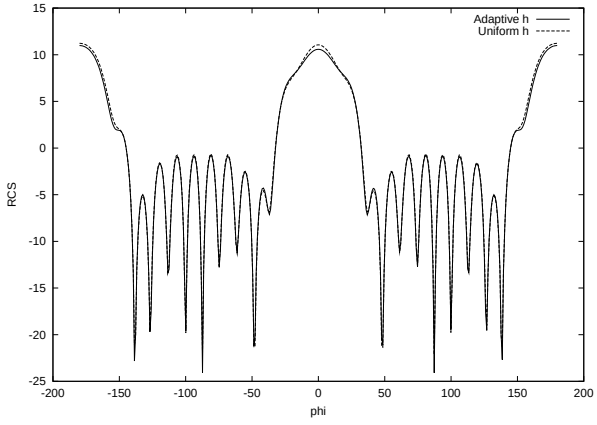

Figure 8.21: Scattering of a TE wave cavity of electrical length 4λ: contours of $Re(H_z^s)$ and $Im(H_z^s)$ and the computed distribution of RCS for the converged solution

tering of a TE wave is first considered, and an initial hybrid mesh of 88 quadrilateral elements and 224 triangular elements is generated. Using the dispersion relationship, we obtain that $p = 3$ elements are sufficient to reduce the effects of dispersion to an acceptable level. Using these elements, and an adaptive bounds procedure in which the spacing on the truth mesh is $h = 0.03$ and the tolerance is $\varsigma = 0.03\mathcal{S}(\boldsymbol{U}; \phi)$ for the specific angle of $\phi = 0$, the sequence of adaptive meshes shown in Figure 8.22 (a)–(d) is created. In this figure, it is evident that the adaptive algorithm has flagged elements in the regions surrounding the two corners of the PEC square where $x = 0$. At these regions, discontinuities in $\boldsymbol{n} \wedge \boldsymbol{U}^i$ are known to exist. However, discontinuities do not exist at the locations with $y = 0$ as the change in the sign of the y component of the normal does not effect $\boldsymbol{n} \wedge \boldsymbol{U}^i$ for an angle of incidence of $\theta = 0$. Unfortunately, no saving in the number of unknowns computed given by uniform h–refinement was found for this case. A possible explanation for this is the large number of additional elements that are required to be split to resolve the hanging nodes. We compare the RCS distribution computed on the final adaptive mesh with the distribution given by uniform h–refinement and the solution given by a finite difference, time domain (FDTD) algorithm [8]. This comparison can be found in Figure 8.23. Here, we observe close agreement between the three solutions. To complete the example, contours of $Re(H_z^s)$ and $Im(H_z^s)$ are given in Figure 8.23.

The scattering of a TM wave by a PEC square of electrical length 2λ is now considered. For this example, the mesh of 88 quadrilaterals and 224 triangular elements used in the previous TE example is employed to initiate the bound procedure. Following an adaptive procedure, in which the truth spacing is $h = 0.03$ and the tolerance is $\varsigma = 0.03\mathcal{S}(\boldsymbol{U}; \phi)$ for the specific angle of $\phi = 0$, leads to the sequence of adaptive meshes shown in Figure 8.24. In these meshes, we observe that the adaptive refinement procedure has flagged elements in regions adjacent to all four corners of the square. At these locations, discontinuities in $\boldsymbol{n} \wedge \text{curl}\, \boldsymbol{U}^i$ are known to exist. As in the TE case, no saving in the number of unknowns computed given by uniform h–refinement was found for this case. We compare the RCS distribution

computed on the final adaptive mesh with a the case of uniform h–refinement and the solution given by a finite difference, time domain algorithm. This comparison can be found in Figure 8.25 and, as in the TE case we observe good agreement between the three solutions. To complete the example, contours of $Re(E_z^s)$ and $Im(E_z^s)$ are given in Figure 8.25.

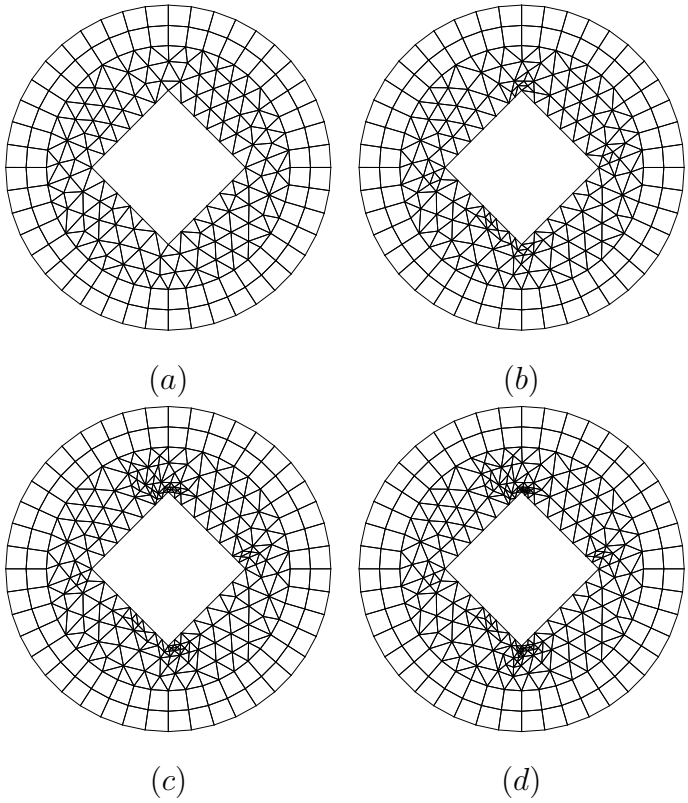

Figure 8.22: Scattering of a TE wave by a PEC square of electrical length 2λ showing the adaptive meshes:(a) initial mesh, (b) first, (c) second and (d) third mesh refinements

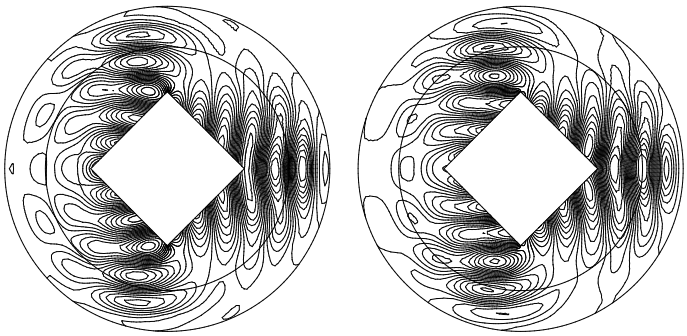

$Re(H_z^s)$ $Im(H_z^s)$

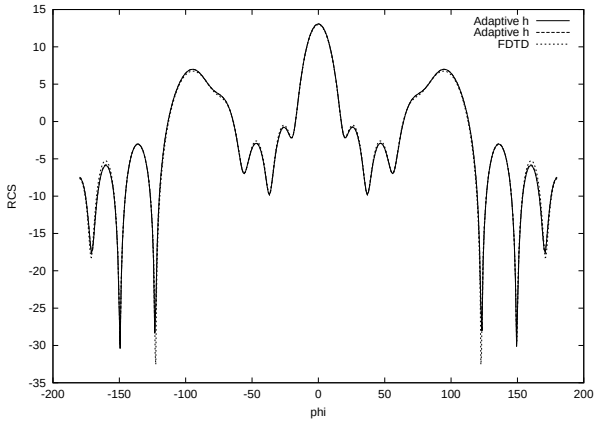

Figure 8.23: Scattering of a TE wave by a PEC square of electrical length 2λ: contours of $Re(H_z^s)$ and $Im(H_z^s)$ and the computed distribution of RCS for the converged solution

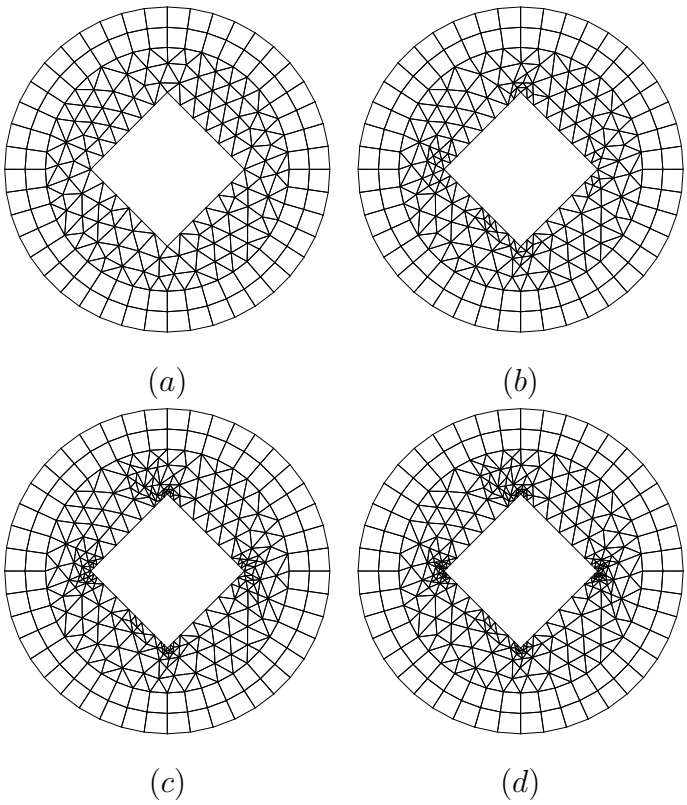

Figure 8.24: Scattering of a TM wave by a PEC square of electrical length 2λ showing the adaptive meshes:(a) initial mesh, (b) first, (c) second and (d) third mesh refinements

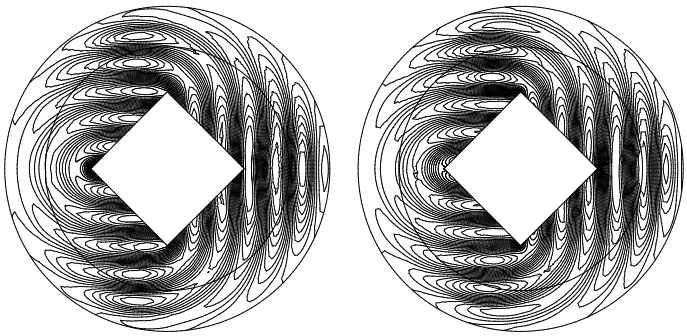

$Re(E_z^s)$ $Im(E_z^s)$

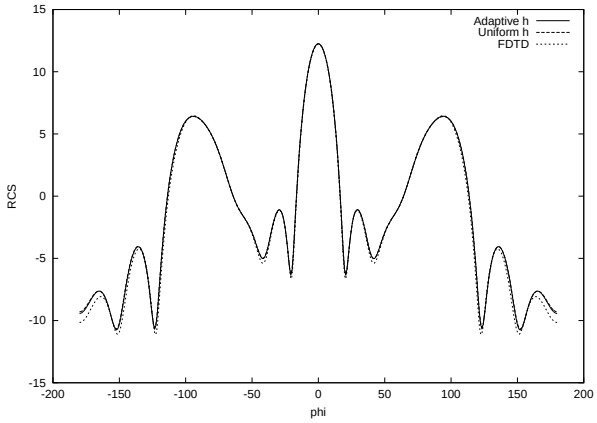

Figure 8.25: Scattering of a TM wave by a PEC square of electrical length 2λ: contours of $Re(E_z^s)$ and $Im(E_z^s)$ and the computed distribution of RCS for the converged solution

Chapter 9

Conclusion and Future Work

The aim of this work was to develop a new adaptive finite element procedure for two dimensional electromagnetic scattering problems. It is felt that this objective has been successfully achieved, with a number of additional observations made through the course of the work. The evidence for this, is illustrated by examining the achievements of each of the chapters contained within the work.

Following the work of Kikuchi [29] and Demkowicz [9, 10, 11, 7] a variational formulation was presented that correctly enforced the divergence condition. Using this scheme ensures that the resulting solutions are free of spurious modes. To discretise this variational statement we showed how to numerically implement the higher order elements of Ainsworth and Coyle [37]. We also gave details of how different geometry approximation schemes could be adopted to improve the accuracy of the scheme. The computational efficiency of the implementation was shown to be improved by adopting static condensation to eliminate the large number of interior degrees of freedom. It was observed that when a Cuthill–McKee algorithm [45] is employed to renumber the edges, the bandwidth of the resulting linear system was reduced.

For a model problem, the convergence of triangular and quadrilateral edge elements was investigated numerically. It was observed that for a smoothly varying field, a uniform polynomial distribution and decreasing mesh spacing results in a algebraic rate of convergence. Conversely, a fixed mesh spacing and increasing

polynomial order leads to an exponential convergence rate. Using the same model problem, the dispersive effects of the edge element implementation were investigated. It was shown that, increases in the order of the approximation to control the effects of dispersion were more beneficial than refining the mesh. For meshes of quadrilateral and triangular elements, a large reduction in the number of unknowns was observed.

A successful implementation of the edge elements of Ainsworth and Coyle [37] coupled with a PML far field boundary technique enabled the solution of a variety of scattering problems in two dimensions. Further efficiency of the computational algorithm, for large electrical lengths was seen for the coupled PML/ABC technique in which the far field boundary can be brought closer to the scatterer. For the scattering problems, contours of the scattered field were plotted and distributions of scattering width output were given. Validation of the scheme was carried out by comparing computed scattering width distributions to known analytical solutions for a series of cylindrical scatterers. The predictive capability of method was shown by considering a number of scatterers which do not admit exact analytical solutions. In all cases, keeping the mesh fixed and using a uniform increase in polynomial order was seen to lead to a fast convergence of the solution.

It was observed that to ensure a mesh independent solution one should adopt the blending function method for geometry representation. By using this method, one ensures that the true geometry of the scatterer is preserved and hence that the correct converged solution is achieved. It was observed that, using a coarse linear representation of the geometry for large electrical lengths can lead to an incorrect solution of the scattering problem.

A refinement strategy in which the order of approximation was increased and the mesh spacing kept fixed was seen to be superior to fixing the order and refining the mesh. This superiority was observed for the scattering of circular cylinder where it was observed that for the same number of unknowns the refinement of the polynomial order produced a more accurate solution than refinement of the mesh.

An error bound estimation procedure was derived. It was shown that the method

is capable of producing quantitative bounds on non–linear outputs of the electromagnetic scattering problem. Specifically, the error bound procedure was applied to the non–linear scattering width output at a number of distinct locations. To illustrate the method, a number of numerical examples were considered in which error bounds were evaluated, these consisted of meshes of quadrilateral and triangular elements employing both h– and p–refinement strategies. It was observed in all cases, that refinement of the discretisations leads to smaller bounds. In addition, it was found that using a p–refinement strategy led to a rapid rate of convergence for the bound gap. The computed bounds were compared to the true error for a problem with a known analytical solution. Here, it was observed that the bound gaps tend to zero when the solution becomes sufficiently smooth.

During the computational experiments for the error analysis, the use of the dispersion relationship of Ainsworth and Coyle [37] was proposed for computing an initial distribution of p. This was seen to reduce the number of refinement stages that are required to obtain the final computational solution. In addition, the use of Monk's [62, 63, 64] alternative technique to evaluate the scattering width distribution also produces an accurate output which is in good agreement with the previous approach [38].

The discretisation was adaptively refined in an attempt to obtain better accuracy in the scattering width distributions. It was observed that when using an adaptive p technique, it is possible to produce solutions which require less unknowns than those required for uniform refinement. Only in extreme cases, when a very coarse initial discretisation was employed, was it found that the error estimator provided a false indication of where refinement should take place. To overcome this problem, the dispersion relation can be employed to generate an initial polynomial distribution from which adaptive refinement can follow. In all cases, the scattering width distributions produced by adaptive and uniform p–refinements were in very close agreement.

When employing adaptive h–refinement techniques, the reduction in number of unknowns was less substantial. This is in part due to the large number of ad-

ditional elements which are created to remove any hanging nodes from the mesh. However, as in the case of adaptive p–refinement, the scattering width distributions for adaptive h–refinement were in close agreement with those produced by uniform refinement. It is therefore clear, that the adaptive p technique coupled with an discretisation generated by the dispersion relationship is superior to the h–adaptive technique for the adaptive refinement of scattering problems. This is with one exception. When large elements are combined with a high p, it may also be desirable to employ a graded mesh, in which the spacing is reduced in the vicinity of singular points, so as to localise their effects.

To sum up, an implementation of Ainsworth and Coyles [37] higher order edge elements has been successfully implemented for electromagnetic scattering problems in two dimensions. The use of a curvilinear PML far field technique with the option of coupling to an ABC has enabled close placement of the farfield boundary over a large range of electrical lengths and the derivation of the error estimation technique has enabled strict quantitative bounds to be placed on the scattering width output. Using these techniques, aerospace engineers can now compute accurate solutions for large electrical length problems with confidence. They will now be able to iterate refinements until the desired tolerance is achieved on the scattering width output.

9.1 Future Work

There is still much scope for future work in this project. One aspect which is of great interest to industry is the extension of the technique to three dimensional problems. This would require an extension of the current set of two dimensional basis functions proposed by Ainsworth and Coyle and with larger problem sizes envisaged in 3 dimensions an efficient iterative solver would also be required.

Another aspect of the work which has shown great promise, is the work of error bound evaluation. In this work, we focused on the evaluation of bounds at a number of specified locations. A future extension to this work, would be to implement a

lower order modeling technique so that bounds could be obtained for the complete spectrum of angles. In this way, one could obtain an error envelope in which one could predict the region in which the true scattering width distribution exists. Another extension of the work would be to apply the error estimation technique to a different computational output in electromagnetics.

Finally, an extension of the current adaptive technique could be undertaken so that simultaneous adaptive refinement of both h and p is automated. A method for determining whether an element's spacing should be reduced or polynomial order increased has been proposed by Ainsworth and Senior [48]. However, their method would be difficult to combine with the scheme proposed in this thesis, as it requires the generation of two distinct truth discretisations. A combined h– and p–adaptive strategy would have to address this issue to become successful.

Appendix A

Mixed Formulation for Scattering Problems

The purpose of this appendix is to show that a mixed formulation is not required for scattering problems in which ω is specified. To do this, we first examine the spaces

$$Z^D = \{\boldsymbol{u} \,|\, \boldsymbol{u} \in \mathcal{H}(\text{curl}; \Omega);\ \boldsymbol{n} \wedge \boldsymbol{u} = -\boldsymbol{n} \wedge \boldsymbol{U}^i \text{ on } \Gamma_2;\ \boldsymbol{n} \wedge \boldsymbol{u} = \boldsymbol{0} \text{ on } \Gamma_3\} \quad \text{(A.1)}$$

$$Z = \{\boldsymbol{u} \,|\, \boldsymbol{u} \in \mathcal{H}(\text{curl}; \Omega);\ \boldsymbol{n} \wedge \boldsymbol{u} = \boldsymbol{0} \text{ on } \Gamma_2,\ \boldsymbol{n} \wedge \boldsymbol{u} = \boldsymbol{0} \text{ on } \Gamma_3\} \quad \text{(A.2)}$$

which were given in Chapter 5. Here it was also shown that a weak variational formulation of the problem is: find $\boldsymbol{U}^s \in Z^D$, such that

$$\begin{aligned}\int_{\Omega_f+\Omega_p+\Omega_d} \left(\boldsymbol{\Lambda}_1^{-1}\text{curl}\,\boldsymbol{U}^s \cdot \text{curl}\,\overline{\boldsymbol{W}} - \omega^2 \boldsymbol{\Lambda}_2 \boldsymbol{U}^s \cdot \overline{\boldsymbol{W}}\right) \mathrm{d}\Omega = \\ - \int_{\Gamma_1} \left(\boldsymbol{n} \wedge \boldsymbol{\Lambda}_1^{-1}\text{curl}\,\boldsymbol{U}^s\right) \cdot \overline{\boldsymbol{W}}\, \mathrm{d}\Gamma \\ - \left\{ \int_{\Omega_d} \left(\boldsymbol{\Lambda}_1^{-1} - \boldsymbol{I}\right) \text{curl}\,\boldsymbol{U}^i \cdot \text{curl}\,\overline{\boldsymbol{W}} - \omega^2 \left(\boldsymbol{\Lambda}_2 - \boldsymbol{I}\right) \boldsymbol{U}^i \cdot \overline{\boldsymbol{W}}\, \mathrm{d}\Omega \right\}\end{aligned} \quad \text{(A.3)}$$

for all $\boldsymbol{W}$ in Z. Following the approach outlined in Chapter 2, a mixed variational statement is obtained by substituting $\boldsymbol{W} = \text{grad}\, q$ in to equation (A.3) to give

$$\begin{aligned}-\omega^2 \int_{\Omega_f+\Omega_p+\Omega_d} (\boldsymbol{\Lambda}_2 \boldsymbol{U}^s \cdot \text{grad}\,\overline{q})\, \mathrm{d}\Omega = - \int_{\Gamma_1} \left(\boldsymbol{n} \wedge \boldsymbol{\Lambda}_1^{-1}\text{curl}\,\boldsymbol{U}^s\right) \cdot \text{grad}\,\overline{q}\, \mathrm{d}\Gamma \\ + \omega^2 \int_{\Omega_d} \left(\boldsymbol{\Lambda}_2 - \boldsymbol{I}\right) \boldsymbol{U}^i \cdot \text{grad}\,\overline{q}\, \mathrm{d}\Omega\end{aligned} \quad \text{(A.4)}$$

By replacing $\boldsymbol{U}^s$ by $\boldsymbol{U}^s + \operatorname{grad} p$ we obtain the mixed form: find $\boldsymbol{U}^s \in Z_D$ and $p \in \{\mathcal{H}^1, p = 0 \text{ on } \Gamma_2 \text{ and } \Gamma_3\}$ such that

$$\begin{aligned}\int_{\Omega_f+\Omega_p+\Omega_d} \left(\boldsymbol{\Lambda}_1^{-1}\operatorname{curl}\boldsymbol{U}^s \cdot \operatorname{curl}\overline{\boldsymbol{W}} - \omega^2\boldsymbol{\Lambda}_2(\boldsymbol{U}^s + \operatorname{grad} p)\cdot\overline{\boldsymbol{W}}\right)\mathrm{d}\Omega = \\ -\int_{\Gamma_1}\left(\boldsymbol{n}\wedge\boldsymbol{\Lambda}_1^{-1}\operatorname{curl}\boldsymbol{U}^s\right)\cdot\overline{\boldsymbol{W}}\,\mathrm{d}\Gamma \\ -\left\{\int_{\Omega_d}\left(\boldsymbol{\Lambda}_1^{-1}-\boldsymbol{I}\right)\operatorname{curl}\boldsymbol{U}^i\cdot\operatorname{curl}\overline{\boldsymbol{W}} - \omega^2\left(\boldsymbol{\Lambda}_2-\boldsymbol{I}\right)\boldsymbol{U}^i\cdot\overline{\boldsymbol{W}}\,\mathrm{d}\Omega\right\} \quad \text{(A.5)}\\ -\omega^2\int_{\Omega_f+\Omega_p+\Omega_d}(\boldsymbol{\Lambda}_2\boldsymbol{U}^s\cdot\operatorname{grad}\overline{q})\,\mathrm{d}\Omega = -\int_{\Gamma_1}\left(\boldsymbol{n}\wedge\boldsymbol{\Lambda}_1^{-1}\operatorname{curl}\boldsymbol{U}^s\right)\cdot\operatorname{grad}\overline{q}\,\mathrm{d}\Gamma \\ +\omega^2\int_{\Omega_d}\left(\boldsymbol{\Lambda}_2-\boldsymbol{I}\right)\boldsymbol{U}^i\cdot\operatorname{grad}\overline{q}\,\mathrm{d}\Omega \quad \text{(A.6)}\end{aligned}$$

for all $\boldsymbol{W} \in Z$ and for all $q \in \{\mathcal{H}^1, q = 0 \text{ on } \Gamma_2 \text{ and } \Gamma_3\}$.

To show that this mixed formulation is not required, we follow the approach given in Chapter 2, and substitute $\boldsymbol{W} = \operatorname{grad} q$ in equation (A.5) to obtain

$$\begin{aligned}-\omega^2\int_{\Omega_f+\Omega_p+\Omega_d}(\boldsymbol{\Lambda}_2(\boldsymbol{U}^s+\operatorname{grad}p)\cdot\operatorname{grad}\overline{q})\,\mathrm{d}\Omega = \\ -\int_{\Gamma_1}\left(\boldsymbol{n}\wedge\boldsymbol{\Lambda}_1^{-1}\operatorname{curl}\boldsymbol{U}^s\right)\cdot\operatorname{grad}\overline{q}\,\mathrm{d}\Gamma \\ +\omega^2\int_{\Omega_d}\left(\boldsymbol{\Lambda}_2-\boldsymbol{I}\right)\boldsymbol{U}^i\cdot\operatorname{grad}\overline{q}\,\mathrm{d}\Omega \quad \text{(A.7)}\end{aligned}$$

Substitution of equation (A.6) in to this expression leads to

$$\omega^2\int_{\Omega_f+\Omega_p+\Omega_d}(\boldsymbol{\Lambda}_2\operatorname{grad}p\cdot\operatorname{grad}\overline{q})\;\mathrm{d}\Omega = 0 \quad \text{(A.8)}$$

We now follow the arguments given in Chapter 2 to show that p may be omitted. If $\omega \gg 0$ is specified, then equation (A.8) implies that p is a constant, and it follows that since $p = 0$ on Γ_1 and Γ_2 this constant is equal to 0. For any solution $\boldsymbol{U}^s \in \mathcal{H}(\operatorname{curl};\Omega)$ the Lagrange multiplier is zero and may therefore be omitted. Hence, the weak variational statement given in equation (A.3) may be adopted.

Bibliography

[1] K.S. Yee. Numerical solution of the initial boundary value problems in isotropic media. *IEEE Transactions on Antennas and Propagation*, 14:302–307, 1966.

[2] O.C. Zienkiewicz. *The Finite Element Method*. McGraw-Hill, New York, 3rd edition, 1977.

[3] K. Morgan, P.J. Brookes, O. Hassan, and N.P. Weatherill. Parallel processing for the simulation of problems involving scattering of electromagnetic waves. *Computer Methods in Applied Mechanics*, 152:157–174, 1998.

[4] J.S. Hesthaven and T. Warburton. High–order/spectral unstructured grid methods for the time–domain solution of Maxwell's equations. In *Fourth International Workshop on Computational Electromagnetics in the Time Domain:TLM/FDTD and Related Techniques, Nottingham*, 2001.

[5] P. Bettess. *Infinite Elements*. Penshaw Press, Sunderland, 1992.

[6] J.–P. Berenger. A perfectly matched layer for the absorption of electromagnetic waves. *Journal of Computational Physics*, 114:185–200, 1994.

[7] W. Cecot, L. Demkowicz, and W. Rachowicz. A two dimensional infinite element for Maxwells equations. *Computer Methods in Applied Mechanics and Engineering*, 188:625–643, 2000.

[8] M. El-Hachemi, O. Hassan, K. Morgan, and N. Weatherill. The solution of the 2D Maxwell's equations on overlapping orthogonal grids. In *Proceedings of the ECCOMAS CFD Conference Swansea, Wales*, 2001.

[9] L. Demkowicz and L. Vardapetyan. Modeling of electromagnetic absorption/scattering problems using *hp*–adaptive finite elements. *Computer Methods in Applied Mechanics and Engineering*, 152:103–124, 1998.

[10] L. Vardapetyan and L. Demkowicz. hp–adaptive finite elements in electromagnetics. Technical Report 97–18, TICAM, 1997.

[11] L. Demkowicz and W. Rachowicz. A 2D hp–adaptive finite element package for electromagnetics (2dhp90em). Technical Report 98–15, TICAM, 1998.

[12] L. Demkowicz. A posteriori error analysis for steady state Maxwells equations. In P. Ladaveze and Oden J.T., editors, *New Advances in Adaptive Computational Methods in Mechanics*. Elsevier, New York, 1998.

[13] P.D. Ledger, K. Morgan, O. Hassan, and N.P. Weatherill. Arbitrary order edge elements for electromagnetic scattering simulations using hybrid meshes and a PML. *International Journal of Numerical Methods in Engineering*, In print.

[14] P.D. Ledger, O. Hassan, K. Morgan, and N.P. Weatherill. Arbitrary order edge elements and hybrid meshes for electromagnetic scattering problems. In *Proceedings of the First MIT Conference on Computational Fluid and Solid Mechanics*, 2001.

[15] M. Ainsworth, J. Coyle, P.D. Ledger, Morgan K., O. Hassan, and N.P. Weatherill. hp–finite element approximations of Maxwells equations on curvilinear hybrid meshes. In *Proceedings of the European Conference on Computational Mechanics, Cracow, Poland*, 2001.

[16] M. Ainsworth, J. Coyle, O. Hassan, P.D. Ledger, K. Morgan, and N.P. Weatherill. Hybrid arbitrary order edge based finite element methods for electro-

magnetic scattering problems. In *17th Annual Review of Progress in Applied Computational Electromagnetics, Monterey CA*, 2001.

[17] P.D. Ledger, K. Morgan, O. Hassan, and N.P. Weatherill. A hybrid arbitrary order edge element scheme for electromagnetic scattering. In *Proceedings of the ECCOMAS CFD Conference, Swansea, Wales*, 2001.

[18] K. Morgan, O. Hassan, P.D. Ledger, and N.P. Weatherill. Finite element algorithms for electromagnetic scattering simulation. In *Computational Mechanics for the Twenty–First Century*, 2000.

[19] R. J. Astley. Mapped spheroidal wave–envelope elements for unbounded wave problems. *International Journal for Numerical Methods in Engineering*, 41:1235–1254, 1988.

[20] O. Laghrouche, P. Bettess, and A.J. Astley. Modelling of short wave diffraction problems using approximating systems of plane waves. *International Journal for Numerical Methods in Engineering*, Submitted 2000.

[21] M. Kamon, M.J. Tusk, and J.K. White. FASTHENRY: a multipole accelerated 3D inductance extraction program. *IEEE Transactions on Microwave Theory and Technology*, 42:1750–1758, 1994.

[22] M. Ainworth and J.T. Oden. *A Posteriori Error Estimation in Finite Element Analysis*. John Wiley & Sons, New York, 2000.

[23] Y. Maday, A.T. Patera, and J. Peraire. A general framework for a–posteriori bounds for output functionals of partial differential equations; application to the eigenvalue problem. *C.R. Acad. Sci. Paris*, 2000.

[24] J. Peraire and A. T. Patera. Asymptotic *a–posteriori* finite element bounds for the outputs of noncoercive problems: the Helmholtz and Burgers equations. *Computer Methods and Applied Mechanics*, 171:77–86, 1999.

[25] J. Sarrate, J. Peraire, and A. Patera. A posteriori error bounds for nonlinear outputs of the Helmholtz equation. *Journal of Numerical Methods in Fluids*, 31:17–36, 1999.

[26] P.D. Ledger, J. Peraire, K. Morgan, O. Hassan, and N.P. Weatherill. Error estimation applied to finite element methods for computational electromagnetics. Final Report on EPSRC Research Grant GR/N09084/01, Department of Civil Engineering, University of Wales, Swansea, 2001.

[27] S. Seely. *Introduction to Electromagnetic Fields*. McGraw Hill, York, Toronto, 1960.

[28] C. A. Balanis. *Advanced Engineering Electromagnetics*. John Wiley & Sons, New York, 1989.

[29] F. Kikuchi. Mixed and penalty formulations for finite element analysis of an eigenvalue problem in electromagnetism. *Computer Methods in Applied Mechanics and Engineering*, 64:509–521, 1987.

[30] S., C. Brenner, and L. R. Scott. *The Mathematical Theory of Finite Element Methods*. Springer-Verlag, New York, Berlin, 1994.

[31] B. Szabó and I. Babuska. *Finite Element Analysis*. John Wiley and Sons, New York, 1991.

[32] J.C. Nédélec. Computation of eddy currents on a surface in $\mathbb{R}^3$ by finite element methods. *SIAM Journal of Numerical Analysis*, 15:580–594, 1978.

[33] J.C. Nédélec. Mixed finite elements in $\mathbb{R}^3$. *Numerische Mathematik*, 35:315–341, 1980.

[34] J.F. Lee. Analysis of passive microwave devices by using 3 dimensional tangential vector finite element fields. *International Journal of Numerical Modeling: Electronic Networks, Devices and Fields*, 3:235–246, 1990.

[35] P. Monk. On the p– and hp–extension of Nédélec curl–conforming elements. *Journal of Computational and Applied Mathematics*, 53:117–137, 1994.

[36] P. Monk. An analysis of Nédélec's method for the spatial discretisation of Maxwells equations. *Journal of Computational and Applied Mathematics*, 47:101–121, 1993.

[37] M. Ainsworth and J. Coyle. Hierarchic hp–edge element families for Maxwell's equations on hybrid quadrilateral/triangular meshes. *Computer Methods in Applied Mechanics and Engineering*, 190:6709–6733, 2001.

[38] P. D. Ledger. Edge elements for waveguide and scattering problems. Master's thesis, University of Wales, Swansea, 1999.

[39] J.P. Webb and B. Forghani. Hierarchical scaler and vector tetrahedra. *IEEE Transactions on Magnetics*, 29:1495–1498, 1993.

[40] R. Miniowitz and J.P. Webb. Covariant projection quadrilateral elements for the analysis of waveguides with sharp edges. *IEEE Transactions on Magnetics*, 39(3):301–305, 1991.

[41] I. A. Abramowitz, M.and Stegun. *Handbook of Mathematical Functions with Formulas, Graphs and Mathematical Tables*. National Bureau of Standards, Washington D.C., 1964.

[42] J. A. Stratton. *Electromagnetic Theory*. McGraw–Hill, New York, 1941.

[43] J. Peraire, M. Vahdati, K. Morgan, and O. C. Zienkiewicz. Adaptive remeshing for compressible flow computations. *Journal of Computational Physics*, 72:449–466, 1987.

[44] J. Peraire, J. Perió, and K. Morgan. Adaptive re–meshing for three–dimensional compressible flow computations. *Journal of Computational Physics*, 103:269–285, 1992.

[45] W. Liu and A. H. Sherman. Comparative analysis of the Cuthill–McKee and the reverse Cuthill–McKee ordering algorithms for sparse matrices. *SIAM Journal of Numerical Analysis*, 13:198–213, 1976.

[46] H. Kardestuncer. *Finite Element Handbook*. McGraw–Hill, New York, 1987.

[47] A. Deramaeker, I. Babuska, and P. Bouillard. Dispersion and pollution of the fem solution for the Helmholtz equation in one two and three dimensions. *International Journal of Numerical Methods in Engineering*, 46:471–499, 1999.

[48] A. Ainsworth and B. Senoir. Aspects of an adaptive hp–finite element method: Adaptive strategy conforming approximation and efficient solvers. *Computer Methods in Applied Mechanics and Engineering*, 150:65–67, 1997.

[49] A. Bayliss and E. Turkel. Radiation boundary conditions for wave–like equations. *Communications in Pure and Applied Mathematics*, 33:707–725, 1980.

[50] A. F. Peterson. Absorbing boundary conditions for the vector wave equation. *Microwave and Optical Technical Letters*, 1:62–64, 1988.

[51] D. Givoli. *Numerical Methods for Problems in Infinite Domains*. Elsevier, Amsterdam, 1992.

[52] J.–M. Jin, J. L. Volakis, and J. D. Collins. A finite element–boundary integral method for scattering and radiation by two– and three–dimensional structures. *IEEE Antennas and Propagation Magazine*, 33:22–32, 1991.

[53] M. Salazar–Palma, T.K. Sarker, L. Garcia–Castillo, T. Roy, and A. Djordjevic. *Iterative and Self Adaptive Finite Elements in Electromagnetic Modelling*. Artech House, Boston London, 1998.

[54] F. Collino and P. Monk. The perfectly matched layer in curvilinear coordinates. *SIAM Journal Scientific Computing*, 19:2061–2090, 1998.

[55] M. Kuzuoglu and R. Mittra. Investigation of nonplanar perfectly matched absorber for finite element mesh truncation. *IEEE Transactions on Antennas and Propagation*, 45:474–486, 1997.

[56] R.F. Harrington. *Time-Harmonic Electromagnetic Fields*. McGraw-Hill, New York, London, Boston, 1961.

[57] G.A. Watson. *A Treatise on the Theory of Bessel Functions*. Cambridge University Press, Cambridge, New York, Melbourne, 1944.

[58] P.D. Ledger, K. Morgan, N.P. Weatherill, and O. Hassan. Hybrid meshes of triangular and quadrilateral elements for electromagnetic scattering problems. In *8th annual ACME Conference, The University of Greenwich London*, 2000.

[59] K. Morgan, O. Hassan, and J. Peraire. A time domain unstructured grid approach to the simulation of electromagnetic scattering in piecewise homogeneous media. *Computer Methods in Applied Mechanics and Engineering*, 134:17–36, 1996.

[60] L. Machiels, A.T. Patera, J. Peraire, and Y. Maday. A general framework for finite element a posteriori error control: application to linear and nonlinear convection dominated problems. In *ICFD Conference on Numerical Methods in Fluid Dynamics, Oxford, England*, 1998.

[61] J. Peraire and A.T Patera. Bounds for linear functional outputs of coercive partial differential equations: local indicators and adaptive refinement. In *Proceedings of the Workshop on New Advances in Adaptive Computational Mechanics*, 1997.

[62] P. Monk. The near to far field transformation. *COMPEL The International Journal for Computation and Mathematics in Electrical and Electronic Engineering*, 14:41–56, 1995.

[63] P. Monk and E. Suli. The adaptive computation of far field patterns by a posteriori error estimation of linear functionals. *SIAM Journal of Numerical Analysis*, 36:251–274, 1998.

[64] P. Monk and K. Parrott. Phase accuracy and improved farfield estimates for 3–D edge elements on tetrahedral meshes. *Journal of Computational Physics*, In Print.